Methods for the Estimation of the Tissue Motion Using Digitized Ultrasound Echo Signals

by

Reza Zahiri Azar

B.A.Sc., Sharif University of Technology, 2003
M.A.Sc., University of British Columbia, 2005

A THESIS SUBMITTED IN PARTIAL FULFILLMENT OF
THE REQUIREMENTS FOR THE DEGREE OF

Doctor of Philosophy

in

The Faculty of Graduate Studies

(Electrical and Computer Engineering)

The University of British Columbia

(Vancouver)

December, 2009

Abstract

Tissue motion estimation in ultrasound images plays a central role in many modern signal processing applications, including tissue characterization, strain and velocity imaging, and tissue viscoelasticity imaging. Therefore, the performance of tissue motion estimation is of significant importance. Also, its computational cost determines if it can be implemented in real-time so that it can be used clinically. This thesis presents several efficient methods for accurate estimation of tissue motion using digitized ultrasound echo signals.

First, sample tracking algorithms are presented as a new class of motion estimators. These algorithms are based on the tracking of individual samples using a continuous representation of the reference echo signal. Simulations and experimental results on tissue mimicking phantoms show that sample tracking algorithms significantly outperform common algorithms in terms of accuracy, precision, sensitivity, and resolution. However, their performance degrades in the presence of noise.

To improve the performance of motion estimation in multi-dimensions, pattern matching interpolation techniques are studied and new interpolation techniques are presented. Simulation and experimental results show that, with small computational overhead, the proposed interpolation techniques significantly improve the accuracy and the precision of motion estimation in both 2D and 3D. Employing these techniques, real-time 2D motion tracking software is developed. Furthermore, the performance of the proposed 2D estimators is compared with that of 2D tracking using angular compounding. The results show that the proposed interpolation methods bring the performance of pattern matching techniques close to that of 2D compound tracking.

Finally, angular compounding is combined with custom pulse sequencing and delay cancellation techniques to develop a system that estimates the motion vectors at very high frame rates ($> 500\,\mathrm{Hz}$) in real-time. The application of the system in the study of the propagation of mechanical waves for tissue characterization is also presented.

Table of Contents

Abstract . . . ii

Table of Contents . . . iii

List of Tables . . . vii

List of Figures . . . viii

List of Abbreviations . . . x

Acknowledgments . . . xi

Dedication . . . xii

Statement of Co-Authorship . . . xiii

1 Introduction . . . 1
- 1.1 Background . . . 1
  - 1.1.1 Ultrasound Imaging . . . 1
  - 1.1.2 1D Motion Estimation Techniques . . . 2
  - 1.1.3 2D/3D Motion Estimation Techniques . . . 3
  - 1.1.4 Compound Tracking Techniques . . . 3
  - 1.1.5 High Frame Rate Tracking Techniques . . . 4
  - 1.1.6 Current *in-vivo* Applications . . . 5
- 1.2 Thesis Objectives . . . 5
- 1.3 Thesis Outline . . . 6

References . . . 8

2 Time-Delay Estimation in Ultrasound Echo Signals Using Individual Sample Tracking . . . 17
- 2.1 Introduction . . . 17
- 2.2 Proposed Algorithms . . . 19
  - 2.2.1 Sample Tracking . . . 19
  - 2.2.2 Spline-based Zero-Crossing Tracking . . . 21
- 2.3 Simulation Methods . . . 23
- 2.4 Simulation Results and Discussions . . . 24
- 2.5 Experimental Performance . . . 33
- 2.6 Conclusions . . . 35

References . . . 36

3 2D Estimation of Sub-Sample Motion from Digitized Ultrasound Echo Signals . . . 39
3.1 Introduction . . . 39
3.2 Methods . . . 41
3.2.1 Independent 1D Method . . . 43
3.2.2 Grid Slope . . . 43
3.2.3 Iterative 1D Method . . . 43
3.2.4 2D Method . . . 44
3.3 Simulations . . . 46
3.3.1 Simulation Setup . . . 46
3.3.2 Rigid Motion . . . 47
3.3.3 Deformation . . . 48
3.3.4 Simulation Results . . . 49
3.4 Experiments . . . 57
3.4.1 Experimental Setup . . . 57
3.4.2 Experimental Results . . . 58
3.5 Real-Time Implementation . . . 61
3.6 Discussions . . . 62
3.7 Conclusion and Future Work . . . 64

References . . . 65

4 3D Estimation of Sub-Sample Motion from Digitized Ultrasound Echo Signals . . . 71
4.1 Introduction . . . 71
4.2 Methods . . . 72
4.2.1 Independent 1D Methods . . . 73
4.2.2 3D Methods . . . 73
4.3 Simulations . . . 76
4.3.1 Simulation Setup . . . 76
4.3.2 Motion Estimation . . . 77
4.3.3 Simulation Results . . . 77
4.4 Experiments . . . 82
4.4.1 Experimental Setup . . . 82
4.4.2 Motion Estimation . . . 87
4.4.3 Conversion to Units of Distance . . . 87
4.4.4 Coordinate Transformation . . . 88
4.4.5 Experimental Results . . . 90
4.5 Discussions and Conclusion . . . 90

References . . . 94

5 Comparison Between Pattern Matching Techniques Employing 2D Sub-sample Estimation and 2D Tracking Using Angular Compounding 99
5.1 Introduction 99
5.2 Methods 100
5.2.1 Pattern Matching 101
5.2.2 Angular Compounding 101
5.3 Simulations 102
5.3.1 Simulation Setup 102
5.3.2 Simulation Results 103
5.4 Experiments 109
5.4.1 Experimental Setup 109
5.4.2 Experimental Results 110
5.5 Discussions and Conclusion 111

References 115

6 High Frame Rate Ultrasound for 2D Motion Estimation 118
6.1 Introduction 118
6.2 Data Acquisition 120
6.3 Signal Processing 121
6.3.1 Motion Estimation and Phasor Computation 121
6.3.2 Phase Correction 121
6.3.3 2D Reconstruction 123
6.4 Experimental Results 123
6.4.1 2D Flow Measurements 124
6.4.2 2D Wave Propagation Measurements 125
6.5 Discussion 128
6.6 Conclusion 130

References 131

7 Conclusions and Future Research 135
7.1 Multi-Dimensional Motion Estimation Techniques 135
7.2 Real-Time Motion Estimation 136
7.3 High Frame Rate Tracking 137
7.4 Summary of Contributions 137
7.5 Future Work 138

References 140

Appendices

A Local Polynomial Fitting 143

B Strain Signal to Noise Ratio 144

C 2D Normalized Cross Correlation 145

D 1D Sub-Sample Estimation 147

E 2D Sub-Sample Estimation 148
E.0.1 2D Paraboloid Fitting 148
E.0.2 2D Polynomial Fitting 148

F 3D Normalized Cross Correlation 150

G 3D Polynomial Fitting 152

List of Tables

3.1 Maximum values of biases and standard deviations obtained from the 2D noise-free simulations for window of $2 \times 2\,mm^2$. 53
3.2 The overall performance of 2D motion estimation techniques estimated from compression test for window of $2 \times 2\,mm^2$. 55
3.3 Maximum values of bias and standard deviation obtained from the 2D experimental data for window of $2 \times 2\,mm^2$. 61

4.1 Maximum values of biases and standard deviations of different 3D motion estimation techniques evaluated from simulated data in units of sample. 79

5.1 The overall performance of speckle pattern tracking using iterative 1D cosine fitting and compound imaging using 1D cosine fitting in simulated data. . . . 109
5.2 The overall performance of speckle pattern tracking using 2D polynomial fitting and compound imaging using 1D parabola fitting in simulated data. 110

List of Figures

2.1 Schematic of sample tracking . . . 19
2.2 Schematic representation of the zero-crossings tracking algorithm . . . 22
2.3 Bias and standard deviation of all the delay estimators . . . 25
2.4 Bias and standard deviation of all the techniques for different window sizes . . . 26
2.5 The bias of all the techniques and the standard deviation of window-based delay estimators . . . 27
2.6 Standard deviation of the delay estimators as a function of signal to noise ratio 30
2.7 Time-delay estimation images at different compression levels . . . 31
2.8 Signal-to-noise ratio of estimated strain as a function of applied compression . 32
2.9 Experimental displacement estimates using the sample tracking algorithm . . . 33
2.10 Displacement estimates using normalized cross correlation plus cosine fit and sample tracking algorithm of a phantom with a cylindrical hard inclusion . . . 34

3.1 Common techniques to reduce the error of discrete pattern matching functions 40
3.2 Different schemes for sub-sample displacement estimation in 2D . . . 42
3.3 Scatterer distributions and a Field II simulated sonogram . . . 47
3.4 FEM mesh, deformation constraints, scatterer distributions, and an example of the displacements of scatterers . . . 48
3.5 Biases and standard deviations of different pattern matching interpolation techniques as a function of sub-sample shift on a 11×11 grid. . . . 50
3.6 Grey level representations of the biases and standard deviations of different techniques. . . . 51
3.7 Grey level representations of the biases and standard deviations of different techniques using individual colorbars. . . . 52
3.8 Maximum values of biases and standard deviations obtained from the 2D simulations . . . 53
3.9 Axial and lateral displacement images computed by the FEM and estimated by different techniques . . . 54
3.10 Displacement vector images computed by the FEM and estimated by different techniques . . . 56
3.11 Biases and standard deviations of different pattern matching interpolation techniques on envelope signals . . . 57
3.12 Displacement estimates at actual scale . . . 58
3.13 Experimental set up . . . 59
3.14 Biases and standard deviations of different pattern matching interpolation techniques on a 9x9 grid . . . 60
3.15 Screen shots of the real-time 2D motion tracking software . . . 63

4.1 Different schemes for sub-sample displacement estimation in 3D 74
4.2 Scatterer distributions and a Field II simulated sonogram 76
4.3 Biases and standard deviations on a 3D grid 78
4.4 Grey level representations of the biases and standard deviations on a 3D grid . 80
4.5 Grey level representations of the biases and standard deviations on a 3D grid . 81
4.6 The overall performance of different 3D motion estimation techniques 83
4.7 The biases and the standard deviations on a 3D grid at the actual scale 84
4.8 The experimental setup 85
4.9 Second experimental setup 86
4.10 Variation of the spacing between lines as a function of depth 88
4.11 The transducer's coordinate frame and Cartesian coordinates 89
4.12 The estimated axial, lateral, and elevational components of the motion resulted from translations of the phantom in the water tank. 91
4.13 Simulated (top) axial, lateral, and elevational components of the displacement, resulted from axial compression of a phantom with a hard inclusion and the experimental results 92

5.1 Schematics for 2D motion tracking using pattern matching and beam steering . 101
5.2 Scatterer distributions and a Field II simulated sonograms when different steering angles are employed to acquire the data 104
5.3 Point target phantom imaged for different steering angles 105
5.4 Biases and standard deviations of the pattern matching method and beam steering employing different angles 106
5.5 Biases and standard deviations of the pattern matching method and beam steering employing different angles 107
5.6 The overall performance of all beam steering methods averaged over the simulated motion grid 108
5.7 The overall performance of all methods averaged over the simulated motion grid 111
5.8 The experimental setup 112
5.9 Experimental displacement estimates of 2D pattern matching techniques and beam steering techniques 113

6.1 Two different techniques to acquire high frame rate from two steering angles . 122
6.2 A diagram showing the basic signal processing blocks used in 2D high frame rate imaging. 123
6.3 Schematics for the reconstruction of a 2D measurement using 1D measurements estimated from two steering angles. 124
6.4 Schematics of the experimental setup used for testing the system using flow phantom. 125
6.5 Spatially aligned 1D motions estimated for different steering angles and axial and lateral components of the motion reconstructed from the same set of data . 126
6.6 Schematics of the experimental setup used for testing the system using a mechanical vibrator. 127
6.7 Snapshot of wave images after 1D motions estimation and phase correction for both steering angles are shown 129

List of Abbreviations

1D/2D/3D	One/Two/Three Dimensional
ARFI	Acoustic Radiation Force Impulse
BS	Beam Steering
c	Speed of Sound
CNR	Contrast to Noise Ratio
CTDE	Continuous Time Delay Estimator
decorrelated	less similar
downsampling	discarding samples to reduce the sampling rate
ECG	Electrocardiogram
FEM	Finite Element Method
FOV	Field Of View
inhomogeneities	locations where physical properties change
insonification	transmission of ultrasound (into a tissue)
PM	Pattern Matching
PVC	Polyvinyl Chloride
RF	Radio Frequency echo signals
ROI	Region of Interest
scatterers	small inhomogeneities that reflect ultrasound
SNR	Signal to Noise Ratio
sonogram	a conventional ultrasound image; a 2D image showing the envelope of ultrasound signals
ST	Sample Tracking
STD	Standard Deviation
TDE	Time Delay Estimator
subsample	between samples; a fraction of the sample spacing
transducer	any device converting signals between different physical bases (e.g. from ultrasonic pressure waves to electrical signals)
upsampling	increasing the number of samples to increase the sampling rate
ZCT	Zero Crossing Tracking

Acknowledgments

I would primarily like to thank my supervisor Professor Tim Salcudean for his valuable insight into my research and support during the course of this thesis. Without his guidance and inspiration throughout the process, none of this would have been possible. My thanks also go to Professor Jonathan Ophir, Professor Peter Lawrence, and Professor Robert Rohling for their continually helpful advice. I would also like to thank Kris Dickie and Laurent Pelissier from Ultrasonix Medical Corporation for their help and technical support throughout this research. I am grateful to all my friends and colleagues in the Robotics and Control lab, Julian, Ehsan, Hani, Orcun, and Sara for their help and advices. I owe my loving thanks to my wife Sara, who has been with me at every step. Without her support, encouragement and understanding it would have been impossible for me to finish this work. Finally, I am sincerely grateful to my parents who have always been the biggest motivation throughout my studies and whose years of unconditional love and support created the opportunity for me to chase my dreams.

Dedication

To my parents

Statement of Co-Authorship

This thesis is based on several manuscripts, resulting from collaboration between multiple researchers.

A version of Chapter 2 has been published. This paper was co-authored with Dr. Tim Salcudean. The author's contribution in that paper was developing the idea, numerical simulation, phantom fabrication, experimental evaluation of the algorithms and writing the manuscript.

A version of Chapter 3 has been submitted for publication. The paper was co-authored with Orcun Goksel, Ehsan Dehghan, David Yao, Dr. Joseph Yan, and Dr. Tim Salcudean. The author's contribution in that papers was developing the algorithms, numerical simulation, phantom fabrication, experimental evaluation, and implementation of the algorithms for real-time performance on ultrasound machine. Orcun Goksel helped with data simulation using Field II and FEM as well as editing the manuscript. Ehsan Dehghan helped with implementation of the algorithms. David Yao and Dr. Joseph Yan helped with the design and calibration of the 2D motion stage for the experimental validation.

A version of Chapter 4 has been submitted for publication. The paper was co-authored with Orcun Goksel and Dr. Tim Salcudean. The author's contribution in that paper was developing the algorithms, numerical simulation, phantom fabrication, and experimental evaluation. Orcun Goksel helped with data simulation using Field II as well as editing the manuscript.

A version of Chapter 5 will be submitted for publication. This paper was co-authored with Dr. Tim Salcudean. The author's contribution in that paper was developing the algorithms, numerical simulation, phantom fabrication, and experimental evaluation.

A version of Chapter 6 has been submitted for publication. This paper was co-authored with Ali Baghani and Dr. Tim Salcudean. The author's contribution in that paper was expanding the previously introduced high frame rate system to two dimensions using beam steering techniques, phantom fabrication, and experimental evaluation as well as writing the manuscript. Ali Baghani helped with delay compensation techniques used in the system.

In addition to general research directions, Dr. Salcudean as my supervisor helped with his numerous suggestions in the course of enhancing the data acquisition, data processing, and visualizing the results, as well as editing all the manuscripts.

Chapter 1

Introduction

1.1 Background

The basis of medical imaging is the measurement of a property of tissue that varies with spatial location. Medical images are formed by displaying these properties measured at multiple locations in the body. From such images, a depiction of anatomy or pathology is gained. Each imaging modality in common use, such as X-ray, computed tomography, ultrasound and magnetic resonance imaging, measures a different property of tissue. But none of the properties measured by these modalities depict directly the mechanical properties of soft tissue even though such images have proven to be useful in numerous clinical applications.

Changes in the mechanical properties of biological tissue often represent a warning sign for disease and imaging these properties provides a way of differentiating normal from abnormal tissues [1–3]. Elastography, as a relatively new imaging technique, aims to produce images that depict these mechanical properties for clinical applications. In the past two decades a great number of techniques have been suggested in the literature to provide these type of images. All these techniques use multiple measurements of tissue displacements to infer local tissue mechanical properties and are typically categorized based on (i) the type of excitation used, such as quasi-static compressions [4–8], harmonic waves [9–12], wide-band excitations [12, 13], or transient/pulsed waves [14–18], (ii) the way these excitations are generated, for instance using internal tissue motions due to heartbeat or breathing [19–23], acoustic radiation force [12, 24–27], or an external actuation applied through a mechanical exciter or transducer motion [7, 14, 28–30]), (iii) the imaging modality used to estimate the resulting tissue motion, namely ultrasound, [4, 14, 25] or the use of hydrophone [27], magnetic resonance imaging [30–32], or optical imaging [33], and (iv) the type of image they produce, such as strain [4, 5, 34], compliance [13, 35], displacement amplitude [9, 10], compressibility [36], relative visco-elasticity [24, 28, 29], or absolute viso-elasticity [11, 12, 14, 30, 37–39].

Regardless of which technique is employed, tissue motion estimation lies at the heart of all the above methods. Because of its central importance, its accuracy, precision, and computational cost are of critical importance. As mentioned above, in principle, several imaging modalities can be used in order to estimate the tissue motion for elastography but ultrasound has received the most attention due to its safety, low cost, real-time performance, quick setup procedure and easy access to digital data. Thus, in this thesis we focus on the estimation of tissue motion in sequences of ultrasound echo signals.

1.1.1 Ultrasound Imaging

An ultrasound imaging system acquires data through the generation of an ultrasound wave directed toward the area to be examined, followed by measurement of the echoes generated by the interaction of the ultrasound wave with the tissue. The ultrasound system consists

of a transducer for generating the ultrasound pulses and measurement of the echoes, and a computation system to convert the echo signals into an image. The ultrasound transducer sends out a short burst of ultrasound and listens for the returning echoes. The time between the sent pulse and the received echo is used to calculate the depth of the interfaces assuming the speed of sound is constant throughout the media. The form of the transmitted wave is an amplitude modulated signal with a fixed carrier frequency determined by the probe and the returning echoes are sampled during the listening interval. These unprocessed digitized echo signals are known as radio frequency (RF) data. The RF data go through envelope detection, logarithmic amplitude compression, and conversion to regular spatial coordinates (called scan conversion). An image formed this way is generally called a B-image (i.e. Brightness image) or a sonogram [40–42].

1.1.2 1D Motion Estimation Techniques

Since ultrasound imaging provides higher resolution in the direction of beam propagation, the estimation of the axial component of the motion has received the most attention in the literature. Due to the nature of ultrasound, where the echo signals are acquired as a function of time, 1D motion estimators are generally being referred to as delay estimators. Delay estimators measure displacement of the backscattered signals with respect to the transducer. This displacement appears as a time-shift or phase-shift between sequences of echo signals [43]. Delay estimators are typically classified based on the type of signal (RF, envelope, in-phase and quadrature I/Q) and the domain on which they operate (i.e. time, phase, or frequency). These estimators have been studied and compared extensively in the literature [44–47].

Phase-shift estimators were initially used for blood flow measurement. Later, the same techniques were used in other fields in order to estimate tissue motion. Phase-shift estimators find the average phase-shift over a number of samples within a window with respect to the nominal or estimated central frequency of the transmitted pulse. Complex cross correlation of the RF echo signals [48, 49] or complex-valued Doppler signals [43, 50] are typically used in these techniques.

Time-shift estimators typically consist of the identification of the maximum/minimum of a pattern matching function. The shape of the signal within a specific window in the reference echo signal is set to be the pattern and a matching algorithm is used to find the best match in the delayed echo signal. Several pattern matching techniques are currently employed, each offering trade offs between complexity and accuracy [44, 51, 52]. The estimation error of the pattern matching techniques can be as large as half the sample spacing. Several techniques have been suggested in the literature to reduce the error introduced by finite sampling intervals. These techniques are categorized as: (i) echo signal up-sampling [47,53,54], (ii) interpolation of the echo signals [47,53,55,56], and (iii) interpolation of the pattern matching function [57–60].

Up-sampling of the echo signal as in (i) reduces the error by the up-sampling factor [47,54]. Curve or polynomial fitting to the echo signals as in (ii) results in a continuous pattern matching function, whose extremum determines the location of the best match [47, 53, 55, 56]. These techniques can be computationally demanding [56, 61], whereas curve or polynomial fitting to the pattern matching function as in (iii) often has significantly smaller computational overhead. Thus, even though they may introduce some bias in the estimation process, they are widely used for motion estimation. Many 1D pattern matching interpolation methods have been proposed for 1D axial motion estimation with sub-sample accuracy. These include parabolic

fitting [60], spline fitting [59], grid slope [62], and cosine fitting [58], and have been thoroughly investigated in the literature [44].

Some of the alternative approaches that make use of feature extraction have also been attempted in the literature. Zero-crossing tracking (ZCT) [63] identifies the zero-crossings of the echo signals using linear interpolation. Peak tracking and level-crossing tracking, wherein tracking is performed on a predefined amplitude level, have also been suggested in [63] as extensions of ZCT. The peak searching algorithm [64] identifies the peaks of the echo signals using a wavelet transform. The distances between the zero-crossings (or level-crossings) or peaks represent the time-shifts. ZCT and PSA provide as many measurement points as there are zero/level crossings or peaks within the signals. As a result they have the potential to provide much higher resolution than window-based techniques.

1.1.3 2D/3D Motion Estimation Techniques

Tracking the motion in one direction introduces some limitations for different applications. In blood flow and tissue velocity estimation using Doppler techniques, tracking along the beam propagation results in a poor estimation of the flow and tissue velocity due to the unknown Doppler angle between the velocity vector and the beam direction. Poor estimates can result even if the angle is manually adjusted [65,66]. In quasi-static elastography, tracking the motion in the axial direction results in estimation of only one component of the strain tensor (i.e. axial), with all the other components remaining unknown [67]. Finally, in dynamic elastography, using the wave equations, the estimation of a single component of motion limits modulus estimation algorithms to a less accurate partial inversion rather than a full inversion [68].

Techniques based on pattern matching functions are the most straightforward approaches used to estimate the axial motion from digitized ultrasound echo signals [4, 62, 69, 70]. Extensions of these techniques to 2D and 3D motion estimation have been proposed in the literature [71, 72] As mentioned above, the estimation error of the pattern matching techniques can be as large as half the sample spacing, which is important especially when the motion is small and the sample spacing is large. This error becomes more significant in the lateral and elevational directions where the sample spacing is very large. Similarly to 1D tracking, techniques like echo signal up-sampling [54] and interpolation of the echo signals [55, 56] in multi dimensions have been suggested in the literature. Also the same 1D sub-sample estimation techniques have been applied independently for each direction in 2D or 3D motion estimation to estimate the sub-sample lateral and elevational motions [55, 73].

1.1.4 Compound Tracking Techniques

Angular compounding has also been attempted in the literature to estimate the motion vectors [74–78]. With this technique the data from the region of interest is acquired from multiple look angles. The multiple look angles can originate from a single transducer when it is moved mechanically, or they can originate from multiple transducers [74]. The multiple look angles can also originate from a single transducer using single transmit and multiple receive angles [77–79] or multiple electronically steered transmit and receive angles [75,78,80]. Once the data from multiple angles are acquired, previously introduced 1D motion estimators are employed to estimate the motion along the direction of beam propagation for each angle independently.

Estimations are then compounded to construct the 2D motion vectors inside the overlapping region.

1.1.5 High Frame Rate Tracking Techniques

Conventional ultrasound systems are based on line by line acquisition of the echo signals in order to acquire the entire 2D image. As a result, the acquisition time of each frame in these systems is proportional to the number of scan lines and the acquisition time of each scan line in that frame. However, high frame rate motion estimation is critical for a wide range of clinically used ultrasound imaging modes. Several techniques have been attempted in the literature in order to increase the imaging frame rates. In one simple approach high frame rate is achieved by reducing the number of scan lines. This technique increases the frame rates but results in reduction in the field of view (FOV) and/or spatial resolution depending on the spacing between scan lines. This technique has been used in [23, 81] to study myocardial motion.

In another approach high temporal resolution is achieved by beam interleaving techniques [82]. This technique divides the region of interest (ROI) into small sectors and acquires each sector at a high temporal resolution (200 Hz to 10 kHz depending on the number of scan lines per sector and the imaging depth) for a short period of time before moving on to the next sector, etc until all the observations for the entire ROI are acquired. Assuming that the time between the acquisitions of neighboring scan lines is small, the acquisition in each sector can be considered as a snapshot of the speckle movements. This technique will provide both high spatial resolution and temporal resolution. However, large delays are introduced between the data acquired from different sectors. This technique is commonly used in conventional color flow imaging, power Doppler imaging, and B flow imaging [82, 83]. The same technique is also used in [84] to evaluate regional myocardial deformation and in [11] to study the propagation of crawling waves in tissue using tissue Doppler imaging. Using the same acquisition scheme, compounding Doppler imaging has also been attempted in the literature to estimate the motion vectors using both beam steering and multi-synthetic aperture beamforming [77, 78].

With the help of parallel receive beamformers, techniques like multi-line-acquisitions (MLA) have also been used to increase the frame rate of conventional ultrasound machines where multiple echo signals (typically 2-8) are acquired from single transmit [85], thus, multiplying the effective frame rate by the same factor at little cost to the resolution [22]. In [86], MLA was used to reduce transducer heating and acoustic exposure, and to facilitate data acquisition for real-time ARFI imaging. The idea of MLA was also extended to the acquisition of the entire image as opposed to multiple lines, thus, drastically increasing the effective frame rates (>5 kHz). This method is generally being referred to as ultrafast imaging where a single unfocused plane wave is used for transmit and parallel receive beamformers (typically 64-128) are used to generate the scan lines. In [17, 87], ultrafast imaging was used to capture the propagation of the transient shear wave in soft tissue and to estimate the tissue elasticity. In [79] ultrafast imaging was combined with angular compounding using multi-synthetic aperture beamforming to follow both the axial and the lateral components of the motion during the shear wave propagation at a frame rate of 6 kHz. Even though very effective, both MLA and ultrafast imaging are not generally available on conventional ultrasound systems. Additional hardware overhead is required to implement each of these techniques on conventional ultrasound systems.

Techniques like coded excitations have also been introduced in the literature to increase the frame rate of the ultrasound acquisition [88–90]. However, these techniques increase the

beam density and similar to MLA and ultrafast imaging require specialized hardware.

In another approach to achieve high frame rates, synchronization techniques have been employed in the literature. The data acquisition in these techniques is similar to that of conventional color flow and power Doppler imaging to achieve high temporal resolution. However, to eliminate long delays between sectors, the start of data acquisition for each sector is synchronized with the exciter which varies from an external actuator (e.g. mechanical vibrator) to a signal generated in the body (e.g. electrocardiogram ECG). In [91], by synchronizing the data acquisition and an external exciter the shear-wave propagation in the scan plane was imaged at a frame rate of 6 kHz using a single element transducer. A similar approach was used in [92] to study both the transient and harmonic shear-wave scattering in both two and three dimensions using linear array transducers at a frame rate of 4 kHz. By synchronizing the image acquisition with the ECG signals, the propagation of several transient mechanical waves was imaged in different regions of the myocardium in mice at a frame rate of 8 kHz in [93] and in humans at a frame rate of 481 Hz in [20]. These techniques require additional hardware to synchronize the excitation and the data acquisition. Also, at the end of imaging of each sector, the system needs to wait long enough to make sure the tissue returns back to its initial position prior to the next excitation. Otherwise, artifacts will appear in the final image when different sectors are stitched together. This waiting time will generally increase the total data acquisition time in these techniques.

1.1.6 Current *in-vivo* Applications

Mechanical properties of tissue are often associated with tissue state. Thus, they can be used for diagnosis. Medical applications of both quasi-static and dynamic elastography methods with the underlaying motion tracking algorithms span a wide range of modern clinical applications. These applications include but are not limited to tumor detection and classification in breast [5,8,14,34,94–97], prostate [11,98,99], and skin [100], detection of diffuse diseases such as liver fibrosis [12], myocardial elasticity imaging [19, 81, 84, 93], distinguishing between normal and lymphedematous tissues [36], characterization of vascular plaques [21], the impact of aging and gender on brain viscoelasticity [101], monitoring aging of deep venous thrombosis [102, 103], imaging of thermal lesion in the liver [104, 105], monitoring renal transplant for early rejection [106], quantifying hepatic elasticity [107], imaging the abdomen [108], and the study of skeletal muscle contraction [109].

1.2 Thesis Objectives

The following objectives are defined in this thesis:

1. Developing new algorithms for the estimation of motion in sequences of ultrasound echo signal in 1D (axial component only), 2D (both axial and lateral components), and 3D (axial, lateral, and elevational components), with high accuracy and precision and small computational overhead, to make them suitable for real-time applications.

2. Studying the performance of these techniques using both simulation and experimental data in terms of accuracy, precision, sensitivity, and resolution and comparing them with state of the art techniques.

3. Implementing a system based on the proposed methods to estimate the motion in multiple dimensions at commonly used ultrasound frame rates (up to 50 Hz).

4. Overcoming the inherent low frame rate of conventional ultrasound and implementing a system to facilitate motion tracking in several dimensions at high frame rates (> 500 Hz).

1.3 Thesis Outline

The thesis presented here is written in the manuscript-based style, as permitted by the Faculty of Graduate Studies at the University of British Columbia. In the manuscript-based thesis, each chapter represents an individual work that has been published, submitted or prepared for submission to a peer reviewed publication. Each chapter is self-contained in the sense that it includes an introduction to the work presented in that chapter, the methodology, simulations and experiments, results and discussion. The references are summarized in the bibliography found at the end of each chapter. The appendices pertaining to each chapter are presented at the end of the thesis.

In the course of achieving the primary objectives of this thesis, the following contributions were made:

1. In Chapter 2 a new class of time-delay estimators based on the tracking of the individual echo samples called Sample Tracking (ST) is presented to improve the accuracy, precision, resolution, and sensitivity of one dimensional motion estimation. The use of the same interpolation approach to improve the performance of a previously developed ZCT delay estimator [63] is also presented. Simulation results show that sample tracking algorithms significantly outperform commonly used window based algorithms in terms of bias and standard deviation. ST algorithms also have higher sensitivity and resolution compared to traditional delay estimators, including recently introduced spline-based continuous time-delay estimators as they provide the displacement of individual samples. However, their performance degrades as the SNR of the echo signals becomes low. Experimental results demonstrating the viability of ST in addition to their extension to several dimensions are also presented.

2. In Chapter 3 we consider the problem of estimating 2D motion in ultrasound echo data images with sub-sample accuracy. We propose an approach based on iterative 1D interpolation, as well as approaches based on 2D interpolation. We study these techniques using both simulated and experimental data and compare them to other methods in the literature. The results show that the proposed methods significantly outperform other techniques in terms of both accuracy and precision. Employing the proposed methods, a real-time implementation of a 2D motion tracking algorithm is also presented.

3. Extending our previous 2D work, in Chapter 4 we introduce 3D sub-sample estimation techniques. We study this method using a synthetic phantom and the Field II ultrasound simulation software. A comparison with other reported methods shows that the proposed 3D interpolation-based method outperforms other common techniques in terms of accuracy and precision. Experimental results demonstrating the viability of the proposed method are also presented.

4. In Chapter 5, we study and compare the performance of 2D pattern matching techniques employing 2D sub-sample estimation with that of 2D tracking using angular compounding. Simulations using the Field II ultrasound simulation software on a synthetic phantom and real ultrasound data acquired from tissue mimicking phantoms were used for this study. The results show that our proposed 2D interpolation techniques bring the performance of the 2D pattern matching close to that of motion vector imaging using angular compounding.

5. In Chapter 6 to overcome the inherent low frame rate of ultrasound for motion estimation in several dimensions, the delay cancellation techniques previously introduced in our laboratory are combined with angular compounding to develop a system that reconstructs the motion vectors at high frame rates. The system achieves both high spatial (line density of up to 128) and high temporal resolution ($> 500\,\text{Hz}$) at an imaging depth of 5 cm and a 100% field of view. Applications of the system in studying the wave propagation in two dimensions, and flow vector imaging are presented with experimental results from phantoms.

6. In Chapter 7 the results of the collected works are related to one another and a unified goal of the thesis is discussed. The strengths and weaknesses of the research are then presented, along with future directions for research.

References

[1] J. Ophir, S. Alam, B. Garra, F. Kallel, E. Konofagou, T. Krouskop, C. Merritt, R. Righetti, R. Souchon, S. Srinivasan, and T. Varghese, "Elastography: Imaging the Elastic Properties of Soft Tissues with Ultrasound," *Medical Ultrasound*, vol. 29, pp. 155–171, 2002.

[2] J. Greenleaf, M. Fatemi, and M. Insana, "Selected Methods for Imaging Elastic Properties of Biological Tissues," *Annual Review of Biomedical Engineering*, vol. 5, pp. 57–78, August 2000.

[3] L. Gao, K. Parker, R. Lerner, and S. Levinson, "Imaging of the elastic properties of tissue-a review," *Ultrasound in Medicine and Biology*, vol. 22, pp. 959–77, 1996.

[4] J. Ophir, I. Cespedes, H. Ponnekanti, Y. Yazdi, and X. Li, "Elastography: a quantitative method for imaging the elasticity of biological tissues," *Ultrasonic Imaging*, vol. 13, pp. 111–134, April 1991.

[5] I. Cespedes, J. Ophir, H. Ponnekanti, and N. F. Maklad, "Elastography: elasticity imaging using ultrasound with application to muscle and breast in vivo," *Ultrasonic Imaging*, vol. 15, pp. 73–88, 1993.

[6] J. Ophir, S. Alam, B. Garra, F. Kallel, E. Konofagou, T. Krouskop, and T. Varghese, "Elastography: ultrasonic estimation and imaging of the elastic properties of tissues," *Ultrasonic Imaging*, vol. 213, pp. 203–33, 1999.

[7] T. Hall, Z. Yanning, and C. Spalding, "In vivo real-time freehand palpation imaging." *Ultrasound in medicine and biology*, vol. 29, pp. 427–435, 2003.

[8] M. Doyley, J. Bamber, F. Fuechsel, and N. Bush, "A freehand elastographic imaging approach for clinical breast imaging: System development and performance evaluation," *Ultrasound in Medicine and Biology*, vol. 27, pp. 1347–1357, 2001.

[9] R. Lerner, S. Huang, and K. Parker, "'Sonoelasticity' images derived from ultrasound signals in mechanically vibrated tissues," *Ultrasound in Medicine and Biology*, vol. 16, no. 3, pp. 231–239, 1990.

[10] K. Parker, S. Huang, R. Musulin, and R. Lerner, "Tissue response to mechanical vibrations for 'sonoelasticity imaging'," *Ultrasound in Medicine and Biology*, vol. 16, no. 3, pp. 241–246, 1990.

[11] K. Hoyt, K. Parker, and J. Rubens, "Real-Time Shear Velocity Imaging Using Sonoelastographic Techniques," *Ultrasound in Medicine and Biology*, vol. 33, p. 10861097, 2007.

[12] S. Chen, M. Urban, C. Pislaru, R. Kinnick, Y. Zheng, A. Yao, and J. Greenleaf, "Shearwave dispersion ultrasound vibrometry (SDUV) for measuring tissue elasticity and viscosity," *IEEE Transactions on Ultrasonics, Ferroelectrics, and Frequency Control*, vol. 56, pp. 55–62, Jan 2009.

[13] E. Turgay, S. Salcudean, and R. Rohling, "Identifying Mechanical properties of Tissue by Ultrasound." *Ultrasound in Medicine and Biology*, vol. 32, pp. 221–235, 2006.

[14] J. Bercoff, S. Chaffai, M. Tanter, L. Sandrin, S. Catheline, J. Fink M., Gennisson, and M. Meunier, "In vivo breast tumor detection using transient elastography." *Ultrasound in Medicine and Biology*, vol. 29, pp. 1387–1396, Oct 2003.

[15] J. Bercoff, M. Tanter, and M. Fink, "Supersonic shear imaging: a new technique for soft tissue elasticity mapping," *IEEE Transactions on Ultrasonics, Ferroelectrics and Frequency Control*, vol. 51, pp. 396–4009, April 2004.

[16] S. Catheline, J.-L. Thomas, F. Wu, and M. Fink, "Diffraction field of a low frequency vibrator in soft tissues using transient elastography," *IEEE Transactions on Ultrasonics, Ferroelectrics and Frequency Control*, vol. 46, pp. 1013–19, July 1999.

[17] S. Catheline, J.-L. Gennisson, G. Delon, and M. Fink, "Viscoelastic properties of soft solids using transient elastography," in *Second International Conference on the Ultrasonic Measurement and Imaging of Tissue Elasticity*, Corpus Christi, U.S., October 2003, pp. 25–25.

[18] L. Sandrin, M. Tanter, D. Cassereau, S. Catheline, and M. Fink, "Low-frequency shear wave beam forming in time-resolved 2D pulsed elastography," *Proceedings of the IEEE Ultrasonics Symposium*, vol. 2, pp. 1803–1808, October 2000.

[19] W. Lee, C. M. Ingrassia, S. D. Fung-Kee-Fung, K. D. Costa, J. W. Holmes, and E. Konofagou, "Theoretical Quality Assessment of Myocardial Elastography with In Vivo Validation," *IEEE Transactions on Ultrasonics, Ferroelectrics and Frequency Control*, vol. 54, pp. 2233–2245, 2007.

[20] S. Wang, W. Lee, J. Provost, L. Jianwen, and E. Konofagou, "A composite high-framerate system for clinical cardiovascular imaging." *IEEE Transactions on Ultrasonics, Ferroelectrics and Frequency Control*, vol. 55, pp. 2221–2233, Oct 2008.

[21] C. de Korte, A. van der Steen, E. Cspedes, G. Pasterkamp, S. Carlier, F. Mastik, A. Schoneveld, P. Serruys, and N. Bom, "Characterisation of plaque components and vulnerability with Intravascular Ultrasound Elastography," *Physics in Medicine and Biology*, vol. 45, pp. 1465–1475, 2000.

[22] K. Kaluzynski, C. Xunchang, S. Emelianov, A. Skovoroda, and M. O'Donnell, "Strain rate imaging using two-dimensional speckle tracking." *IEEE Transactions on Ultrasonics, Ferroelectrics and Frequency Control*, vol. 48, pp. 1111–1123, July 2001.

[23] H. Kanai, Y. Koiwa, and J. Zhang, "Real-time measurements of local myocardium motion and arterial wall thickening." *IEEE Transactions on Ultrasonics, Ferroelectrics and Frequency Control*, vol. 46, pp. 1229–1241, 1999.

[24] A. Sarvazyan, O. Rudenko, S. Swanson, J. Fowlkes, and E. S.Y., "Shear wave elasticity imaging: a new ultrasonic technology of medical diagnostics," *Ultrasound in Medicine and Biology*, vol. 24, pp. 1419–35, December 1998.

[25] K. Nightingale, M. Palmeri, R. Nightingale, and G. Trahey, "On the feasibility of remote palpation using acoustic radiation force," *Journal of the Acoustical Society of America*, vol. 110, pp. 625–34, July 2001.

[26] W. Walker, F. Fernandez, and L. Negron, "A method of imaging viscoelastic parameters with acoustic radiation force." *Physics in Medicine and Biology*, vol. 45, pp. 1437–1447, 2000.

[27] M. Fatemi and J. Greenleaf, "Probing the dynamics of tissue at low frequencies with the radiation force of ultrasound," *Physics in Medicine and Biology*, vol. 45, pp. 1449–64, June 2000.

[28] H. Eskandari, S. Salcudean, and R. Rohling, "Viscoelastic Parameter Estimation Based on Spectral Analysis." *IEEE Transactions on Ultrasonics, Ferroelectrics, and Frequency control*, vol. 55, pp. 1611–1625, July 2008.

[29] H. Eskandari, S. Salcudean, R. Rohling, and J. Ohayon, "Viscoelastic Characterization of Soft Tissue from Dynamic Finite Element Models." *Physics in Medicine and Biology*, vol. 53, pp. 6569–6590, Nov 2008.

[30] S. Papazoglou, U. Hamhaber, J. Braun, and I. Sack, "Algebraic Helmholtz inversion in planar magnetic resonance elastography." *Physics in Medicine and Biology*, vol. 53, pp. 3147–3158, 2008.

[31] R. Muthupillai, D. Lomas, P. Rossman, J. Greenleaf, A. Manduca, and R. Ehman, "Magnetic resonance elastography by direct visualization of propagating acoustic strain waves," *Science*, vol. 269, pp. 1854–7, September 1995.

[32] T. Oliphant, "Direct Methods for Dynamic Elastography Reconstruction: Optimal Inversion of the Interior Helmholtz Problem." Ph.D. dissertation, Mayo Graduate School, 2001.

[33] J. Jurvelin, M. Buschmann, and E. Hunziker, "Optical and mechanical determination of Poisson's ratio of adult bovine humeral articular cartilage," *Journal of Biomechanics*, vol. 30, pp. 235–41, March 1997.

[34] A. Thitaikumar, L. Mobbs, C. Kraemer-Chant, B. Garra, and J. Ophir, "Breast Tumor Classification using axial shear strain elastography: a feasibility study," *Physics in Medicine and Biology*, vol. 53, pp. 4809–4823, 2008.

[35] S. Papazoglou, C. Xu, U. Hamhaber, E. Siebert, G. Bohner, R. Klingebiel, J. Braun, and I. Sack, "Scatter-based magnetic resonance elastography." *Physics in Medicine and Biology*, vol. 54, pp. 2229–2241, 2009.

[36] R. Righetti, J. Ophir, S. Srinivasan, and T. Krouskop, "The Feasibility of Using Elastography for Imaging the Poissons Ratio in Porous Media," *Ultrasound in Medicine and Biology*, vol. 30, pp. 215–228, 2004.

[37] A. Skovoroda, S. Emelianov, and M. O'Donnell, "Tissue Elasticity Reconstruction Based on Ultrasonic Displacement and Strain Images." *IEEE Transactions on Ultrasonics, Ferroelectrics and Frequency Control*, vol. 42, pp. 747–65, July 1995.

[38] P. Barbone, "A variational formulation leading to direct elastic modulus reconstruction," in *Second International Conference on the Ultrasonic Measurement and Imaging of Tissue Elasticity*, Corpus Christi, U.S., October 2003, pp. 67–67.

[39] S. Aglyamov, A. Skovoroda, J. Rubin, M. O'Donnell, and E. SY, "Young's modulus reconstruction in DVT elasticity imaging," in *In: Linzer M, ed. 27th International Symposium on Ultrasonic Imaging and Tissue Characterization.* Arlington, VA: Ultrason Imaging, 2002, p. 174.

[40] F. Kremkau, Ed., *Diagnostic Ultrasound: Principles and Instruments, 4th Edition.* W.B. Saunders Company, 1993, ch. 1.

[41] W. McDicken, Ed., *Diagnostic Ultrasonics: Principles and use of Instruments, 3rd Edition.* Churchill Livingstone, 1991, ch. 1.

[42] A. Christensen, Ed., *Ultrasonic Bioinstrumentation.* John Wiley and Sons, 1988, ch. 6.

[43] T. Loupas, R. Peterson, and R. Gill, "Experimental evaluation of velocity and power estimation forultrasound blood flow imaging, by means of a two-dimensional autocorrelation approach." *IEEE Transactions on Ultrasonics, Ferroelectrics and Frequency Control*, vol. 42, pp. 689–699, Jul 1995.

[44] F. Viola and W. Walker, "A comparison of the performance of time-delay estimators in medical ultrasound." *IEEE Transactions on Ultrasonics, Ferroelectrics and Frequency Control*, vol. 50, pp. 392–401, April 2003.

[45] G. Pinton, J. Dahl, and G. Trahey, "Rapid tracking of small displacements with ultrasound." *IEEE Transactions on Ultrasonics, Ferroelectrics and Frequency Control*, vol. 53, pp. 1103– 1117, June 2006.

[46] I. Hein and W. O'Brien, "Current time-domain methods for assessing tissue motion by analysis from reflected ultrasound echoes-a review." *IEEE Transactions on Ultrasonics, Ferroelectrics and Frequency Control*, vol. 40, pp. 84–102, March 1993.

[47] G. Pinton and G. Trahey, "Continuous Delay Estimation with Polynomial Splines." *IEEE Transactions on Ultrasonics, Ferroelectrics and Frequency Control*, vol. 53, pp. 2026–2035, 2006.

[48] M. O'Donnell, A. Scovoroda, B. Shapo, and S. Emelianov, "Internal Displacement and Strain Imaging Using Ultrasonic Speckle Tracking," *IEEE Transactions on Ultrasonics, Ferroelectrics and Frequency Control*, vol. 41, pp. 314–25, May 1994.

[49] A. Pesavento, C. Perrey, M. Krueger, and H. Ermert, "A time efficient and accurate strain estimation concept for ultrasonic elastography using iterative phase zero estimation," *IEEE Transactions on Ultrasonics, Ferroelectrics, and Frequency Control*, vol. 46, pp. 1057–1067, 1999.

[50] C. Kasai, K. Namekawa, A. Koyano, and R. Omoto, "Real-time two-dimensional blood flow imaging using an autocorrelation technique." *IEEE Transactions on Sonics and Ultrasonics*, vol. 32, pp. 458–464, 1985.

[51] G. Jacovitti and G. Scarano, "Discrete time techniques for time delay estimation." *IEEE Transactions on Acoustics, Speech, and Signal Processing*, vol. 41, pp. 525–533, Feb 1993.

[52] S. Langeland, J. Dapos, H. Torp, B. Bijnens, and P. Suetens, "A simulation study on the performance of different estimators for two-dimensional velocity estimation." in *Proceedings of the IEEE Ultrasonics Symposium.* Volume 2: IEEE, 8-11 Oct 2002, pp. 1859–1862.

[53] F. Viola and W. Walker, "A Spline-Based Algorithm for Continuous Time-Delay Estimation Using Sampled Data." *IEEE Transactions on Ultrasonics, Ferroelectrics and Frequency Control*, vol. 52, pp. 80–93, January 2005.

[54] E. Konofagou and J. Ophir, "A new elastographic method for estimation and imaging of lateral displacements, lateral strains, corrected axial strains and Poisson's ratios in tissues," *Ultrasound in Medicine and Biology*, vol. 24, pp. 1183–99, October 1998.

[55] F. Viola, R. Coe, O. K., D. Guenther, and W. Walker, "MUlti-Dimensional Spline-Based Estimator (MUSE) for Motion Estimation: Algorithm Development and Initial Results." *Annals of Biomedical Engineering*, vol. 36, pp. 1942–1960, September 2008.

[56] R. Zahiri-Azar and S. Salcudean, "Time-Delay Estimation in Ultrasound Echo Signals Using Individual Sample Tracking." *IEEE Transactions on Ultrasonics, Ferroelectrics and Frequency Control*, vol. 55, pp. 2640–2650, 2008.

[57] I. Cespedes, Y. Huang, J. Ophir, and S. Spratt, "Methods for the estimation of subsample time-delays of digitized echo signals," *Ultrasonic Imaging*, vol. 17, pp. 142–171, 1995.

[58] P. de Jong, T. Arts, A. Hoeks, and R. Reneman, "Determination of Tissue Motion Velocity by Correlation Interpolation of Pulsed Ultrasonic Echo Signals," *Ultrasonics Imaging*, vol. 12, pp. 84–98, 1990.

[59] B. Geiman, L. Bohs, M. Anderson, S. Breit, and G. Trahey, "A comparison of algorithms for tracking sub-pixel speckle motion." in *Proceedings of the IEEE Ultrasonics Symposium.* Volume 2: IEEE, 5-8 Oct 1997, pp. 1239–1242.

[60] S. Foster, P. Embree, and W. O'Brien, "Flow velocity profile via time-domain correlation: error analysis and computer simulation," *IEEE Transactions on Ultrasonics, Ferroelectrics and Frequency Control*, vol. 37, pp. 164–175, May 1990.

[61] F. Viola and W. Walker, "Computationally Efficient Spline-Based Time Delay Estimation." *IEEE Transactions on Ultrasonics, Ferroelectrics and Frequency Control*, vol. 55, pp. 2084–2091, September 2008.

[62] L. Geiman, BJ.and Bohs, M. Anderson, S. Breit, and T. G.E., "A novel interpolation strategy for estimating subsample speckle motion." *Physics in Medicine and Biology*, vol. 45, pp. 1541–1552, 2000.

[63] S. Srinivasan and J. Ophir, "A zero-crossing strain estimator in elastography," *Ultrasound in Med and Bio*, vol. 29, pp. 227–238, 2003.

[64] H. Eskandari, S. Salcudean, and R. Rohling, "Tissue strain imaging using a wavelet transform-based peak search algorithm." *IEEE Trans Ultrason Ferroelectr Freq Control*, vol. 54, pp. 1118–30, June 2007.

[65] P. Wells, "Ultrasonic colour flow imaging," *Physics in Medicine and Biology*, vol. 39, pp. 2113–2145, 1994.

[66] R. Gill, "Measurement of blood flow by ultrasound: accuracy and sources of error." *Ultrasound in Medicine and Biology*, vol. 11, pp. 625–641, Aug 1985.

[67] E. Konofagou and J. Ophir, "Precision Estimation and Imaging of Normal and Shear Components of the 3D Strain Tensor in elastography," *Physics in Medicine and Biology*, vol. 45, pp. 1553–1563, 2000.

[68] M. Greenleaf J., Fatemi and M. Insana, "Selected methods for imaging elastic properties of biological tissues." *Annual Review of Biomedical Engineering*, vol. 5, p. 5778, 2003.

[69] M. Lubinski, S. Emelianov, and M. O'Donnell, "Speckle tracking methods for ultrasonic elasticity imaging using short-time correlation," *IEEE Transactions on Ultrasonics, Ferroelectrics and Frequency Control*, vol. 46, pp. 82–96, January 1999.

[70] H. Shi and T. Varghese, "Two-dimensional multi-level strain estimation for discontinuous tissue." *Physics in Medicine and Biology*, vol. 52, pp. 389–401, Nov 2007.

[71] L. Bohs and G. Trahey, "A novel method for angle independent ultrasonic imaging of blood flow and tissue motion," *IEEE Transactions on Biomedical Engineering*, vol. 38, pp. 280–286, March 1991.

[72] G. Trahey, J. Allison, and O. Von Ramm, "Angle independent ultrasonic detection of blood flow," *IEEE Transactions on Biomedical Engineering*, vol. 34, pp. 965–7, December 1987.

[73] R. Lopata, M. Nillesena, H. Hansena, I. Gerritsa, T. J., and C. de Korte, "Performance Evaluation of Methods for Two-Dimensional Displacement and Strain Estimation Using Ultrasound Radio Frequency Data." *Ultrasound in medicine and biology*, vol. 35, pp. 796–812, 2009.

[74] U. Techavipoo, Q. Chen, T. Varghese, and J. Zagzebski, "Estimation of displacement vectors and strain tensors in elastography using angular insonifications." *IEEE Transactions on Medical Imaging*, vol. 23, pp. 1479–1489, 2004.

[75] M. Rao, Q. Chen, H. Shi, T. Varghese, E. Madsen, J. Zagzebski, and T. Wilson, "Normal and shear strain estimation using beam steering on linear-array transducers." *Ultrasound in Medicine and Biology*, vol. 33, pp. 57–66, Jan 2007.

[76] H. Chen and T. Varghese, "Noise analysis and improvement of displacement vector estimation from angular displacements." *Medical physics*, vol. 35, pp. 2007–2017, 2008.

[77] L. Capineri, M. Scabia, and L. Masotti, "Vector Doppler: spatial sampling analysis and presentation techniques for real time systems." *Journal of Electronic Imaging.*, vol. 12, p. 489498, July 2003.

[78] O. Kripfgans, J. Rubin, A. Hall, and J. Fowlkes, "Vector Doppler imaging of a spinning disc ultrasound Doppler phantom." *Ultrasound in Medicine and Biology.*, vol. 32, pp. 1037–1046, 2006.

[79] L. Sandrin, M. Tanter, D. Cassereau, S. Catheline, and M. Fink, "ultrafast compound imaging for 2D motion vector estimation: Application to Transient elastography," *IEEE Transactions on Ultrasonics, Ferroelectrics and Frequency Control*, vol. 49, pp. 1363–1374, October 2002.

[80] M. Rao and T. Varghese, "Spatial angular compounding for elastography without the incompressibility assumption." *Ultrasonic imaging.*, vol. 27, pp. 256–270, 2005.

[81] E. Konofagou, J. D'hooge, and J. Ophir, "Myocardial elastography - A feasibility study in vivo," *Ultrasound in Medicine and Biology*, vol. 28, pp. 475–482, October 2002.

[82] L. Lvstakken, S. Bjaerum, D. Martens, and H. Torp, "Blood flow imaging–A new real-time, 2-D flow imaging technique." *IEEE Transactions on Ultrasonics, Ferroelectrics and Frequency Control*, vol. 53, pp. 289–99, Feb 2006.

[83] J. Jensen and I. Lacasa, "Estimation of blood velocity vectors using transverse ultrasound beam focusing and cross-correlation," in *Proceedings of the IEEE Ultrasonics Symposium.* IEEE, Oct 1999, pp. 1493–1497 vol.2.

[84] A. Heimdal, A. Stoylen, H. Torp, and T. Skjaerpe, "Real-time strain rate imaging of the left ventricle by ultrasound." *Journal of American Soc Echocardiography*, vol. 11, pp. 1013–1019, Nov 1998.

[85] M. Fabian, K. Ballu, J. Hossack, T. Blalock, and W. Walker, "Development of a parallel acquisition system for ultrasound research." in *Proc. SPIE vol. 4325*, Feb 2001, pp. 54–62.

[86] J. Dahl, G. Pinton, M. Palmeri, V. Agrawal, K. Nightingale, and G. Trahey, "A Parallel Tracking Method for Acoustic Radiation Force Impulse Imaging." *IEEE Transactions on Ultrasonics, Ferroelectrics and Frequency Control*, vol. 54, pp. 301–312, 2007.

[87] J. Bercoff, M. Tanter, M. Muller, and M. Fink, "Study of viscous and elastic properties of soft tissues using supersonic shear imaging," in *Proceedings of the IEEE Ultrasonic Symposium*, 2003.

[88] T. Misaridis and J. Jensen, "Use of modulated excitation signals in medical ultrasound. Part I: basic concepts and expected benefits." *IEEE Transactions on Ultrasonics, Ferroelectrics and Frequency Control*, vol. 52, pp. 177–191, Feb 2005.

[89] ——, "Use of modulated excitation signals in medical ultrasound. Part II: Design and performance for medical imaging applications." *IEEE Transactions on Ultrasonics, Ferroelectrics and Frequency Control*, vol. 52, pp. 192–207, 2005.

[90] ——, "Use of modulated excitation signals in medical ultrasound. Part III: High frame rate imaging." *IEEE Transactions on Ultrasonics, Ferroelectrics and Frequency Control*, vol. 52, pp. 208–219, 2005.

[91] V. Dutt, R. Kinnick, R. Muthupillai, T. Oliphant, R. Ehman, and J. Greenleaf, "Acoustic shear-wave imaging using echo ultrasound compared to magnetic resonance elastography," *Ultrasound in Medicine and Biology*, vol. 26, pp. 397–403, 2000.

[92] A. Henni, C. Schmitt, and G. Cloutier, "Three-dimensional transient and harmonic shear-wave scattering by a soft cylinder for dynamic vascular elastography." *Journal of the Acoustical Society of America*, vol. 124, pp. 2394–2405, Oct 2008.

[93] M. Pernot, K. Fujikura, S. Fung-Kee-Fung, and K. E., "ECG-gated, mechanical and electromechanical wave imaging of cardiovascular tissues in vivo." *Ultrasound in Medicine and Biology*, vol. 33, p. 10751085, 2007.

[94] M. Insana, C. Pellot-Barakat, M. Sridhar, and K. Lindfors, "Viscoelastic imaging of breast tumor microenvironment with ultrasound." *Journal of Mammary Gland Biology and Neoplasia*, vol. 9, pp. 393–04, 2004.

[95] E. Fleury, J. Rinaldi, S. Piato, J. Fleury, and D. Roveda Junior, "Appearance of breast masses on sonoelastography with special focus on the diagnosis of fibroadenomas." *European Radiology*, vol. 19, pp. 1337–46, Jan 2009.

[96] B. Garra, E. Cespedes, J. Ophir, and et al., "Elastography of breast lesions: Initial clinical results," *Radiology*, vol. 202, pp. 79–86, January 1997.

[97] R. Sinkus, J. Lorenzen, D. Schrader, M. Lorenzen, M. Dargatz, and D. Holz, "High-resolution tensor MR elastography for breast tumor detection," *Physics in Medicine and Biology*, vol. 45, pp. 1649–64, June 2000.

[98] S. Salcudean, D. French, S. Bachmann, X. Zahiri-Azar, R.and Wen, and J. Morris, "Viscoelasticity modelling of the prostate region using vibro-elastography." in *9th MICCAI Conference*. Denmark: MICCAI, Oct 2006, pp. 389–396.

[99] A. Lorenz, H. Sommerfeld, M. Schurmann, and et al, "A new system for the acquisition of ultrasonic multicompression strain images of the human prostate in vivo," *IEEE Transactions on Ultrasonics, Ferroelectrics and Frequency Control*, vol. 46, pp. 969–1147–1154, 1999.

[100] R. Gaspari, D. Blehar, M. Mendoza, M. Montoya, C. Moon, and D. Polan, "Use of Ultrasound Elastography for Skin and Subcutaneous Abscesses." *Journal of Ultrasound in Medicine*, vol. 28, pp. 855–860, 2009.

[101] I. Sack, B. Beierbach, J. Wuerfel, D. Klatt, U. Hamhaber, S. Papazoglou, P. Martus, and J. Braun, "The impact of aging and gender on brain viscoelasticity." *Neuroimage*, vol. 46, pp. 652–657, 2009.

[102] S. Emelianov, X. Chen, M. O'Donnell, B. Knipp, D. Myers, T. Wakefield, and J. Rubin, "Triplex ultrasound: Elasticity imaging to age deep venous thrombosis," *Ultrasound in Medicine and Biology*, vol. 28, pp. 757–767, 2002.

[103] J. Rubin, S. Aglyamov, T. Wakefield, M. O'Donnell, and S. Emelianov, "Clinical Application of Sonographic Elasticity Imaging for Aging of Deep Venous Thrombosis: Preliminary Findings," *Ultrasound Medicine*, vol. 22, pp. 443–448, 2003.

[104] T. Varghese, J. Zagzebski, and J. Jee, "Elastography imaging of thermal lesion in the liver in vivo following radio frequency ablation: Preliminary results," *Ultrasound in Medicine and Biology*, vol. 28, pp. 1467–1473, 2002.

[105] R. Righetti, F. Kallel, R. Stafford, and et al, "Elastographic characterization of HIFU-induced lesions in canine livers," *Ultrasound in Medicine and Biology*, vol. 25, pp. 1099–1113, 1999.

[106] S. Emelianov, M. Lubinski, A. Skovoroda, R. Erkamp, and S. Leavey, "Reconstructive ultrasound elasticity imaging for renal transplant diagnosis: kidney ex-vivo results," *Ultrasonic Imaging*, vol. 22, pp. 178–194, 2000.

[107] M. Palmeri, M. Wang, J. Dahl, K. Frinkley, and K. Nightingale, "Quantifying Hepatic Shear Modulus in vivo Using Acoustic Radiation Force." *Ultrasound in Medicine and Biology*, vol. 34, pp. 546–558, 2008.

[108] B. Fahey, K. Nightingale, R. Nelson, M. Palmeri, and G. Trahey, "Acoustic radiation force impulse imaging of the abdomen: Demonstration of feasibility and utility." *Ultrasound in Medicine and Biology*, vol. 31, pp. 1185–1198, 2005.

[109] S. Levinson, M. Shinagawa, and T. Sato, "Sonoelastic determination of human skeletal muscle elasticity." *Journal of Biomechanics*, vol. 28, pp. 1145–1154, 1995.

Chapter 2

Time-Delay Estimation in Ultrasound Echo Signals Using Individual Sample Tracking[1]

2.1 Introduction

Motion estimation as a time-delay estimation in sequences of ultrasound echo signals is essential for a wide range of modern ultrasound based signal processing applications. Time-delay estimation lies at the heart of blood flow estimation, tissue velocity estimation [1–3], tissue elasticity estimation [4–8], radiation force imaging [9–11], and many other applications.

Time-delay estimators measure displacement of the backscattered signals with respect to the transducer. This displacement appears as time-shift or phase-shift between sequences of echo signals [2]. Time-delay estimators are typically classified based on the type of signal (radio frequency signal RF, envelope signal, in-phase and quadrature signals I/Q) and the domain on which they operate (i.e. time, phase, or frequency). These estimators have been studied and compared extensively in the literature [12–15]. Phase-shift estimators were initially used for blood flow measurement. Later, these were used in other fields in order to estimate tissue motion. Phase-shift estimators find the average phase-shift over a number of samples within a window with respect to the nominal or estimated central frequency of the transmitted pulse. Complex cross correlation of the RF echo signals [16,17] or complex-valued Doppler signals [1,2] are typically used in these techniques.

Time-shift estimators are widely used in estimating tissue motion. Typically, they consist of the identification of the maximum/minimum of a pattern matching function. The shape of the signal within a specific window in the reference echo signal is set to be the pattern and a matching algorithm is used to find the best match in the delayed echo signal. Many pattern matching techniques are currently employed, each offering trade offs between complexity and accuracy [12, 18, 19]. To reduce the bias and variance introduced by finite sampling intervals, pattern matching function interpolation methods such as curve fitting and polynomial interpolation techniques have been introduced [20]. These techniques include parabolic fitting [21], spline fitting [22], cosine fitting [23], and grid slope [24]. While the computational cost of these methods is small, they suffer from relatively high bias and variance. In an effort to reduce the bias and variance of the delay estimators, at the expense of computational cost, spline-based *continuous time-shift estimators* have been introduced [15,25]. In these techniques the sampled echo signal is interpolated by spline polynomials. The coefficients of the polynomials are then

[1] A version of this chapter has been published. R. Zahiri Azar and S. E. Salcudean, (2008) "Time-Delay Estimation in Ultrasound Echo Signals Using Individual Sample Tracking", IEEE Transactions on Ultrasonics, Ferroelectrics and Frequency Control, vol. 55, no. 12, pp. 2640-2650

used to generate a *continuous* pattern matching function. Time-shifts are estimated by finding the minimum/maximum of the generated continuous pattern matching function analytically. By keeping the displaced signals discrete and representing the reference echo signal by polynomials only, a continuous time-shift estimator has been derived by Viola and Walker [25]. At the expense of higher computational cost, Pinton and Trahey derived another algorithm where continuous representations of both the reference and the delayed echo signals are used to calculate a continuous pattern matching function [15]. These authors have shown that continuous time-shift estimators significantly outperform other algorithms in terms of standard deviation and bias over a broad range of conditions.

All the above-mentioned techniques fall in the category of *window-based delay estimators*. Indeed, they all measure the average time-shift/phase-shift of a number of samples within a certain window. The size of the window and the overlap between windows play an important role in the performance of these time-delay estimators [26]. Trade offs exist between the signal-to-noise ratio and resolution of the time-shift estimators when different window sizes are used [13, 27, 28]. In an effort to alleviate problems related to windowing, time-delay estimation using multiple window sizes [29, 30] have been introduced in the literature. Some of the alternative approaches to window-based time-delay estimation make use of feature extraction. Zero-crossing tracking (ZCT) [4] identifies the zero-crossings of the echo signals using linear interpolation. Peak tracking and level-crossing tracking, wherein tracking is performed on a predefined amplitude level, have also been suggested in [4] as extensions of ZCT. The peak searching algorithm [31] identifies the peaks of the echo signals using a wavelet transform. The distances between the zero-crossings (or level-crossings) or peaks represent the time-shifts. ZCT and peak searching algorithms provide as many measurement points as there are zero/level crossings or peaks within the signals. As a result they have the potential to provide much higher resolution than window-based techniques.

In this paper we propose a new delay estimation algorithm called the Sample Tracking (ST) algorithm. With this algorithm, the time-shift of each sample in a delayed echo signal is measured with respect to a continuous, interpolated representation of the reference echo signal. ST does not require windowing and can be implemented with a number of interpolation schemes that provide continuous approximations to the original signal. The interpolation schemes trade off delay estimation accuracy *vs* computational requirements. ST provides the time-delay estimates with much higher density compared to conventional window based methods. We also introduce a spline-based ZCT where a spline-based interpolation method is used to find the zero-crossings of the echo signals instead of the previously used linear interpolation technique.

The paper is structured as follows: Section 2.2 presents the ST and the spline-based zero-crossing algorithms. Section 2.3 and 2.4 present simulation methods and simulation results that compare the performance of the algorithms introduced in Section 2.2 to some of the best and most widely used delay estimators. A discussion of the results is provided. Section 2.5 summarizes experimental results with a tissue phantom to demonstrate the feasibility of the proposed approach. Conclusions are presented in Section 2.6, along with avenues for future research.

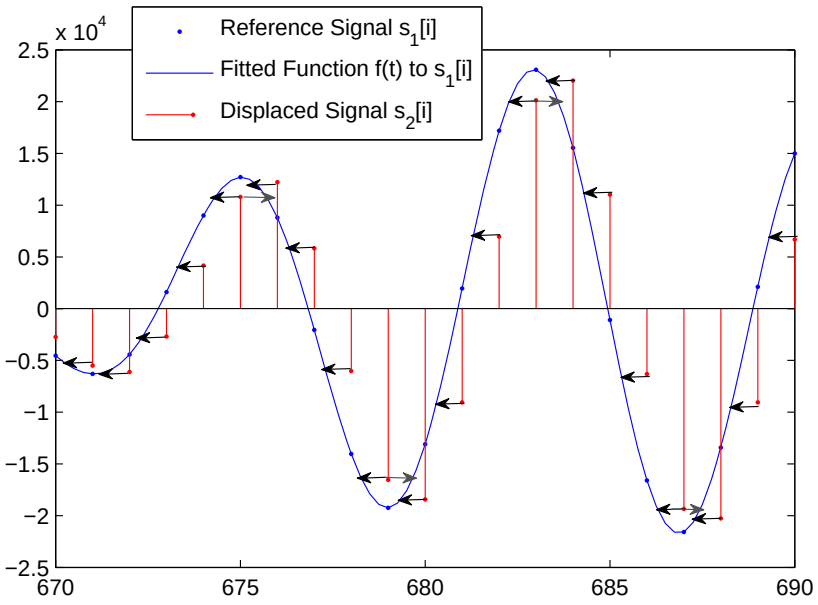

Figure 2.1: Schematic of ST. The markers represent the discrete samples in the reference $s_1[i]$ and delayed $s_2[i]$ signals and the continuous line shows a polynomial interpolation $f(t)$ to the reference signal. Black arrows show the actual displacements of each sample and gray arrows show other displacement candidates.

2.2 Proposed Algorithms

2.2.1 Sample Tracking

Let $s_1[i]$, $i = 0, 1, ..., n-1$ be a sampled reference echo signal and $s_2[i]$, $i = 0, 1, ..., n-1$ be a sampled, delayed, echo signal, where n is the number of discrete samples in the echo signals. Let $f(t)$, $t \in [0, \infty)$, be a continuous interpolation of s_1, , i.e. f is such that $f(iT) = s_1[i]$, $\forall i$, where T is the sampling period. The displacement of each individual discrete sample of the delayed echo signal $s_2[i]$ with respect to the reference signal $s_1[i]$ can be estimated by finding t such that

$$f(t) = s_2[i]. \tag{2.1}$$

This is shown in Fig 2.1. Any technique that has been used previously to interpolate the pattern matching function can be used here to interpolate the reference echo signal. The complexity and accuracy of the ST algorithm depend strongly on the form of the polynomial representation of the echo signal.

Cubic splines are commonly used in signal processing due to their excellent balance between ease of computation and accuracy [15,25,32]. To implement ST using a cubic spline polynomial, without involving any windowing, a continuous representation of the entire reference signal is generated according to the following equation:

$$f(iT+t) = f_i(t) = a_i t^3 + b_i t^2 + c_i t + d_i, t \in [0, T] \tag{2.2}$$

where a_i, b_i, c_i, d_i are the coefficients of the fitted spline polynomial at the i^{th} sample. Alternatively, local fitting of polynomials using neighboring samples can be used to generate the corresponding coefficients at each sample location. The details of local polynomial fitting are provided in Appendix A.

The individual delays $\hat{\Delta}[i]$ of the discrete samples $s_2[i]$, $i = 0, 1, , n-1$, of the delayed echo signal are estimated by finding the root of $(f_i(t) - s_2[i])$ that is nearest to $s_2[i]$, within the interval $[0, T]$:

$$\hat{\Delta}[i] = \{t \in [0, T] | f_i(t) = s_2[i]\}. \tag{2.3}$$

These delay estimates are not subject to sampling quantization. For negative time-shifts where the time-shift estimates fall in the interval $[-T, 0]$, the process described above can be repeated by shifting the reference sampled signal by one sample and using the coefficients $a_{i-1}, b_{i-1}, c_{i-1}, d_{i-1}$ to find the root of $(f_{i-1}(t) - s_2[i])$, within the interval $[0, T]$. This will result in estimating a time-shift in the interval $-T + [0, T] = [-T, 0]$. This process is analogous to the shifting process used in conventional window based time-delay estimation using pattern matching functions.

In addition to polynomial fitting, fitting a cosine function to neighboring samples can also be employed to generate a continuous representation of the reference echo signal (i.e. $f_i(t) = A_i \cos(\alpha_i t + \beta_i)$). The individual delays $\hat{\Delta}[i]$ of the discrete samples of the delayed echo signal are estimated by solving for t and selecting the root (i.e. $(\pm a \cos(s_2[i]/A_i) - \beta_i)/\alpha_i$) that is nearest to $s_2[i]$, within the interval $[-T, T]$.

ST algorithms provide a time-delay estimate for each sample of the echo signal, as opposed to window-based methods, which provide the same time-delay estimate for all the samples within a window. As a result, the delay estimates provided by ST are much denser than those provided by conventional window-based methods.

Due to signal variations, ST may not always find a root. Samples for which equation (2.1) does not have a root can be marked and removed. They can also be replaced with the average time-shifts of neighboring samples. Furthermore, without any prior knowledge about the displacement of each sample, ST may find more than one candidate for the delay estimate of each sample (i.e. (2.1) has more than one root). Several possible scenarios are shown in Fig 2.1. On the peak/valley of the echo signal, ST might select the root to the right or the one to the left (black or gray arrow). Selecting a false root will result in a *spike* in the sample delay estimate. The problem of false roots in ST is similar to the selection of false peaks in pattern matching functions. As done in methods based on pattern matching [28], non-linear filtering can be used to remove false roots in ST. In the ST algorithms presented in this paper, false roots and unknown delays are removed by applying 1D median filtering with a kernel size of five data points.

The ST algorithm is different from the ZCT/level crossing or the peak searching algorithms. In ZCT, a single level-crossing is defined. In ST, each sample of the delayed signal defines a level-crossing to be found in the reference signal (Fig 2.1). Thus, in ST, a new level is defined for every sample, as opposed to tracking a fixed and predefined amplitude level as suggested in [4].

ST can also be derived from the spline-based continuous time-delay estimator [25]. In [25], the error between the reference and the delayed signal is defined for a given window as the following quadratic function:

$$\epsilon(t) = \sum_{i=1}^{W} \left(f_i(t) - s_2[i]\right)^2, \tag{2.4}$$

where W is the number of samples in the window. The time delay t that minimizes $\epsilon(t)$ is found analytically by taking the derivative with respect to t and setting the result equal to zero, then solving for t. By setting $W = 1$ in (2.4) the error function and its derivative can be written as $\epsilon(t) = \left(f_i(t) - s_2[i]\right)^2$ and $\partial\epsilon(t)/\partial t = 2\left(f_i(t) - s_2[i]\right)$, respectively. By setting the derivative equal to zero, we obtain

$$\partial\epsilon(t)/\partial t = 0 \rightarrow f_i(t) = s_2[i], \tag{2.5}$$

which is the same equation that we used for ST. It should be noted that the error function defined in (2.4) does not result in the estimation of the average of the displacement of the individual samples inside the window. Therefore similar results are not expected and are not obtained when time-delay estimates of several samples are averaged and compared with the method from [25].

Similarly to phase-shift estimators which fail to estimate delays outside $[-\lambda/2, \lambda/2]$, where λ is the wavelength, ST is envisaged to be used primarily for tiny delays (i.e. within $[-\lambda/4, \lambda/4]$), for which sub-sample delay estimation becomes very important and common window based algorithms suffer from relatively high bias and standard deviation. With this property, ST algorithms are readily applicable to estimating delays in high frame-rate tissue imaging, where delays between successive acquisitions are small, and ARFI imaging, where maximum delays are small. For larger time-shifts, previously estimated time-shifts can be used to find the coarse location of the current sample. This approach has been used in [33] to guide the search for the pattern matching function. The same approach has been used in [17] to unwrap the phase-shifts outside $[-\lambda/2, \lambda/2]$. Alternatively, other methods, such as pattern matching, can be used first to find the coarse estimation of the time-shifts. ST can then be applied to find the fine sub-sample time-shift of each sample. Thus the time-shift of each sample will be equal to the coarse time-shift, estimated with the pattern matching function, plus the fine sub-sample time-shift, estimated with ST. This approach was implemented in this work to accurately estimate large delays using ST.

2.2.2 Spline-based Zero-Crossing Tracking

The ZCT estimator identifies the zero-crossings of $s_1[i]$ and $s_2[i]$. The displacements are then estimated from the distance between the zero-crossings. The initial implementation of the ZCT employed linear interpolation between consecutive samples of the two RF signals that have different signs [4]. With a trade off of higher computational cost, the performance of the ZCT is expected to improve when more accurate representations of the echo signals are employed to find the zero-crossings. Let $f(t)$, $g(t)$ be continuous representations of the echo signals $s_1[i]$, $s_2[i]$, respectively, generated using spline polynomials as in (2.1) above. The locations of the zero-crossings $z_1[j]$, $z_2[j]$, where j is the zero-crossing index, are found as the roots of the fitted functions, i.e. $z_1[j] = t|_{f(t)=0}$ and $z_2[j] = t|_{g(t)=0}$. Finally the displacements

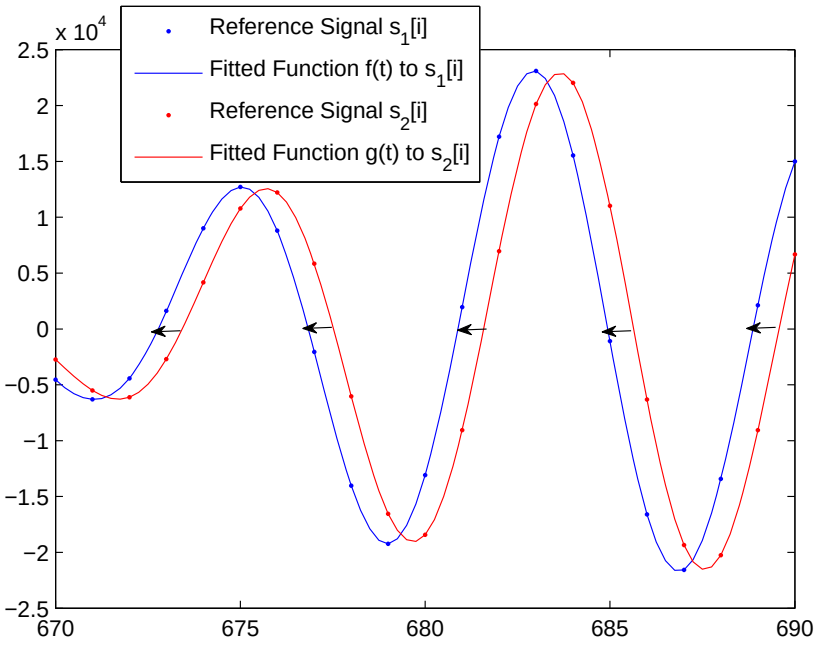

Figure 2.2: Schematic representation of the ZCT algorithm. The circle markers show discrete samples and the continuous lines show the fitted polynomials to the reference and delayed signals. The arrows show the displacements of the zero-crossings.

are estimated from the distance between the locations of the corresponding zero-crossings (Fig 2.2):

$$\hat{\Delta}[j] = z_1[j] - z_2[j]. \tag{2.6}$$

Equation (2.6) was suggested in [4] and assumes that corresponding zero-crossings in the reference and delayed signal share the same index. However, this assumption does not always hold. If some zero-crossings disappear from the reference echo signal or new zero-crossings appear in the delayed signal, corresponding zero-crossings will not share the same index. Therefore, if (2.6) is used directly, large biases may be introduced in time-shift estimates. In order to avoid this problem, prior to using (2.6), a check is added to correct the indexes. In this work, positive large jumps in $\hat{\Delta}[j]$ (e.g., $z_1[j] - z_2[j] > \lambda/4$) are assumed to be the result of the appearance of a zero-crossing. Negative large jumps in $\hat{\Delta}[j]$ (i.e. $z_2[j] - z_1[j] > \lambda/4$) are assumed to be the result of a disappearance of a zero-crossing. Therefore, in the ZCT method presented in this paper, equation (2.6) is re-formulated as follows:

$$\hat{\Delta}[j] = z_1[j+n] - z_2[j+m]. \tag{2.7}$$

where m and n are correction factors accounting for additional or missing zero-crossings. The appearance or disappearance of zero-crossings is a function of the quality of the continuous fit to the sampled signals. The better the fit, the less likely it is that zero crossings will appear or disappear.

2.3 Simulation Methods

A series of computer simulations was performed to study the performance of the proposed algorithms. The proposed algorithms were compared with the following conventional time-shift and phase-shift estimators:

1. Viola's continuous time-delay estimator (CTDE) [25],
2. Parabola fitting to normalized cross-correlation [21],
3. Cosine fitting to normalized cross-correlation [23],
4. Spline fitting to normalized cross-correlation [22],
5. Kasai's phase-shift estimator (1D autocorrelator) [1],
6. Loupas' phase-shift estimator (2D autocorrelator) [2].

Detailed descriptions of the normalized correlation and associated interpolation schemes as time-shift estimators are provided in [25]. Detailed descriptions of the 1D and 2D autocorrelators as phase-shift estimators are provided in [13].

The performance of each estimator is considered in terms of its bias and standard deviation as a function of sub-sample shift [25, 28], window size [13, 26], and resolution [13, 27].

The RF data was constructed to simulate line scatterers moving axially toward the transducer. Similarly to previously reported work, the base signal was created by convolving Gaussian distributed white noise (zero mean and unit standard deviation) with a sinc-enveloped sinusoid point spread function (PSF) [25, 28] given by:

$$\mathrm{PSF(t)} = \frac{\sin(\pi B f_0 t)}{\pi B f_0 t} \sin(2\pi f_0 t), \tag{2.8}$$

where $f_0 = 5$ MHz is the center frequency and $B = 0.5$ is the fractional bandwidth. A sinc-enveloped sinusoid PSF was chosen over Gaussian-enveloped sinusoid [13, 15] to facilitate the comparison of the results with [25, 28]. The PSF(t) was sampled from $-1.5/(Bf_0)$ to $1.5/(Bf_0)$ at a frequency equal to the sampling rate. Oversampling the base signal by a factor of 100 ($f_s = 4$ GHz) was used to obtain the necessary sub-sample displacement resolution to study the bias and standard deviation of the time-delay estimators. Reference and delayed signals, $s_1[i]$ and $s_2[i]$, were formed by decimating the base signal by a factor of 100 ($f_s = 40$ MHz). The base signal was decimated starting at different samples to produce reference and delayed signals with a known sub-sample delay. For example, to produce a 0.1 sub-sample shift, the base RF signal was down-sampled by a factor of 100 starting at the 1st and 11th sample to produce the reference and delayed signals, respectively. Sub-sample delays were varied from 0 to 0.95 samples in steps of 0.05 samples, so that a total of 20 different delays were evaluated. A total of 1,200,000 RF samples were generated in the base signal which resulted in 12,000 samples for each step after decimation. Window based displacement calculations are based on data with an axial extent (or window length) of 24 samples (1.5λ or $\approx 450\,\mu$m) which resulted in $M = 500$ independent realizations for each delay. Gaussian white noise was also added to the reference and delayed signals to generate echo signals with different signal-to-noise ratios (SNR).

The following equations were used to estimate the bias b and standard deviation σ:

$$b(\hat{\Delta}) = \frac{1}{M}\sum_{k=1}^{M}(\hat{\Delta}[k] - \Delta[k]) \tag{2.9}$$

$$\sigma(\hat{\Delta}) = \sqrt{\frac{1}{M}\sum_{k=1}^{M}(\hat{\Delta}[k] - \frac{1}{M}\sum_{k=1}^{M}\hat{\Delta}[k])^2} \tag{2.10}$$

where M is the number of measurements, $\Delta[k]$ are the true time delays, and $\hat{\Delta}[k]$ are the estimated time delays.

In order to study the resolution of the proposed estimators, their displacement step responses have been studied as in [13, 27]. A step discontinuity was mimicked by inducing a square wave displacement profile in the echo signals. Twenty independent realizations of the reference and the delayed echo signals were generated for the same square wave displacement profile.

Bias, standard deviation and resolution are the most commonly used metrics in studying the performance of time-delay estimators. In order to study and compare the sensitivity of ST in the presence of decorrelation as a strain estimator, its strain filter has also been studied.

A reference 2D RF frame was generated with a 1D simulation for each RF line as explained above. A total of 100 independent lines were simulated to generate the reference RF frame. To mimic the deformed signals at different compression ratios, the motion of scatterers for each RF line was modeled using a serial connection of springs. A stiffness map was assigned to each RF line. The stiffness was set to be the same across the entire image which leads to uniform compression of the point scatterers. The displacements of point scatterers were calculated by compressing the model with different compression ratios [33]. Compressions were generated in the range of 0.0001% to 10% (equivalent to 4.0×10^{-5} mm $\approx 2.0 \times 10^{-3}$ of a sample to 4.0 mm $\approx 2.0 \times 10^{2}$ samples maximum displacement) on a logarithmic scale. The deformed RF signals were then calculated by convolving the compressed point scatterers with the original PSF (2.8). The strain signal-to-noise ratios SNR_e as defined in Appendix B were computed from these data and were used to generate the strain filter of the ST algorithm in the presence of decorrelation noise.

2.4 Simulation Results and Discussions

Simulations were performed by applying different time-delay estimators to the simulated ultrasonic RF data. All calculations were performed in MATLAB (MathWorks Inc., Natick, MA). Since the ZCT and ST methods provide a higher number of estimate points than window-based tracking (6 times higher for ZCT and 24 times higher for ST for a window length of 1.5λ), the delay estimates from ZCT and ST algorithms were lumped following the estimation. A delay estimate for each window was obtained by taking the average of the delay estimates that fall within the window. These average delay estimates were then used to study and compare the performance of the ZCT and the ST algorithms with conventional window-based techniques.

Simulation results are shown in Figs 2.3-2.8. Fig 2.3 shows the bias and standard deviation of all the methods considered as a function of the sub-sample shift as discussed in Section 2.3.

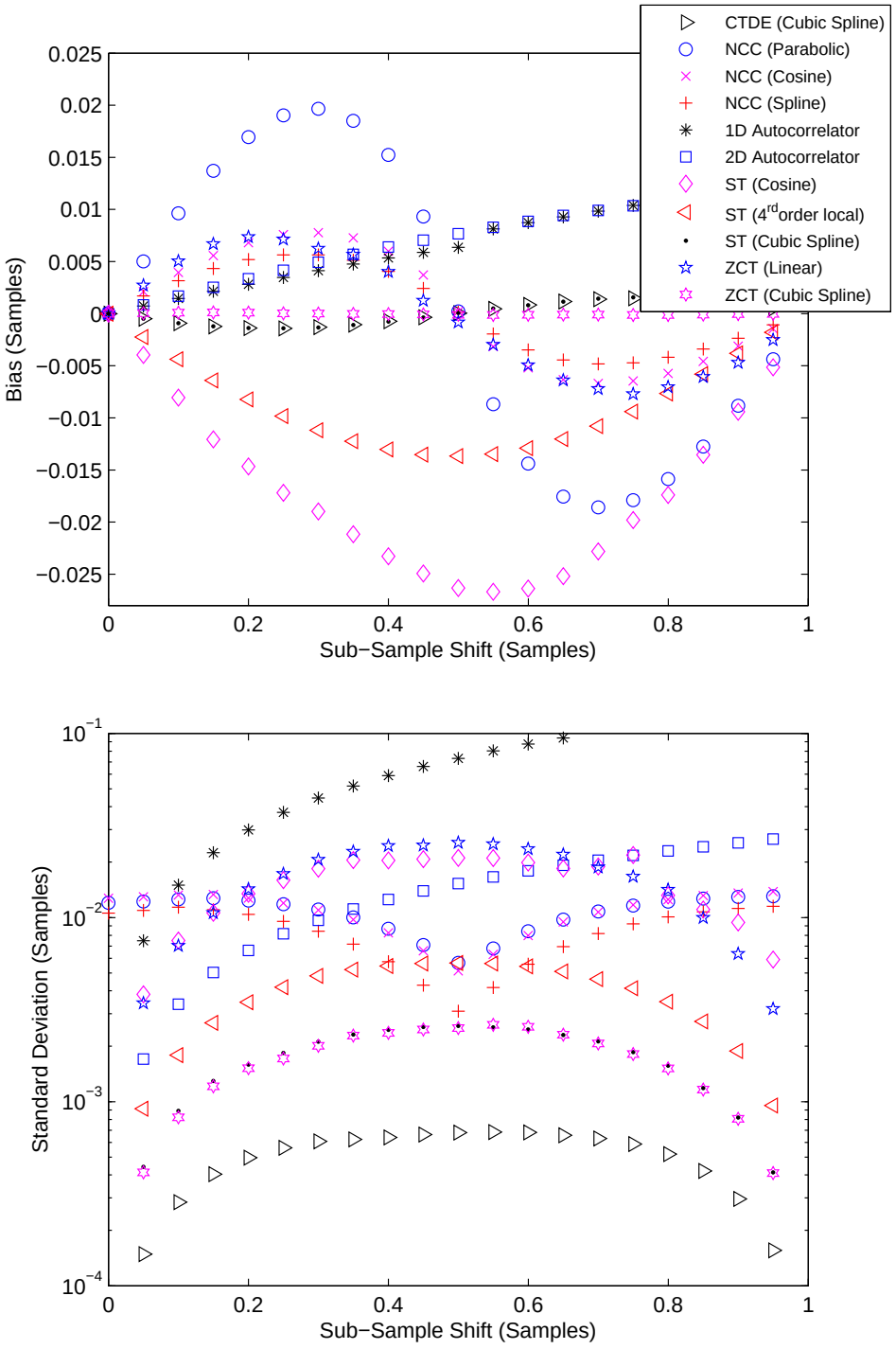

Figure 2.3: Bias and standard deviation of all the delay estimators. The reference and delayed signals were identical, except for a sub-sample shift. For each delay, 500 independent realizations were used ($f_s = 40$ MHz, $f_o = 5$ MHz, $B = 0.5$, and $W = 1.5\lambda$).

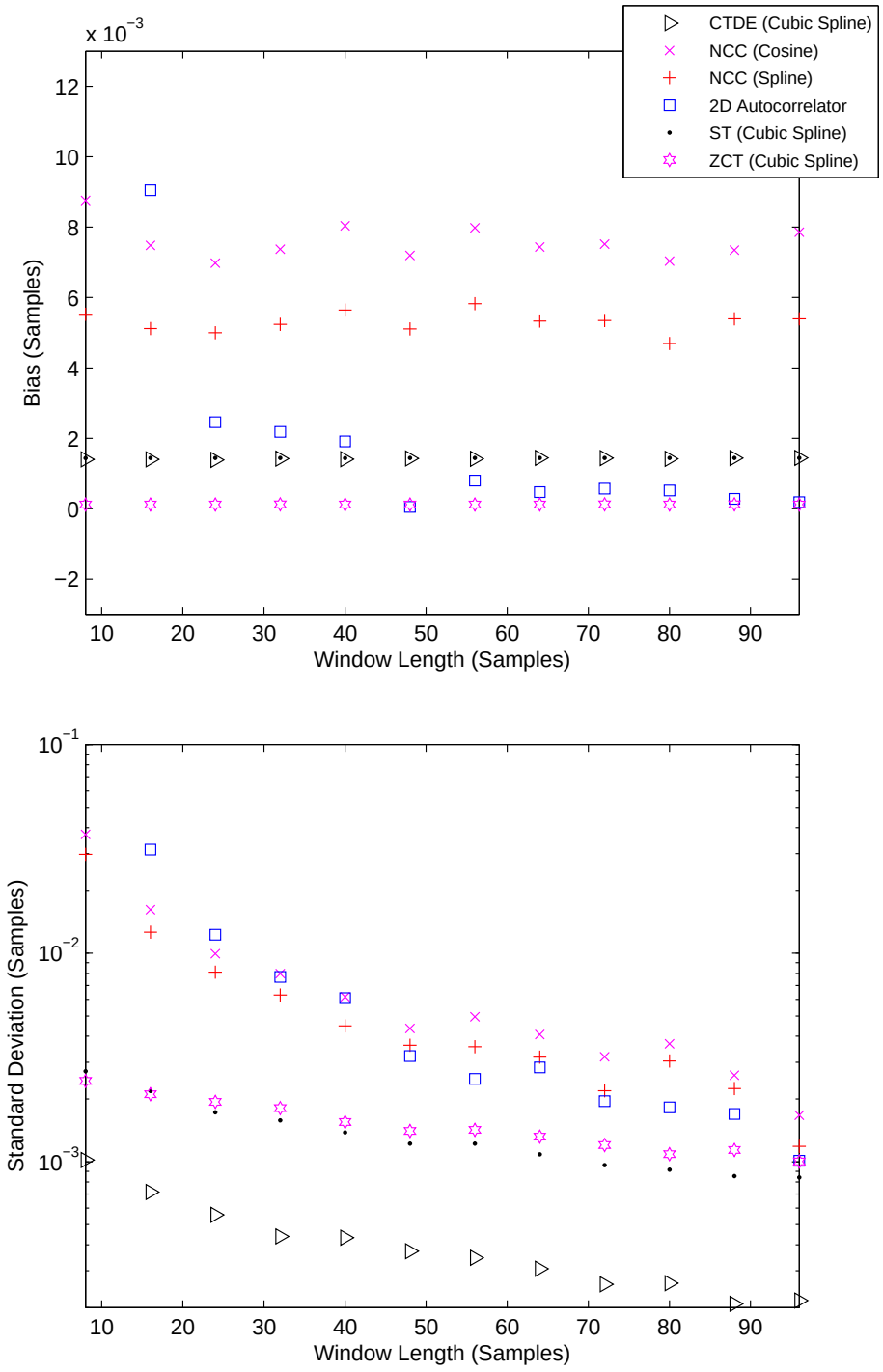

Figure 2.4: Bias and standard deviation of all the techniques for different window sizes. The reference and delayed signals were identical, except for a sub-sample shift of 0.25 sample ($f_s = 40$ MHz, $f_o = 5$ MHz, $Depth = 50$ mm, no window overlap).

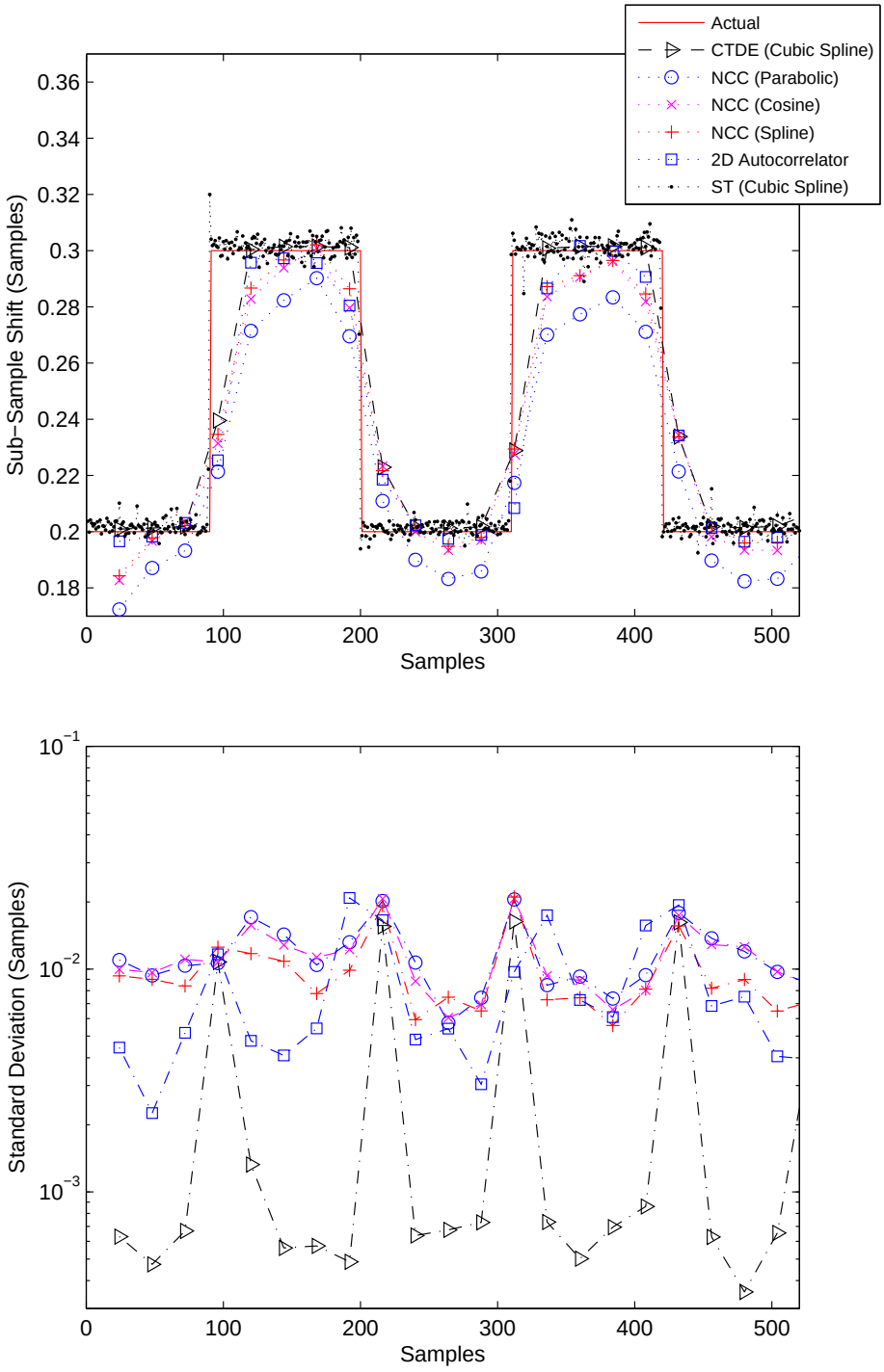

Figure 2.5: The bias of all the techniques (left) and the standard deviation of window-based delay estimators (right). The results are the average displacement estimates over 20 realizations $f_s = 40$ MHz, $f_o = 5$ MHz, $B = 0.5$, $W = 24$ samples for window based techniques.

A signal and its exact shifted replica were used. The vertical axis for standard deviation is shown on a logarithmic scale in order to provide a clear differentiation. Fig 2.3 shows the bias and standard deviation of the ST algorithm when three point cosine fitting, fourth order local polynomial fitting, and cubic spline fitting are used to generate the continuous representation of the reference echo signal. The accuracy of tracking individual samples increased with the quality of the polynomial interpolation. This result is shown in Fig 2.3. ST algorithms using cubic spline fitting and CTDE significantly outperform all the window-based techniques and provide exact results, in terms of bias in estimating the average delays. These results are consistent with the results provided in Section 2.2, where it was shown that ST algorithms can be derived from CTDE with $W = 1$. For ZCT algorithms, Fig 2.3 shows that both the bias and standard deviation drop significantly as we use spline functions to locate the zero-crossings instead of previously used linear interpolations. These expected results are the outcome of the increased accuracy of tracking the zero-crossings, as the interpolating polynomial becomes a better representation for the actual discrete data. The results also show that when using linear interpolation, ZCT performance closely resembles that of the correlation based algorithms. These results are consistent with the results that were reported by Srinivasan in [4], where ZCT was reported to generate strain images with lower signal-to-noise ratios in comparison to normalized correlation.

Fig 2.3 shows that the spline-based ZCT algorithm achieves the smallest bias among all the techniques and performed better than the spline-based ST and CTDE algorithms. This is due to the fact that ZCT fits a spline polynomial to both the reference and delayed echo signals while ST keeps the reference signal discrete. Similar results have been reported in the literature for window based continuous time-delay estimation. In [15] it has been shown that, with the trade-off of higher computational cost, fitting spline functions to both the reference and displaced signals, as opposed to the reference signal only [25], improves the performance of time-delay estimators. However, ST algorithms have several advantages compared to ZCT methods. First, ST provides many more measurement points compared to ZCT since the number of samples is always greater than the number of zero/level crossings. Second, the spacing between the time-shift estimates is fixed in ST and is equal to the spacing between echo samples. The ZCT algorithms provide the time-shift estimate only at the location of the predefined level (zero or other) crossings. These are not always equally spaced. Third, unlike ZCT, ST can be applied to the envelope signals equally effectively. Fourth, ST does not have the problem of losing track of motion, as mentioned in Section 2.2 for ZCT. This is due to the fact that the time-shift estimation of each sample is independent from that of other samples.

Fig 2.3 also shows that CTDE produces the lowest standard deviation among all techniques, followed by ST and ZCT. Fig 2.3 shows that the normalized correlation with cosine fit and spline fit achieve lower bias than parabolic fit. The 2D autocorrelator as a phase-shift estimator, which estimates the center frequency, outperforms the 1D-autocorrelator, which assumes a fixed center frequency equal to that of the transmitted pulse. These results are all consistent with previously published results [12, 13, 20, 22, 25, 34].

Fig 2.4 shows the bias and standard deviation of all methods as a function of window size. An echo signal with sub-sample shift of 0.25 samples was used for this study. The ZCT algorithm has the smallest bias followed by ST and CTDE. Similarly to the results in Fig 2.3, the bias of ST is the same as the bias of the CTDE for all window sizes. For spline-based methods (i.e. ZCT, ST, and CTDE) the size of the window does not affect the bias of the

estimator. Fig 2.4 shows that for large window sizes, the bias of the 2D autocorrelator phase-shift estimator becomes comparable to that of spline-based techniques.

For all the methods considered the standard deviation increases as we reduce the size of the window. This is consistent with the result published in [28], where it was shown that the lower bound of the standard deviation of the delay estimators is inversely proportional to the square root of the size of the window. Therefore the standard deviation is expected to increase as we reduce the size of the window. Fig 2.4 shows that the biases of all the methods remain larger than that of the CTDE.

It should be noted that the results depicted in Fig 2.3 and 2.4 are in favor of window-based methods since all the samples were experiencing the exact same shift inside the window. To study a more realistic case in which the samples inside a window experience different delays, we used a step discontinuity in the delays. The step responses (square wave responses) of the techniques we study indicates their resolution, and are shown in Fig 2.5. The step responses of the window-based techniques are compared with ST when no averaging is applied to the estimated delays. Fig 2.5 shows that ST outperforms all methods. For ST the transition from one step to the next happens instantly while for all the window-based methods including CTDE, the transition is smooth. This was expected as ST has the capability of tracking individual samples as opposed to tracking a group of samples within a window. Thus its performance is not limited by the size of the window.

Fig 2.6 depicts the relationship between the standard deviation and the SNR. The SNR was varied from 10 dB to 60 dB. The results show that the performance of both ST and ZCT rapidly degrade as the SNR becomes smaller. This is also expected as, unlike window-based methods, neither ST nor ZCT take advantage of averaging to improve time-delay estimates. Measurements based on single samples or zero-crossings are more susceptible to errors when compared to tracking a group of samples within a window.

To study the ST performance as a strain estimator and compare it with commonly used techniques, the algorithm was employed to estimate the delay when the echo signal changed due to sample compression. The performance of the cubic spline-based ST was compared with normalized correlation with cosine fit and cubic spline-based CTDE. The time-delay estimates at different compression levels are shown in Fig 2.7. The normalized correlation was used to find the coarse location of the time-shift for both techniques. The sizes of the windows were set to be 3λ and the windows were set to have 50% overlap as typically used in strain estimation [26]. The time-delay estimates for varying compression levels are shown in Fig 2.7 for all three methods.

Fig 2.7 shows that window tracking with cosine fit fails to estimate small strains and shows poor sensitivity while spline-based methods estimate even 0.0001% compression (4.0×10^{-5} mm $\approx 2.0 \times 10^{-3}$ of a sample maximum displacement) without any ambiguity. These results are consistent with the results shown in Fig 2.3 and Fig 2.4, where ST and CTDE were shown to have much smaller bias and standard deviation when compared to the normalized correlation with cosine fit. For large compression levels (i.e. 7% to 10%), all the algorithms failed to estimate the delays correctly. This is due to the fact that they all depend on the normalized cross-correlation to provide them with estimation delays that are within the sampling accuracy. As a result, when the normalized correlation fails at large compression levels, all the algorithms fail as well.

In order to study the sensitivity quantitatively, the strain filters of all the above methods

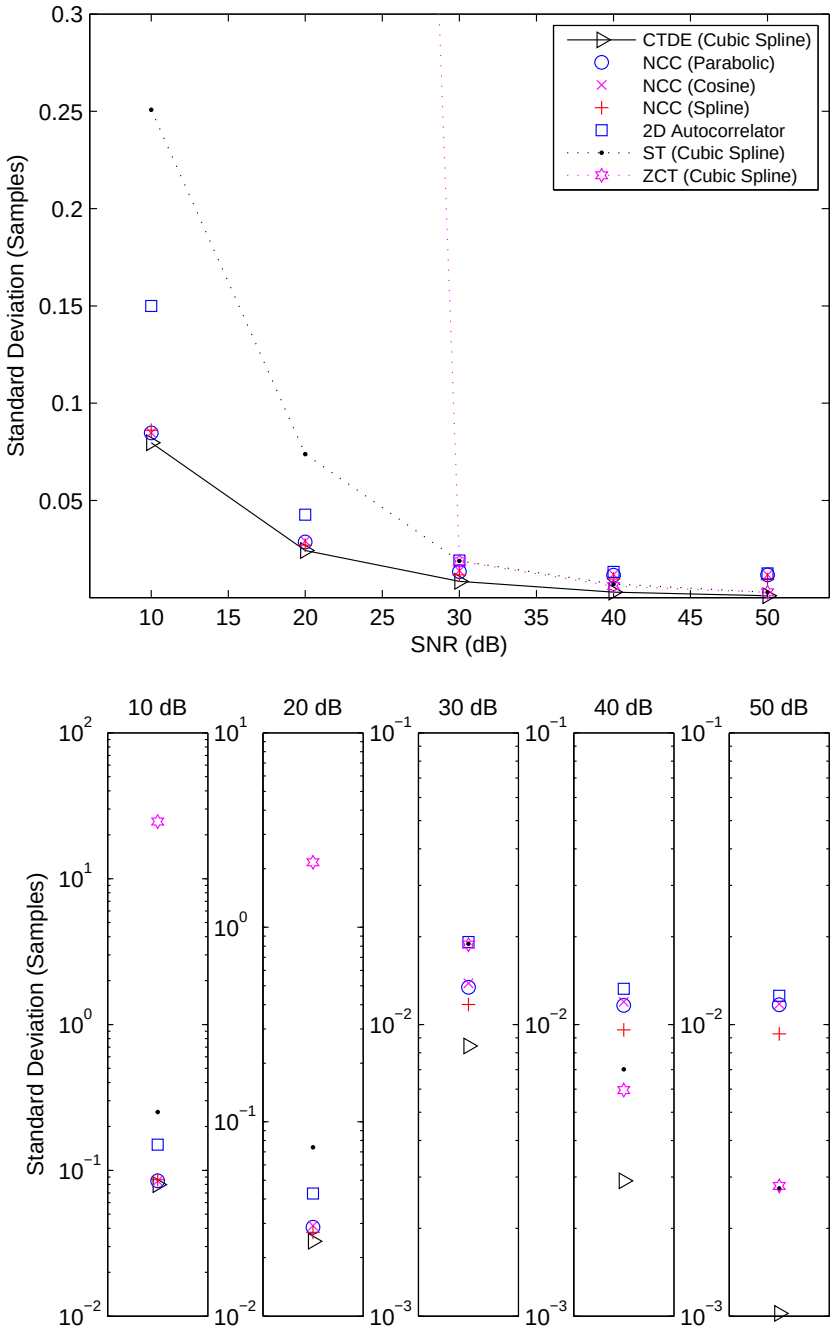

Figure 2.6: Standard deviation of the delay estimators as a function of SNR. The bottom panel depicts an expanded view of each condition tested. The reference and delayed signals were identical, except for a sub-sample shift. 500 independent realizations were used to generate the results ($f_s = 40$ MHz, $f_o = 5$ MHz, $B = 0.5$, and $W = 1.5\lambda$).

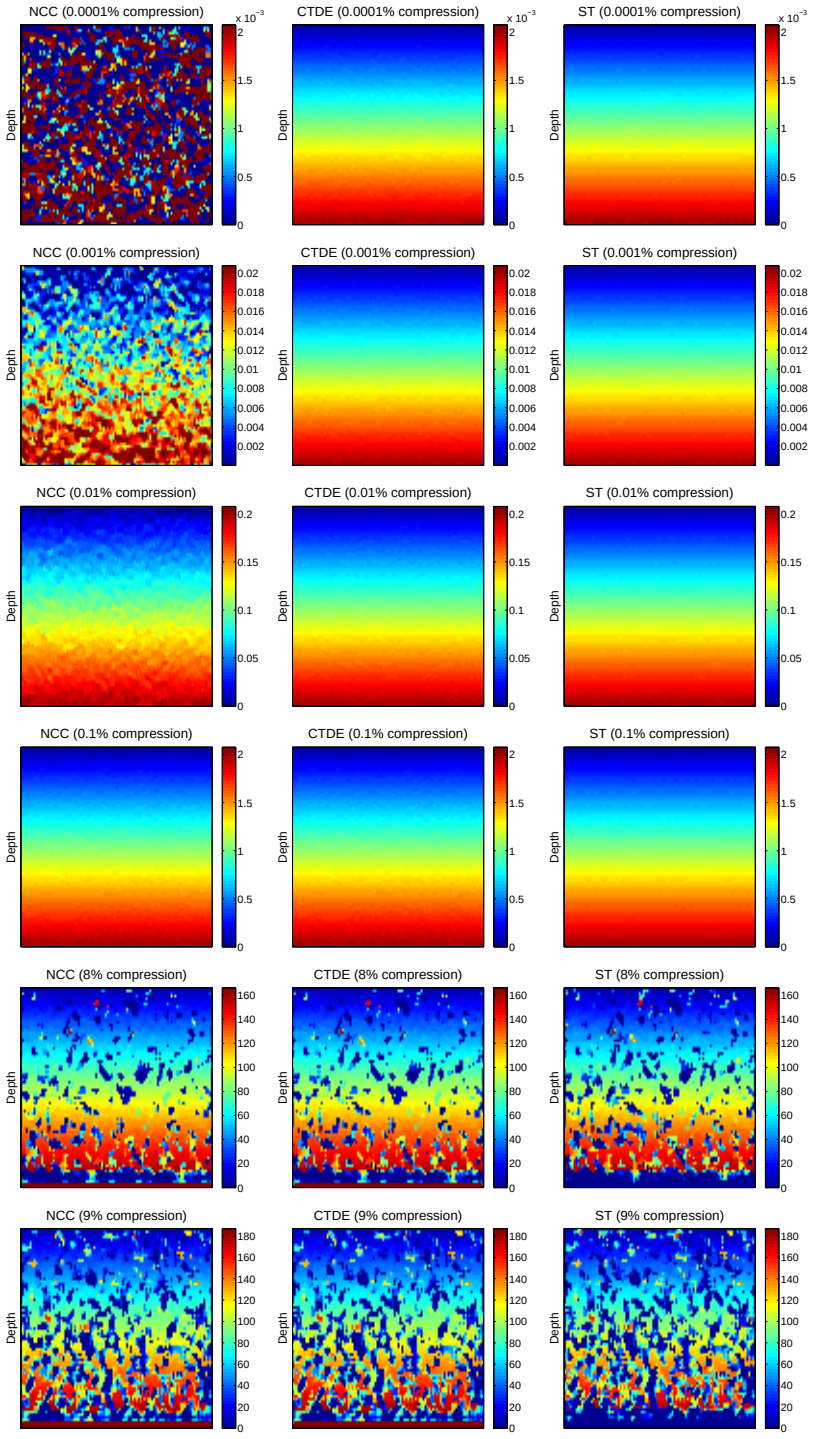

Figure 2.7: Time-delay estimation images at different compression levels (0.0001%∼0.1% and 8%∼9% strain on a logarithmic scale) using normalized cross correlation with cosine fit (left), CTDE with cubic spline fit (center) and ST with cubic spline fit (right). The window size was set to 3λ with 50% window overlap. Colorbars are in sample.

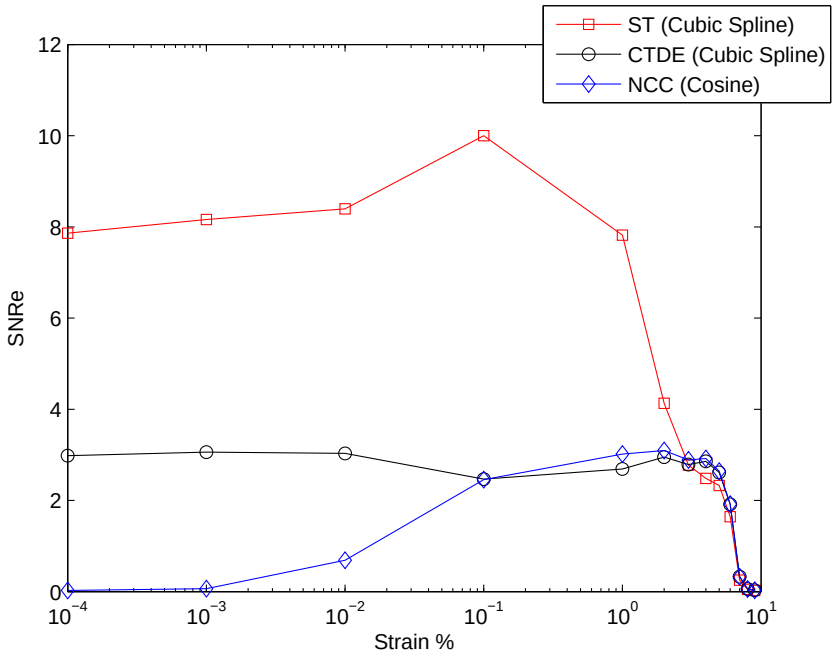

Figure 2.8: Signal-to-noise ratio of estimated strain as a function of applied compression for window tracking and ST. ST shows much higher sensitivity compared to window tracking since it is capable of estimating very small strains.

were estimated and shown in Fig 2.8. Fig 2.8 shows that compared to CTDE, ST provides strain images with much higher sensitivity. The performances of all the methods are similar for large deformations.

To compare the computational cost of ZCT and ST with that of CTDE, note that both ST and ZCT preserve the order of fitted polynomials for the root estimation process. However, the square term in (2.4) doubles the order of the polynomial for the continuous time-delay estimation. Therefore, the root estimation routine is simpler for both ST and ZCT. However, both ST and ZCT require calling the root estimation process more often than the window based continuous time-delay estimators. As a result, the ST and ZCT methods have higher computational cost than the corresponding window-based continuous delay estimators. However, estimating the delay for a different window size with a window-based method requires re-estimating the delays for each window, while in ST and ZCT, only the windowing must be repeated since the sample or the zero-crossing shift does not change. Thus, ST and ZCT methods offer the flexibility of a variable resolution, depending on the window size used to average the displacement estimates, without significantly increasing the computation time. In contrast, window-based techniques need to repeat the entire estimation once the window size is changed.

Although we have only considered 1D tracking, the generalization of ST to higher dimensions is possible. In the 2D case, for example, a 2D function needs to be fitted to the reference echo signal. The displacement that satisfies (2.1) in both directions needs to be calculated. This would result in a 2D estimate of the displacement for each sample. The use of 2D spline

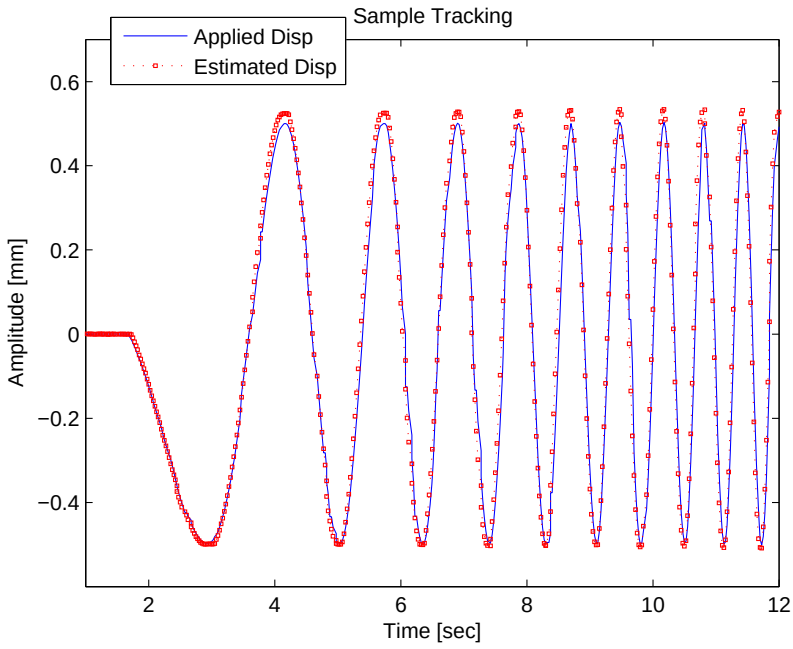

Figure 2.9: Experimental displacement estimates using the ST algorithm. The straight line shows the displacement applied to the probe and the dotted line shows the average of measurements over the region of interest. ($f_s = 40$ MHz, $f_o = 5$ MHz, $Depth = 40$ mm, $W = 3\lambda$, no window overlap).

polynomials to describe the echo signal to estimate 2D motion has been reported in [35].

2.5 Experimental Performance

In order to study the performance of the ST algorithm with real data, an experiment was conducted. The transducer was mounted on top of a leadscrew stage that provides controlled motion. An experiment was performed on a $40 \times 40 \times 40$ mm^3 uniformly elastic phantom. The phantom was prepared using a 100% polyvinyl chloride (PVC) plasticizer (M-F Manufacturing Co., Inc. Fort Worth, TX, USA) with two percent cellulose (Sigma-Aldrich Inc., St Louis, MO, USA) as scatterers [36]. The phantom was placed in a tank full of degassed water at room temperature. The phantom was placed 2 mm away from the transducer. In this way the transducer was able to move without deforming the phantom, producing a rigid motion. The probe was moved axially in sinusoidal trajectories with 0.5 mm amplitude and variable frequency. The phantom was imaged to a depth of 40 mm (2 mm water gap plus 38 mm phantom) with a linear array of 128 elements with 0.3 mm lateral spacing, with a 5 MHz center frequency, digitized at 40 MHz, of a SonixRP ultrasound machine (Ultrasonix Medical Corporation, Richmond, BC). The RF frames and transducer position were recorded at 40 Hz and dumped into a file for off-line processing (a total of 800 frames). The transducer position was measured through the encoder (as an applied motion) and was synchronized with the RF ultrasound images of the phantom.

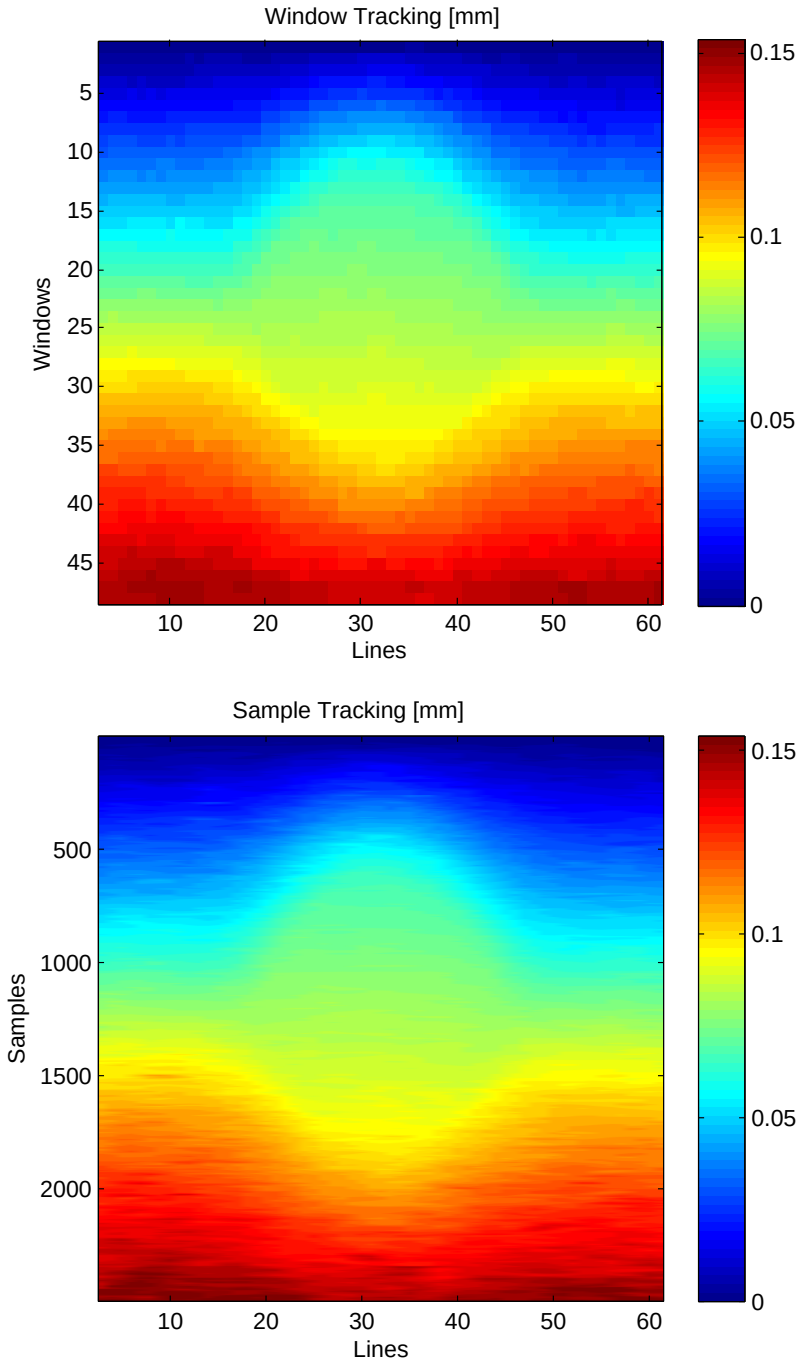

Figure 2.10: Displacement estimates using normalized cross correlation plus cosine fit (top), ST algorithm (bottom) of a phantom with a cylindrical hard inclusion when it undergoes small uniaxial compression ($f_s = 40$ MHz, $f_o = 5$ MHz, $Depth = 50$ mm, $W = 3\lambda$, no window overlap).

For time-delay estimation, RF signals were divided into non-overlapping windows. The coarse displacements were measured using the normalized cross correlation applied to the non-overlapping windows. The displacements of the individual samples within the windows were then estimated using cubic spline-based ST. The estimated time-delays inside a 25 mm $\times$ 25 mm (84 lines and 1300 samples) region of interest at each time were averaged and compared with the applied displacement. The experimental results are shown in Fig 2.9. The results show that ST tracks the displacement very accurately in the presence of noise. The average error was measured to be 8μm over the entire motion.

In order to study the ST performance qualitatively, another experiment was performed on a phantom with a hard cylindrical inclusion. The phantom was prepared using a 100% PVC plasticizer for the inclusion and 66.7% PVC plasticizer and 33.3% plastic softener (M-F Manufacturing Co., Inc. Fort Worth, TX, USA) for the background. Two percent cellulose was used as scatterers for both inclusion and background. The phantom was placed in front of the probe. Using the same setup, the phantom was imaged once to capture the reference RF frame (i.e. pre-compression RF frame). The phantom was then compressed 150 μm uniaxially. The second RF frame (i.e. post-compression RF frame) was captured while the phantom was under the compression. The resulting displacements between the echo signals were measured with both cubic spline-based ST and normalized cross correlation with cosine fit. The results are shown in Fig 2.10. Compared to the standard technique which provides measurement points equal to the number of windows (i.e. 50) per each line, ST provides measurement points equal to the number of samples (i.e. 2500) for each line and provides a smoother image.

2.6 Conclusions

A new class of time-delay estimators based on the tracking of the individual measured echo samples has been presented in this paper. ST algorithms generate time-shift estimates with much higher density compared to commonly used window-based methods. Simulation results show that these algorithms outperform conventional window based time-delay estimators in terms of bias and standard deviation when applied to high SNR echo signals. Simulation results also show that ST algorithms have higher resolution and sensitivity when used as strain estimators compared to commonly used strain estimation algorithms, including the recently introduced spline-based continuous time-delay estimator.

In addition to ST algorithms, based on the previously introduced zero-crossings tracking algorithm, a new spline-based zero-crossings tracking algorithm has also been presented. Simulation results show that the new zero-crossing tracking algorithm significantly outperforms the original linear interpolation based ZCT. The proposed ZCT has similar performance to that of the presented ST algorithm.

The proposed algorithms have potential applications in medical ultrasound, including fine tissue motion estimation, strain estimation, elasticity estimation, and acoustic radiation force impulse imaging.

References

[1] C. Kasai, K. Namekawa, A. Koyano, and R. Omoto, "Real-time two-dimensional blood flow imaging using an autocorrelation technique." *IEEE Transactions on Sonics and Ultrasonics*, vol. 32, pp. 458–464, 1985.

[2] T. Loupas, R. Peterson, and R. Gill, "Experimental evaluation of velocity and power estimation forultrasound blood flow imaging, by means of a two-dimensional autocorrelation approach." *IEEE Transactions on Ultrasonics, Ferroelectrics and Frequency Control*, vol. 42, pp. 689–699, Jul 1995.

[3] H. Torp, K. Kristoffersen, and B. Angelsen, "Autocorrelation Techniques in Color Flow Imaging. Signal model and statistical properties of the Autocorrelation estimates." *IEEE Transactions on Ultrasonics, Ferroelectrics, and Frequency control*, vol. 41, pp. 604–612, 1994.

[4] S. Srinivasan and J. Ophir, "A zero-crossing strain estimator in elastography," *Ultrasound in Med and Bio*, vol. 29, pp. 227–238, 2003.

[5] J. Ophir, I. Cespedes, H. Ponnekanti, Y. Yazdi, and X. Li, "Elastography: a quantitative method for imaging the elasticity of biological tissues," *Ultrasonic Imaging*, vol. 13, pp. 111–134, April 1991.

[6] A. Heimdal, A. Stoylen, H. Torp, and T. Skjaerpe, "Real-time strain rate imaging of the left ventricle by ultrasound." *Journal of American Soc Echocardiography*, vol. 11, pp. 1013–1019, Nov 1998.

[7] L. Bohs, B. Friemel, and G. Trahey, "Experimental velocity profiles and volumetric flow via two-dimensional speckle tracking." *Ultrasound in Medicine and Biology*, vol. 21, pp. 885–98, 1995.

[8] M. Lubinski, S. Emelianov, and M. O'Donnell, "Speckle tracking methods for ultrasonic elasticity imaging using short-time correlation," *IEEE Transactions on Ultrasonics, Ferroelectrics and Frequency Control*, vol. 46, pp. 82–96, January 1999.

[9] K. Nightingale, M. Palmeri, R. Nightingale, and G. Trahey, "On the feasibility of remote palpation using acoustic radiation force," *Journal of the Acoustical Society of America*, vol. 110, pp. 625–34, July 2001.

[10] W. Walker, F. Fernandez, and L. Negron, "A method of imaging viscoelastic parameters with acoustic radiation force." *Physics in Medicine and Biology*, vol. 45, pp. 1437–1447, 2000.

[11] M. Fatemi and J. Greenleaf, "Probing the dynamics of tissue at low frequencies with the radiation force of ultrasound," *Physics in Medicine and Biology*, vol. 45, pp. 1449–64, June 2000.

[12] F. Viola and W. Walker, "A comparison of the performance of time-delay estimators in medical ultrasound." *IEEE Transactions on Ultrasonics, Ferroelectrics and Frequency Control*, vol. 50, pp. 392–401, April 2003.

[13] G. Pinton, J. Dahl, and G. Trahey, "Rapid tracking of small displacements with ultrasound." *IEEE Transactions on Ultrasonics, Ferroelectrics and Frequency Control*, vol. 53, pp. 1103– 1117, June 2006.

[14] I. Hein and W. O'Brien, "Current time-domain methods for assessing tissue motion by analysis from reflected ultrasound echoes-a review." *IEEE Transactions on Ultrasonics, Ferroelectrics and Frequency Control*, vol. 40, pp. 84–102, March 1993.

[15] G. Pinton and G. Trahey, "Continuous Delay Estimation with Polynomial Splines." *IEEE Transactions on Ultrasonics, Ferroelectrics and Frequency Control*, vol. 53, pp. 2026–2035, 2006.

[16] M. O'Donnell, A. Scovoroda, B. Shapo, and S. Emelianov, "Internal Displacement and Strain Imaging Using Ultrasonic Speckle Tracking," *IEEE Transactions on Ultrasonics, Ferroelectrics and Frequency Control*, vol. 41, pp. 314–25, May 1994.

[17] A. Pesavento, C. Perrey, M. Krueger, and H. Ermert, "A time efficient and accurate strain estimation concept for ultrasonic elastography using iterative phase zero estimation," *IEEE Transactions on Ultrasonics, Ferroelectrics, and Frequency Control*, vol. 46, pp. 1057–1067, 1999.

[18] G. Jacovitti and G. Scarano, "Discrete time techniques for time delay estimation." *IEEE Transactions on Acoustics, Speech, and Signal Processing*, vol. 41, pp. 525–533, Feb 1993.

[19] S. Langeland, J. Dapos, H. Torp, B. Bijnens, and P. Suetens, "A simulation study on the performance of different estimators for two-dimensional velocity estimation." in *Proceedings of the IEEE Ultrasonics Symposium.* Volume 2: IEEE, 8-11 Oct 2002, pp. 1859–1862.

[20] I. Cespedes, Y. Huang, J. Ophir, and S. Spratt, "Methods for the estimation of subsample time-delays of digitized echo signals," *Ultrasonic Imaging*, vol. 17, pp. 142–171, 1995.

[21] S. Foster, P. Embree, and W. O'Brien, "Flow velocity profile via time-domain correlation: error analysis and computer simulation," *IEEE Transactions on Ultrasonics, Ferroelectrics and Frequency Control*, vol. 37, pp. 164–175, May 1990.

[22] B. Geiman, L. Bohs, M. Anderson, S. Breit, and G. Trahey, "A comparison of algorithms for tracking sub-pixel speckle motion." in *Proceedings of the IEEE Ultrasonics Symposium.* Volume 2: IEEE, 5-8 Oct 1997, pp. 1239–1242.

[23] P. de Jong, T. Arts, A. Hoeks, and R. Reneman, "Determination of Tissue Motion Velocity by Correlation Interpolation of Pulsed Ultrasonic Echo Signals," *Ultrasonics Imaging*, vol. 12, pp. 84–98, 1990.

[24] L. Geiman, BJ.and Bohs, M. Anderson, S. Breit, and T. G.E., "A novel interpolation strategy for estimating subsample speckle motion." *Physics in Medicine and Biology*, vol. 45, pp. 1541–1552, 2000.

[25] F. Viola and W. Walker, "A Spline-Based Algorithm for Continuous Time-Delay Estimation Using Sampled Data." *IEEE Transactions on Ultrasonics, Ferroelectrics and Frequency Control*, vol. 52, pp. 80–93, January 2005.

[26] T. Varghese, J. Ophir, E. Konofagou, F. Kallel, and R. Righetti, "Tradeoffs In Elastographic Imaging, Ultrasonic Imaging," *Ultrasonic Imaging*, vol. 23, pp. 216–248, October 2001.

[27] S. Srinivasan, R. Righetti, and J. Ophir, "Tradeoffs between the axial resolution and the signal-to-noise ratio in elastography," *Ultrasound in Medicine and Biology*, vol. 29, pp. 847–866, 2003.

[28] F. Walker and E. Trahey, "A fundamental limit on delay estimation using partially correlated speckle signals," *IEEE Transactions on Ultrasonics, Ferroelectrics and Frequency Control*, vol. 42, pp. 301–308, 1995.

[29] H. Shi and T. Varghese, "Two-dimensional multi-level strain estimation for discontinuous tissue." *Physics in Medicine and Biology*, vol. 52, pp. 389–401, Nov 2007.

[30] C. Sumi, "Fine elasticity imaging utilizing the iterative RF-echo phase matching method." *IEEE Transactions on Ultrasonics, Ferroelectrics, and Frequency control*, vol. 46, pp. 158–166, Jan 1999.

[31] H. Eskandari, S. Salcudean, and R. Rohling, "Tissue strain imaging using a wavelet transform-based peak search algorithm." *IEEE Trans Ultrason Ferroelectr Freq Control*, vol. 54, pp. 1118–30, June 2007.

[32] M. Unser, "Splines: a perfect fit for signal and image processing." *Signal Processing Magazine, IEEE*, vol. 16, pp. 22–38, Nov 1999.

[33] R. Zahiri-Azar and S. Salcudean, "Motion Estimation in Ultrasound Images Using Time Domain Cross Correlation With Prior Estimates." *IEEE Transactions on Biomedical Engineering*, vol. 53, pp. 1990–2000, 2006.

[34] F. Viola and W. Walker, "A comparison between spline-based and phase-domain time-delay estimators." *IEEE Transactions on Ultrasonics, Ferroelectrics and Frequency Control*, vol. 53, pp. 515–517, March 2006.

[35] W. Walker, D. Guenther, R. Coe, and F. Viola, "A Novel Spline-Based Algorithm for Multidimensional Displacement and Strain Estimation." in *Proceedings of the IEEE Ultrasonics Symposium*. IEEE, Oct 2006, pp. 1221–1225.

[36] S. DiMaio and S. Salcudean, "Needle insertion modelling and simulation," *IEEE Transactions on Robotics and Automation: Special Issue on Medical Robotics*, vol. 19, pp. 864–875, 2003.

Chapter 3

2D Estimation of Sub-Sample Motion from Digitized Ultrasound Echo Signals[2]

3.1 Introduction

Motion estimation in sequences of ultrasound echo signals is essential for a wide range of modern ultrasound-based signal processing applications. These applications include blood flow estimation, tissue velocity estimation [1–3], strain and strain rate imaging [4–6], tissue elasticity imaging [7], vibro-elastography [8,9], poro-elastography [10], myocardial imaging [11], tumor classification [12], and acoustic radiation force impulse imaging [13–15]. Because of its central importance, its accuracy, precision, and computational cost are of critical importance.

Motion estimators measure displacement of the backscattered signals with respect to the transducer. Motion estimators are typically classified based on the type of signal (RF, envelope, in-phase and quadrature I/Q) and the domain on which they operate (i.e. time, phase, or frequency). These estimators have been studied and compared extensively in the literature [16–20].

Phase-shift estimators were initially used for blood flow measurement [1, 2]. Later, the same techniques were used to estimate the tissue motion. Phase-shift estimators find the average phase-shift over a number of samples within a window with respect to the nominal or estimated central frequency of the transmitted pulse. Complex cross correlation of the RF echo signals [21, 22] or complex-valued Doppler signals [1, 2] are typically used in these techniques. The extension of phase shift estimations to 2D has also been studied in the literature [23–27].

In another approach, frequency-shift estimators have also been introduced in the literature [20, 28, 29]. However their extension to 2D has yet to be studied.

Pattern matching techniques were initially used in video and image processing. Later, the same techniques were borrowed in the field of ultrasound to estimate motion/time-shift from sampled ultrasound radio-frequency (RF) echo signals [4,26,30,31]. Estimation of motion from envelope signals and combination of RF and envelope signals have also been reported [32, 33]. These techniques typically consist of the identification of the maximum/minimum of a pattern matching function. The shape of the signal within a specific window in the reference echo signal is set to be the pattern and a matching algorithm is used to find the best match in the delayed echo signal.

[2] A version of this chapter has been peer reviewed and published in the proceedings of the international Conference on IEEE EMBS. A version of this chapter has also been submitted for publication. Reza Zahiri-Azar, Orcun Goksel, and Septimiu E. Salcudean, "A Comparative Study of 2D Pattern Matching Function Interpolation Methods using Ultrasound Echo signals with Application to Real-Time Elastography".

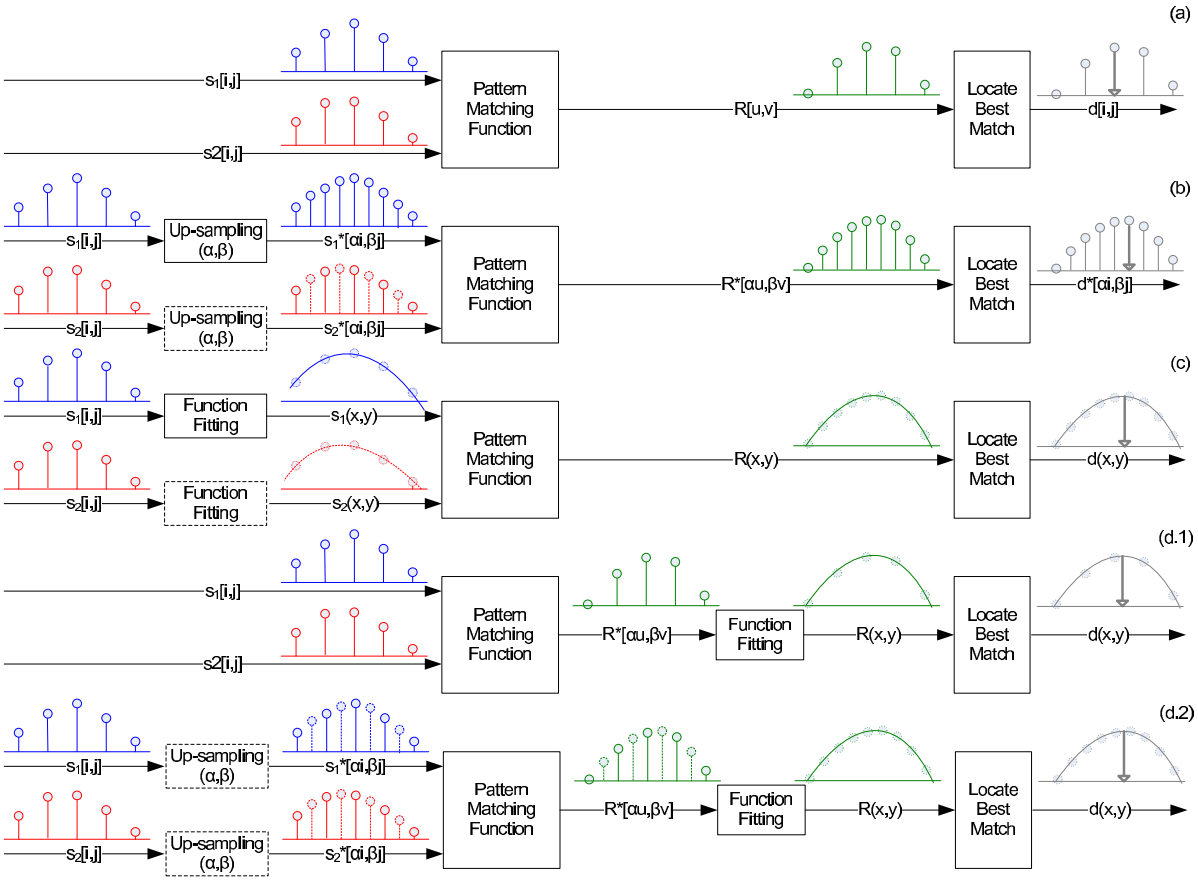

Figure 3.1: Common techniques to reduce the error of discrete pattern matching functions. Dashed boxes show optional steps. (a) Basic pattern matching function. (b) Pattern matching function with echo signal up-sampling where α and β are the up-sampling factor in the axial and the lateral directions. (c) Continuous pattern matching function generated from curve or polynomial fitting to one or both of the echo signals. (d) Pattern matching function interpolation which can be implemented without (d.1) and with (d.2) signal up-sampling.

Several pattern matching techniques have been used in the field of ultrasound, such as normalized cross correlation, sum of square differences, and sum of absolute differences, each offering trade offs between complexity and accuracy [16,34,35]. Extensions of these techniques to 2D (or even 3D) has also been suggested [26,31,33,36–40].

The estimation error of pattern matching techniques can be as large as half the sample spacing. This results in significant errors when accurate and precise tracking of the motion is the goal. This error become more significant in the lateral (or the elevational) direction were the sample spacing is an order of magnitude larger compared to the axial direction.

Several techniques have been suggested in the literature to reduce the error introduced by finite sampling intervals. These techniques are categorized as: (i) echo signal up-sampling [19,37,41,42], (ii) interpolation of the echo signals [19,38,41,43], and (iii) interpolation of the pattern matching function [44–47]. These approaches are schematically represented in Fig 3.1.

Up-sampling the echo signal (i) reduces the error by the up-sampling factor (Fig. 3.1(b)),

but can increase the computational cost significantly [11,19,37,42]. This is due to the fact that, in addition to the up-sampling operations, the pattern matching function needs to be computed at a higher sampling rate. Curve or polynomial fitting to the echo signals (ii) results in a continuous representation of the echo signal and subsequently in a continuous pattern matching function [19, 38, 41, 43]. The location of the best match can then be identified from the continuous pattern matching function without the sample spacing limitation (Fig. 3.1(c)). It has been shown that these techniques outperform other algorithms but, similarly to up-sampling methods, they can be computationally demanding [43, 48]. Pattern matching interpolation techniques (iii) are computationally more efficient than up-sampling or continuous representation (Fig. 3.1(d)). Therefore, even though they introduce some bias in the estimation process, they are widely used in motion estimation. These techniques will be the topic of this work.

A number of 1D pattern matching interpolation methods such as parabolic fitting [47], spline fitting [46], grid slope [31, 36], cosine fitting [45], zero padding, and reconstructive methods [44] have been introduced and thoroughly investigated in the literature [16, 41, 43]. Applying the same 1D interpolation techniques independently to each direction (2-1D) has also been used widely in the literature to estimate the sub-sample motion in two (or even three) dimensions [31, 36, 38, 49–51]. Applying iterative 1D interpolation [52, 53] and 2D interpolation techniques [53–55] have also been attempted in the literature. However, there is no comprehensive study in the literature that quantifies and compares the performance of these various techniques.

In this work, the performance of these interpolation methods are studied and compared on ultrasound radio frequency and envelope data. Both simulation and experimental results are used to produce a comparative performance assessment. Furthermore, due to small computational cost, pattern matching interpolation methods facilitate the estimation of sub-sample motions in real-time. By implementing these interpolation methods, we extend our previously introduced 1D motion tracking algorithm [56] to 2D, and report an implementation of a motion tracking software that estimates both axial and lateral motions with sub-sample accuracy in real-time.

The paper is structured as follows: Section 3.2 presents the interpolation techniques. Section 3.3 and 3.4 present the performance comparison between the different methods by studying both simulation and experimental results. Section 3.5 presents an implementation of the interpolation algorithms for 2D motion tracking in real-time, followed by a discussion in Section 3.6. Section 3.7 presents conclusions along with avenues for future research.

Throughout this work, it is assumed that the echo signals are 2D radio frequency (RF) signals. In Section 3.3, the performance of sub-sample estimation methods are also studied for 2D envelope data. Without loss of generality, it is assumed that the pattern matching function optimization involves maximization of the normalized cross correlation. A detailed description of a pattern matching function is provided in Appendix C. The pattern matching function values will be referred to as the *matching coefficients*.

3.2 Methods

Let $R[u, v]$ be the discrete 2D pattern matching function between the windowed reference and the displaced echo signal over a predefined search region. Given $R[u, v]$ the coarse axial d_a and lateral d_l estimates of the motion in the axial (x) and the lateral (y) directions are achieved

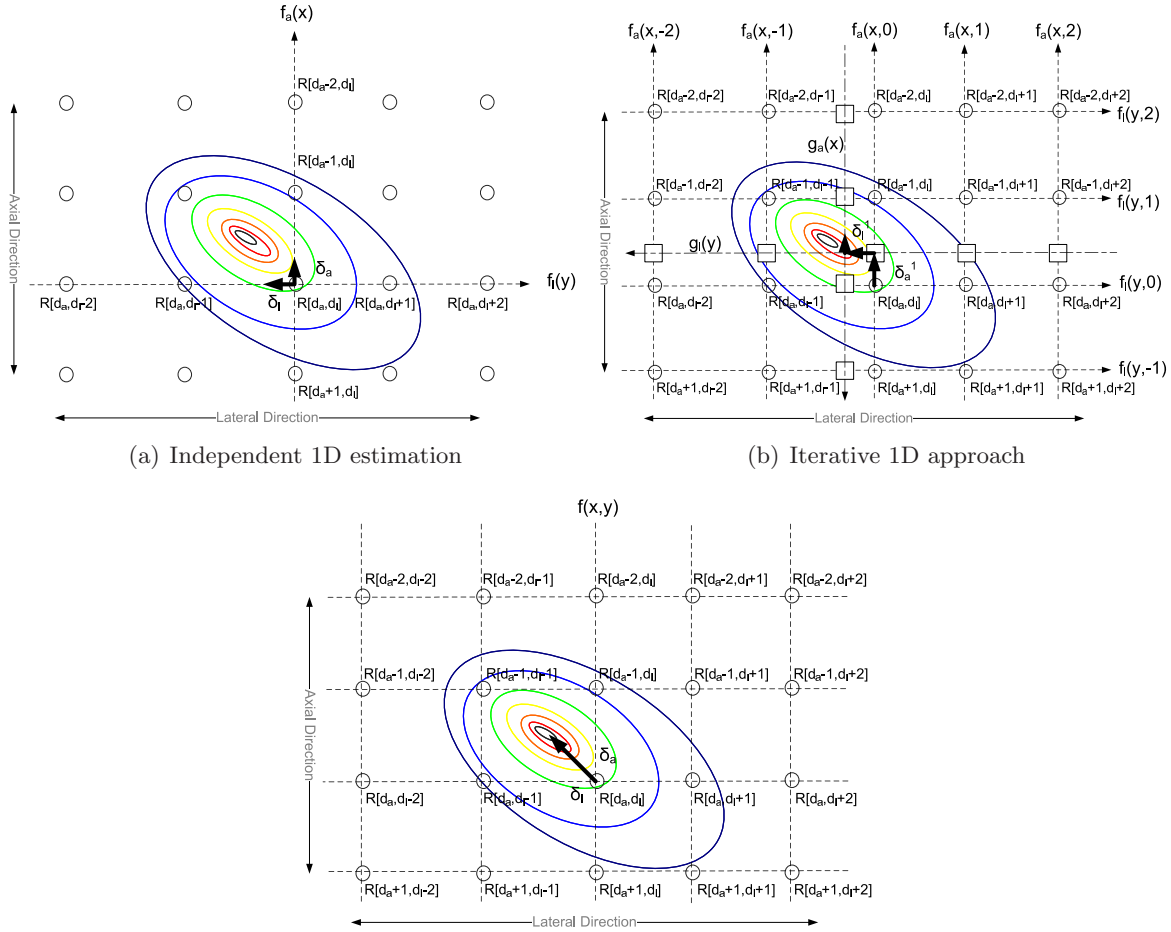

(a) Independent 1D estimation

(b) Iterative 1D approach

(c) 2D joint estimation

Figure 3.2: Different schemes for sub-sample displacement estimation in 2D, using coefficients of the cross correlation function in the neighborhood of its maximum. For the first two techniques ((a) and (b)) only 1D interpolation is required while for the last method (c), 2D interpolation is necessary. Solid circles show the actual matching coefficients and squares show the interpolated matching coefficients. Ellipses show equal value contours of underlaying correlation function.

by locating the maximum of the 2D discrete pattern matching function $R[u, v]$. The estimates d_a and d_l are given by

$$[d_a, d_l] = \arg\max_{u,v} R[u, v]. \tag{3.1}$$

Following the coarse estimation of the motion within the sampling accuracy, the following methods are used to estimate the sub-sample displacements (δ_a, δ_l) in the axial and the lateral directions respectively, using the matching coefficients at neighboring lags (Fig. 3.1(d)).

3.2.1 Independent 1D Method

Referring to Fig. 3.2(a), let $f_a(x)$ be an axial 1-D interpolation function passing through the 2D pattern matching function at $[d_a, d_l]$ and its axial lags (i.e. $R[d_a + i, d_l]$ where $i \in \{0, \pm1, \pm2, ..., \pm M_a\}$, where M_a is the fitting radius in the axial direction) and $f_l(y)$ be a lateral 1-D interpolation function passing through the 2D pattern matching function at $[d_a, d_l]$ and its lateral lags (i.e. $R[d_a, d_l + j]$ where $j \in \{0, \pm1, \pm2, ..., \pm M_l\}$, where M_l is the fitting radius in the lateral direction). The sub-sample motion estimates δ_a, δ_l at (d_a, d_l) are computed from their corresponding axial and lateral interpolation functions as follows:

$$\begin{aligned} \delta_a &= \arg\max_x f_a(x), \\ \delta_l &= \arg\max_y f_l(y). \end{aligned} \tag{3.2}$$

These methods are the most commonly used techniques to estimate the sub-sample motion in 2D [38, 49–51]. For the purpose of this work, (i) the three point 1D parabola fitting [47], where the axial and the lateral sub-sample shifts are estimated from $f_a(x) = a_a + b_a x + e_a x^2$ and $f_l(y) = a_l + b_l y + c_l y^2$, and (ii) the three point cosine fitting [45], where the axial and the lateral sub-sample shifts are estimated from $f(x) = A_a \cos(\alpha_a x + \beta_a)$ and $f(y) = A_l \cos(\alpha_l y + \beta_l)$, have been implemented due to their relative computational simplicity [41, 44]. Detailed descriptions of these common techniques are provided in Appendix D. The independent 1D methods using three point function fitting ($M_a = M_l = 1$), require matching coefficients to be available at five lags (i.e. the maximum in the center and the two immediate neighboring lags in each direction).

3.2.2 Grid Slope

This method was proposed in [31, 36]. It has also been studied in [41] when estimating the motion in axial direction only. In order to apply this technique, it is necessary to compute the pattern matching function between the reference and displaced signals R, and the pattern matching function between the reference signal and itself R_0. Similarly to above mentioned techniques, the grid slope technique estimates the axial and lateral sub-sample motion independently. Thus, it can be classified as an independent 1D interpolation method.

3.2.3 Iterative 1D Method

In an iterative approach, the achieved sub-sample accuracy in one direction can be used to estimate the sub-sample displacement in the other direction [52, 53]. Referring to Fig. 3.2(b), let $f_a(x, j), x \in \Re$ and $j \in \{0, \pm1, \pm2, ..., \pm M_l\}$ be a set of functions such that for every

value of j, $f_a(x,j)$ is an axial 1-D interpolation function passing through $R[d_a+i, d_l+j], i \in \{0, \pm1, \pm2, ..., \pm M_a\}$ and $f_l(y,i), y \in \Re$ and $i \in \{0, \pm1, \pm2, ..., \pm M_a\}$ be a set of functions such that for every value of i, $f_l(y,i)$ is a lateral 1-D interpolation function passing through $R[d_a+i, d_l+j], j \in \{0, \pm1, \pm2, ..., \pm M_l\}$. The iterative 1D method can be formulated as follows:

1. $k = 0$, $\delta_l^0 = 0$,
2. $g_a^k(x) :=$ 1-D interpolating function passing through $f_l(\delta_l^k, i)), i \in \{0, \pm1, \pm2, ..., \pm M_a\}$,
3. $\delta_a^k = \arg\max_x g_a^k(x)$,
4. $g_l^k(y) :=$ 1-D interpolating function passing through $f_a(\delta_a^k, j), j \in \{0, \pm1, \pm2, ..., \pm M_l\}$,
5. $\delta_l^k = \arg\max_y g_l^k(y)$,
6. if stopping criterion not met, $k = k + 1$, return to (2).

where k is the index of iteration.

In the algorithm presented above the f_a, f_l are the interpolation functions passing through actual matching coefficients, and g_a^k, g_l^k are the interpolation functions passing through interpolated matching coefficients. It should be noted that in the first iteration $g_a^0(x) = f_a(x, 0)$ since $\delta_l^0 = 0$ and interpolated values are the same as the discrete values.

In contrast to independent 1D methods, iterative 1D methods use the estimated sub-sample motion in one direction to calculate the sub-sample motion in the other direction. The iterative 1D methods use the interpolated matching coefficients at the estimated sub-sample locations. Thus, they require more matching coefficients than used in the independent 1D method. Similarly to independent 1D methods, the same three point parabola fitting using $f_a(x) = a_a + b_a x + c_a x^2$, $f_l(y) = a_l + b_l y + c_l y^2$) and cosine fitting $f_a(x) = A_a \cos(\alpha_a x + \beta_a)$, $f_l(x) = A_l \cos(\alpha_l y + \beta_l)$), have been implemented. The iterative 1D method using three point function fitting ($M_a = M_l = 1$), requires matching coefficients to be available at nine lags (i.e. the maximum in the center, and its 8 neighboring lags).

3.2.4 2D Method

In a more general approach a 2D function can be fitted to the discrete matching coefficients in both the axial and the lateral directions [53, 54]. Joint estimation with sub-sampling accuracy can then be achieved in both directions by finding the peak of the fitted function analytically.

Referring to Fig. 3.2(c), let $f(x,y)$ be a 2-D interpolation function passing through the 2D pattern matching function at $[d_a, d_l]$ and its neighbors (i.e. $R[d_a + i, d_l + j]$ where $i \in \{0, \pm1, \pm2, ... \pm M_a\}, j \in \{0, \pm1, \pm2, ... \pm M_l\}$). The sub-sample motion estimates δ_a, δ_l at (d_a, d_l) are computed jointly from the corresponding 2D interpolation functions as follows:

$$[\delta_a, \delta_l] = \arg\max_{x,y} f(x,y). \tag{3.3}$$

The following 2D polynomial fitting are implemented in this paper:

$$
\begin{aligned}
f_5(x,y) &= a_1 + a_2x + a_3y + a_4x^2 + a_5y^2, && (3.4)\\
f_6(x,y) &= a_1 + a_2x + a_3y + a_4xy + a_5x^2 + a_6y^2, && (3.5)\\
f_9(x,y) &= a_1 + a_2x + a_3y + a_4xy + a_5x^2 + a_6y^2 + a_7xy^2 && (3.6)\\
&\quad + a_8x^2y + a_9x^2y^2,\\
f_{16}(x,y) &= a_1 + a_2x + a_3y + a_4xy + a_5x^2 + a_6y^2 + a_7xy^2 && (3.7)\\
&\quad + a_8x^2y + a_9x^2y^2 + a_{10}x^3 + a_{11}x^3y + a_{12}x^3y^2\\
&\quad + a_{13}y^3 + a_{14}xy^3 + a_{15}x^2y^3 + a_{16}x^3y^3,\\
f_{25}(x,y) &= a_1 + a_2x + a_3y + a_4xy + a_5x^2 + a_6y^2 + a_7xy^2 && (3.8)\\
&\quad + a_8x^2y + a_9x^2y^2 + a_{10}x^3 + a_{11}x^3y + a_{12}x^3y^2\\
&\quad + a_{13}y^3 + a_{14}xy^3 + a_{15}x^2y^3 + a_{16}x^3y^3\\
&\quad + a_{17}x^4 + a_{18}x^4y + a_{19}x^4y^2 + a_{20}x^4y^3\\
&\quad + a_{21}y^4 + a_{22}xy^4 + a_{23}x^2y^4 + a_{24}x^3y^4 + a_{25}x^4y^4
\end{aligned}
$$

$f_5(x,y)$

This polynomial is used in [57] for tracking single fluorescent particles. The polynomial is fitted to five points of the discrete pattern matching function, the maximum and four immediate neighbors. Since there is no cross term in this polynomial (i.e. dependence on xy), this 2D joint estimator is equivalent to two independent 1D parabola interpolation that is discussed in Section 3.2.1. For this reason, this polynomial is not studied separately.

$f_6(x,y)$

This 2D polynomial with six coefficients is proposed in [55] for spatial shift estimation. The same polynomial has also been used in [58] to reduce the computational cost of modern video codecs. The cross term in this polynomial makes it a non-separable 2D polynomial. Two different implementation of this polynomial are studied in this work. In one approach the polynomial is fitted to six points of the discrete pattern matching function, the maximum, four immediate neighbors, and one diagonal neighbor as proposed in [55]. This approach is expected to bias the results toward the selection of the sixth matching coefficient. To resolve this issue, in another approach, the 2D polynomial is fitted to nine points of the discrete pattern matching function, the maximum and its eight immediate neighbors ($M_a = M_l = 1$), using a least squares fit. This method will be referred to as $\overline{f_6(x,y)}$. Detailed descriptions of this 2D paraboloid fitting and the corresponding maximization are provided in Appendix E.

$f_9(x,y)$

This non-separable 2D polynomial with nine coefficients which is resulted from multiplying $[1, x, x^2]$ and $[1, y, y^2]$ terms (quadratic spline) is used in [53] to estimate the sub-sample motion in 2D. The polynomial is fitted to the maximum of the discrete pattern matching function and all its eight neighboring lags. Detailed descriptions of this 2D polynomial fitting and the corresponding maximization are provided in Appendix E.

$f_{16}(x, y)$

This 2D polynomial with sixteen coefficients is resulted from multiplying $[1, x, x^2, x^3]$ and $[1, y, y^2, y^3]$ terms (cubic spline). The polynomial is fitted to the maximum of the discrete pattern matching function and all its twenty four neighboring lags ($M_a = M_l = 2$) using the Spline Toolbox (MathWorks Inc., Natick, MA). A modified version of this polynomial has been used in [38] to generate a continuous representation of the echo signal itself in order to generate a continuous pattern matching function in 2D.

$f_{25}(x, y)$

This 2D polynomial with twenty five coefficients is resulted from multiplying $[1, x, x^2, x^3, x^4]$ and $[1, y, y^2, y^3, y^4]$ terms (quartic spline) [59]. The polynomial is fitted to the maximum of the discrete pattern matching function and all its twenty four neighboring lags ($M_a = M_l = 2$). 1D version of this polynomial has also been used in [43] to generate a continuous representation of the echo signal itself in order to estimate motion of individual samples in one direction.

3.3 Simulations

3.3.1 Simulation Setup

A series of computer simulations were performed to study the performance of all the pattern matching function interpolation methods. All calculations were performed in MATLAB (MathWorks Inc., Natick, MA). The simulation assumed a 5 MHz center frequency, 40 MHz sampling frequency, line spacing of 300 μm, and a sample spacing of $\approx 20\,\mu$m. Unless mentioned otherwise, the window size for the pattern matching function is set to be approximately $2 \times 2\,mm^2$ (i.e. 104 samples axially and 7 samples laterally). The size of the search area for the pattern matching function is set to be approximately $3 \times 3\,mm^2$ (i.e. 156 samples axially and 11 samples laterally). In order to have accurate estimation of the cross correlation at the edges of the search region, the actual data from the echo signals were used instead of zero-padding. The stopping criterion for the iterative 1D method was set to be $\left\| \left[\delta_a^k, \delta_l^k\right] - \left[\delta_a^{k-1}, \delta_l^{k-1}\right] \right\| / \left\| \left[\delta_a^k, \delta_l^k\right] \right\| < 10^{-5}$, where $\|.\|$ is the Euclidean norm. In all the simulations this criterion was met in less than three iterations.

A $50 \times 60 \times 10\,mm^3$ virtual phantom was simulated by randomly allocating scatterers, with random scattering amplitudes. Field II [60,61] was then used to simulate the ultrasound radio frequency echo signals (RF frames) and envelope signals from these scatterers. A linear probe was modeled with 5 MHz center frequency and 40 MHz sampling rate. A linear scan of the phantom was done with a 128 element transducer, using 64 active elements. A single transmit focus was placed at 30 mm, and dynamic receive focusing was employed to generate the RF lines. 128 RF lines were simulated along a width of 38 mm. The number of scatterers per smallest sampling volume was set to be 10 to ensure that the speckle of the ultrasound images is fully developed. A generated sonogram is shown in Fig 3.3.

Both sub-sample rigid and non-rigid motions were simulated. Simulations were performed by applying the estimation algorithms to simulated RF frames. For all the data the normalized cross correlation was used as a pattern matching function to find the coarse motion within

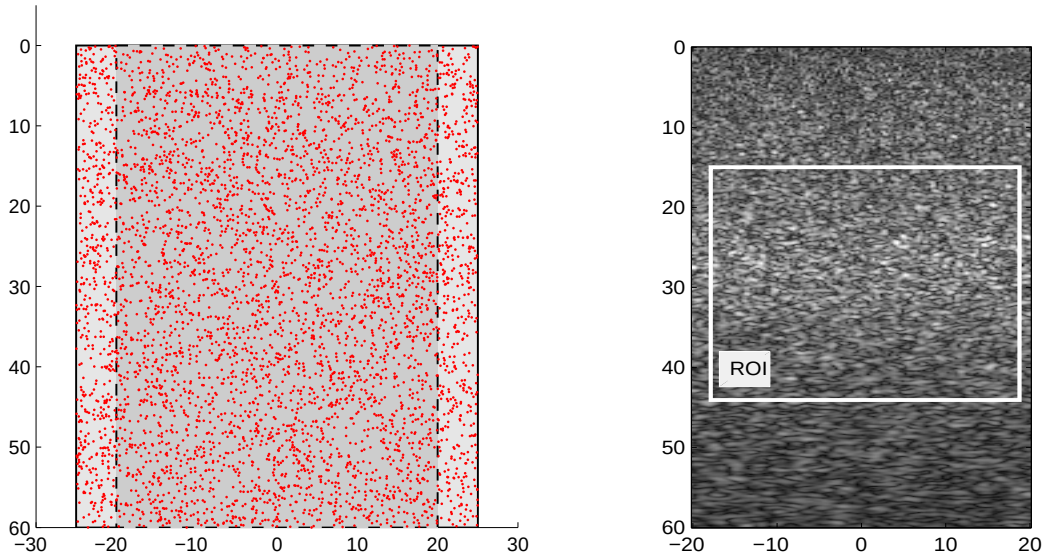

(a) (b)

Figure 3.3: Scatterers distributions (a) (only a small fraction of all scatterers are plotted for better visualization) and a Field II simulated sonogram (b). The region of interest (ROI) that is used for motion tracking validations is also shown on the sonogram. The ROI was centered around the transmit focus and data from both near-field and far-field were removed from the study.

sampling accuracy. The sub-sample motion estimators from Section 3.2 were then applied to find the 2D sub-sample motion.

3.3.2 Rigid Motion

The transducer was displaced on a 2D grid with sub-sample distances (i.e. smaller than the axial and the lateral RF signal sample spacing) in both the axial and the lateral directions to simulate rigid motions on a 2D grid using Field II. This way the motion grid was simulated without using any interpolation. The RF frames corresponding to each of the displaced scatterers configurations were then simulated.

For both the axial and the lateral displacements, a step size of 1/10 of the sample spacing in the corresponding axis was chosen (i.e. $2\,\mu$m axial spacing and $30\,\mu$m laterally), forming a grid of 11x11=121 distinct displacement configurations. These simulated RF frames were then used in conjunction with the RF frame in the center, as a reference frame, to estimate the motion. This resulted in a grid spanning ± 0.5 of a sample in both the axial and lateral directions. Similarly to [38,41,43], these estimated motions were used to study and compare the performances of all the estimators in terms of their bias and standard deviation as a function of sub-sample shift in both the axial and the lateral directions to study their accuracy and precision.

Simulation time of 121 frames, where each frame contains 128 RF lines, is more than 5000 hours on a single core computer using Field II. Four multi-core processor computers were used

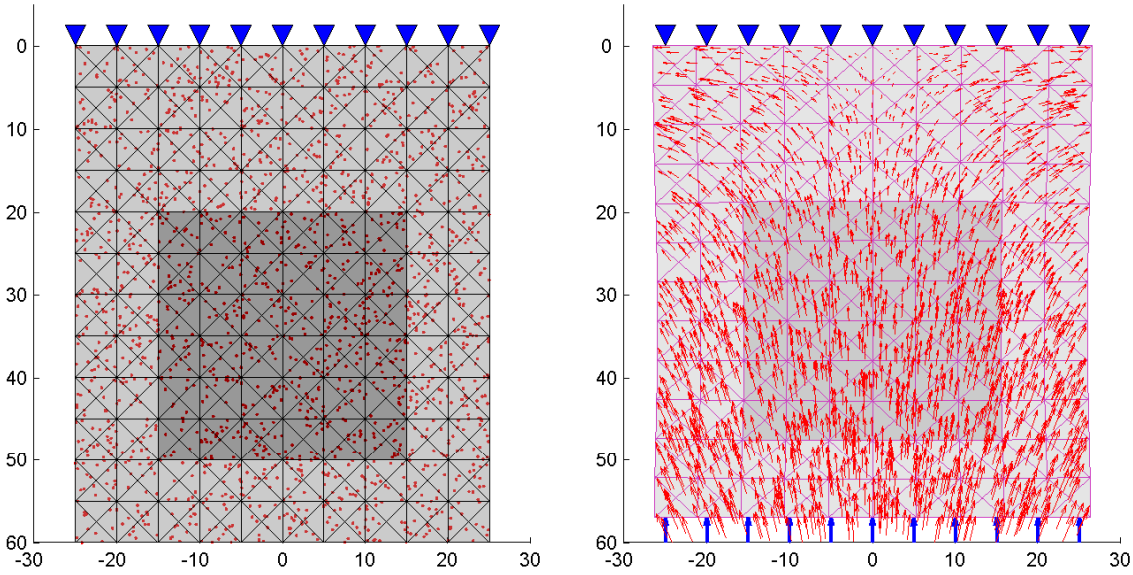

Figure 3.4: (a) FEM mesh, deformation constraints, and scatterer distributions; (b) an example of the displacements of scatterers during a sample compression (only a small fraction of all scatterers are plotted for better visualization).

in parallel to simulate these RF lines.

3.3.3 Deformation

To study and compare the performance of all the estimators in the presence of deformations, the virtual phantom mentioned above was meshed using a Finite Element Method (FEM). The compression is modeled by fixing the top side, touching the probe surface, and moving the bottom side upwards. This is shown Fig. 3.4. The displacements of both top and bottom sides are constrained vertically, but not horizontally. This is done considering that the lubricated tissue surface in reality is free to slide on the probe. Note that throughout this paper the vertical and horizontal axes here are referred to as the axial and lateral directions, respectively, considering the frame of reference of the probe.

A symmetrical mesh is used with four times finer resolution than shown in Fig. 3.4. The mesh contained a square inclusion of 30 mm with its Young's modulus being twice that of the background. The Poisson's ratio is set to 0.49 for all the elements. A detailed description of the FEM used in this study is provided in [62]. A compression of 1% of the depth was applied to the phantom, resulting in a 0.6 mm maximum displacement. The FEM-computed motion field is then applied to the nominal scatterer's positions in order to find their post-deformation positions. The pre- and post-deformation RF echo signals were then generated from the pre- and post-deformation scatterers positions using the same Field II imaging parameters mentioned above.

3.3.4 Simulation Results

Bias and standard deviation of all the methods are shown in Fig 3.5. To estimate the bias and standard deviations from the independent speckle pattern, no window overlap was employed in estimating the rigid motions. This resulted in more than 1000 estimations for each sub-sample motion on a grid. For better visualization of the accuracy, the axial and the lateral bias for each sub-sample shift on the grid are shown with a vector. Error vectors connecting the true displacements to the mean estimated displacements illustrate the directional bias for each of the 121 simulations. In order to show the precision in both directions, an ellipse representation is also used to show the standard deviations for each of the simulations. The ellipses are centered on the mean displacement estimations and the radius of each ellipse in each direction is set to be the standard deviation of motion estimation in that given direction.

Fig 3.5 shows that the independent 1D interpolation methods including the grid slope method perform well only if the displacements have either axial or lateral component (i.e. $\delta_a = 0$ or $\delta_l = 0$). As expected, these methods exhibit large biases (i.e. large vectors) and standard deviations (i.e. stretched ellipses) when the displacements have both axial and lateral components. Both iterative 1D and 2D interpolation methods significantly outperform the commonly used independent 1D methods both in terms of bias and standard deviation (i.e. smaller vectors and ellipses). As we expected, the $f_6(x, y)$ proposed in [55] does not generate symmetric results and its performance depends on the selection of the sixth coefficient. This problem is alleviated when $\overline{f_6(x, y)}$ is employed instead. Fig 3.5 shows that both the iterative 1D and 2D methods (i.e. $\overline{f_6(x, y)}$, $f_9(x, y)$, $f_{16}(x, y)$, and $f_{25}(x, y)$) are able to recover the underlying motion from the RF frames.

In order to study the results quantitatively, the biases and standard deviations for all estimators are shown in Fig 3.6, using an approach similar to the one presented in [38]. The first two columns depict the axial bias and standard deviation while the second two columns depict the lateral bias and standard deviation of displacement estimates. To simplify the comparison, the bias and standard deviation errors are displayed using the same color bar scale for the axial and lateral performances, for all the methods. It should be noted that bias is signed and is smaller when it is closer to the center of the color bar (i.e. gray) while standard deviation is positive and is smaller when it is closer to the bottom of the color bar (i.e. black). Fig 3.6 shows that the maximum axial biases and standard deviations of the independent 1D interpolation methods are larger than 0.05 of a sample (i.e. 1 μm). The same figure shows that the maximum lateral biases and standard deviations of the common independent 1D interpolation methods are larger than 0.1 of a sample (i.e. 30 μm). These results are consistent with the results reported in [38]. Fig 3.6 also shows that the maximum lateral bias and standard deviation of iterative 1D and 2D interpolation methods are at least one order of magnitude smaller than those of the common independent 1D interpolation methods.

For better visualization of the performance of the iterative 1D and 2D interpolation methods, the axial and lateral biases and standard deviations of all these methods are shown in Fig 3.7 using separate color bars. The performance of all the techniques in terms of their maximum absolute bias and standard deviations in both directions is summarized in Table 3.1. For easier comparison the same results are also depicted in Fig. 3.8. The results show that 2D interpolation using high order polynomials (cubic and quartic spline) performs better than iterative 1D interpolation followed by 2D interpolation using low order polynomials and independent 1D interpolation techniques. The results also show that 2D cubic spline fit performs

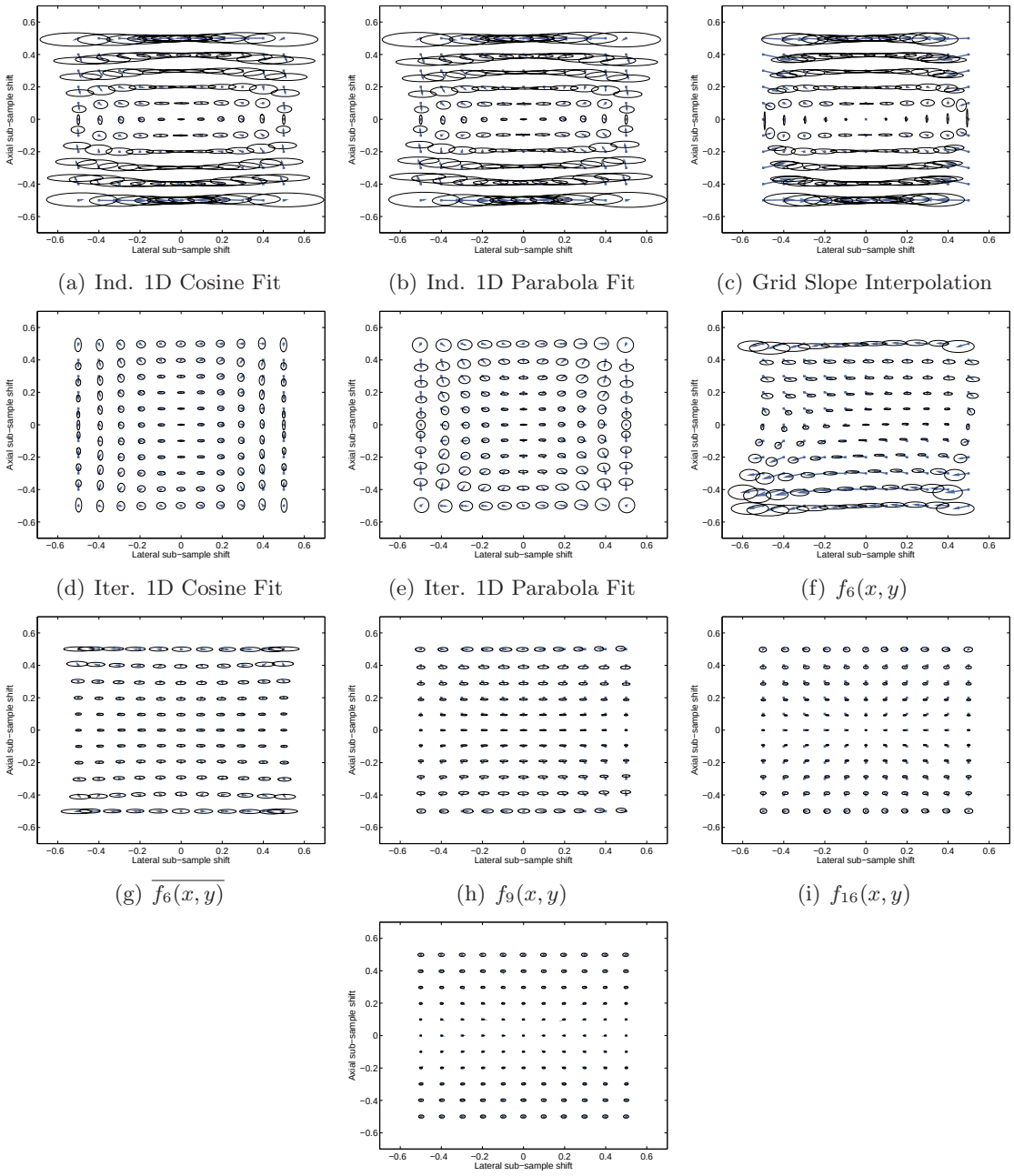

(a) Ind. 1D Cosine Fit (b) Ind. 1D Parabola Fit (c) Grid Slope Interpolation

(d) Iter. 1D Cosine Fit (e) Iter. 1D Parabola Fit (f) $f_6(x, y)$

(g) $\overline{f_6(x, y)}$ (h) $f_9(x, y)$ (i) $f_{16}(x, y)$

(j) $f_{25}(x, y)$

Figure 3.5: Biases and standard deviations of different pattern matching interpolation techniques as a function of sub-sample shift on a 11×11 grid. Field II was used to simulate the echo signals. A total of 1000 windows in the pattern matching function were used to generate each bias vector and standard deviation ellipse (window size is $\approx 2 \times 2\, mm^2$, which is equivalent to 104 samples axially and 7 samples laterally).

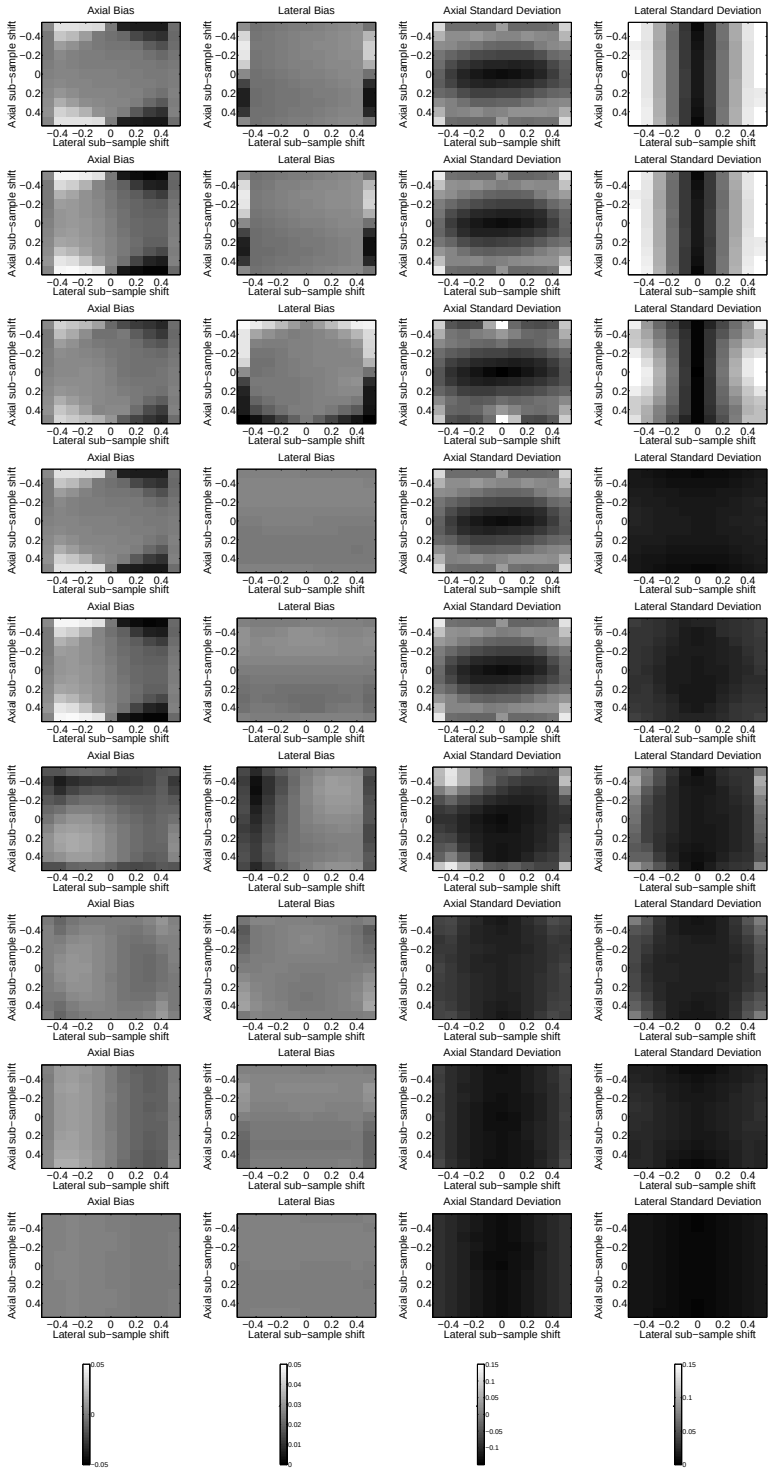

(a) Axial Bias (b) Axial STD (c) Lateral Bias (d) Lateral STD

Figure 3.6: Grey level representations of the biases and standard deviations of Independent 1D cosine (1^{st} row), Independent 1D parabola (2^{nd} row), Grid slope (3^{rd} row), iterative 1D cosine (4^{th} row), iterative 1D parabola (5^{th} row), $f_6(x, y)$ (6^{th} row), $\overline{f_6(x, y)}$ (7^{st} row), $f_9(x, y)$ (8^{th} row), and $f_{25}(x, y)$ (9^{th} row) as a function of sub-sample shift on a 11×11 grid.

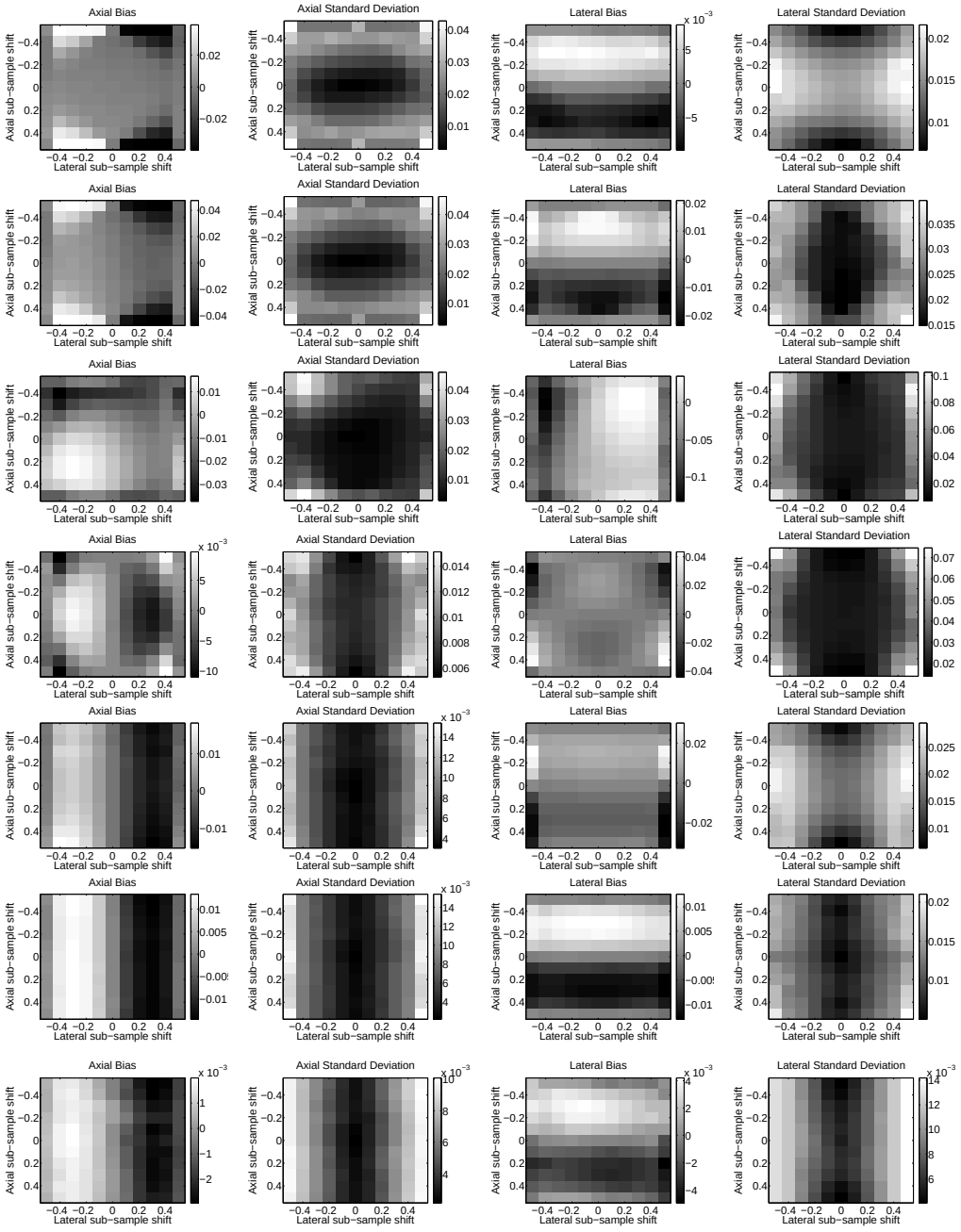

(a) Axial Bias (b) Axial STD (c) Lateral Bias (d) Lateral STD

Figure 3.7: Grey level representations of the biases and standard deviations of iterative 1D cosine fit (1^{st} row), iterative 1D parabola fit (2^{nd} row), $f_6(x, y)$ fit (3^{rd} row), $\overline{f_6(x, y)}$ fit (4^{st} row), $f_9(x, y)$ fit (5^{th} row), $f_{16}(x, y)$ fit (6^{th} row), and $f_{25}(x, y)$ fit (7^{th} row), as a function of sub-sample shift on a 11×11 grid.

Table 3.1: Maximum values of biases and standard deviations obtained from the 2D noise-free simulations for window of $2 \times 2\,mm^2$.

Method	Max Error (samples)				Max Error (microns)			
	Axial		Lateral		Axial		Lateral	
	$\lvert b_{ax} \rvert$	σ_{ax}	$\lvert b_{lat} \rvert$	σ_{lat}	$\lvert b_{ax} \rvert$	σ_{ax}	$\lvert b_{lat} \rvert$	σ_{lat}
Ind. 1D Cos	0.0389	0.0428	0.1234	0.1844	0.7483	0.8239	38.5543	57.6356
Ind. 1D Par	0.0475	0.0461	0.1251	0.1855	0.9145	0.8871	39.0811	57.9665
Grid Slope	0.0335	0.0556	0.1421	0.1686	0.6443	1.0704	44.3963	52.6929
Iter. 1D Cos	0.0389	0.0428	0.0086	0.0217	0.7483	0.8239	2.6956	6.7682
Iter. 1D Par	0.0475	0.0461	0.0209	0.0396	0.9145	0.8871	6.5191	12.3699
$f_6(x,y)$	0.0375	0.0460	0.1322	0.1024	0.7228	0.8846	41.3209	32.0002
$\overline{f_6(x,y)}$	0.0097	0.0151	0.0435	0.0747	0.1860	0.2914	13.5821	23.3300
$f_9(x,y)$	0.0182	0.0154	0.0301	0.0295	0.3513	0.2965	9.4055	9.2043
$f_{16}(x,y)$	0.0133	0.0154	0.0126	0.0210	0.2564	0.2961	3.9309	6.5654
$f_{25}(x,y)$	0.0020	0.0101	0.0042	0.0142	0.0383	0.1939	1.3125	4.4314

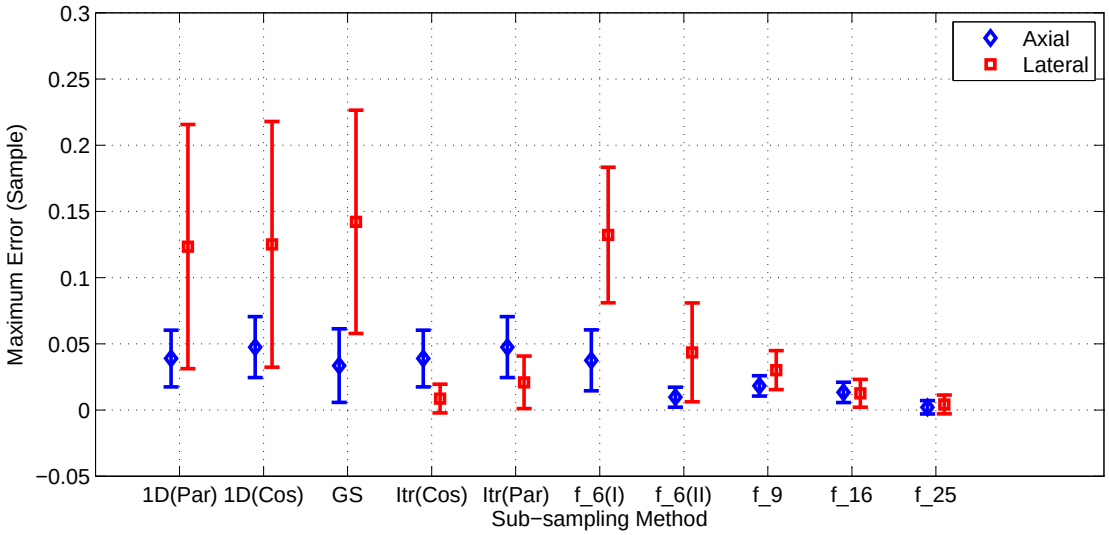

Figure 3.8: Maximum values of biases and standard deviations in both the axial and the lateral directions obtained from the 2D noise-free simulations for window of $2 \times 2\,mm^2$.

better than iterative 1D cosine fit followed by the iterative 1D parabola fit in agreement with previously reported work for 1D sub-sample estimation [16, 41, 43].

The maximum axial and lateral biases of the $f_{25}(x,y)$ fit are found to be 0.0020 and 0.0042 of a sample, which corresponds to 38 nm and 1.31 μm at the simulated $\approx 20\,\mu$m sample spacing and 300 μm line spacing. The maximum standard deviation of $f_{25}(x,y)$ fit are found to be 0.0101 and 0.0142 of a sample, which corresponds to 193 nm and 4.43 μm. For the same set of simulated data, the maximum axial and lateral biases and standard deviations of the independent 1D methods were found to be an order of magnitude larger.

The performance of different estimators in the presence of deformation are shown in Figs. 3.9 and 3.10. To estimate the motion in the presence of deformation, 50% window overlap was employed as commonly used in elastography applications [63]. It should be noted that in the 1% compression presented here, the displacement in the axial direction reaches the maximum

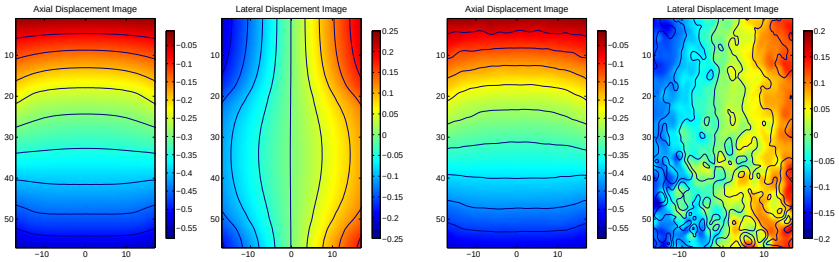

(a) FEM

(b) Ind. 1D Cosine

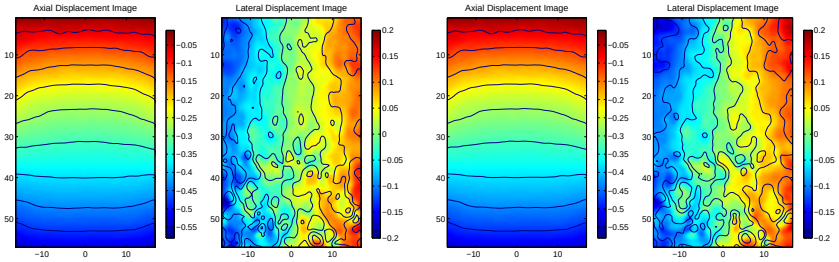

(c) Ind. 1D Parabola

(d) Grid Slope

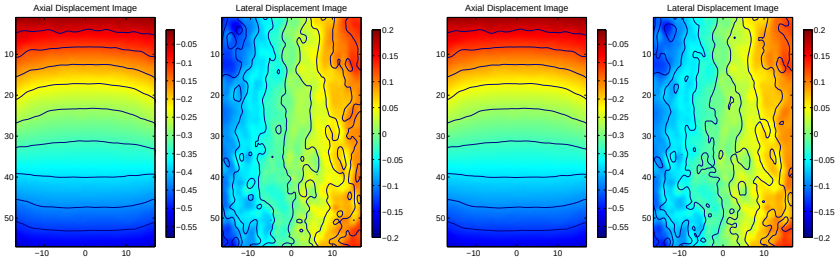

(e) Iterative 1D Cosine

(f) Iterative 1D Parabola

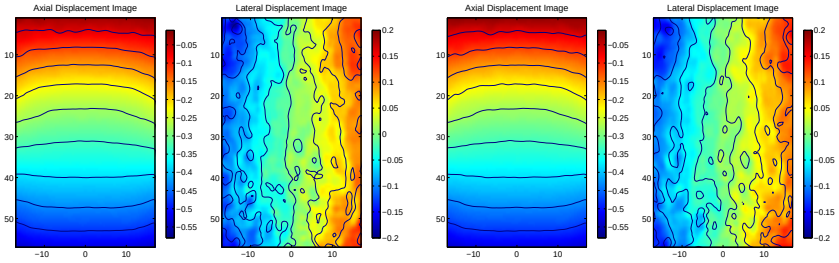

(g) $f_6(x, y)$

(h) $\overline{f_6(x, y)}$

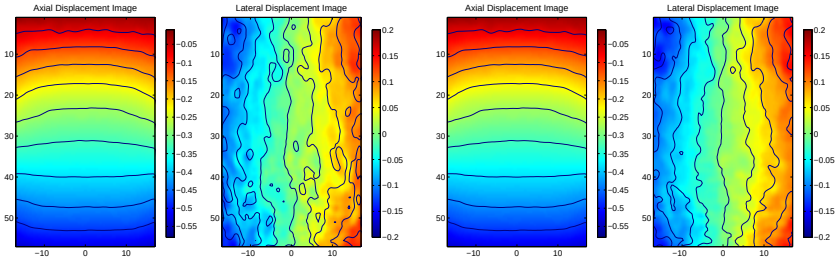

(i) $f_9(x, y)$

(j) $f_{25}(x, y)$

Figure 3.9: Axial (left) and lateral displacement (right) images computed by the FEM (a) and estimated by different techniques (b-j).

Table 3.2: The overall performance of 2D motion estimation techniques estimated from compression test for window of $2 \times 2\,mm^2$.

Method	Absolute Error (microns)				Absolute Error (%)			
	Axial		Lateral		Axial		Lateral	
	Mean	STD	Mean	STD	Mean	STD	Mean	STD
Ind. 1D Cos	0.4008	0.4958	11.6922	15.1145	1.4883	0.1510	25.4610	32.9133
Ind. 1D Par	0.4029	0.4964	11.6794	15.1491	1.4886	0.1512	25.4332	32.9888
Grid Slope	0.3976	0.4923	9.3275	12.4825	1.4892	0.1499	20.3115	27.1820
Iter. 1D Cos	0.4008	0.4958	6.0302	7.6899	1.4883	0.1510	13.1313	16.7455
Iter. 1D Par	0.4029	0.4964	6.2540	8.0595	1.4886	0.1512	13.6187	17.5503
$f_6(x,y)$	0.4203	0.5020	7.3661	8.4090	1.4571	0.1529	16.0403	18.3114
$\overline{f_6(x,y)}$	0.4287	0.5213	6.0537	7.5425	1.4803	0.1588	13.1826	16.4245
$f_9(x,y)$	0.3654	0.4368	6.1065	7.6603	1.4785	0.1330	13.2976	16.6810
$f_{16}(x,y)$	0.3644	0.4369	5.3262	6.7801	1.4763	0.1331	10.3311	13.4458
$f_{25}(x,y)$	0.3637	0.4375	2.8548	3.4952	1.4712	0.1331	6.2166	7.6112

of 32 samples. As a result, the accuracy and precision of sub-sample estimation in the axial direction becomes less significant. However, for the same data set, the maximum lateral displacement is smaller than the line spacing. Thus, the accuracy and precision of sub-sample estimation in the lateral direction is critical. To study and compare the performance of different estimators in the presence of deformation quantitatively, the estimated displacement at each window were compared with the displacements calculated using FEM at the same window location. The estimation errors are summarized in Table 3.2. Figs. 3.9 and 3.10 show that iterative 1D interpolation and 2D interpolation methods perform well in estimating the lateral motion, while independent 1D methods produce larger errors. This is clear in both estimated lateral motions and displacement vectors. Figs. 3.9 and 3.10 also show the performance of 2D interpolation methods improves as we increase the order of the 2D polynomials. These results are in agreement with the results reported for estimations of rigid motions.

So far we only considered estimation of the motion in the sequences of the RF signals. Fig 3.11 shows the performance of different estimators on the 2D envelope signal rather than on the raw 2D RF signal. Since there is no carrier frequency in the envelope signals, independent 1D parabola fit, $f_9(x,y)$ fit, and $f_{25}(x,y)$ are used for this study. As expected, the accuracy and precision of tracking in axial direction becomes poor when the envelope signals are used. This figure shows that the performance of the independent 1D estimators is improved in estimating the lateral motion. This is consistent with the results published in [33], where it was suggested that RF signals be used to estimate the axial motion and envelope signals to estimate the lateral motion. The results also show that 2D interpolation methods can also be employed to envelope data to increase both the accuracy and precision of the motion estimation in 2D.

Fig. 3.5 visualizes the biases and standard deviations as a fraction of a sample assuming equal sample spacing in both directions. As mentioned before, the sample spacing in the lateral direction is much larger than the sample spacing in the axial direction (approximately fifteen times in this work). In order to show the true length of the bias vectors and real shape of the standard deviation ellipses, Fig 3.12 compares the performance of the independent 1D cosine fit, the iterative 1D cosine fit, and $f_{25}(x,y)$ fit (Fig. 3.5(a),(d), and (j)) in units of distance, as opposed to fraction of a sample. Fig 3.12 depicts how errors of a fraction of a sample translate to large actual errors especially in the lateral direction. This figure shows the importance of accuracy and precision of sub-sample estimation especially in the lateral direction.

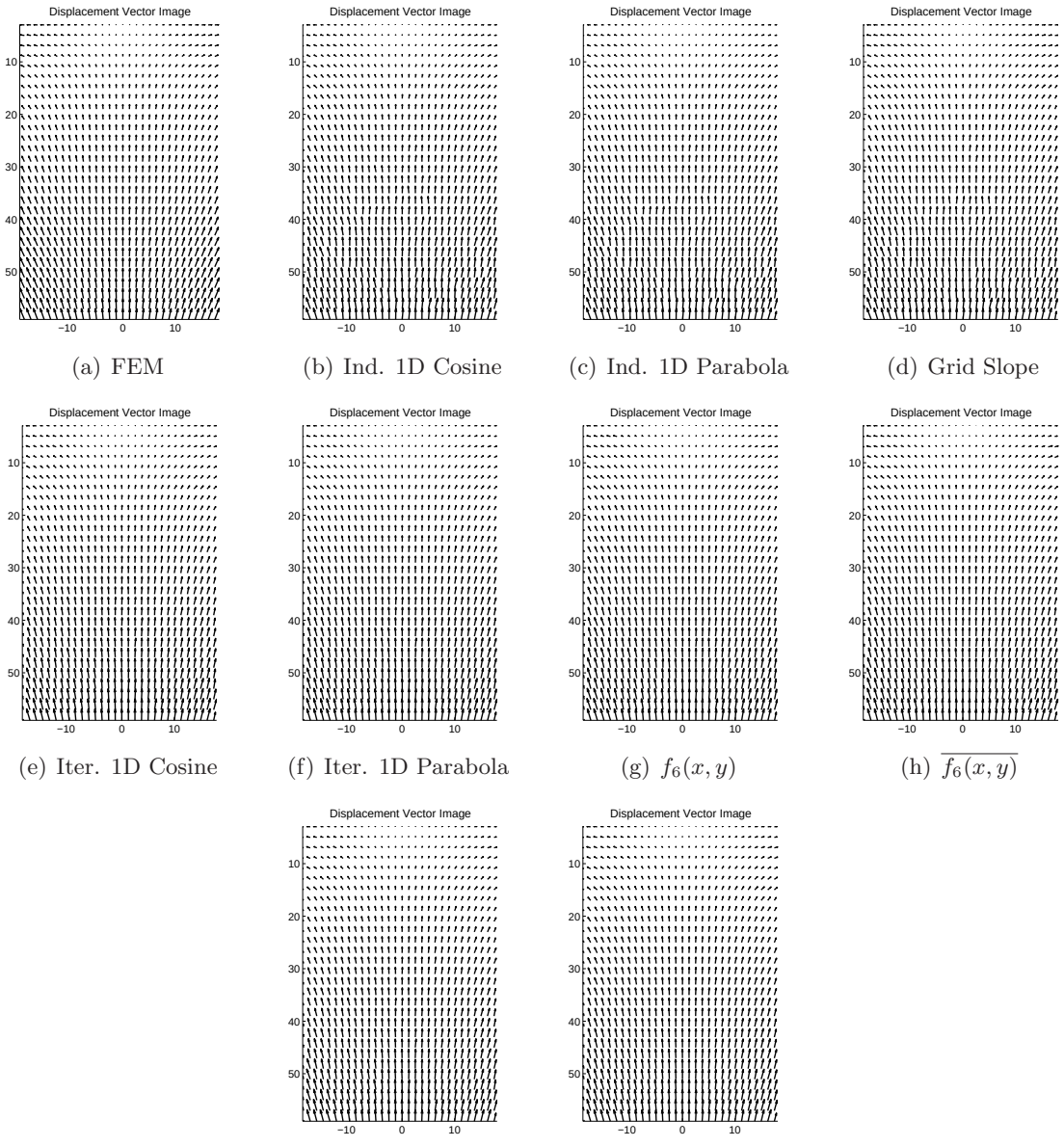

(a) FEM (b) Ind. 1D Cosine (c) Ind. 1D Parabola (d) Grid Slope

(e) Iter. 1D Cosine (f) Iter. 1D Parabola (g) $f_6(x, y)$ (h) $\overline{f_6(x, y)}$

(i) $f_9(x, y)$ (j) $f_{25}(x, y)$ Fit

Figure 3.10: Displacement vector images computed by the FEM (a) and estimated by different techniques (b-j).

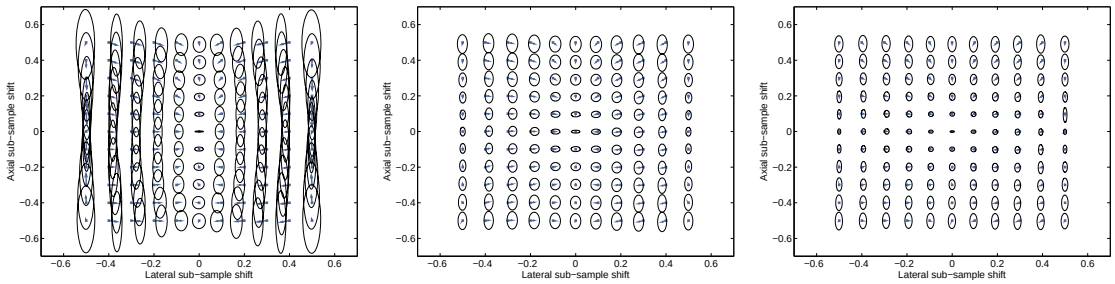

(a) Ind. 1D Par Fit (b) $f_9(x, y)$ Fit (c) $f_{25}(x, y)$ Fit

Figure 3.11: Biases and standard deviations of different pattern matching interpolation techniques as a function of sub-sample shift on envelope signals. Field II was used to simulate the echo signals. A total of 1000 windows in the pattern matching function were used to generate each bias vector and standard deviation ellipse (window size is $\approx 2 \times 2\,mm^2$).

3.4 Experiments

3.4.1 Experimental Setup

In order to further study the performance of all the methods using ultrasound data, the following experiment was conducted. A tissue-mimicking phantom was constructed from 100% polyvinyl chloride (PVC) plasticizer (M-F Manufacturing Co., Inc. Fort Worth, TX, USA). Two percent Cellulose (Sigma-Aldrich Inc., St. Louis, MO, USA) was added as scattering particles [43, 64]. The phantom was imaged using a SonixRP ultrasound machine (Ultrasonix Medical Corporation, Richmond, BC, Canada) with a L9-4/38 linear array transducer with 5 MHz center frequency and 300 μm line spacing. The RF signal, digitized at 40 MHz, was collected to a depth of 50 mm.

The experimental setup is shown in Fig 3.13. To generate motion without applying any deformation, the phantom was firmly secured within a large cubic container where one face was replaced by an ultrasound transparent plastic wrap. The phantom was oriented parallel to and 5 mm away from the plastic wrap. The container was then filled with degassed water and was mounted on a piezoelectric motor stage system. The stage system consists of an HR1-1800E and an HR2-1800E motor stage (ALIO Industries, Wheat Ridge, CO, USA) with reported resolution of 50 nm, providing 2D motion. A PMAC2A-PC/104 motor controller (Delta Tau Data Systems Inc., Chatsworth, CA, USA) was used to control each motor through AB1A-3U amplifiers. The motor positions were measured through RGB25H00R08 encoder interfaces (Renishaw Plc., Hillesley, Gloucestershire, UK). Due to a limitation in the number of points that could be programmed for a 2D motion grid, a larger step size was used in the experimental setup compared to the simulation setup. For both the axial and the lateral displacements, a step size was set to be 1/8 of the sample spacing in the corresponding axis (i.e. 2.5 μm axially and 37.5 μm laterally), forming a grid of $9 \times 9 = 81$ distinct displacement configurations. The RF frames were captured at each step. These RF frames in conjunction with the reference frame in the center, were ran through the same estimators that were used for the simulated data. This resulted in a grid spanning ± 0.5 of a sample in both directions.

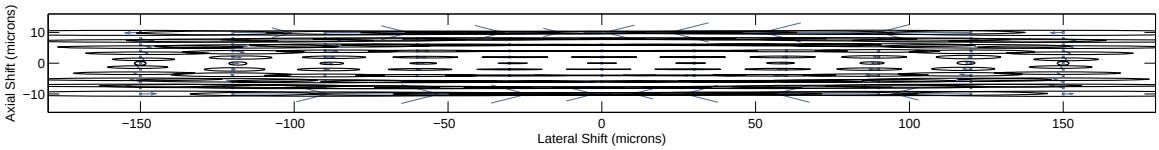

(a) Independent 1D Cosine Fit

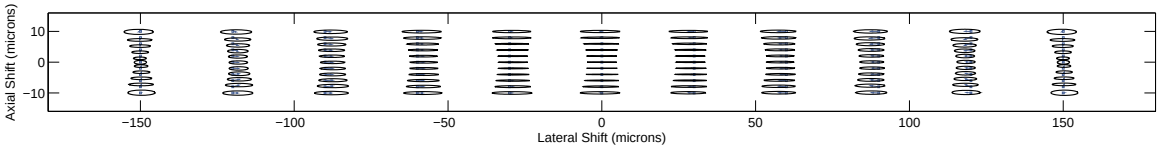

(b) Iterative 1D Cosine Fit

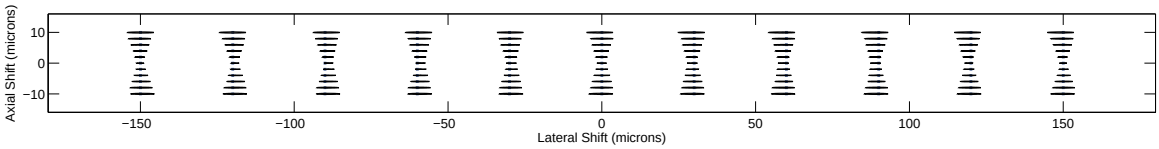

(c) $f_{25}(x, y)$ Fit

Figure 3.12: Displacement estimates of the independent 1D cosine fit (a) and the iterative 1D cosine fit (b) at actual scale. 2D biases are visualized with error vectors from the true motion to the mean displacement at each location on a simulated 11×11 2D grid. Radii of the ellipses which are centered at the location of the mean displacement correspond to the standard deviation of the measurements at the same location. Data was acquired at a 40 MHz temporal sampling rate and a $300\,\mu m$ line spacing (window size is $\approx 2 \times 2\,mm^2$).

3.4.2 Experimental Results

Experimental results are shown in Fig. 3.14. The experimental results are in good agreement with the simulation results. Due to the experimental errors and the electromechanical noise in the system, larger biases and standard deviations were observed in the experimental data. Similarly to the simulation results generated by Field II, results from experiments show that the independent 1D methods exhibit large biases and standard deviations when the displacements have both the axial and the lateral components. Both iterative 1D and 2D interpolation methods significantly outperform commonly used independent 1D methods in terms of bias and standard deviation and are able to recover the underlying motion from the RF frames. 2D interpolations with high order polynomials outperform all the other techniques.

The overall performance of all the techniques in terms of their maximum biases and standard deviations for experimental data is presented in Table 3.3. The maximum axial and lateral biases of the $f_{25}(x, y)$ fit are found to be 551 nm and $5.92\,\mu$m, respectively. The maximum axial and lateral standard deviations of the $f_{25}(x, y)$ fit are found to be $2.04\,\mu$m and $5.90\,\mu$m, respectively. For the same set of data the maximum axial and lateral biases and standard deviations of the independent 1D methods are found to be at least five times larger.

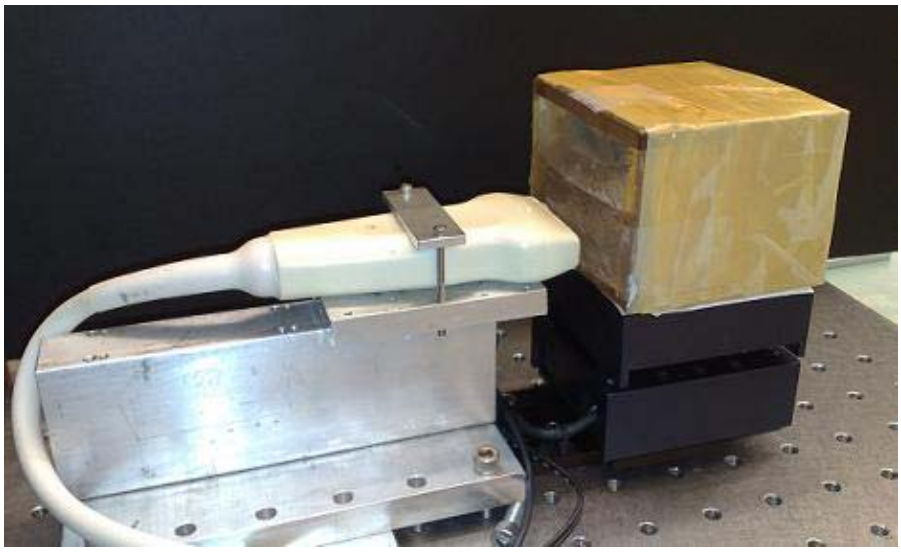

(a) Experimental Setup

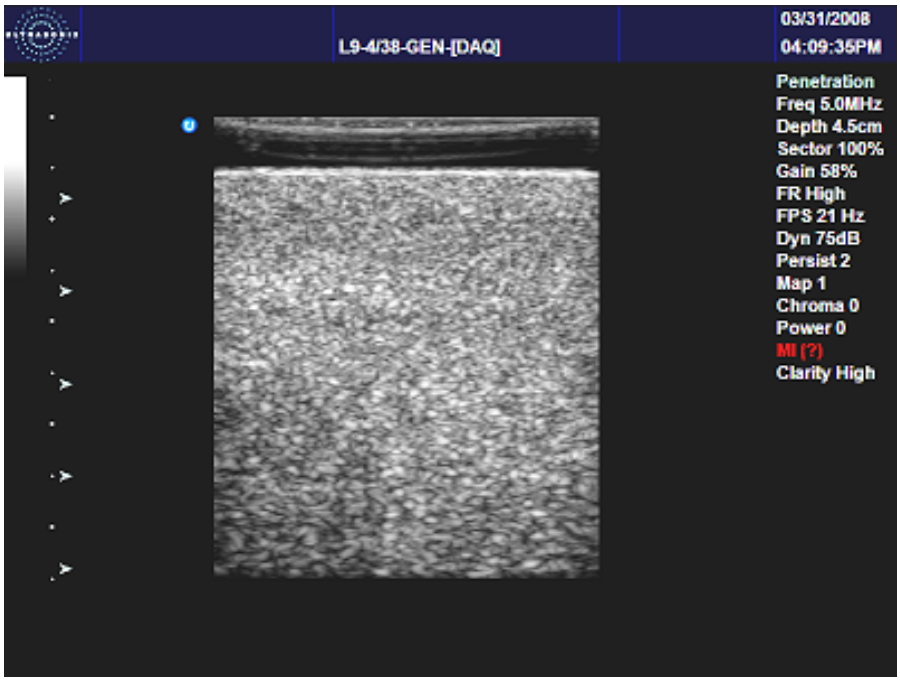

(b) Sonogram

Figure 3.13: Experimental set up (a) shows the positioning of the transducer with respect to the phantom and plastic wrap. A sample sonogram acquired from SonixRP ultrasound machine (b) is also shown. The dark layer on top of the sonogram is the water gap between the probe and the phantom and the markers on the left represent the focal points.

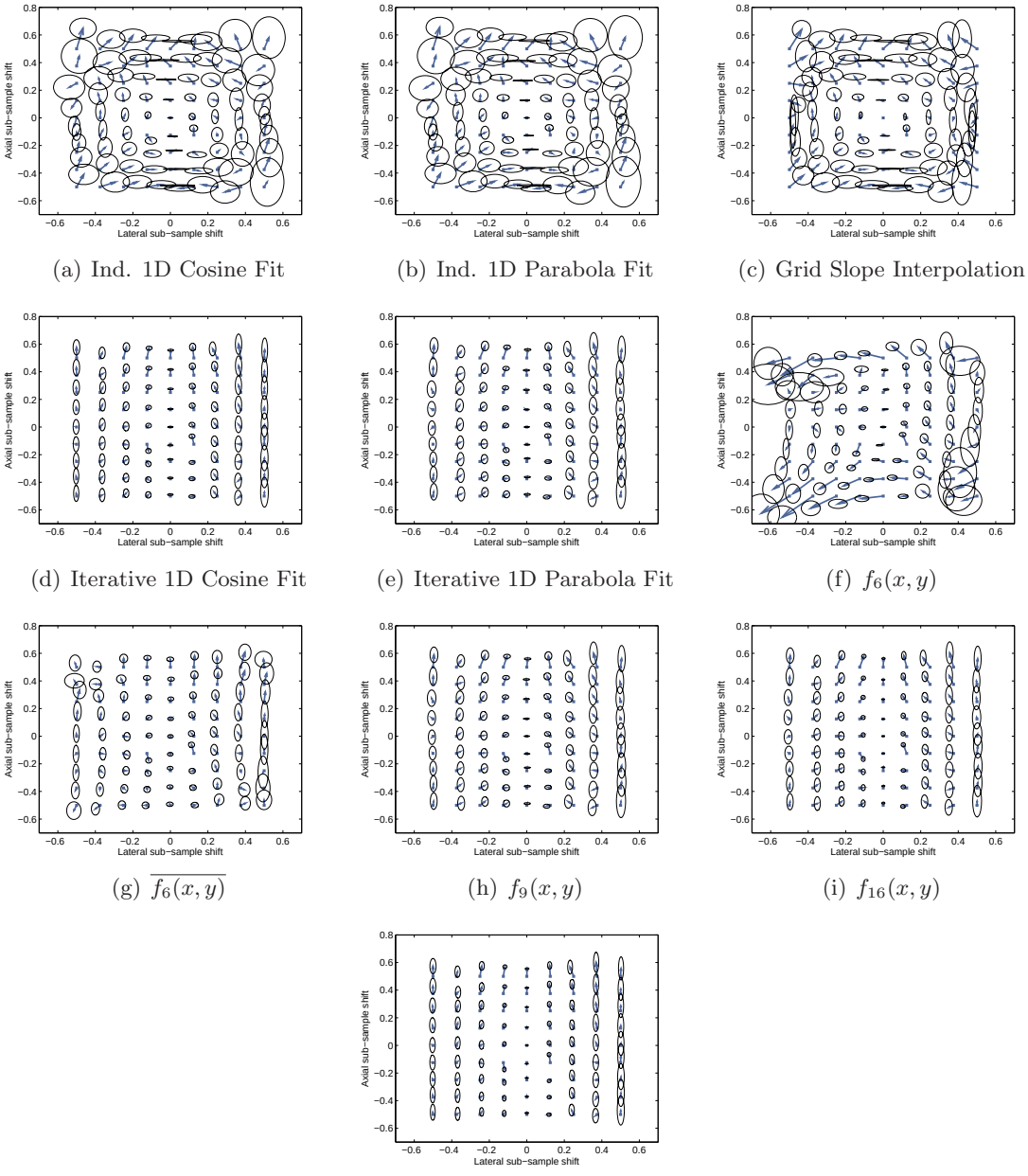

(a) Ind. 1D Cosine Fit (b) Ind. 1D Parabola Fit (c) Grid Slope Interpolation

(d) Iterative 1D Cosine Fit (e) Iterative 1D Parabola Fit (f) $f_6(x, y)$

(g) $\overline{f_6(x, y)}$ (h) $f_9(x, y)$ (i) $f_{16}(x, y)$

(j) $f_{25}(x, y)$

Figure 3.14: Biases and standard deviations of different pattern matching interpolation techniques on a 9x9 grid. Echo signals were captured using an ultrasound machine. A total of 1000 windows in the pattern matching function were used to generate each error ellipse (window size $\approx 2\,mm \times 2\,mm$ equivalent to 104 samples axially and 7 samples laterally).

Table 3.3: Maximum values of bias and standard deviation obtained from the 2D experimental data for window of $2 \times 2\,mm^2$.

Method	Max Error (samples)				Max Error (microns)			
	Axial		Lateral		Axial		Lateral	
	$\lvert b_{ax} \rvert$	σ_{ax}	$\lvert b_{lat} \rvert$	σ_{lat}	$\lvert b_{ax} \rvert$	σ_{ax}	$\lvert b_{lat} \rvert$	σ_{lat}
Ind. 1D Cos	0.1490	0.1764	0.0831	0.0960	0.7373	3.3959	25.9563	29.9898
Ind. 1D Par	0.1561	0.1827	0.0899	0.0991	0.7421	3.5173	28.0848	30.9681
Grid Slope	0.1396	0.1626	0.0881	0.1045	0.7176	3.1293	27.5185	32.6549
Iter. 1D Cos	0.1490	0.1764	0.0313	0.0409	0.7373	3.3959	9.7814	12.7773
Iter. 1D Par	0.1561	0.1827	0.0399	0.0440	0.7421	3.5173	12.4588	13.7417
$f_6(x, y)$	0.1540	0.1817	0.1642	0.1434	0.7845	3.4984	51.3202	44.8161
$\overline{f_6(x, y)}$	0.1079	0.1189	0.0252	0.0523	0.5803	2.2893	7.8800	16.3330
$f_9(x, y)$	0.1013	0.1190	0.0346	0.0244	0.5584	2.2906	10.8107	7.6387
$f_{16}(x, y)$	0.1013	0.1145	0.0317	0.0236	0.5526	2.2036	10.0311	7.3321
$f_{25}(x, y)$	0.1013	0.1062	0.0189	0.0189	0.5515	2.0437	5.9210	5.9079

3.5 Real-Time Implementation

Real-time estimation of the motion for elastography has been reported by several groups [22, 65–67] and has been implemented on different commercial machines. Since ultrasound imaging provides higher resolution in the axial direction, in all these methods, only the estimation of the axial component of the motion has been considered. Tracking in lateral (or even elevational) direction has been used mainly to correct for the axial component of the motion [30, 68].

Due to the small computational cost of pattern matching interpolation methods, they can be used to estimate sub-sample motions in real-time. By implementing these 2D interpolation techniques, we extend our previously introduced 1D motion tracking algorithm [56] to 2D, and report an implementation of a motion tracking software that estimates both axial and lateral motions with sub-sample accuracy in real-time.

As mentioned in Section 3.2, 2D motion estimation with pattern matching algorithms consists of the following two steps: (i) locating the maximum of the discrete pattern matching function in 2D, and (ii) estimating the peak offset in 2D using interpolation techniques. The key to achieve real-time performance is to reduce the computational cost of first step (i.e. locating the maximum of the discrete pattern matching function), since the sub-sample estimation is computationally inexpensive.

Most motion estimation algorithms ignore the strong spatial correlations of the motion field. The size of the search region for locating the maximum of the pattern matching function stays the same throughout the tracking. Thus the estimation becomes computationally expensive and not suitable for real-time applications. We have previously introduced TDPE as a predictive and corrective motion estimation algorithm [56] that uses prior estimates to reduce the size of the search region. This is accomplished by centering the search region on the previously estimated motion of neighboring windows. To avoid losing track of motion, TDPE also checks the correlation coefficient to validate the estimation results. A recovery search is triggered when the correlation coefficient is small.

The previous implementation of the TDPE uses 1D windows and applies 1D normalized cross correlation to find the coarse location of the motion (i.e. 1D window, 1D search). 1D interpolation is then used to estimate the sub-sample component of the motion in the axial direction. In this work, employing 2D windows, the previous implementation is extended to 2D by locating the maximum of the discrete pattern matching function in two dimensions (i.e.

2D window, 2D search). Both iterative 1D and 2D interpolation methods are implemented to estimate the sub-sample components of the motion in both the axial and the lateral directions. The $f_{16}(x, y)$ and $f_{25}(x, y)$ are excluded since, in addition to the computational overhead for polynomial fitting and root estimation process, they require the pattern matching function to be evaluated at least for twenty five lags for each window.

The 2D motion tracking algorithm was implemented as a client-software on the Sonix RP PC-based US machine. The software connects to the US machine to capture RF frames in real-time. The displacements are then estimated by comparing the sequences of these RF frames. The estimation of 2D motion runs at a refresh rate of more than 25 frames per second for 2D displacement images with 6,000 estimation overlapping windows of each $2 \times 2\,mm^2$. Typical images displayed by the software interface are shown in Fig. 3.15.

3.6 Discussions

In the simulations, the line spacing was intentionally set to be $300\,\mu$m in order to be consistent with our experimental setup. However, this spacing is larger than would be expected for most ultrasound imaging systems. The bias and the standard deviation of all the estimators are expected to improve with improved lateral resolution. Moreover, to save simulation time and to be consistent with our experimental setup, single transmit focus was used to generate the RF signals. However, the accuracy and the precision of all the estimators are also expected to improve by increasing the number of transmit focal points.

Although not shown here, the performance of different estimators was also studied when different window sizes were employed in the pattern matching function. As expected, the accuracy and precision of all the methods improve, in estimating the rigid motion, when the size of the window is increased.

Although we have only considered 2D sub-sample estimation, the generalization of the same methods to higher dimensions is possible. For example, in three dimensions, a 3D polynomial can be fitted to the discrete matching coefficients in the axial, lateral, and the elevational directions (i.e. $f(x, y, z)$). Joint sub-sample motion estimation can then be achieved in all directions by finding the maximum of the fitted polynomial ($\nabla f = 0$).

The reader should note that the iterative 1D interpolation method studied in this work is fundamentally different from the iterative 1D cross correlation and recorrelation technique suggested in [11,37]. In this work, the discrete 2D pattern matching function is evaluated once, and iterations are used just to find the exact location of the match in that same function. However, in [11, 37], a new pattern matching function is evaluated at each iteration. The above mentioned methods use the same common independent 1D interpolation method (i.e. 1D cosine fitting) to estimate the sub-sample motion. The iterative 1D and 2D interpolations methods presented in this paper can also be used in [11, 37] to improve the performance of sub-sample estimation.

The assumption of small motions and deformation which is considered and studied in this work is valid for fast imaging for dynamic [7] and real-time elastography as presented in this work, where inter-frame displacements and deformations are small and the echo signals are highly correlated. This is also the case in acoustic radiation force imaging [7, 13–15] where induced displacements and deformations are very small. Thus, the 2D interpolation methods can be readily used in these applications. However, the assumption of small motions and

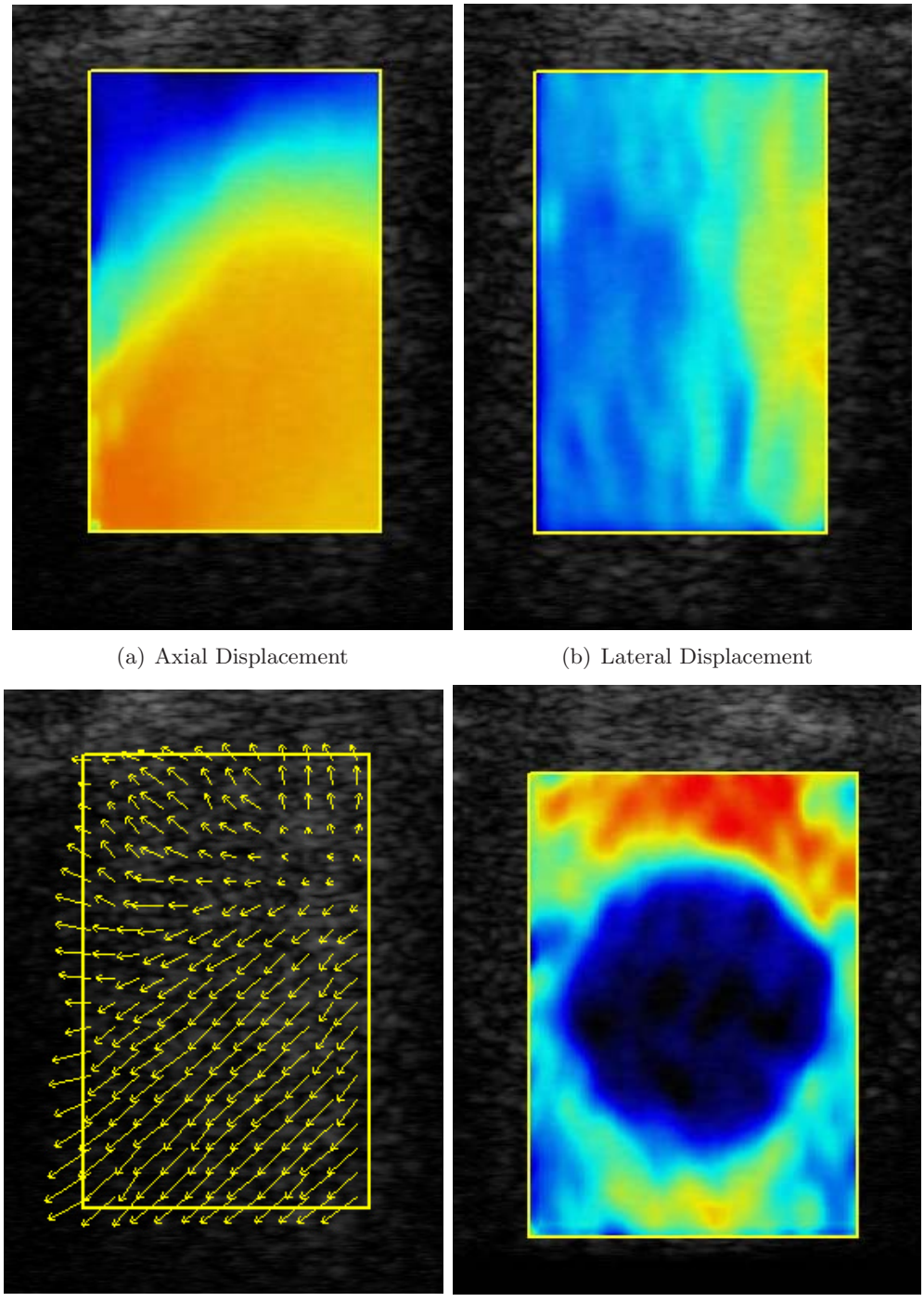

(a) Axial Displacement (b) Lateral Displacement

(c) Displacement Vector (d) Axial Strain

Figure 3.15: Screen shots of the real-time 2D motion tracking software. Color coded estimated axial displacement (a), lateral displacement (b), displacement vector (c), and axial strain image (d) estimated inside a region of interest are shown. The images are imposed over the sonogram in the background.

deformations does not hold when large deformations exist and echo signals are decorrelated. This is generally the case in quasi-static elastography [63,69] where large external compressions are applied to the tissue and cause the tissue to experience large deformations. This is also the case in myocardial elastography [11] where the tissue experiences large internal motions and deformations. The performance of all the pattern matching function interpolation techniques, including those presented in this work, rely on the matching coefficients estimated by the pattern matching algorithms and is expected to degrade when the echo signals are decorrelated and can not be matched correctly. In order to adapt all these methods to the estimation of displacements resulting from large deformations, previously introduced compounding methods should be applied to the raw echo signals [68, 70, 71] prior to the motion estimation process. Once the effect of signal decorrelation is suppressed, the pattern matching algorithms followed by the 2D interpolation methods can be applied to estimate the 2D motion with sub-sample accuracy. Alternatively, techniques such as iterative 1D cross correlation with recorrelation [11, 37], which are more robust in the presence of deccorelation, can be employed to estimate the motion.

3.7 Conclusion and Future Work

The results in this paper show that the common method of applying a separate 1D sub-sample estimation to the quantized 2D pattern matching function in each direction independently is not valid when estimating motion in sequences of ultrasound RF echo signals. Results from both simulations and experiments show that both iterative 1D and 2D interpolation methods outperform independent methods in terms of bias and standard deviation. The framework presented here is well suited to study the performance of other 2D motion estimators in the future.

Both iterative 1D and 2D sub-sample motion estimation methods are shown to provide a good balance between accuracy, precision, and computational cost. Although they add computational overhead, compared to independent 1D methods, they still perform at real-time rates as presented. The presented real-time motion tracking implementation has several potential applications throughout the field of signal processing. Specific applications in medical ultrasound include fine 2D tissue motion tracking, velocity vector imaging, shear strain imaging, strain tensor imaging, poro-elastography, and tissue viscoelastography.

In this work we only studied the pattern matching interpolation techniques to estimate the sub-sample motion in 2D. However, as we mentioned before, with a trade off of higher computational cost, accurate tracking of the motion in 2D has been reported in literature by up-sampling the echo signal in the lateral direction with large up-sampling factor and employing iterative 1D estimation and recorrelation [11, 37, 51], using continuous pattern matching functions [38], and the phase of RF signal in the axial [23, 25, 26] and the lateral direction using synthetic lateral phase [27]. Further investigation is required to compare the performance of these estimators with pattern matching function interpolation methods. Furthermore, in this work we only used cross correlation as a pattern matching technique. The performance of the interpolation methods on other pattern matching techniques such as sum of squared differences and sum of absolute differences needs to be studied. Moreover, the effects of line spacing, focusing, transmit frequency, and sampling frequency in the echo signals also needs further study. These will be the topics of our future work.

References

[1] C. Kasai, K. Namekawa, A. Koyano, and R. Omoto, "Real-time two-dimensional blood flow imaging using an autocorrelation technique." *IEEE Transactions on Sonics and Ultrasonics*, vol. 32, pp. 458–464, 1985.

[2] T. Loupas, R. Peterson, and R. Gill, "Experimental evaluation of velocity and power estimation forultrasound blood flow imaging, by means of a two-dimensional autocorrelation approach." *IEEE Transactions on Ultrasonics, Ferroelectrics and Frequency Control*, vol. 42, pp. 689–699, Jul 1995.

[3] H. Torp, K. Kristoffersen, and B. Angelsen, "Autocorrelation Techniques in Color Flow Imaging. Signal model and statistical properties of the Autocorrelation estimates." *IEEE Transactions on Ultrasonics, Ferroelectrics, and Frequency control*, vol. 41, pp. 604–612, 1994.

[4] J. Ophir, I. Cespedes, H. Ponnekanti, Y. Yazdi, and X. Li, "Elastography: a quantitative method for imaging the elasticity of biological tissues," *Ultrasonic Imaging*, vol. 13, pp. 111–134, April 1991.

[5] A. Heimdal, A. Stoylen, H. Torp, and T. Skjaerpe, "Real-time strain rate imaging of the left ventricle by ultrasound." *Journal of American Soc Echocardiography*, vol. 11, pp. 1013–1019, Nov 1998.

[6] L. Bohs, B. Friemel, and G. Trahey, "Experimental velocity profiles and volumetric flow via two-dimensional speckle tracking." *Ultrasound in Medicine and Biology*, vol. 21, pp. 885–98, 1995.

[7] J. Bercoff, M. Tanter, and M. Fink, "Supersonic shear imaging: a new technique for soft tissue elasticity mapping," *IEEE Transactions on Ultrasonics, Ferroelectrics and Frequency Control*, vol. 51, pp. 396–4009, April 2004.

[8] E. Turgay, S. Salcudean, and R. Rohling, "Identifying Mechanical properties of Tissue by Ultrasound." *Ultrasound in Medicine and Biology*, vol. 32, pp. 221–235, 2006.

[9] H. Eskandari, S. Salcudean, and R. Rohling, "Viscoelastic Parameter Estimation Based on Spectral Analysis." *IEEE Transactions on Ultrasonics, Ferroelectrics, and Frequency control*, vol. 55, pp. 1611–1625, July 2008.

[10] R. Righetti, J. Ophir, S. Srinivasan, and T. Krouskop, "The Feasibility of Using Elastography for Imaging the Poissons Ratio in Porous Media," *Ultrasound in Medicine and Biology*, vol. 30, pp. 215–228, 2004.

[11] W. Lee, C. M. Ingrassia, S. D. Fung-Kee-Fung, K. D. Costa, J. W. Holmes, and E. Konofagou, "Theoretical Quality Assessment of Myocardial Elastography with In Vivo Validation," *IEEE Transactions on Ultrasonics, Ferroelectrics and Frequency Control*, vol. 54, pp. 2233–2245, 2007.

[12] A. Thitaikumar, L. Mobbs, C. Kraemer-Chant, B. Garra, and J. Ophir, "Breast Tumor Classification using axial shear strain elastography: a feasibility study," *Physics in Medicine and Biology*, vol. 53, pp. 4809–4823, 2008.

[13] K. Nightingale, M. Palmeri, R. Nightingale, and G. Trahey, "On the feasibility of remote palpation using acoustic radiation force," *Journal of the Acoustical Society of America*, vol. 110, pp. 625–34, July 2001.

[14] W. Walker, F. Fernandez, and L. Negron, "A method of imaging viscoelastic parameters with acoustic radiation force." *Physics in Medicine and Biology*, vol. 45, pp. 1437–1447, 2000.

[15] M. Fatemi and J. Greenleaf, "Probing the dynamics of tissue at low frequencies with the radiation force of ultrasound," *Physics in Medicine and Biology*, vol. 45, pp. 1449–64, June 2000.

[16] F. Viola and W. Walker, "A comparison of the performance of time-delay estimators in medical ultrasound." *IEEE Transactions on Ultrasonics, Ferroelectrics and Frequency Control*, vol. 50, pp. 392–401, April 2003.

[17] G. Pinton, J. Dahl, and G. Trahey, "Rapid tracking of small displacements with ultrasound." *IEEE Transactions on Ultrasonics, Ferroelectrics and Frequency Control*, vol. 53, pp. 1103– 1117, June 2006.

[18] I. Hein and W. O'Brien, "Current time-domain methods for assessing tissue motion by analysis from reflected ultrasound echoes-a review." *IEEE Transactions on Ultrasonics, Ferroelectrics and Frequency Control*, vol. 40, pp. 84–102, March 1993.

[19] G. Pinton and G. Trahey, "Continuous Delay Estimation with Polynomial Splines." *IEEE Transactions on Ultrasonics, Ferroelectrics and Frequency Control*, vol. 53, pp. 2026–2035, 2006.

[20] K. Hoyt, F. Forsberg, and J. Ophir, "Comparison of shift estimation strategies in spectral elastogaphy," *Ultrasonics*, vol. 44, pp. 99–108, 2006.

[21] M. O'Donnell, A. Scovoroda, B. Shapo, and S. Emelianov, "Internal Displacement and Strain Imaging Using Ultrasonic Speckle Tracking," *IEEE Transactions on Ultrasonics, Ferroelectrics and Frequency Control*, vol. 41, pp. 314–25, May 1994.

[22] A. Pesavento, C. Perrey, M. Krueger, and H. Ermert, "A time efficient and accurate strain estimation concept for ultrasonic elastography using iterative phase zero estimation," *IEEE Transactions on Ultrasonics, Ferroelectrics, and Frequency Control*, vol. 46, pp. 1057–1067, 1999.

[23] A. Basarab, H. Liebgott, and P. Delachartre, "Analytic estimation of subsample spatial shift using the phases of multidimensional analytic signals." *IEEE Transactions on Image Processing*, vol. 18, pp. 440–447, 2009.

[24] C. Sumi, "Fine Elasticity Imaging Utilizing the Iterative RF-echo Phase Matching Method," *IEEE Transactions on Ultrasonics, Ferroelectrics and Frequency Control*, vol. 46, pp. 158–166, January 1999.

[25] ——, "Displacement Vector Measurement Using Instantaneous Ultrasound Signal Phase-Multidimensional Autocorrelation and Doppler Methods," *IEEE Transactions on Ultrasonics, Ferroelectrics, and Frequency control*, vol. 55, pp. 24–43, Jan 2008.

[26] M. Lubinski, S. Emelianov, and M. O'Donnell, "Speckle tracking methods for ultrasonic elasticity imaging using short-time correlation," *IEEE Transactions on Ultrasonics, Ferroelectrics and Frequency Control*, vol. 46, pp. 82–96, January 1999.

[27] C. Xunchang, M. Zohdy, E. SY., and M. O'Donnell, "Lateral speckle tracking using synthetic lateral phase." *IEEE Transactions on Ultrasonics, Ferroelectrics and Frequency Control*, vol. 51, pp. 540– 550, May 2004.

[28] E. Konofagou, T. Varghese, J. Ophir, and S. Alam, "Power spectral strain estimators in elastography," *Ultrasound in Medicine and Biology*, vol. 25, pp. 1115–29, September 1999.

[29] T. Varghese, E. Konofagou, J. Ophir, S. Alam, and M. Bilgen, "Direct strain estimation in elastography using spectral cross-correlation," *Ultrasound in Medicine and Biology*, vol. 26, pp. 1525–1537, November 2000.

[30] H. Shi and T. Varghese, "Two-dimensional multi-level strain estimation for discontinuous tissue." *Physics in Medicine and Biology*, vol. 52, pp. 389–401, Nov 2007.

[31] L. Geiman, BJ.and Bohs, M. Anderson, S. Breit, and T. G.E., "A novel interpolation strategy for estimating subsample speckle motion." *Physics in Medicine and Biology*, vol. 45, pp. 1541–1552, 2000.

[32] T. Varghese and O. J., "Characterization of elastographic noise using the envelope of echo signals," *Ultrasound in Medicine and Biology*, vol. 24, pp. 543–555, 1998.

[33] L. Bohs and G. Trahey, "A novel method for angle independent ultrasonic imaging of blood flow and tissue motion," *IEEE Transactions on Biomedical Engineering*, vol. 38, pp. 280–286, March 1991.

[34] G. Jacovitti and G. Scarano, "Discrete time techniques for time delay estimation." *IEEE Transactions on Acoustics, Speech, and Signal Processing*, vol. 41, pp. 525–533, Feb 1993.

[35] S. Langeland, J. Dapos, H. Torp, B. Bijnens, and P. Suetens, "A simulation study on the performance of different estimators for two-dimensional velocity estimation." in *Proceedings of the IEEE Ultrasonics Symposium.* Volume 2: IEEE, 8-11 Oct 2002, pp. 1859–1862.

[36] L. Bohs, B. Geiman, M. Anderson, S. Breit, and G. Trahey, "Ensemble Tracking for 2D Vector Velocity Measurement: Experimental and Initial Clinical Results." *IEEE Transactions on Ultrasonics, Ferroelectrics and Frequency Control*, vol. 45, pp. 912–924, July 1998.

[37] E. Konofagou and J. Ophir, "A new elastographic method for estimation and imaging of lateral displacements, lateral strains, corrected axial strains and Poisson's ratios in tissues," *Ultrasound in Medicine and Biology*, vol. 24, pp. 1183–99, October 1998.

[38] F. Viola, R. Coe, O. K., D. Guenther, and W. Walker, "MUlti-Dimensional Spline-Based Estimator (MUSE) for Motion Estimation: Algorithm Development and Initial Results." *Annals of Biomedical Engineering*, vol. 36, pp. 1942–1960, September 2008.

[39] E. Konofagou, F. Kallel, and J. Ophir, "Three-dimensional motion estimation in elastography," *Proceedings of the IEEE Ultrasonics Symposium*, pp. 1745–8 vol.2, October 1998.

[40] M. Bilgen, "Dynamics of errors in 3D motion estimation and implications for strain-tensor imaging in acoustic elastography," *Physics in Medicine and Biology*, vol. 45, pp. 1565–1578, 2000.

[41] F. Viola and W. Walker, "A Spline-Based Algorithm for Continuous Time-Delay Estimation Using Sampled Data." *IEEE Transactions on Ultrasonics, Ferroelectrics and Frequency Control*, vol. 52, pp. 80–93, January 2005.

[42] A. Basarab, H. Liebgott, F. Morestin, A. Lyshchik, T. Higashi, R. Asato, and P. Delachartre, "A method for vector displacement estimation with ultrasound images and its application for thyroid nodular disease." *Medical Image Analysis*, vol. 12, pp. 259–274, 2008.

[43] R. Zahiri-Azar and S. Salcudean, "Time-Delay Estimation in Ultrasound Echo Signals Using Individual Sample Tracking." *IEEE Transactions on Ultrasonics, Ferroelectrics and Frequency Control*, vol. 55, pp. 2640–2650, 2008.

[44] I. Cespedes, Y. Huang, J. Ophir, and S. Spratt, "Methods for the estimation of subsample time-delays of digitized echo signals," *Ultrasonic Imaging*, vol. 17, pp. 142–171, 1995.

[45] P. de Jong, T. Arts, A. Hoeks, and R. Reneman, "Determination of Tissue Motion Velocity by Correlation Interpolation of Pulsed Ultrasonic Echo Signals," *Ultrasonics Imaging*, vol. 12, pp. 84–98, 1990.

[46] B. Geiman, L. Bohs, M. Anderson, S. Breit, and G. Trahey, "A comparison of algorithms for tracking sub-pixel speckle motion." in *Proceedings of the IEEE Ultrasonics Symposium.* Volume 2: IEEE, 5-8 Oct 1997, pp. 1239–1242.

[47] S. Foster, P. Embree, and W. O'Brien, "Flow velocity profile via time-domain correlation: error analysis and computer simulation," *IEEE Transactions on Ultrasonics, Ferroelectrics and Frequency Control*, vol. 37, pp. 164–175, May 1990.

[48] F. Viola and W. Walker, "Computationally Efficient Spline-Based Time Delay Estimation." *IEEE Transactions on Ultrasonics, Ferroelectrics and Frequency Control*, vol. 55, pp. 2084–2091, September 2008.

[49] Y. Mofid, S. Gahagnon, F. Patat, F. Ossant, and G. Josse, "In vivo high frequency elastography for mechanical behavior of human skin under suction stress: elastograms and kinetics of shear, axial and lateral strain fields." in *Proceedings of the IEEE Ultrasonics Symposium*. Vancouver: IEEE, Oct 2006, pp. 1041–1044.

[50] R. Lopata, M. Nillesen, I. Gerrits, J. Thijssen, L. Kapusta, F. van de Vosse, and C. de Korte, " In Vivo 3D Cardiac and Skeletal Muscle Strain Estimation ," in *Proceedings of the IEEE Ultrasonics Symposium*. Vancouver: IEEE, Oct 2006, pp. 744–747.

[51] R. Lopata, M. Nillesena, H. Hansena, I. Gerritsa, T. J., and C. de Korte, "Performance Evaluation of Methods for Two-Dimensional Displacement and Strain Estimation Using Ultrasound Radio Frequency Data." *Ultrasound in medicine and biology*, vol. 35, pp. 796–812, 2009.

[52] R. Zahiri-Azar and S. Salcudean, "Real-Time Estimation of Lateral Displacement Using Time Domain Cross Correlation with Prior Estimates ," in *Proceedings of the IEEE Ultrasonics Symposium*. IEEE, Oct 2006, pp. 1209–1212.

[53] R. Zahiri-Azar, O. Goksel, T. Yao, E. Dehghan, J. Yan, and S. Salcudean, " Methods for the estimation of sub-sample motion of digitized ultrasound echo signals in two dimensions ," in *Proceedings of the IEEE Engineering in Medicine and Biology*. IEEE, Aug 2008, pp. 5581–5584.

[54] R. Lopata, M. Nillesen, I. Gerrits, J. Thijssen, L. Kapusta, and C. de Korte, " 4D Cardiac Strain Imaging: Methods and Initial Results ," in *Proceedings of the IEEE Ultrasonics Symposium*. IEEE, Oct 2007, pp. 872–875.

[55] G. Giunta, "Fine estimators of two-dimensional parameters and application to spatial shift estimation," *IEEE Transactions on Signal Processing*, vol. 47, pp. 3201–3207, 1999.

[56] R. Zahiri-Azar and S. Salcudean, "Motion Estimation in Ultrasound Images Using Time Domain Cross Correlation With Prior Estimates." *IEEE Transactions on Biomedical Engineering*, vol. 53, pp. 1990–2000, 2006.

[57] M. Cheezum, W. Walker, and G. WH., "Quantitative comparison of algorithms for tracking single fluorescent particles." *Biophysical Journal*, vol. 81, pp. 2378–2388, Oct 2001.

[58] P. Hill, T. Chiew, D. Bull, and C. Canagarajah, "Interpolation Free Subpixel Accuracy Motion Estimation," *IEEE Transactions on Circuits and Systems for Video Technology*, vol. 16, pp. 1519–1526, 2006.

[59] Y. Zhu, "Quartic-Spline Collocation Methods for Fourth-Order Two-Point Boundary Value Problems." Master's thesis, Department of Computer Science, University of Toronto, 2001.

[60] J. A. Jensen, "A model for the propagation and scattering of ultrasound in tissue," *Journal of the Acoustical Society of America*, vol. 89, pp. 182–191, 1991.

[61] J. Jensen, Ed., *Ultrasound Imaging and its modeling.* Springer Verlag, 2002, ch. Chapter for the Springer Verlag book Imaging of Complex Media with Acoustic and Seismic Waves, Topics in Applied Physics.

[62] O. Goksel, R. Zahiri-Azar, and S. Salcudean, "Simulation of Ultrasound Radio-Frequency Signals in Deformed Tissue for Validation of 2D Motion Estimation with Sub-Sample Accuracy," in *Proceedings of the IEEE Engineering in Medicine and Biology.* IEEE, August 2007, pp. 2159–2162.

[63] T. Varghese, J. Ophir, E. Konofagou, F. Kallel, and R. Righetti, "Tradeoffs In Elastographic Imaging, Ultrasonic Imaging," *Ultrasonic Imaging*, vol. 23, pp. 216–248, October 2001.

[64] S. DiMaio and S. Salcudean, "Needle insertion modelling and simulation," *IEEE Transactions on Robotics and Automation: Special Issue on Medical Robotics*, vol. 19, pp. 864–875, 2003.

[65] T. Hall, Z. Yanning, C. Spalding, and L. Cook, "In vivo results of real-time freehand elasticity imaging." in *Proceedings of the IEEE Ultrasonics Symposium.* Volume 2: IEEE, 2001, pp. 1653–1657.

[66] T. Shiina, N. Nitta, E. Ueno, and J. Bamber, "Real Time Tissue Elasticity Imaging using Combined Autocorrelation Method," *Medical Ultrasonics*, vol. 26, pp. 57–66, 1999.

[67] G. Treece, J. Lindop, A. Gee, and R. Prager, "Freehand ultrasound elastography with a 3D probe," *Ultrasound in Medicine and Biology*, vol. 34, pp. 463–474, March 2008.

[68] P. Chaturvedi, M. Insana, and T. Hall, "2D companding for noise reduction in strain imaging," *IEEE Transactions on Ultrasonics, Ferroelectrics and Frequency Control*, vol. 45, pp. 179–191, 1998.

[69] E. Brusseau, J. Kybic, J. Deprez, and O. Basset, "2-D Locally Regularized Tissue Strain Estimation From Radio-Frequency Ultrasound Images: Theoretical Developments and Results on Experimental Data." *IEEE Transactions on Medical Imaging*, vol. 27, pp. 145 – 160, Feb 2008.

[70] S. Alam, J. Ophir, and E. Konofagou, "An adaptive strain estimator for elastography," *IEEE Transactions on Ultrasonics, Ferroelectrics and Frequency Control*, vol. 45, pp. 461–72, March 1998.

[71] T. Varghese and J. Ophir, "Enhancement of echo-signal correlation in elastography using temporal stretching," *IEEE Transactions on Ultrasonics, Ferroelectrics and Frequency Control*, vol. 44, pp. 173–180, January 1997.

Chapter 4

3D Estimation of Sub-Sample Motion from Digitized Ultrasound Echo Signals[3]

4.1 Introduction

Motion estimation in sequences of ultrasound echo signals has many applications such as blood flow estimation, tissue velocity estimation [1–3], strain and strain rate imaging [4–6], tissue elasticity imaging [7], vibro-elastography [8,9], poro-elastography [10], myocardial imaging [11], tumor classification [12], and acoustic radiation force impulse imaging [13–15].

Since ultrasound imaging provides higher resolution in the axial direction, the estimation of the axial component of the motion has received the most attention in the literature. However, tracking the motion in one direction introduces several limitations. In blood flow and tissue velocity estimation using Doppler techniques, tracking along the beam propagation results in a poor estimation of the flow and tissue velocity due to the unknown Doppler angle between the velocity vector and the beam direction. Poor estimates can result even if the angle is manually adjusted [16,17]. In quasi-static elastography, tracking the motion in the axial direction results in estimation of only the axial component of the strain tensor, with all the other components remaining unknown [18]. Finally, in dynamic elastography, using the wave equations, the estimation of a single component of motion limits modulus estimation algorithms to a less accurate partial inversion rather than a full inversion [19].

A great number of motion estimation algorithms have been introduced in the literature and have been studied in our previous work. Techniques based on pattern matching functions are the most straightforward approaches used to estimate the axial motion from digitized ultrasound radio frequency (RF) echo signals [4, 20–22]. Extensions of these techniques to 2D and 3D motion estimation have also been proposed in the literature [23, 24]. With these techniques, the reference ultrasound echo signal is divided into a number of windows, which may have overlap with each other. The reference echo signal within each window is then set to be the *pattern* to be matched with the displaced echo signal over a predefined search region. Finally, the motion of the window is found by locating the best match. Several pattern matching functions have been suggested in the literature, such as normalized cross correlation, sum of square differences, and sum of absolute differences [25, 26]. Estimation of the motion from envelope signals and from a combination of RF and envelope signals have also been

[3] A version of this chapter has been peer reviewed and published in the proceedings of the international Conference on IEEE Ultrasonics Symposium. A version of this chapter has also been submitted for publication. Reza Zahiri-Azar, Orcun Goksel, and Septimiu E. Salcudean, "3D Estimation of Sub-Sample Motion from Digitized Ultrasound Echo Signals".

reported [23, 27].

The estimation error of these techniques can be as large as half the sample spacing, which is important especially when the motion is small and the sample spacing is large. This estimation error becomes more significant in the lateral and elevational directions where the sample spacing is very large. Several techniques have been suggested in the literature to reduce the error introduced by finite sampling intervals. These techniques are categorized as: (i) echo signal up-sampling [28–30], (ii) interpolation of the echo signals [28, 29, 31, 32], and (iii) interpolation of the pattern matching function [33–36].

Up-sampling of the echo signal as in (i) reduces the error by the up-sampling factor [29, 30]. Curve or polynomial fitting to the echo signals as in (ii) results in a continuous pattern matching function, whose extremum determines the location of the best match [28, 29, 31, 32]. It has been shown that these techniques outperform other algorithms but, similarly to up-sampling methods, they can be computationally demanding [32, 37], whereas curve or polynomial fitting to the pattern matching function as in (iii) often have significantly smaller computational overhead. Thus, even though they may introduce some bias in the estimation process, they are widely used for motion estimation. These techniques will be the topic of this work.

A number of 1D pattern matching interpolation methods such as parabolic fitting [36], spline fitting [35], grid slope [22, 38], cosine fitting [34], zero padding, and reconstructive methods [33] have been introduced and thoroughly investigated in the literature [25, 28, 32]. Applying the same 1D interpolation techniques independently to each direction (2-1D) has also been used in the literature to estimate the sub-sample motion in 2D and 3D [22, 31, 38–41]. Applying iterative 1D interpolation [42, 43] and 2D interpolation techniques [43–45] have also been attempted in the literature.

In our previous work we studied all these techniques in 2D and showed that independent 1D sub-sample motion estimation in each direction results in estimates with poor accuracy and precision. We showed that 2D interpolation significantly outperform other interpolation techniques in estimating both the axial and the lateral sub-sample motions. In this work, we extend our previous work to 3D and study and compare the performance of (i) independent 1D and (ii) 3D interpolation pattern matching interpolation techniques in estimating axial, lateral, and elevational sub-sample motions on ultrasound radio frequency data.

The paper is structured as follows: Section 4.2 presents the interpolation algorithms. Section 4.3 presents the simulation method and a comparison between the algorithms. Section 4.4 presents the experimental results. Finally, Section 4.5 presents a discussion and conclusions along with avenues for future research.

Throughout this work, it is assumed that the echo signals are 2D radio frequency (RF) signals. Without loss of generality, it is assumed that the pattern matching function optimization involves maximization of the normalized cross correlation. The pattern matching function values will be referred to as the *matching coefficients*.

4.2 Methods

Let $R[u, v, w]$ be the 3D discrete pattern matching function between a reference window and displaced echo signals over a predefined search region. The pattern matching function can be the normalized correlation as discussed in Appendix F. Given the discrete 3D pattern matching function $R[u, v, w]$, the coarse axial d_a, lateral d_l, and elevational d_e estimates of the motion in

the axial (x), lateral (y), and elevational (z) directions, respectively, are achieved by locating the maximum of this 3D discrete function:

$$[d_a, d_l, d_e] = \arg\max_{u,v,w} R[u, v, w]. \tag{4.1}$$

Following the coarse estimation of the motion within the sampling accuracy, the following methods are used to estimate the sub-sample displacements δ_a, δ_l, and δ_e in the axial, the lateral, and the elevational directions, respectively, using the matching coefficients at adjacent lags.

4.2.1 Independent 1D Methods

The most common approach for estimating sub-sample motion is to apply conventional 1D interpolation techniques such as parabola, cosine, or spline fitting to the axial, lateral, and elevational directions in an independent manner.

Referring to Fig. 4.1(a), let $f_a(x)$ be an axial 1D interpolation function passing through the 3D pattern matching function at $[d_a, d_l, d_e]$ and its axial lags (i.e. $R[d_a+i, d_l, d_e]$ where i is in an axial fitting interval $-M_a, ..., M_a$), $f_l(y)$ be a lateral 1D interpolation function passing through the 3D pattern matching function at $[d_a, d_l, d_e]$ and its lateral lags (i.e. $R[d_i, d_l + j, d_e]$ where j is in a lateral fitting interval $\{-M_l, ..., M_l\}$), and $f_e(z)$ be an elevational 1D interpolation function passing through the 3D pattern matching function at $[d_a, d_l, d_e]$ and its elevational lags (i.e. $R[d_i, d_l, d_e + k]$ where k is in an elevational fitting interval $\{-M_e, ..., M_e\}$. The sub-sample motion estimates δ_a, δ_l, and δ_l, at (d_a, d_l, d_e) are computed from their corresponding axial, lateral, and elevational interpolation functions as follows:

$$\begin{aligned} \delta_a &= \arg\max_x f_a(x), \\ \delta_l &= \arg\max_y f_l(y), \\ \delta_e &= \arg\max_y f_e(z). \end{aligned} \tag{4.2}$$

For the purpose of this work, the following two interpolation functions have been implemented: (i) three point 1D parabola fitting [36], where $f_a(x) = a_a + b_a x + c_a x^2$, $f_l(y) = a_l + b_l y + c_l y^2$, and $f_e(z) = a_e + b_e z + c_e z^2$ and (ii) three point cosine fitting [34], where $f_a(x) = A_a \cos(\alpha_a x + \beta_a)$, $f_l(y) = A_l \cos(\alpha_l y + \beta_l)$, and $f_e(z) = A_e \cos(\alpha_e z + \beta_e)$. The independent 1D methods using three point function fitting ($M_a = M_l = M_e = 1$), require matching coefficients to be available at seven lags (i.e. the maximum in the center and the two immediate neighboring lags in each direction). Detailed descriptions of these techniques are provided in our previous work and are not repeated here.

4.2.2 3D Methods

In a more general approach a 3D function can be fitted to the discrete matching coefficients in the axial, lateral, and elevational directions. Estimation with sub-sample accuracy can then be achieved in all directions by finding the peak of the fitted function, analytically.

Referring to Fig. 4.1(b), let $f(x, y, z)$ be a 3D interpolation function passing through the 3D pattern matching function at $[d_a, d_l, d_e]$ and its neighbors (i.e. $R[d_a + i, d_l + j, d_e + k]$ where $i \in \{-M_a, ..., M_a\}$, $j \in \{-M_l, ..., M_l\}$, $k \in \{-M_e, ..., M_e\}$). The sub-sample motion estimates

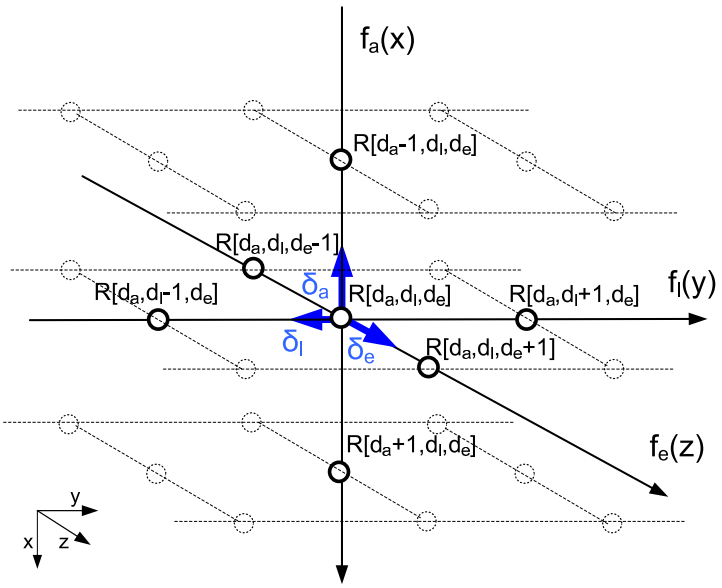

(a) Independent 1D estimation

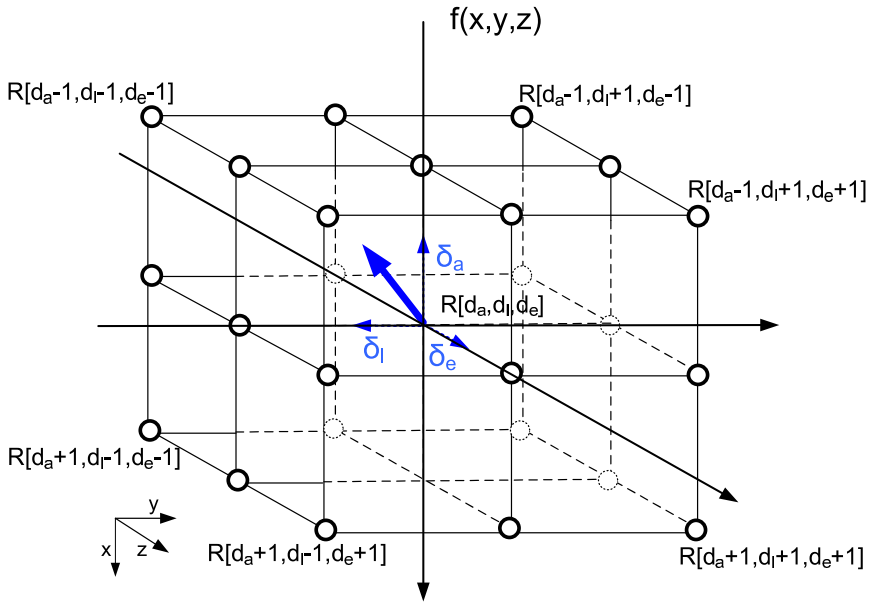

(b) 3D estimation

Figure 4.1: Different schemes for sub-sample displacement estimation in 3D using the coefficients of the cross correlation function in the neighborhood of its maximum. For the first technique, only 1D interpolation is required while 3D interpolation is needed for the second method.

δ_a, δ_l, and δ_e at (d_a, d_l, d_e) are computed simultaneously from the corresponding 3D interpolation functions as follows:

$$[\delta_a, \delta_l, \delta_e] = \arg\max_{x,y,z} f(x, y, z). \tag{4.3}$$

The following non-separable 3D polynomials:

$$\begin{aligned} f_{10}(x, y, z) &= a_1 + a_2x + a_3y + a_4z + a_5xy \\ &\quad + a_6xz + a_7yz + a_8x^2 + a_9y^2 + a_{10}z^2, \end{aligned} \tag{4.4}$$

$$\begin{aligned} f_{27}(x, y, z) &= a_1 + a_2x + a_3y + a_4z + a_5xy \\ &\quad + a_6xz + a_7yz + a_8x^2 + a_9y^2 + a_{10}z^2 \\ &\quad + a_{11}x^2y + a_{12}x^2z + a_{13}y^2x + a_{14}y^2z \\ &\quad + a_{15}z^2x + a_{16}z^2y + a_{17}xyz + a_{18}x^2y^2 \\ &\quad + a_{19}x^2z^2 + a_{20}y^2z^2 + a_{21}x^2yz \\ &\quad + a_{22}y^2xz + a_{23}z^2xy + a_{24}x^2y^2z \\ &\quad + a_{25}x^2z^2y + a_{26}y^2z^2x + a_{27}x^2y^2z^2, \end{aligned} \tag{4.5}$$

with 10 and 27 coefficients are implemented in this paper, where $f_{10}(x, y, z)$ is a multinomial of degree 2 and $f_{27}(x, y, z)$ results from multiplying the $[1, x, x^2]$, $[1, y, y^2]$, and $[1, z, z^2]$ terms (quadratic spline). Higher order polynomials such as cubic and quartic splines are not considered in this work (please see the Discussions Section).

The two 3D polynomials are fitted to 27 points of the discrete pattern matching function, the maximum and its 26 immediate neighbors, using a least squares fit. A detailed description of the 3D polynomial fitting is provided in Appendix G. The location of the unconstrained maximum of this fitted 3D polynomial (i.e. $\nabla f(x, y, z) = (\partial f/\partial x, \partial f/\partial y, \partial f/\partial z) = 0$) is then found using the following closed form solution:

$$\begin{bmatrix} x \\ y \\ z \end{bmatrix} = -\begin{bmatrix} 2a_8 & a_5 & a_6 \\ a_5 & 2a_9 & a_7 \\ a_6 & a_7 & 2a_{10} \end{bmatrix}^{-1} \begin{bmatrix} a_2 \\ a_3 \\ a_4 \end{bmatrix}, \tag{4.6}$$

for $f_{10}(x, y, z)$, and by using Newton's method (E.4) for $f_{27}(x, y, z)$, where $\kappa = 0, 1, ..., n$ is the index of the iteration, n is the number of iterations. In this work, in order to locate the maximum of f_{27} in Newton's method, x_0, y_0, z_0 are initialized to zero. Note that the fit for f_{10}, followed by (4.6), can be used to generate the starting point for estimating the maximum of f_{27}. This approach will provide a better starting point for Newton's method and therefore will reduce the number of iterations required for convergence, but it will also require the data to be fitted to both f_{10} and f_{27}.

$$\begin{bmatrix} x \\ y \\ z \end{bmatrix}_{\kappa+1} = \begin{bmatrix} x \\ y \\ z \end{bmatrix}_{\kappa} - \begin{bmatrix} \frac{\partial^2 f}{\partial x \partial x} & \frac{\partial^2 f}{\partial x \partial y} & \frac{\partial^2 f}{\partial x \partial z} \\ \frac{\partial^2 f}{\partial y \partial x} & \frac{\partial^2 f}{\partial y \partial y} & \frac{\partial^2 f}{\partial y \partial z} \\ \frac{\partial^2 f}{\partial z \partial x} & \frac{\partial^2 f}{\partial z \partial y} & \frac{\partial^2 f}{\partial z \partial z} \end{bmatrix}^{-1} \begin{bmatrix} \frac{\partial f}{\partial x} \\ \frac{\partial f}{\partial y} \\ \frac{\partial f}{\partial z} \end{bmatrix} \Bigg|_{\substack{x=x_\kappa \\ y=y_\kappa \\ z=z_\kappa}} \tag{4.7}$$

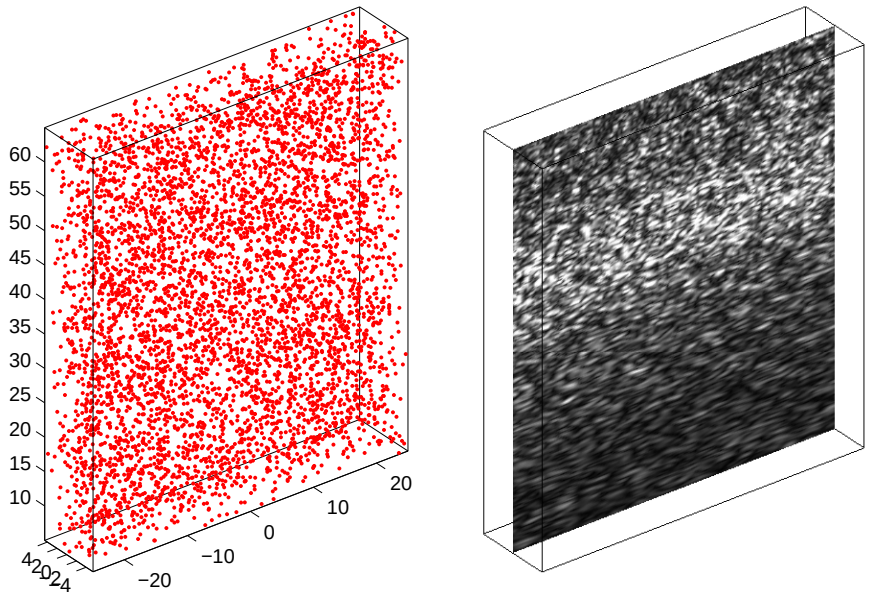

(a) Scatterers (b) Sonogram

Figure 4.2: Scatterers distributions (left) (only a small fraction of all scatterers are plotted for better visualization) and a Field II simulated sonogram (right).

4.3 Simulations

4.3.1 Simulation Setup

A series of computer simulations were performed to study and compare the performance of the sub-sample motion estimators. All calculations were performed in MATLAB (MathWorks Inc., Natick, MA). A $50 \times 60 \times 10\,mm^3$ virtual phantom was simulated (Fig. 4.2(a)) by randomly allocating with random scattering amplitudes. Field II [46] was then used to simulate the ultrasound radio frequency echo volumes (RF volumes) from these scatterers. A linear probe was modeled. The default simulation assumes a 5 MHz center frequency and 40 MHz sampling frequency ($\approx 19.3\,\mu$m sample spacing). A linear scan of the phantom was carried out with a 128 element transducer, using 64 active elements. A single transmit focus was placed at 30 mm, and dynamic receive focusing was employed to generate the RF lines. 128 RF lines were simulated along a width of 38 mm for each frame. This results in a line spacing of $300\,\mu$m. The frames in the volume were simulated by translating the transducer in the elevational direction. An elevational frame spacing of $150\,\mu$m modeling our experimental ultrasound setup was employed. Seven frames were simulated for each volume (i.e. $7 \times 128 = 896$ RF lines per volume). The number of scatterers per smallest sampling volume was set to be 10 to ensure that the speckle of the ultrasound images is fully developed. A sample sonogram generated from one of these simulated RF data sets is shown in Fig. 4.2(b).

In order to simulate rigid motions in all three directions, the scatterers were displaced on a grid in the axial, lateral and elevational directions with sub-sample distances (i.e. a fraction of the sample-spacing along each corresponding axis). For all the displacements, a step size of 1/4 of the sample spacing in the corresponding axis was chosen (i.e. $5\,\mu$m axially,

75 μm laterally, and 37.5 μm elevationally) forming a grid of 5x5x5=125 distinct displacement configurations up to a full sample. The RF volumes corresponding to each of these displaced scatterer configurations were then simulated (i.e. $896 \times 125 = 112,000$ RF lines). These simulated RF volumes were used to estimate the motion in conjunction with the RF volume in the center of the 3D grid as a reference. This resulted in a grid spanning ± 0.5 of a sample in all directions. Simulation of each volume would take more than 500 hours using Field II on a single core computer. Four multi-core processor computers were used in parallel to simulate the RF volumes for this work.

4.3.2 Motion Estimation

Simulations were performed by applying the estimation algorithms to simulated RF volumes. For all the data the normalized cross correlation was used as a pattern matching function to find the coarse motion within the sampling accuracy. Unless mentioned otherwise, the window size for the pattern matching function is set to be approximately $2 \times 2 \times 1\, mm^3$ (i.e. 104 samples axially, 7 samples laterally, and 5 samples elevationally). The size of the search area for the pattern matching function was set to be approximately $3 \times 3 \times 2\, mm^3$ (i.e. 156 samples axially, 9 samples laterally, and 7 samples elevationally), so that it does not introduce any limitation in the estimation process. The sub-sample motion estimators from Section 4.2 were then applied to find the sub-sample motions. In order to have accurate estimation of the cross correlation at the edges of the search region, the actual data from the echo signals were used instead of zero-padding. The start point for Newton's method for estimating the maximum of the 3D polynomial was set to be $x_0 = y_0 = z_0 = 0$ and the iteration was stopped when the variations drop below 0.00001, which is equivalent to 0.001% of the sample spacing. In all the simulations, this criterion was met in less than five iterations (i.e. $\delta_a = x_5, \delta_l = y_5, \delta_e = z_5$ in (E.4)).

To have unbiased measurements, the region of interest (ROI) was centered around the transmit focus and data from both near-field and far-field were removed from the study. The size of the ROI was set to be 30 mm by 30 mm. This resulted in more than 1000 pattern matching windows used for displacement estimations for each sub-sample motion on a grid. The performance of each estimator was studied in terms of its bias and standard deviation as a function of the sub-sample shift in the axial, lateral, and elevational directions to study their accuracy and precision [28, 31, 32].

4.3.3 Simulation Results

Figure 4.3 shows the bias and standard deviation of all the sub-sample estimation techniques as a function of sub-sample shift on a $5 \times 5 \times 5$ grid. For better visualization of the accuracy, the axial, the lateral, and the elevational biases are shown with a vector. Vectors connecting the true displacements to the mean estimated displacements illustrate the directional bias for each of the 125 simulations. In order to show the precision, the standard deviations in all three directions, an ellipsoid error representation is used for each of the simulations. The radius of each ellipse in each direction corresponds to the standard deviation of the motion estimation in that given direction. For better visualization, the ellipsoids are centered on the true motions instead of the estimated motions. Also, every other plane in the elevational direction is eliminated prior to display in this particular format.

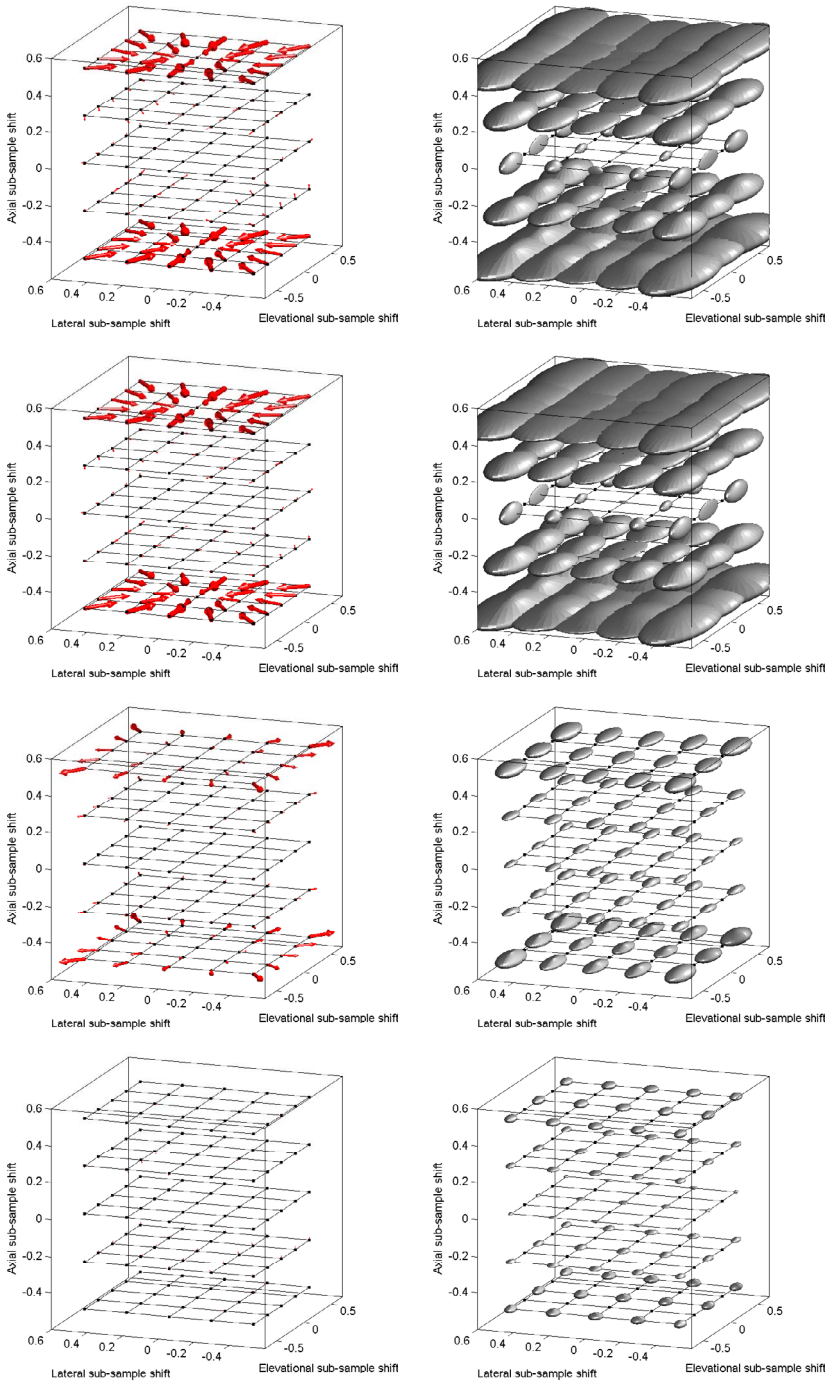

Figure 4.3: Bias Vectors (1st column) and standard deviation ellipsoids (2nd column) of Ind. 1D parabola fit (1st row), Ind. 1D cosine fit (2nd row), f_{10} fit (3rd row), and f_{27} fit (4th row) as a function of sub-sample shift on a $5 \times 5 \times 5$ simulated grid. A total of 1000 windows/patterns were used to generate each bias vector and standard deviation ellipsoid.

Figure 4.3 shows that the common independent 1D methods performs well only if the displacements have either axial, lateral, or elevational component (i.e. $\delta_a \neq 0$ or $\delta_l \neq 0$ or $\delta_e \neq 0$). The 3D methods are able to recover the underlaying motion from the RF volumes and show small biases and standard deviations (i.e. smaller vectors and ellipses). The results show that increasing the number of the coefficients for the 3D polynomial fitting improves the performance of the sub-sample motion estimator. 3D polynomial fitting with 27 coefficients has smaller biases and standard deviations. This is consistent with our previously reported results for 2D sub-sample estimation.

In order to study the results quantitatively, we follow the approach suggested in [31]. The biases and standard deviations of all the above techniques for each individual axes are presented in Fig. 4.4. To simplify the comparison between the results, the biases and standard deviations are displayed using the same color range, for all the methods. It should be noted that bias is signed and is smaller when it is closer to the center of the color bar (i.e. gray) while standard deviation is positive and is smaller when it is closer to the bottom of the color bar (i.e. black). Fig. 4.4 shows that the maximum biases and standard deviations of the 3D methods are significantly smaller than those of the common independent 1D methods. Figure 4.4 shows that the maximum lateral and elevational biases of the independent 1D interpolation methods are as large as 0.15 and 0.25 of a sample, respectively. This figure also shows that the maximum lateral and elevational standard deviations of the independent 1D interpolation methods are as large as 0.20 and 0.50 of a sample, respectively. These results are consistent with our previously reported results in 2D and the results reported in [31]. Figure 4.4 shows that the maximum lateral and elevational biases and standard deviations of all the 3D methods are an order of magnitude smaller than those of the conventional independent 1D interpolation methods. For better visualization of the range of errors of the 3D methods, their biases and standard deviations are shown in Fig. 4.5 using separate color bars. The performance of all the techniques in terms of their maximum bias and standard deviations in both directions is summarized in Table 4.1. For an easier comparison, the same results are shown in Fig. 4.6, using error plots.

The results show that the accuracy and the precision of sub-sample estimation improve in all three directions when the 3D methods are employed instead of the common independent 1D method. The maximum axial, lateral, and elevational biases of the 3D polynomial fitting with 27 coefficients, f_{27}, are found to be 0.0121, 0.0180, and 0.0121 of a sample, which correspond to 232 nm, 5.40 μm, and 1.81 μm, respectively, at the simulated 19.3 μm, 300 μm, and 150 μm axial, lateral, and elevational spacing. The maximum axial, lateral, and elevational standard deviations of f_{27} are found to be 0.0160, 0.0264, and 0.0574 of a sample, which correspond to 307 nm, 7.92 μm, and 8.61 μm, respectively.

Table 4.1: Maximum values of biases and standard deviations of different 3D motion estimation techniques evaluated from simulated data in units of sample.

Method	Max b_{ax}	Max b_{lat}	Max b_{elv}	Max σ_{ax}	Max σ_{lat}	Max σ_{elv}
Ind. 1D Par	0.0201	0.1657	0.2767	0.0517	0.1612	0.4053
Ind. 1D Cos	0.0121	0.1641	0.2769	0.0482	0.1623	0.4041
$f_{10}(x,y,z)$	0.0119	0.0891	0.1411	0.0299	0.0454	0.1348
$f_{27}(x,y,z)$	0.0121	0.0180	0.0121	0.0160	0.0264	0.0574

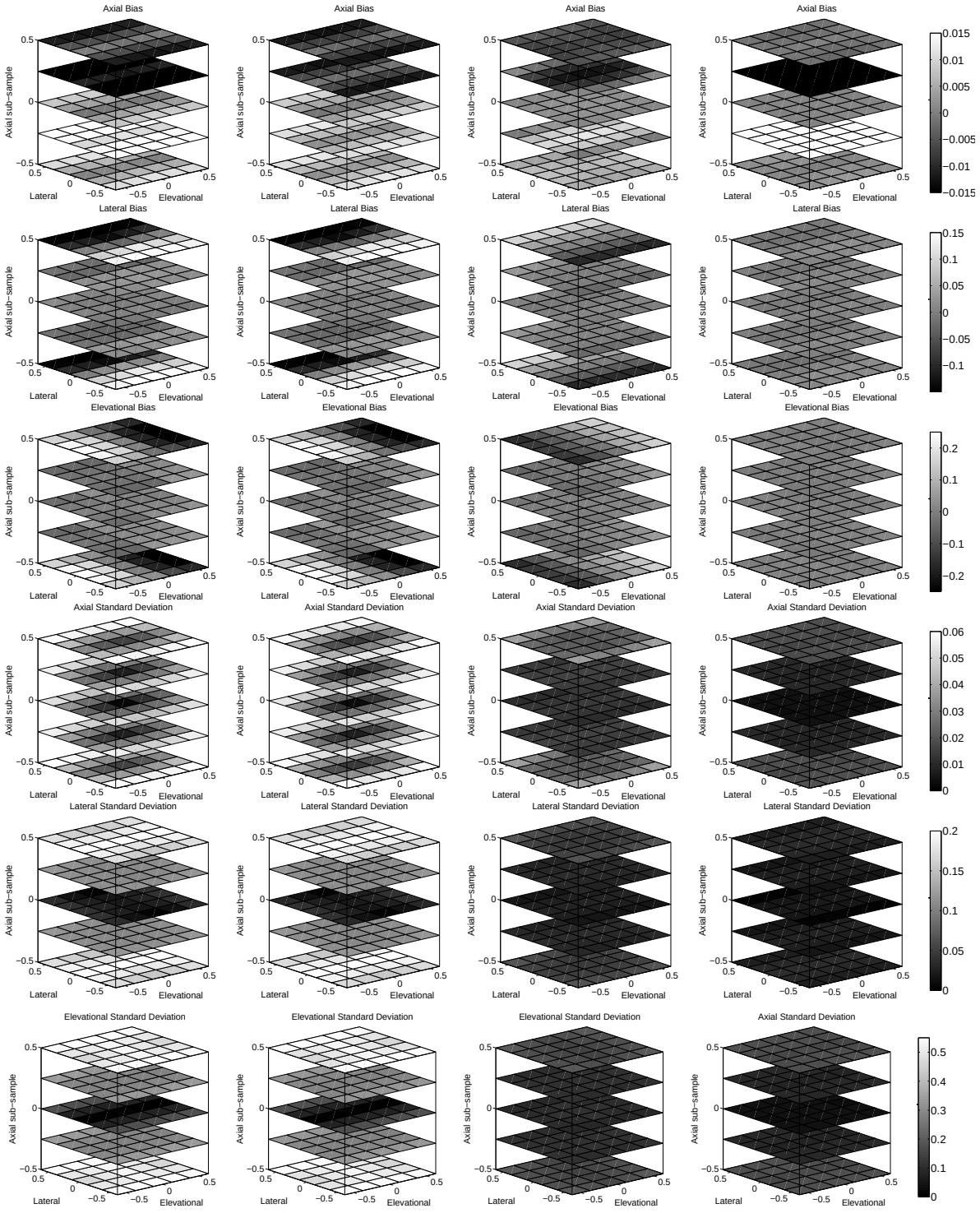

(a) 1D Parabola fit (b) 1D Cosine fit (c) $f_{10}(x, y, z)$ fit (d) $f_{27}(x, y, z)$ fit

Figure 4.4: Biases and standard deviations of the sub-sample estimation techniques as a function of sub-sample shift on a $5 \times 5 \times 5$ grid (window size is 104 samples axially, 7 samples laterally, and 5 samples elevationally $\approx 2 \times 2 \times 1\, mm^3$).

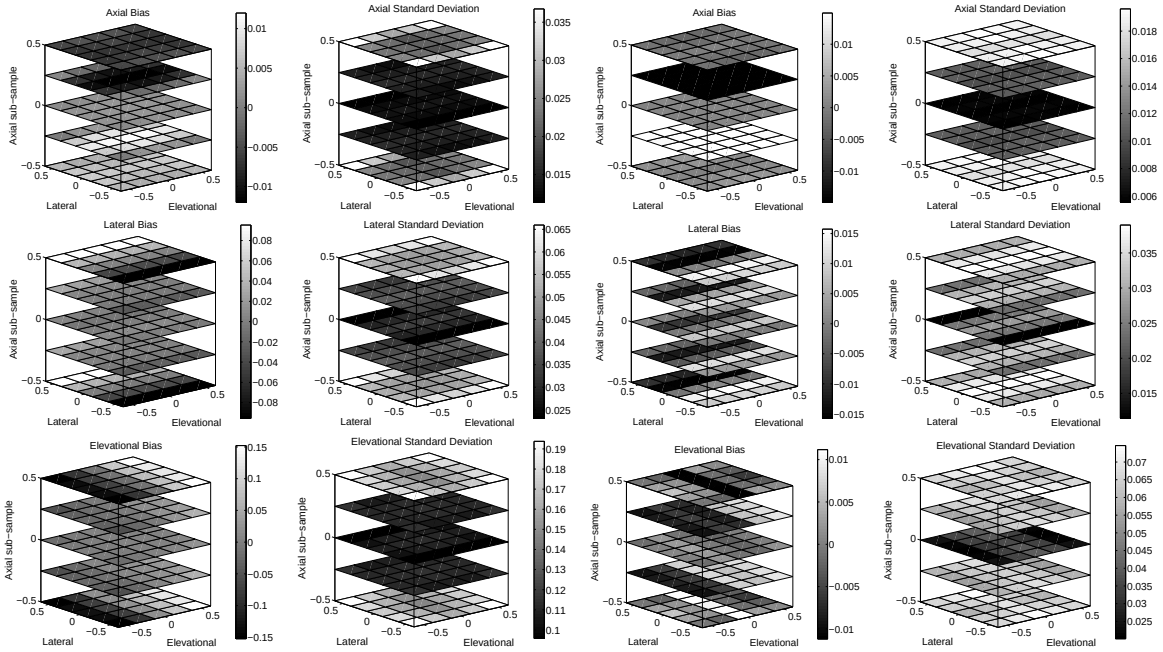

(a) Bias of f_{10} (b) STD of f_{10} (c) Bias of f_{27} (d) STD of f_{27}

Figure 4.5: Biases and Standard deviations of the sub-sample estimation techniques as a function of sub-sample shift on a $5 \times 5 \times 5$ grid (window size is 104 samples axially, 7 samples laterally, and 5 samples elevationally $\approx 2 \times 2 \times 1\, mm^3$).

Fig. 4.3 visualizes the biases and standard deviations as a fraction of a sample assuming equal sample spacing in both directions. However, as mentioned before, the sample spacing in the lateral and elevational directions is much larger than the sample spacing in the axial direction. In order to show the true length of the bias vectors and real shape of the standard deviation ellipsoids, Fig. 4.7 compares the performance of the independent 1D parabola fitting and the 3D polynomial fitting (Fig. 4.3(a),(d)) in units of distance, as opposed to fraction of a sample. Fig. 4.7 depicts how small errors in fraction of a sample, translate to large actual errors especially in the lateral and elevational directions which suffer from large sample spacing. This figure shows the importance of accuracy and precision of sub-sample estimation especially in the lateral and elevational directions.

4.4 Experiments

4.4.1 Experimental Setup

In order to study the performance of the 3D method using actual ultrasound data, the following experiment was conducted. A 3-axis AIMS ultrasound scanning system (Onda Corp., Sunnyvale, CA) with 10 μm resolution in each axis, mounted on a water tank, equipped with the water conditioning system (Onda Corp., Sunnyvale, CA) was used. This experimental setup is shown in Fig. 4.8. Experiments were performed on a $60 \times 40 \times 40\, mm^3$ uniform phantom. The phantom was prepared using a 100% polyvinyl chloride (PVC) plasticizer (M-F Manufacturing Co., Inc. Fort Worth, TX, USA) with two percent cellulose (Sigma-Aldrich Inc., St Louis, MO, USA) as scatterers [47]. The phantom was inserted in a tank of degassed water and placed 2 mm away from the transducer, thus enabling the transducer to move without deforming the phantom producing a rigid motion. The probe was moved in steps of 20 μm once axially, once laterally, and once elevationally up to 100 μm. The phantom was imaged using the 3D transducer (4DC6-3/40) of a SonixRP ultrasound machine (Ultrasonix Medical Corporation, Richmond, BC). Similarly to our simulation setup, a single transmit focus was placed at 30 mm. The phantom was imaged to a depth of 60 mm (2 mm water gap plus 58 mm phantom) using a 128-element motor-driven curved-linear transducer (lateral radius of $r_l = 39.8$ mm and elevational radius of $r_e = 27.5$ mm) with a 5 MHz center frequency digitized at 40 MHz, with 430 μm line spacing at the transducer's surface, and 0.36° frame spacing (i.e. 175 μm frame spacing at the surface of the transducer). 33 frames were acquired per volume (i.e. a total of 11.5° field of view elevationally). In addition to the reference RF volume, 5 RF volumes corresponding to each 20 μm increment, were recorded for each experiment on each axis for off-line processing (total of 16 RF volumes). These acquired RF volumes, in conjunction with first RF volume as a reference, were used to estimate the rigid motions.

In order to further study the performance of the 3D method qualitatively, in the presence of deformation, another experiment was conducted on a commercial phantom. The experiment was performed on a breast phantom (CIRS, Tissue Simulation and Phantom Technology, Norfolk, Virginia, USA). This experimental setup is shown in Fig. 4.9. The transducer was fixed on top of a mechanical stage that provides controlled motion. A mechanical stage was used to compress the phantom in the axial direction. Using the same transducer and imaging setup mentioned above, pre- and post-compression RF volumes were acquired. These acquired RF volumes were used to estimate the motions.

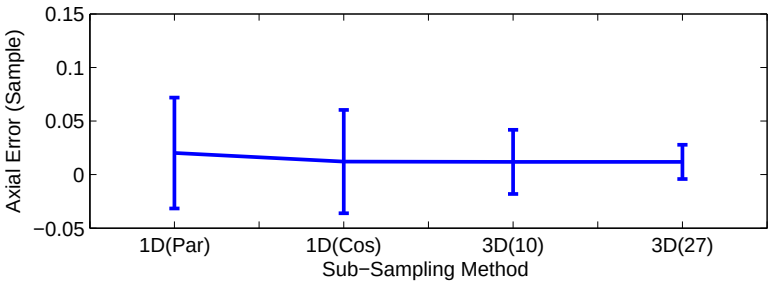

(a)

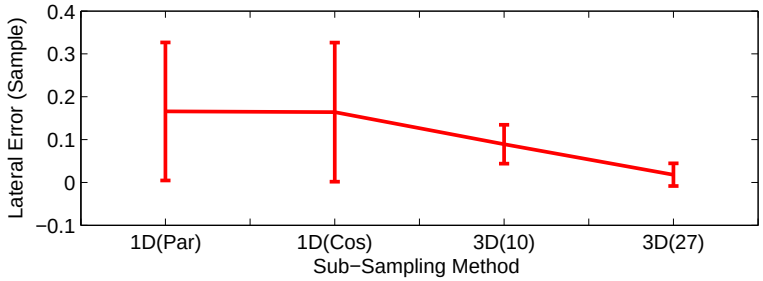

(b)

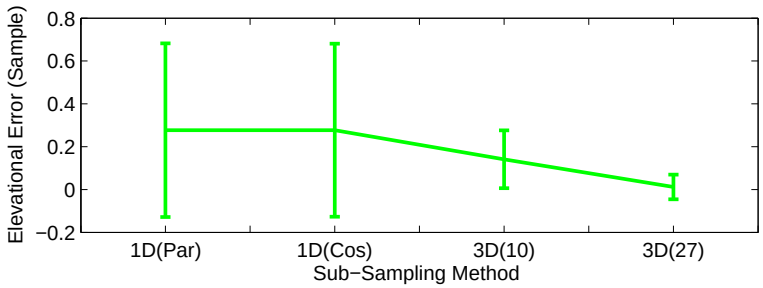

(c)

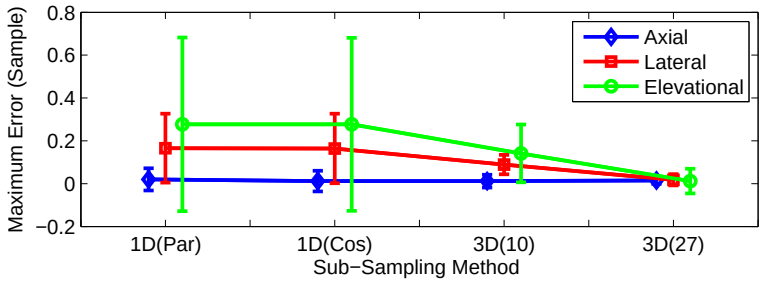

(d)

Figure 4.6: The maximum error of different 3D motion estimation techniques (axial, lateral, and elevational) over the $5 \times 5 \times 5$ simulated motion grid (window size is 104 samples axially, 7 samples laterally, and 5 samples elevationally $\approx 2 \times 2 \times 1\, mm^3$). For better comparison, the results are shown both in separate figures (a)-(c) and together (d).

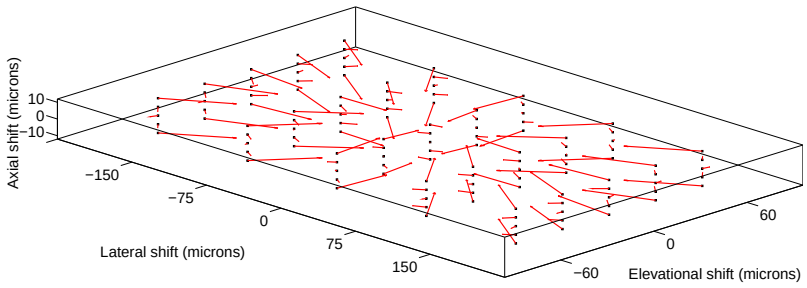

(a) Bias of 1D Parabola Fit

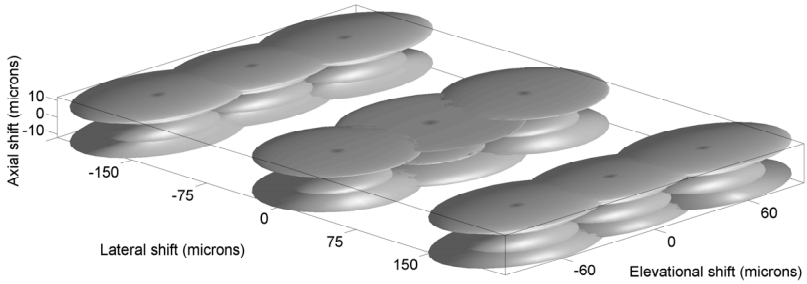

(b) STD of 1D Parabola Fit

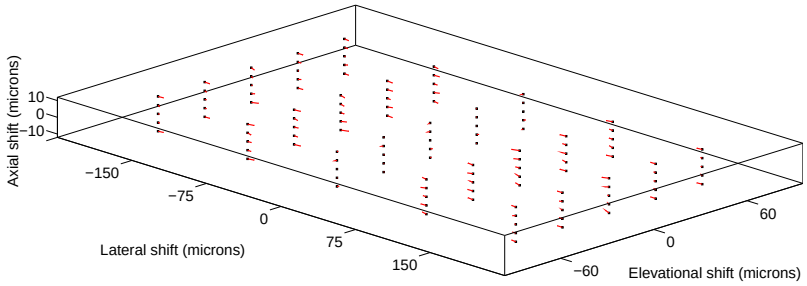

(c) Bias of 3D $f_{27}(x, y, z)$ Fit

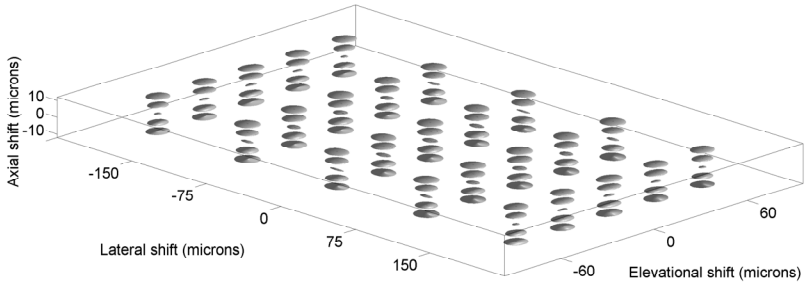

(d) STD of 3D $f_{27}(x, y, z)$ Fit

Figure 4.7: The biases and the standard deviations of the 1D parabola fit (a),(b) and 3D polynomial fit (c),(d) on a $5 \times 5 \times 5$ grid shown at the actual scale. For better visualization of the standard deviation of the independent 1D method, ellipsoids in every other plane in the lateral and elevational directions are eliminated prior to display. For the 3D method, all the ellipsoids are shown since they were small.

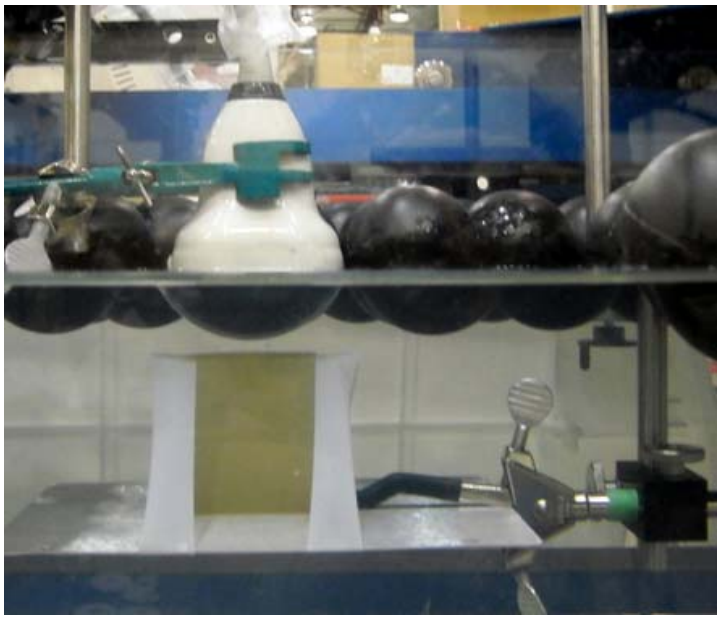

(a) Experimental Setup

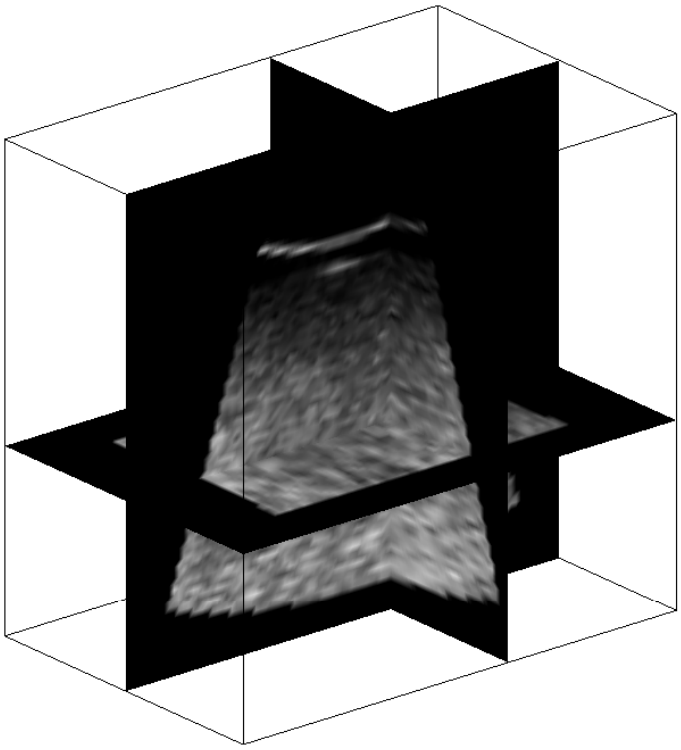

(b) Sonogram

Figure 4.8: The experimental setup (a) showing the positioning of the transducer with respect to the phantom on the 3-axis motion stage inside the water tank. A sample sonogram (b) acquired from ultrasound machine is also shown.

(a) First experimental Setup

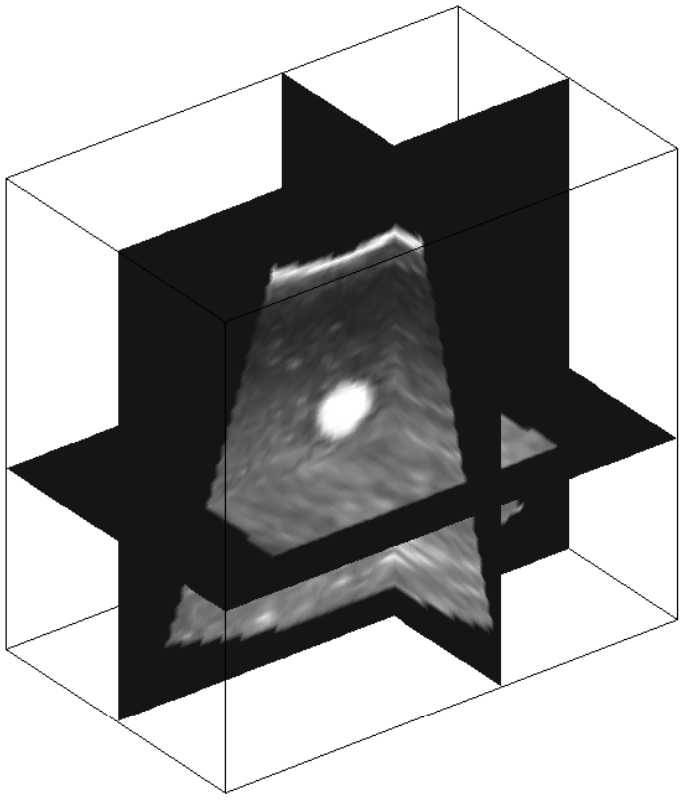

(b) Sonogram

Figure 4.9: The experimental setup (a) showing the positioning of the transducer with respect to the phantom and a sample sonogram (b) acquired using ultrasound machine.

4.4.2 Motion Estimation

In this work, instead of a 1D/2D linear array transducer, a motor-driven curved linear array transducers is used to acquire the echo volumes. In one approach the acquired echo volumes can be interpolated into Cartesian coordinates prior to the motion estimation process. The motion can then be estimated from these interpolated echo volumes. Although this approach will simplify the motion estimation, it requires all the echo volumes to be interpolated into Cartesian coordinate which is computationally intensive. In another approach the motion can be estimated in the transducers coordinates using acquired raw RF volumes. Once motions are estimated, the estimated motion vectors in the transducer's coordinate can be transformed into Cartesian coordinates. To avoid interpolation of the echo volumes, the second approach is used in this work.

The displacements between the sequences of RF volumes were estimated using the normalized cross correlation as a pattern matching function. The Time Domain cross correlation with Prior Estimates (TDPE) [48] was used to find the motion within sampling accuracy in the RF volume. The window size was set to be $2 \times 2 \times 1\,mm^3$ (i.e. 104 samples axially, 7 samples laterally, and 5 samples elevationally) with approximately 50% window overlap in the axial direction. The size of search area for the pattern matching function was set to be approximately $3 \times 3 \times 2\,mm^3$ (i.e. 156 samples axially, 9 samples laterally, and 7 samples elevationally). Once the coarse motion is estimated within the sampling accuracy, the 3D polynomial fitting with 27 coefficients which outperformed all the other methods was used to find the sub-sample components of the motion in all three directions for each window.

4.4.3 Conversion to Units of Distance

1D/2D linear array transducers have fixed sample spacing in all directions. As a result, the displacements estimated in units of samples in each direction are converted to units of distance by multiplying the results with a constant scaling factor (i.e. the sample spacing in the same direction). However, in curved linear array transducers, the sample spacing in the direction of curvature increases with depth. This is shown in Fig. 4.10. Thus, the conversion factors to units of distance need to be increased with depth. The 3D motor-driven curved linear transducer which is used in this study is curved in both the lateral and elevational directions with different curvatures (i.e. $r_e \neq r_l$). Therefore the conversion factors in these two directions need to be increased with depth independently. In this paper, the estimated displacements in units of samples are converted to units of distance using the following equations:

$$\begin{bmatrix} D'_a \\ D'_l \\ D'_e \end{bmatrix} = \begin{bmatrix} s_a(p) & 0 & 0 \\ 0 & s_l(p) & 0 \\ 0 & 0 & s_e(p) \end{bmatrix} \begin{bmatrix} D_a \\ D_l \\ D_e \end{bmatrix} \tag{4.8}$$

where $D_a = d_a + \delta_a$, $D_l = d_l + \delta_l$, and $D_e = d_e + \delta_e$ are estimated axial, lateral, and elevational components of the motion in units of samples at depth p, $s_a(p) = s_a(0)$, $s_l(p) \approx s_l(0)(r_l + p)/r_l$, and $s_e(p) \approx s_e(0)(r_e + p)/r_e$ are the transducer's axial, lateral, and elevational sample spacing at depth p, respectively, $s_a(0) = 19.3\,\mu$m, $s_l(0) = 430\,\mu$m, and $s_e(0) = 175\,\mu$m are the sample spacing at transducer's surface, $r_l = 39.8$ mm and $r_e = 27.5$ mm are the radii of the transducer in the lateral and the elevational directions, and D'_a, D'_l, and D'_e are the estimated components of the motion in units of distance at depth p in transducer's coordinate.

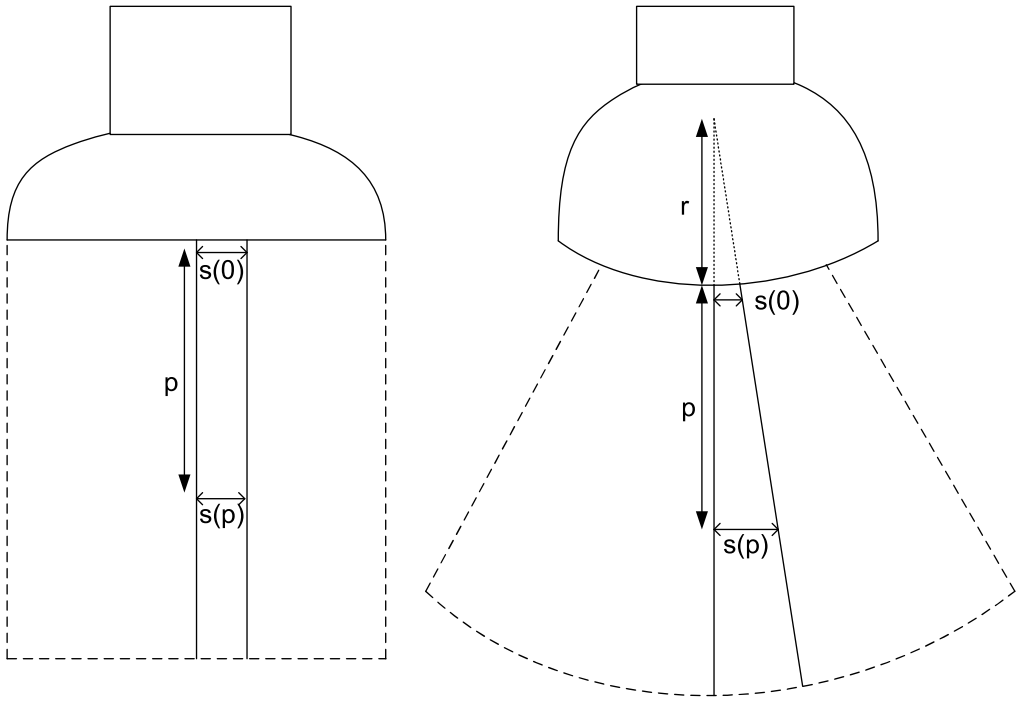

Figure 4.10: Variation of the spacing between lines as a function of depth is shown when a curved array transducer is used to acquire the echo lines. This happens in the lateral and elevational directions due to the curvature of the array ($s(0)$ is the spacing between lines on the transducer surface and $s(p)$ is the spacing between lines at a depth p).

4.4.4 Coordinate Transformation

Once motion vectors are estimated in the transducers coordinate and converted to units of distance, it is necessary to transform the coordinates to Cartesian coordinates. For the 3D motor-driven transducer with different curvatures in lateral and elevational directions that is used in this study, this coordinate transformation consists of two rotations. This is shown in Fig. 4.11. In order to compensate for these, the same rotations need to be applied to the estimated motion vectors in the opposite directions. One rotation is required about the transducer's elevational direction to correct for the curvature in each frame. This rotation will correct for the curvature of the transducer and will transform the estimation in the lateral direction to the true lateral component in Cartesian coordinates. The second rotation is required about the actual lateral direction to correct for the axial and elevational components which will transform them to the Cartesian coordinates. This rotation will correct for the sweeping angle. This transformation can be formulated as follow:

$$\begin{bmatrix} D''_a \\ D''_l \\ D''_e \end{bmatrix} = \begin{bmatrix} cos(\phi) & 0 & sin(\phi) \\ 0 & 1 & 0 \\ -sin(\phi) & 0 & cos(\phi) \end{bmatrix} \begin{bmatrix} cos(\theta) & -sin(\theta) & 0 \\ sin(\theta) & cos(\theta) & 0 \\ 0 & 0 & 1 \end{bmatrix} \begin{bmatrix} D'_a \\ D'_l \\ D'_e \end{bmatrix}, \tag{4.9}$$

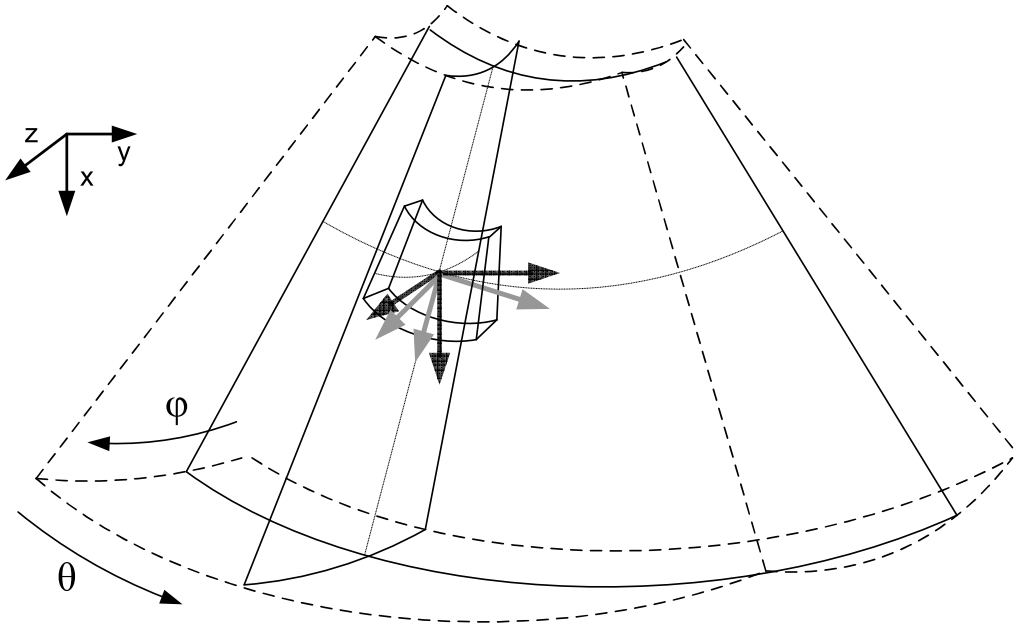

(a) Transducer Coordinate and Cartesian Coordinates

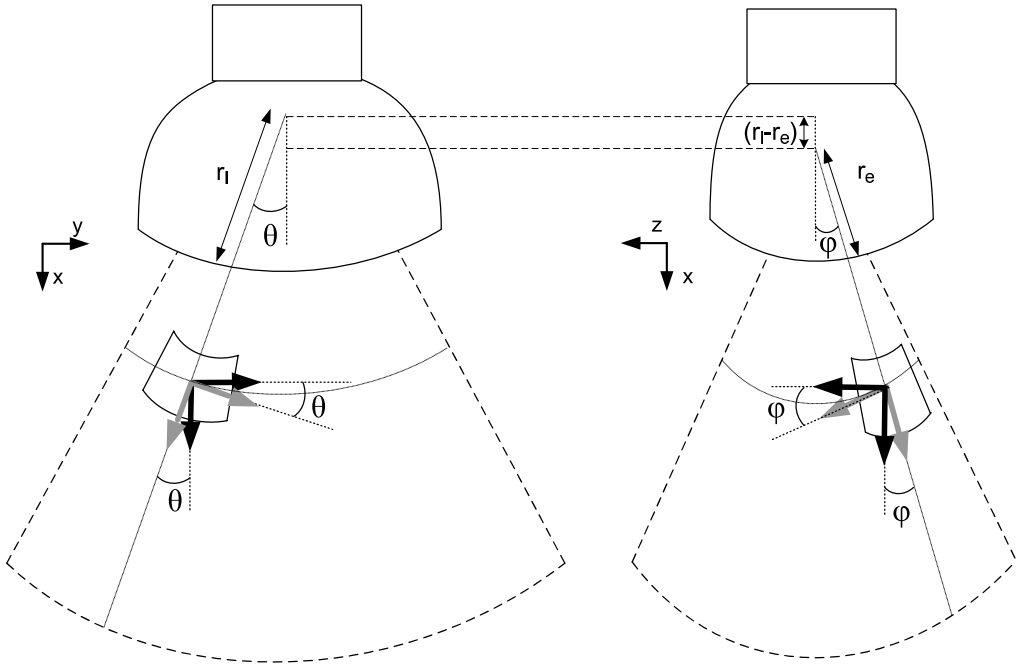

(b) Front View (left) and Side View (right)

Figure 4.11: The transducer's coordinate frame and Cartesian coordinates are shown (a). The coordinate transformation consists of two rotations coming from the curvature of the transducer in both lateral and elevational directions (b).

where D'_a, D'_l, and D'_e are the components of the motion in units of distance in transducer coordinates, θ, ϕ are the rotation angles around elevational and lateral axes, respectively, and D''_a, D''_l, and D''_e are the components of the motion in units of distance in Cartesian coordinates. The rotation angles (i.e. θ, ϕ) are calculated based on the location of the reference window, which is used as the pattern in the matching algorithm, in the 3D volume.

4.4.5 Experimental Results

The estimated axial, lateral, and elevational components of the displacement in Cartesian coordinates, that result from the translation of the phantom in the water tank, are shown in Fig. 4.12. The results show that the 3D method accurately measures all three components of the motion. The maximum tracking error of the 3D method was measured to be 10 μm in all three axes which is the same as the resolution of our experimental setup (i.e. approximately 10 μm).

The estimated axial, lateral, and elevational components of the displacements that resulted from the axial compression of a breast phantom, were scan converted and shown in Fig. 4.13. A multi-planar view was used to visualize the results in 3D. The bright echo in the sonogram (Fig. 4.9(b)) is clearly visible as a hard inclusion in the displacement estimates. For comparison purposes, the results from the axial compression of a phantom with a hard inclusion computed using the finite element method (FEM) are also presented. Fig. 4.13 shows good agreement between the simulated and experimental results.

4.5 Discussions and Conclusion

In this work, we studied several pattern-matching function interpolation schemes that are suited for precise and accurate estimation of motion in 3D. The performance of all the interpolation methods has been characterized through both simulations and experiments. The results show that the 3D interpolation methods significantly outperform common independent 1D interpolation algorithms in terms of bias and standard deviation.

In the simulation, the line spacing was intentionally set to be large in order to match our experimental setup. However, this spacing is much larger than the typical line spacing in state of the art ultrasound imaging systems. We expect both the bias and the standard deviation of all the estimators to improve with better lateral resolution.

As shown in Section 4.2, the interpolation to estimate the sub-sample motion assumes a fix sample spacing in each direction. However, in our experiments section the discrete pattern matching function is evaluated in the transducer's coordinates where the sample spacing varies as a function of depth. Even though we considered this fact during the conversion to units of distance, we ignored it in the interpolation step and assumed equal sample spacing during the interpolation. We believe this is a good assumption since the sample spacing in the axial direction is three orders of magnitude smaller, compared to the position of the pattern matching window with respect to the center of rotation (20 μm *vs* 40 mm). This will result in maximum spacing variation of 0.0005 of a sample in both the lateral and elevational directions which is much smaller than the bias and standard deviation of the 3D interpolation techniques. Alternatively, instead of assuming fixed sample spacing, the 3D polynomial can be fitted to the matching coefficients with corrected sample spacing at each depth. Once the polynomial

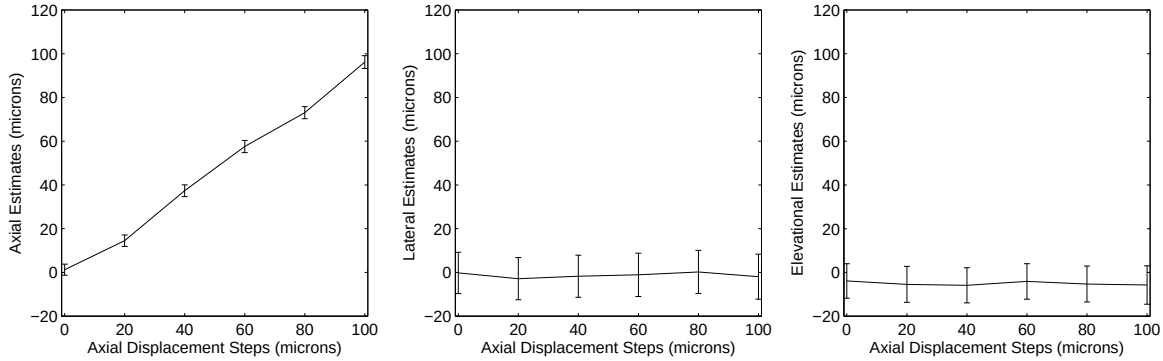

(a) Axial Translation

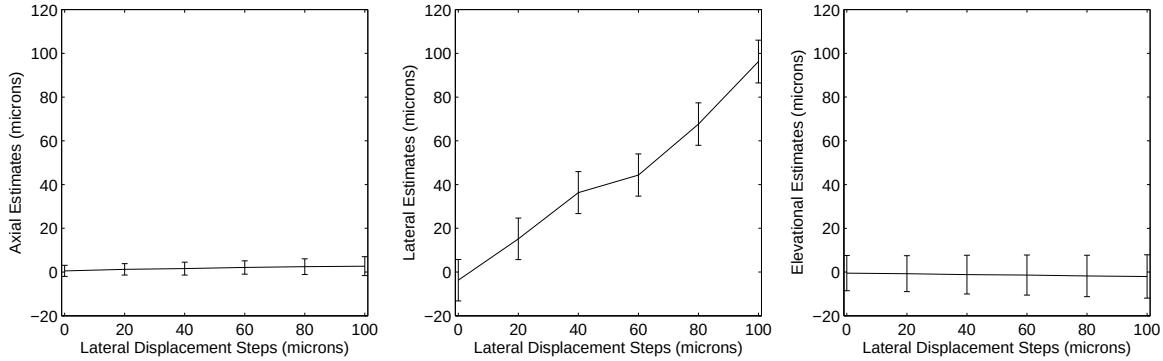

(b) Lateral Translation

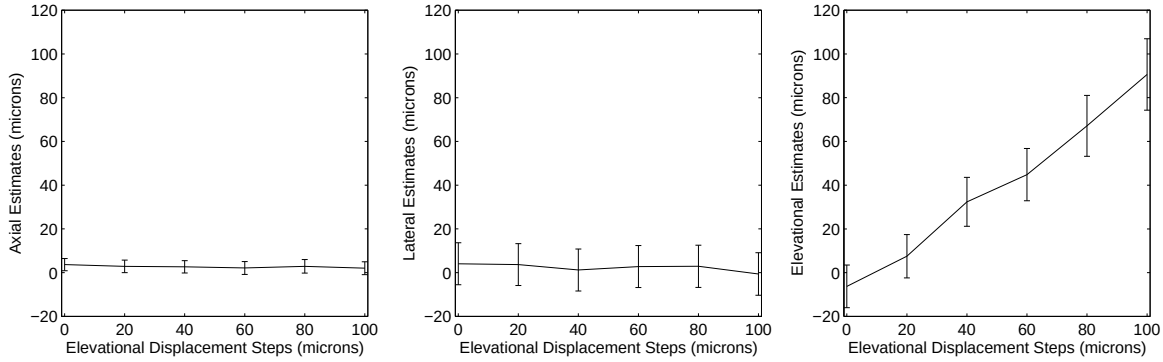

(c) Elevational Translation

Figure 4.12: The estimated axial (1st column), lateral (2nd column), and elevational (3rd column) components of the motion resulted from axial (1st row), lateral (2nd row), and elevational (3rd row) translations of the phantom in the water tank.

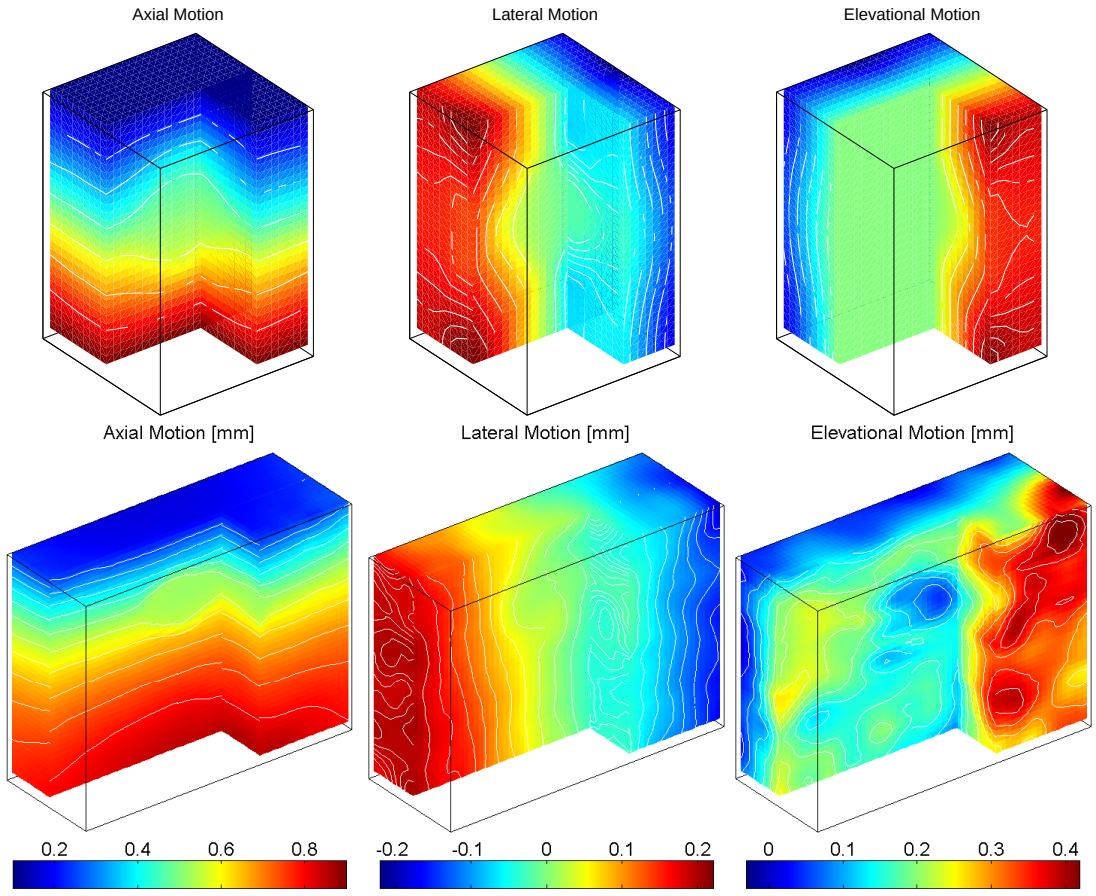

Figure 4.13: Simulated (top) axial, lateral, and elevational component of the displacement, resulted from axial compression of a phantom with a hard inclusion and the experimental results (bottom) on the breast phantom. Multi-planar view is used to visualize the results in 3D. Equal cost contours on the surfaces are also used to show the direction of the displacement.

is fitted, the same root estimation techniques can be applied to find the sub-sample motions.

The performance of all the pattern matching function interpolation techniques, including those presented in this work, rely on the matching coefficients and is expected to degrade when the echo signals are decorrelated and can not be matched correctly. Highly correlated signals are generally the case in ultrafast imaging for dynamic elastography [7] and real-time elastography [48], where displacements and deformations between frames are small. However, this is not the case in quasi-static elastography [49,50] and myocardial elastography [11] where the tissue experiences large internal motions and deformations. In order to adapt all these methods to the estimation of displacements resulting from large deformations, previously introduced compounding methods should be applied to the raw echo signals [51–53] prior to the motion estimation process. Once the effect of signal decorrelation is suppressed, the pattern matching algorithms followed by the 3D interpolation methods can be applied to estimate the 3D motion with sub-sample accuracy.

In our previous work we have studied the performance of quadratic, cubic, and quartic 2D spline polynomials to estimate the sub-sample motion in two dimensions. We showed that, with a trade off of higher computational cost, increasing the order of polynomial improves both the accuracy and the precision of the sub-sample estimation. In this work we extended this study to 3D and compared the performance of 3D quadratic spline polynomials $f_{27}(x, y)$ to interpolate the pattern matching function. Similarly to our previous work, in addition to the above 3D methods studied in this work, 3D cubic and quartic splines with 64 ($f_{64}(x, y)$) and 125 coefficients ($f_{125}(x, y)$), respectively, can also be used to estimate the sub-sample motions in 3D with higher accuracy and precision. However, these polynomials are excluded from this study due to their computational overhead. This is due to the fact that, in addition to the polynomial fitting and root estimation process, these polynomials requires the pattern matching function to be evaluated at least for 125 lags for each window. This significant additional computational overhead diminishes the simplicity advantage of the pattern matching interpolation techniques. Moreover, we showed in our previous work that grid slope interpolation techniques [22, 38] performs as well as independent 1D interpolation techniques. Thus, they are not included in this study as a separate interpolation method.

The 3D sub-sample motion estimation methods studied in this work provide a good balance between accuracy, precision, and computational cost. These methods have several potential applications throughout the field of signal processing. Specific applications in medical ultrasound include fine 3D tissue motion tracking, motion vector estimation, velocity vector imaging, strain tensor estimation, and tissue elasticity estimation.

References

[1] C. Kasai, K. Namekawa, A. Koyano, and R. Omoto, "Real-time two-dimensional blood flow imaging using an autocorrelation technique." *IEEE Transactions on Sonics and Ultrasonics*, vol. 32, pp. 458–464, 1985.

[2] T. Loupas, R. Peterson, and R. Gill, "Experimental evaluation of velocity and power estimation forultrasound blood flow imaging, by means of a two-dimensional autocorrelation approach." *IEEE Transactions on Ultrasonics, Ferroelectrics and Frequency Control*, vol. 42, pp. 689–699, Jul 1995.

[3] H. Torp, K. Kristoffersen, and B. Angelsen, "Autocorrelation Techniques in Color Flow Imaging. Signal model and statistical properties of the Autocorrelation estimates." *IEEE Transactions on Ultrasonics, Ferroelectrics, and Frequency control*, vol. 41, pp. 604–612, 1994.

[4] J. Ophir, I. Cespedes, H. Ponnekanti, Y. Yazdi, and X. Li, "Elastography: a quantitative method for imaging the elasticity of biological tissues," *Ultrasonic Imaging*, vol. 13, pp. 111–134, April 1991.

[5] A. Heimdal, A. Stoylen, H. Torp, and T. Skjaerpe, "Real-time strain rate imaging of the left ventricle by ultrasound." *Journal of American Soc Echocardiography*, vol. 11, pp. 1013–1019, Nov 1998.

[6] L. Bohs, B. Friemel, and G. Trahey, "Experimental velocity profiles and volumetric flow via two-dimensional speckle tracking." *Ultrasound in Medicine and Biology*, vol. 21, pp. 885–98, 1995.

[7] J. Bercoff, M. Tanter, and M. Fink, "Supersonic shear imaging: a new technique for soft tissue elasticity mapping," *IEEE Transactions on Ultrasonics, Ferroelectrics and Frequency Control*, vol. 51, pp. 396–4009, April 2004.

[8] E. Turgay, S. Salcudean, and R. Rohling, "Identifying Mechanical properties of Tissue by Ultrasound." *Ultrasound in Medicine and Biology*, vol. 32, pp. 221–235, 2006.

[9] H. Eskandari, S. Salcudean, and R. Rohling, "Viscoelastic Parameter Estimation Based on Spectral Analysis." *IEEE Transactions on Ultrasonics, Ferroelectrics, and Frequency control*, vol. 55, pp. 1611–1625, July 2008.

[10] R. Righetti, J. Ophir, S. Srinivasan, and T. Krouskop, "The Feasibility of Using Elastography for Imaging the Poissons Ratio in Porous Media," *Ultrasound in Medicine and Biology*, vol. 30, pp. 215–228, 2004.

[11] W. Lee, C. M. Ingrassia, S. D. Fung-Kee-Fung, K. D. Costa, J. W. Holmes, and E. Konofagou, "Theoretical Quality Assessment of Myocardial Elastography with In Vivo Validation," *IEEE Transactions on Ultrasonics, Ferroelectrics and Frequency Control*, vol. 54, pp. 2233–2245, 2007.

[12] A. Thitaikumar, L. Mobbs, C. Kraemer-Chant, B. Garra, and J. Ophir, "Breast Tumor Classification using axial shear strain elastography: a feasibility study," *Physics in Medicine and Biology*, vol. 53, pp. 4809–4823, 2008.

[13] K. Nightingale, M. Palmeri, R. Nightingale, and G. Trahey, "On the feasibility of remote palpation using acoustic radiation force," *Journal of the Acoustical Society of America*, vol. 110, pp. 625–34, July 2001.

[14] W. Walker, F. Fernandez, and L. Negron, "A method of imaging viscoelastic parameters with acoustic radiation force." *Physics in Medicine and Biology*, vol. 45, pp. 1437–1447, 2000.

[15] M. Fatemi and J. Greenleaf, "Probing the dynamics of tissue at low frequencies with the radiation force of ultrasound," *Physics in Medicine and Biology*, vol. 45, pp. 1449–64, June 2000.

[16] P. Wells, "Ultrasonic colour flow imaging," *Physics in Medicine and Biology*, vol. 39, pp. 2113–2145, 1994.

[17] R. Gill, "Measurement of blood flow by ultrasound: accuracy and sources of error." *Ultrasound in Medicine and Biology*, vol. 11, pp. 625–641, Aug 1985.

[18] E. Konofagou and J. Ophir, "Precision Estimation and Imaging of Normal and Shear Components of the 3D Strain Tensor in elastography," *Physics in Medicine and Biology*, vol. 45, pp. 1553–1563, 2000.

[19] M. Greenleaf J., Fatemi and M. Insana, "Selected methods for imaging elastic properties of biological tissues." *Annual Review of Biomedical Engineering*, vol. 5, p. 5778, 2003.

[20] M. Lubinski, S. Emelianov, and M. O'Donnell, "Speckle tracking methods for ultrasonic elasticity imaging using short-time correlation," *IEEE Transactions on Ultrasonics, Ferroelectrics and Frequency Control*, vol. 46, pp. 82–96, January 1999.

[21] H. Shi and T. Varghese, "Two-dimensional multi-level strain estimation for discontinuous tissue." *Physics in Medicine and Biology*, vol. 52, pp. 389–401, Nov 2007.

[22] L. Geiman, BJ.and Bohs, M. Anderson, S. Breit, and T. G.E., "A novel interpolation strategy for estimating subsample speckle motion." *Physics in Medicine and Biology*, vol. 45, pp. 1541–1552, 2000.

[23] L. Bohs and G. Trahey, "A novel method for angle independent ultrasonic imaging of blood flow and tissue motion," *IEEE Transactions on Biomedical Engineering*, vol. 38, pp. 280–286, March 1991.

[24] G. Trahey, J. Allison, and O. Von Ramm, "Angle independent ultrasonic detection of blood flow," *IEEE Transactions on Biomedical Engineering*, vol. 34, pp. 965–7, December 1987.

[25] F. Viola and W. Walker, "A comparison of the performance of time-delay estimators in medical ultrasound." *IEEE Transactions on Ultrasonics, Ferroelectrics and Frequency Control*, vol. 50, pp. 392–401, April 2003.

[26] G. Jacovitti and G. Scarano, "Discrete time techniques for time delay estimation." *IEEE Transactions on Acoustics, Speech, and Signal Processing*, vol. 41, pp. 525–533, Feb 1993.

[27] T. Varghese and O. J., "Characterization of elastographic noise using the envelope of echo signals," *Ultrasound in Medicine and Biology*, vol. 24, pp. 543–555, 1998.

[28] F. Viola and W. Walker, "A Spline-Based Algorithm for Continuous Time-Delay Estimation Using Sampled Data." *IEEE Transactions on Ultrasonics, Ferroelectrics and Frequency Control*, vol. 52, pp. 80–93, January 2005.

[29] G. Pinton and G. Trahey, "Continuous Delay Estimation with Polynomial Splines." *IEEE Transactions on Ultrasonics, Ferroelectrics and Frequency Control*, vol. 53, pp. 2026–2035, 2006.

[30] E. Konofagou and J. Ophir, "A new elastographic method for estimation and imaging of lateral displacements, lateral strains, corrected axial strains and Poisson's ratios in tissues," *Ultrasound in Medicine and Biology*, vol. 24, pp. 1183–99, October 1998.

[31] F. Viola, R. Coe, O. K., D. Guenther, and W. Walker, "MUlti-Dimensional Spline-Based Estimator (MUSE) for Motion Estimation: Algorithm Development and Initial Results." *Annals of Biomedical Engineering*, vol. 36, pp. 1942–1960, September 2008.

[32] R. Zahiri-Azar and S. Salcudean, "Time-Delay Estimation in Ultrasound Echo Signals Using Individual Sample Tracking." *IEEE Transactions on Ultrasonics, Ferroelectrics and Frequency Control*, vol. 55, pp. 2640–2650, 2008.

[33] I. Cespedes, Y. Huang, J. Ophir, and S. Spratt, "Methods for the estimation of subsample time-delays of digitized echo signals," *Ultrasonic Imaging*, vol. 17, pp. 142–171, 1995.

[34] P. de Jong, T. Arts, A. Hoeks, and R. Reneman, "Determination of Tissue Motion Velocity by Correlation Interpolation of Pulsed Ultrasonic Echo Signals," *Ultrasonics Imaging*, vol. 12, pp. 84–98, 1990.

[35] B. Geiman, L. Bohs, M. Anderson, S. Breit, and G. Trahey, "A comparison of algorithms for tracking sub-pixel speckle motion." in *Proceedings of the IEEE Ultrasonics Symposium.* Volume 2: IEEE, 5-8 Oct 1997, pp. 1239–1242.

[36] S. Foster, P. Embree, and W. O'Brien, "Flow velocity profile via time-domain correlation: error analysis and computer simulation," *IEEE Transactions on Ultrasonics, Ferroelectrics and Frequency Control*, vol. 37, pp. 164–175, May 1990.

[37] F. Viola and W. Walker, "Computationally Efficient Spline-Based Time Delay Estimation." *IEEE Transactions on Ultrasonics, Ferroelectrics and Frequency Control*, vol. 55, pp. 2084–2091, September 2008.

[38] L. Bohs, B. Geiman, M. Anderson, S. Breit, and G. Trahey, "Ensemble Tracking for 2D Vector Velocity Measurement: Experimental and Initial Clinical Results." *IEEE Transactions on Ultrasonics, Ferroelectrics and Frequency Control*, vol. 45, pp. 912–924, July 1998.

[39] Y. Mofid, S. Gahagnon, F. Patat, F. Ossant, and G. Josse, "In vivo high frequency elastography for mechanical behavior of human skin under suction stress: elastograms and kinetics of shear, axial and lateral strain fields." in *Proceedings of the IEEE Ultrasonics Symposium*. Vancouver: IEEE, Oct 2006, pp. 1041–1044.

[40] R. Lopata, M. Nillesen, I. Gerrits, J. Thijssen, L. Kapusta, F. van de Vosse, and C. de Korte, " In Vivo 3D Cardiac and Skeletal Muscle Strain Estimation ," in *Proceedings of the IEEE Ultrasonics Symposium*. Vancouver: IEEE, Oct 2006, pp. 744–747.

[41] R. Lopata, M. Nillesena, H. Hansena, I. Gerritsa, T. J., and C. de Korte, "Performance Evaluation of Methods for Two-Dimensional Displacement and Strain Estimation Using Ultrasound Radio Frequency Data." *Ultrasound in medicine and biology*, vol. 35, pp. 796–812, 2009.

[42] R. Zahiri-Azar and S. Salcudean, "Real-Time Estimation of Lateral Displacement Using Time Domain Cross Correlation with Prior Estimates ," in *Proceedings of the IEEE Ultrasonics Symposium*. IEEE, Oct 2006, pp. 1209–1212.

[43] R. Zahiri-Azar, O. Goksel, T. Yao, E. Dehghan, J. Yan, and S. Salcudean, " Methods for the estimation of sub-sample motion of digitized ultrasound echo signals in two dimensions ," in *Proceedings of the IEEE Engineering in Medicine and Biology*. IEEE, Aug 2008, pp. 5581–5584.

[44] R. Lopata, M. Nillesen, I. Gerrits, J. Thijssen, L. Kapusta, and C. de Korte, " 4D Cardiac Strain Imaging: Methods and Initial Results ," in *Proceedings of the IEEE Ultrasonics Symposium*. IEEE, Oct 2007, pp. 872–875.

[45] G. Giunta, "Fine estimators of two-dimensional parameters and application to spatial shift estimation," *IEEE Transactions on Signal Processing*, vol. 47, pp. 3201–3207, 1999.

[46] J. A. Jensen, "A model for the propagation and scattering of ultrasound in tissue," *Journal of the Acoustical Society of America*, vol. 89, pp. 182–191, 1991.

[47] S. DiMaio and S. Salcudean, "Needle insertion modelling and simulation," *IEEE Transactions on Robotics and Automation: Special Issue on Medical Robotics*, vol. 19, pp. 864–875, 2003.

[48] R. Zahiri-Azar and S. Salcudean, "Motion Estimation in Ultrasound Images Using Time Domain Cross Correlation With Prior Estimates." *IEEE Transactions on Biomedical Engineering*, vol. 53, pp. 1990–2000, 2006.

[49] T. Varghese, J. Ophir, E. Konofagou, F. Kallel, and R. Righetti, "Tradeoffs In Elastographic Imaging, Ultrasonic Imaging," *Ultrasonic Imaging*, vol. 23, pp. 216–248, October 2001.

[50] J. Deprez, E. Brusseau, C. Schmitt, G. Cloutier, and O. Basset, "3D estimation of soft biological tissue deformation from radio-frequency ultrasound volume acquisitions." *Medical Image Analysis*, vol. 13, p. 116127, 2009.

[51] S. Alam, J. Ophir, and E. Konofagou, "An adaptive strain estimator for elastography," *IEEE Transactions on Ultrasonics, Ferroelectrics and Frequency Control*, vol. 45, pp. 461–72, March 1998.

[52] P. Chaturvedi, M. Insana, and T. Hall, "2D companding for noise reduction in strain imaging," *IEEE Transactions on Ultrasonics, Ferroelectrics and Frequency Control*, vol. 45, pp. 179–191, 1998.

[53] T. Varghese and J. Ophir, "Enhancement of echo-signal correlation in elastography using temporal stretching," *IEEE Transactions on Ultrasonics, Ferroelectrics and Frequency Control*, vol. 44, pp. 173–180, January 1997.

Chapter 5

Comparison Between Pattern Matching Techniques Employing 2D Sub-sample Estimation and 2D Tracking Using Angular Compounding[4]

5.1 Introduction

Motion estimation in sequences of ultrasound echo signals is essential for blood flow estimation [1, 2], tissue velocity estimation [3, 4], elasticity imaging [5–7], and acoustic radiation force imaging [8–10]. Since ultrasound imaging provides higher resolution in the direction of beam propagation, the estimation of this component of the motion has received the most attention in the literature. However, tracking the motion in one direction introduces some limitations for each of the above mentioned applications. For example, in blood flow and tissue velocity estimation, tracking along the beam propagation results in a poor estimation of the flow and tissue velocity due to the unknown angle between the velocity vector and the beam direction, even if the angle is manually adjusted [11,12]. In quasi-static elastography, tracking the motion in one direction results in estimation of only one component of the strain tensor, with all the other components remaining unknown [13]. In dynamic elastography using wave equations, the estimation of a single component of motion limits modulus estimation algorithms to partial inversion, rather than more accurate full inversion algorithm [14].

Several authors have proposed methods for measuring both axial and lateral motion components using ultrasound radio frequency (RF) eacho signals. Techniques based on 2D pattern matching functions are the most straight forward approaches in estimating the motion from sampled ultrasound echo signals [7, 15–18]. With these techniques, the reference ultrasound echo signal is divided into a number of windows, which may have overlap with each other. The reference echo signal within each window is set to be the *pattern* to be matched with the displaced echo signal over a predefined search region. The motion of the window is then found by finding the location of the best match. To reduce the estimation error introduced by finite sampling intervals, curve or polynomial fitting to the pattern matching function [19–22] have been suggested in the literature to estimate the sub-sample motion.

In another approach, angular compounding has also been attempted in the literature to

[4] A version of this chapter will be submitted for publication. Reza Zahiri-Azar and Septimiu E. Salcudean, "Comparison Between Pattern Matching Techniques Employing 2D Sub-sample Estimation and 2D Tracking Using Angular Compounding".

estimate the motion vectors [23–27]. With these techniques the data from the region of interest is acquired from multiple look angles. The multiple look angles can originate from a single transducer when it is moved mechanically, or they can originate from multiple transducers [23]. The multiple look angles can also originate from a single transducer using single transmit and multiple receive angles [26–28] or multiple electronically steered transmit and receive angles [24, 27, 29]. Once data from multiple angles are acquired, the motions estimated along multiple directions are compounded to construct the motion vectors inside the overlapping region.

We have previously presented 2D interpolation techniques that significantly improve the accuracy and the precision of 2D motion estimation using pattern matching techniques. In these techniques, iterative 1D polynomial fitting or 2D polynomial fitting are used to estimate the sub-sample component of the motion in both the axial and the lateral directions, as opposed to conventional 1D interpolation methods. In this paper, we study and compare the performance of 2D tracking methods using 2D sub-sample estimation techniques with that of conventional angular compounding when beam steering techniques are used to acquire the data from multiple look directions. The paper is structured as follows: Section 5.2 presents the motion tracking algorithms. Section 5.3 presents the simulation method and comparison between the methods using simulated data. Section 5.4 presents the experimental results. Finally, Section 5.5 presents a discussions and conclusion along with avenues for future research.

Throughout this paper, it is assumed that 2D echo radio frequency (RF) signals are available. Without loss of generality, it is assumed that the pattern matching function optimization involves maximization of the normalized cross correlation. The pattern matching function values will be referred to as the *matching coefficients*. Also the component of the motion along the beam propagation and transverse to the beam will be referred to as axial and lateral, respectively, in both steered and non-steered images.

5.2 Methods

Both of the above mentioned techniques rely on correlation techniques to track the displacements. The difference is that angular compounding uses only the component of the motion along the beam direction from multiple angles to reconstruct the motion vectors whereas pattern matching techniques measures the motion vector by tracking the motion both along and transverse to the beam from a single set of data. This is shown in Fig. 5.1.

In a general form, let $s_1^\theta[i,j]$, $s_2^\theta[i,j]$, $i = 0,...,n-1$, $j = 0,...,m-1$ be the sampled reference and displaced/delayed echo signals, respectively, where n is the number of discrete samples and m is the number of acquisition lines in the echo signals, and θ is the steering angle. When $\theta = 0$ we are referring to non-steered images. Let $R^\theta[u,v]$ be the discrete 2D pattern matching function between a windowed of the reference and the displaced echo signals acquired using the same angle (θ) over a predefined search region. Given $R^\theta[u,v]$, the coarse axial d_a^θ and lateral d_l^θ estimates of the motion in the axial (x^θ) and the lateral (y^θ) directions are achieved by locating the maximum of the $R^\theta[u,v]$ as follow

$$[d_a^\theta, d_l^\theta] = \arg\max_{u,v} R^\theta[u,v]. \tag{5.1}$$

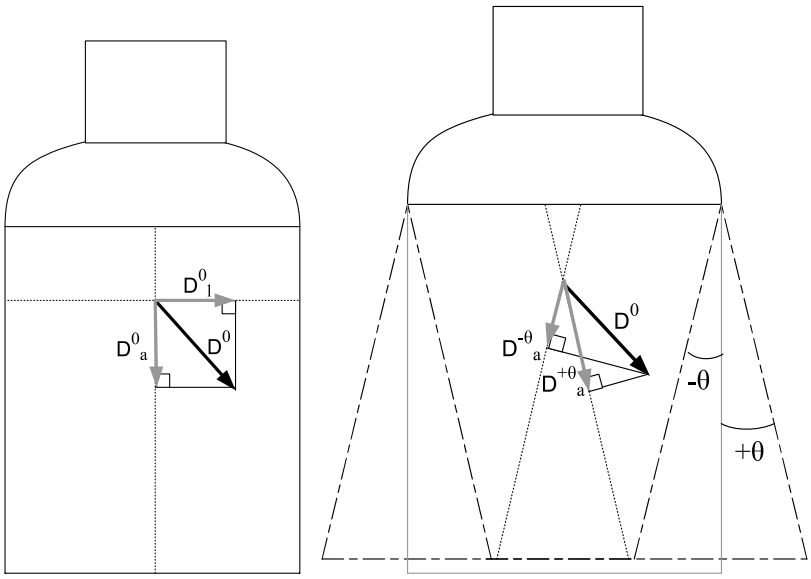

(a) 2D Pattern Matching (b) Beam Steering

Figure 5.1: Schematics for 2D motion tracking using pattern matching (a) and beam steering (b). In 2D pattern matching data are acquired from the region of interest with no steering and 2D displacements are estimated from the estimated axial and lateral components of the motion. In beam steering data from a region of interest are acquired with different steering angles. The 2D displacements in the overlapping region are reconstructed using 1D measurements from the employed steering angles.

5.2.1 Pattern Matching

Following the coarse estimation of the axial and the lateral components of the motion within the sampling accuracy according to (5.1) in non steered images (d_a^0, d_l^0), 2D interpolation techniques are used to find the sub-sample motions employing the matching coefficients in both directions (δ_a^0, δ_l^0). Subsequently, the total 2D displacement is estimated to be $D_a^0 = d_a^0 + \delta_a^0$, $D_l^0 = d_l^0 + \delta_l^0$.

For the purpose of this work, 2D polynomial fitting with nine coefficients (i.e. $f_9(x, y)$) and iterative 1D cosine fitting are used to estimate the sub-sample in both the axial and the lateral directions. Detailed descriptions of the 2D polynomial fitting and iterative 1D cosine fitting are provided in our previous work. These techniques will be referred to as PMP (i.e. pattern matching with 2D polynomial interpolation) and PMC (i.e. pattern matching with iterative 1D Cosine interpolation).

5.2.2 Angular Compounding

Since we are only interested in estimating the component of the motion along the beam direction (x^θ), for each steering angle, following the coarse estimation of the axial component of the motion within the sampling accuracy (d_a^θ) using (5.1), previously introduced 1D interpolation techniques are used to find the sub-sample motion employing the matching coefficients in that same direction (δ_a^θ). Subsequently, the total displacement along the beam is estimated to be

$D_a^\theta = d_a^\theta + \delta_a^\theta$.

The process mentioned above is repeated for two steering angles (i.e. $\pm\theta$ in this work). Once displacements in the direction of beam propagations are estimated (i.e. D_a^θ, $D_a^{-\theta}$), the true axial and the lateral components of the motion is computed according to the following equation at each spatial location [27]:

$$D_a^0 = \frac{D_a^\theta + D_a^{-\theta}}{2\cos\theta}, \tag{5.2}$$

$$D_l^0 = \frac{D_a^\theta - D_a^{-\theta}}{2\sin\theta}. \tag{5.3}$$

In order to have a fair comparison, the common 1D cosine fit [20] and 1D parabola fit [22] are used to estimate the sub-sample motion along the beam (i.e. 2-1D interpolation *vs* 2D interpolation). These technique will be referred to as BSC (i.e. beam steering with 1D cosine interpolation) and BSP (i.e. beam steering with 1D Parabola interpolation).

5.3 Simulations

5.3.1 Simulation Setup

Computer simulations were performed to study the performance of all methods in terms of their accuracy and precision. All calculations were performed in MATLAB (MathWorks Inc., Natick, MA). Similarly to our previous work, a $50\times60\times10\,mm^3$ virtual phantom was simulated by randomly allocating scatterers, with random scattering amplitudes.

Field II [30, 31] was used to simulate the ultrasound radio frequency echo signals (RF frames) and envelope signals from these scatterers. To be consistent with our experimental setup, a linear probe was modeled with 5 MHz center frequency and 40 MHz sampling rate. A linear scan of the phantom was carried out with a 128 element transducer, using 64 active elements. A single transmit focus was placed at 30 mm, and dynamic receive focusing was employed to generate the RF lines. 128 RF lines were simulated along a width of 38 mm resulting in line spacing of 300 μm. In order to simulate translations in both directions, the scatters were displaced on a grid with sub-sample distances in the axial and lateral directions (i.e. smaller than the actual RF sample-spacing in that corresponding axis). For all the displacements, a step size of 1/10 of the sample spacing in the corresponding non-steered axis was chosen (i.e. 2 μm axially and 30 μm laterally) forming a grid of $11 \times 11 = 121$ distinct displacement configurations. The number of scatterers per smallest sampling volume was set to be 10 to ensure that the speckle of the ultrasound images is fully developed.

For each displacement configuration RF frames corresponding to non-steered and 14 different steering angles including 7 pairs of angles (i.e. $\theta = \pm5, \pm7.5, \pm10, ... \pm 20$) were simulated. Sample sonograms generated from one of these simulated RF data sets employing different steering angles are shown in Fig 5.2. For comparison purpose, the point spread functions corresponding to all the steering angles are also depicted in Fig. 5.3.

The simulated non-steered RF frames (i.e. 121 frames) were used to estimate the motion using 2D pattern matching methods (i.e. PMC and PMP) and the pairs of simulated steered RF frames (i.e. $14\times121 = 1694$ frames) were used to estimate the motion using beam steering methods (i.e. BSP and BSC). For all the estimations, the RF frame corresponding to the

center of the 2D motion grid was set to be the reference. This resulted in a grid spanning ±0.5 of a sample in both non-steered axes.

The region of interest for motion estimation was centered around the transmit focus and data from both near-field and far-field were removed from the study. Furthermore, since in beam steering techniques only the data in the overlapping beams can be reconstructed, only these regions were used for the study. The default window size for the pattern matching function was set to be approximately $2 \times 2\,mm^2$ (i.e. 104 samples axially and 7 samples laterally). This resulted in more than 1000 displacement estimations from different speckle patterns for each displacement configuration on a grid. It should be noted that large steps in lateral direction would introduce large motions along the direction of beam when steering is employed. To estimate these motions correctly, the size of the search area for the pattern matching function was set to be approximately $3 \times 3\,mm^2$ (i.e. 156 samples axially and 11 samples laterally). In order to have accurate estimation of the cross correlation at the edges of the search region, the actual data from the echo signals were used instead of zero-padding.

The performances of all the estimators are studied in terms of their bias and standard deviation as a function of the sub-sample shift in the axial and lateral directions [32, 33] in order to study both their accuracy and precision.

Simulation of each RF frame would take more than 100 hours using Field II on a single core computer. Four multi-core processor computers were used in parallel to simulate the RF frames for this study.

5.3.2 Simulation Results

Figure 5.4 shows bias and standard deviation of both 2D pattern matching method employing iterative 1D cosine fit (PMC) and 2D compounding employing 1D cosine fit (BSC) using different angles as a function of sub-sample shift on a 11×11 grid. Figure 5.5 shows the same results for both 2D pattern matching method employing 2D polynomial fit (PMP) and 2D compounding employing 1D parabola fit (BSP). Similarly to our previous work, for better visualization of the accuracy, the axial and the lateral bias for each sub-sample shift on the grid are shown with a vector. Error vectors connecting the true displacements to the mean estimated displacements illustrate the directional bias for each of the 121 simulations. In order to show the precision in both directions, an ellipse representation is also used to show the standard deviations for each of the simulations. The ellipses are centered on the mean displacement estimations and the radius of each ellipse in each direction corresponds to the standard deviation of motion estimation in that given direction (confidence interval of 0.95).

The results show that the performance of 2D tracking using the beam steering method is a function of the employed steering angles. Figs 5.4 and 5.5 show that small steering angles do not provide enough information to accurately track the motion in lateral direction. Also the accuracy of the tracking degrades when large steering angles are employed to acquire the echo signals.

Figs 5.4 and 5.5 show that 2D tracking using beam steering introduces less bias compared to the 2D pattern matching techniques. The results also show that 2D tracking using beam steering experiences larger standard deviations when the lateral component of the motion is large. This is consistent with our previous results reported for non-steered images where we showed that the performance of sub-sample estimation using 1D interpolation degrades in the presence of 2D motion.

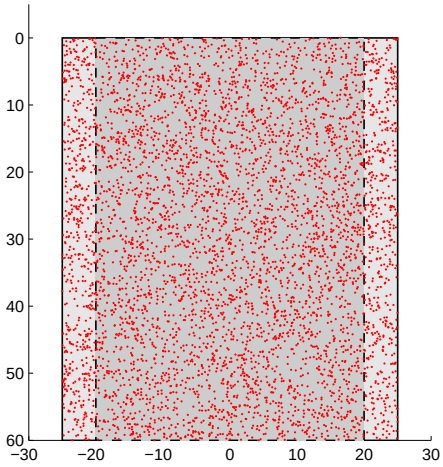

(a) Scatterers

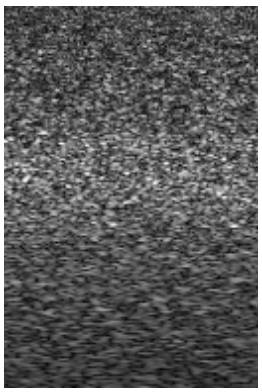

(b) Sonogram ($\theta = 0$)

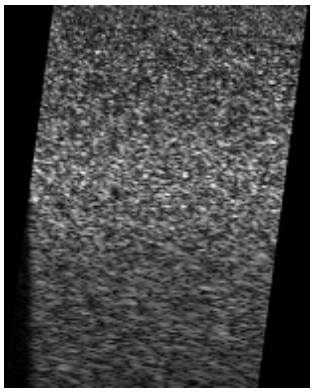

(c) Sonogram ($\theta = -10$)

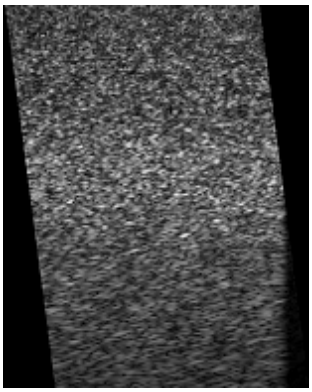

(d) Sonogram ($\theta = 10$)

Figure 5.2: Scatterer distributions (a) (only a small fraction of all scatterers are plotted for better visualization) and a Field II simulated sonograms when different steering angles are employed to acquire the data (b)-(d).

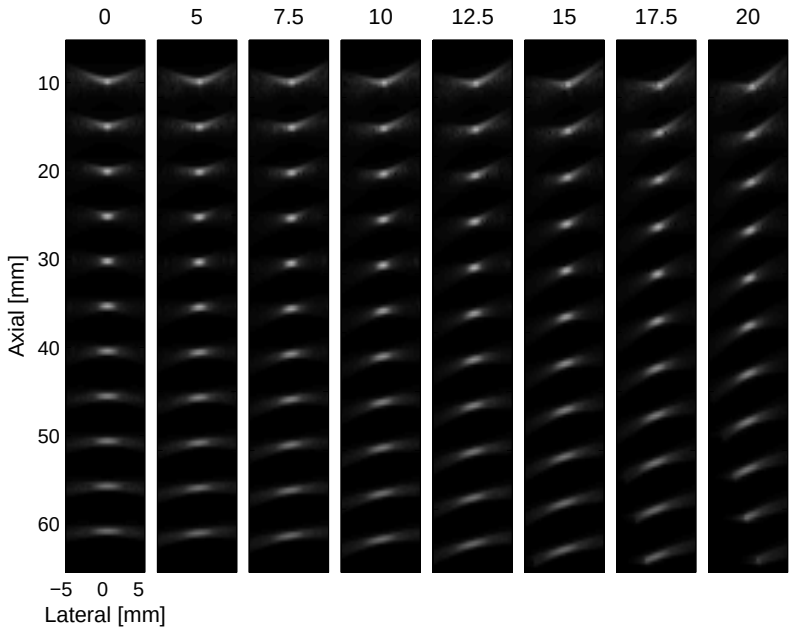

Figure 5.3: Point target phantom imaged for different steering angles. The point spread functions images are generated by placing multiple points at multiple depths in front of the transducer and then sweeping the beam over the points.

To simplify the comparison between the results, the overall performance of beam steering techniques (i.e. BSC and BSP) are shown in Fig 5.6 when different steering angles are employed to acquire the signals. The overall performance is calculated by averaging the absolute biases and standard deviation over the entire 2D motion grid. It should be noted that this is different from our previous work where we looked at maximum biases and standard deviations. Fig 5.6 shows that employing both very small and very large steering angles degrades the performance of the 2D compound tracking methods. Among different steering angles studied in this work, 10-12.5 degree steering angles, provide the most accurate results. Fig 5.6 also shows that for all the steering angles employed in 2D compound tracking, 1D cosine fit outperforms 1D parabola fit. This is consistent with previously published results for non-steered images where it was shown that the cosine fit has smaller bias and standard deviations compared to parabola fit in estimating the motion along the direction of beam propagation [19, 32].

In order to study the results quantitatively, the overall performance of all the methods are summarized in Tables 5.1 and 5.2 (mean absolute biases and standard deviations over the 2D motion grid). Tables 5.1 shows that the mean absolute axial and lateral biases of the 2D pattern matching techniques are 0.0076 and 0.0126 of a sample, for 2D polynomial interpolation (PMP), which corresponds to 146 nm and 3.95 μm at simulated 19.3 μm axial sample spacing and 300 μm lateral line spacing. The mean axial and lateral standard deviations of the same technique are found to be 0.0123 and 0.0273 of a sample, corresponding to 236 nm and 8.6 μm, respectively. For the same data, the mean absolute axial and lateral biases of the 2D pattern matching techniques are found to be 0.0023 and 0.0082 of a sample, for iterative 1D cosine interpolation (PMC), corresponding to 43 nm and 2.58 μm, respectively. The mean axial and lateral standard deviations of the same technique are found to be 0.0117 and 0.0253 of a sample,

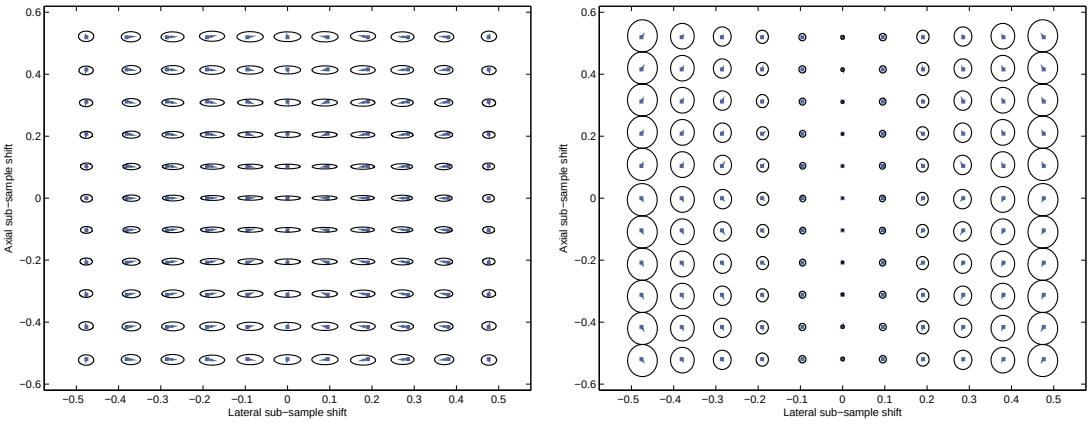

(a) PMC (b) BSC (±5)

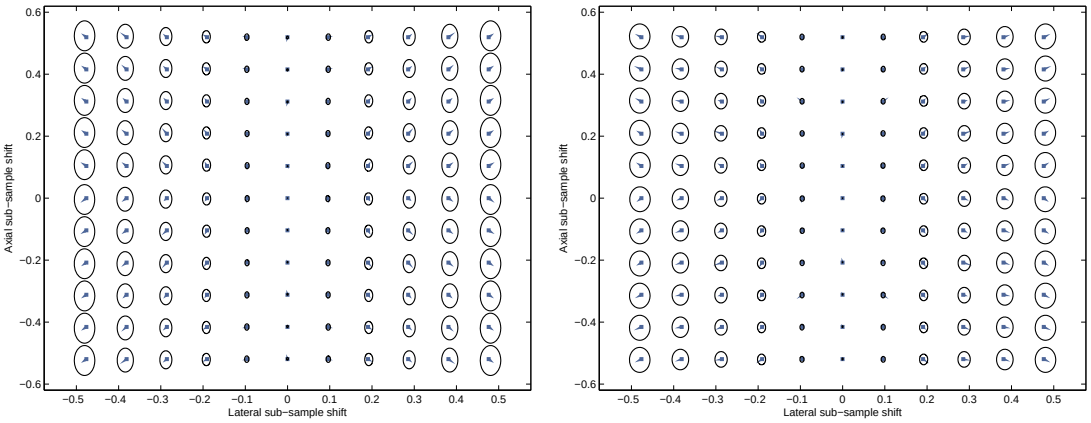

(c) BSC (±7.5) (d) BSC (±10)

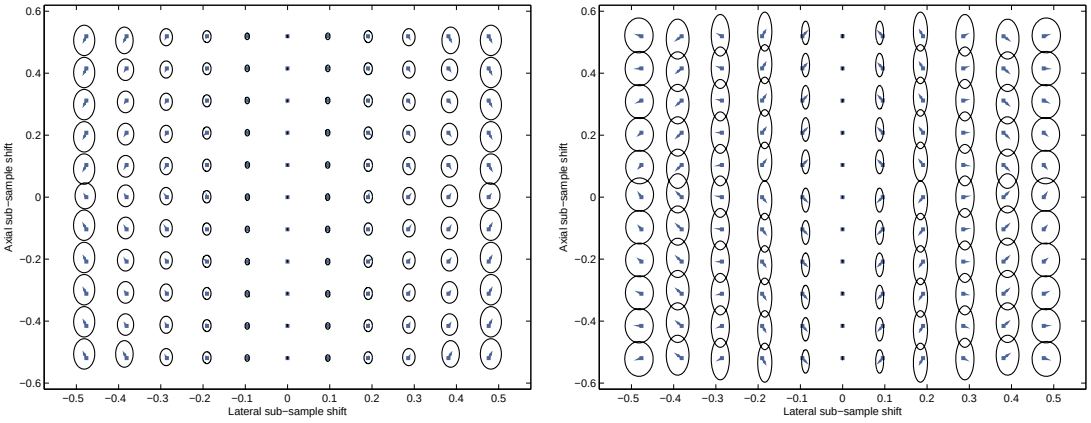

(e) BSC (±12.5) (f) BSC (±20)

Figure 5.4: Biases and standard deviations of the pattern matching method (a) and beam steering employing different angles (b)-(f) as a function of sub-sample shift on a 11×11 grid when iterative 1D cosine fit (a) and conventional 1D cosine fit (b)-(f) are employed to estimate the sub-sample motion. Field II was used to simulate the echo signals. A total of 1000 realizations were used to generate each bias vector and standard deviation ellipse (window size is $\approx$ 2mm$\times$2mm).

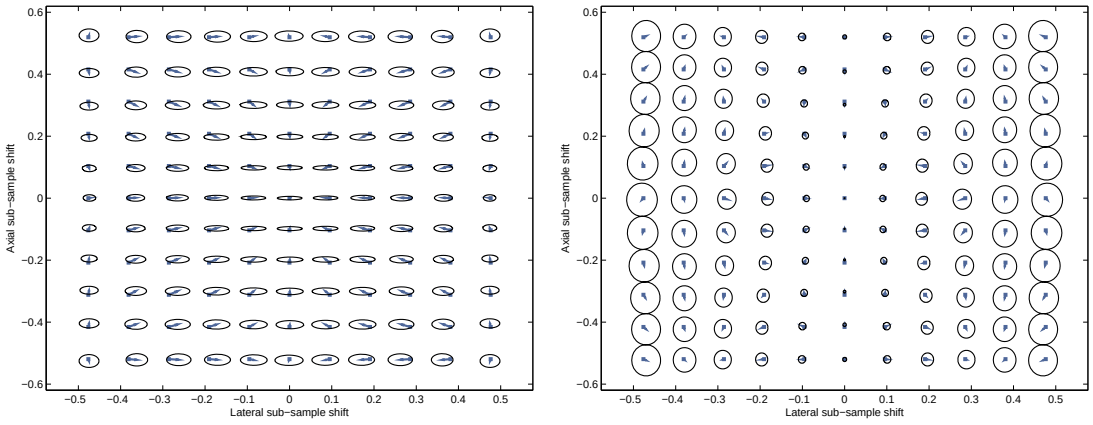

(a) PMP

(b) BSP (±5)

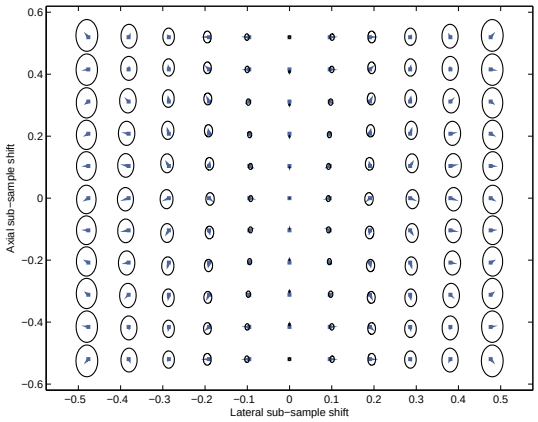

(c) BSP (±7.5)

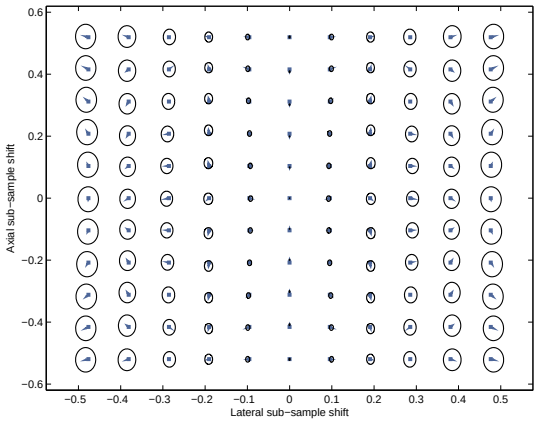

(d) BSP (±10)

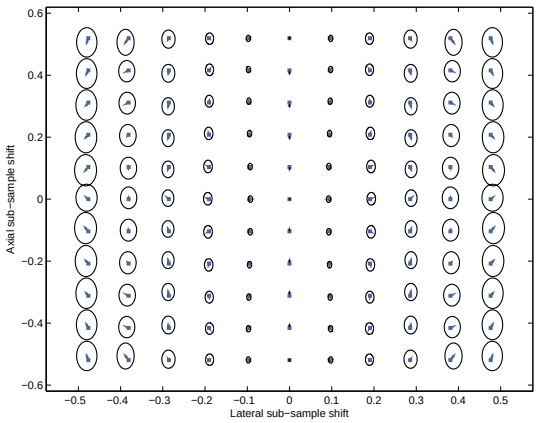

(e) BSP (±12.5)

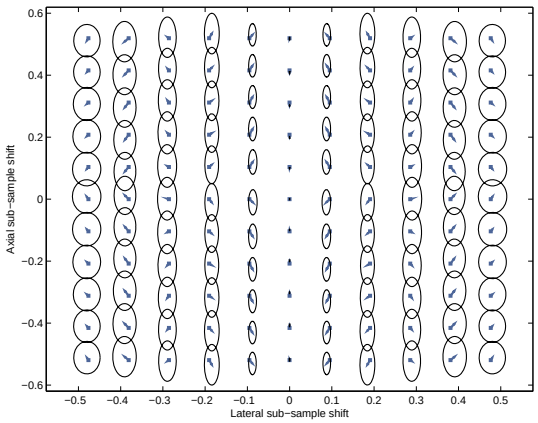

(f) BSP (±20)

Figure 5.5: Biases and standard deviations of the pattern matching method (a) and beam steering employing different angles (b)-(f) as a function of sub-sample shift on a 11×11 grid when 2D polynomial fitting (a) and conventional 1D parabola fitting (b)-(f) are employed to estimate the sub-sample motion. Field II was used to simulate the echo signals. A total of 1000 realizations were used to generate each bias vector and standard deviation ellipse (window size is $\approx$ 2mm$\times$2mm).

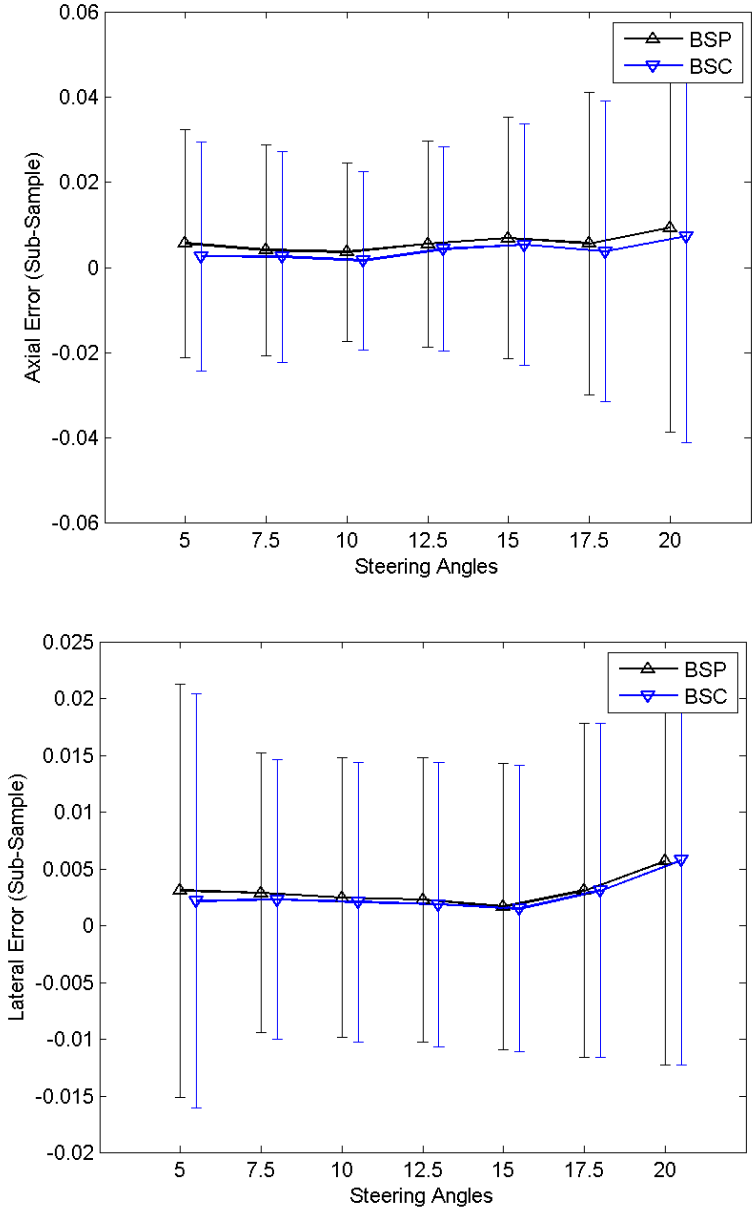

Figure 5.6: The overall performance of all beam steering methods averaged over the simulated motion grid. The error bars are used to show both mean absolute bias and their corresponding mean standard deviation in both axial (left) and lateral (right) directions.

corresponding to 225 nm and 7.97 μm, respectively.

Table 5.2 shows that for the same 2D motion grid, the axial and lateral biases of the 2D tracking using compound techniques are smaller than those of 2D pattern matching techniques. The mean absolute axial and lateral biases of the 2D tracking using beam steering are found to be 0.0036 and 0.0025 of a sample, for 1D parabola interpolation (BSP) for $\pm$10 degree steering angle, which corresponds to 69nm and 793 nm, respectively. The mean absolute axial and lateral biases of the 2D tracking using beam steering are found to be 0.0016 and 0.0021 of a sample, for 1D cosine interpolation (BSC) for $\pm$10 degree steering angle, which corresponds to 30 nm and 650 nm, respectively. For the same data set, the mean axial and lateral standard deviations of the 2D tracking using beam steering are found to be 0.0210 and 0.0123 of a sample, for both 1D parabola and cosine interpolation (BSP, BPC), corresponding to 404 nm and 3.86 μm, respectively.

As a final comparison step, the overall performances of 2D pattern matching techniques and 2D compound tracking when $\pm$10 degree steering angles are employed to acquire the data are shown in Fig. 5.7 using error bars. Fig. 5.7 shows that for both interpolation techniques, 2D tracking using beam steering (i.e. BSC and BSP) outperforms 2D pattern matching technique (i.e. PMC and PMP) in estimating lateral motion even with only two steering angles. However, the estimation of motion in the axial direction does not improve significantly. These results suggest that to have good measurements in both axial and lateral directions one needs to employ more steering angles in the estimation process. Alternatively, non-steered images can be used to estimate the axial motions and steered images can be used to estimate the lateral motions.

Table 5.1: The overall performance of speckle pattern tracking using iterative 1D cosine fitting and compound imaging using 1D cosine fitting in simulated data.

	Mean $\lvert b_{ax}\rvert$		Mean $\lvert b_{lat}\rvert$		Mean σ_{ax}		Mean σ_{lat}	
Method ($\pm\theta$)	sample	μm	sample	μm	sample	μm	sample	μm
PMC	0.0023	0.0435	0.0082	2.5821	0.0117	0.2255	0.0253	7.9712
BSC ($\pm$5)	0.0026	0.0500	0.0022	0.3628	0.0268	0.5159	0.0182	5.7201
BSC ($\pm$7.5)	0.0025	0.0478	0.0023	0.7197	0.0247	0.4746	0.0123	3.8596
BSC ($\pm$10)	0.0016	0.0302	0.0021	0.6510	0.0210	0.4043	0.0123	3.8662
BSC ($\pm$12.5)	0.0043	0.0833	0.0019	0.5940	0.0240	0.4626	0.0125	3.9248
BSC ($\pm$15)	0.0053	0.1024	0.0015	0.4816	0.0283	0.5449	0.0126	3.9719
BSC ($\pm$17.5)	0.0038	0.0732	0.0031	0.9794	0.0353	0.6797	0.0147	4.6440
BSC ($\pm$20)	0.0073	0.1402	0.0058	1.8405	0.0483	0.9289	0.0180	5.6754

5.4 Experiments

5.4.1 Experimental Setup

This experimental setup is shown in Fig. 5.8. A 3-axis AIMS ultrasound scanning system (Onda Corp., Sunnyvale, CA) with 10 μm resolution in each axis, mounted on a water tank, equipped with the water conditioning system (Onda Corp., Sunnyvale, CA) was used. Experiments were performed on a $60 \times 40 \times 40\, mm^3$ uniform phantom. The phantom was prepared using a 100% polyvinyl chloride (PVC) plasticizer (M-F Manufacturing Co., Inc. Fort Worth, TX, USA) with two percent cellulose (Sigma-Aldrich Inc., St Louis, MO, USA) as scatterers [34]. The

Table 5.2: The overall performance of speckle pattern tracking using 2D polynomial fitting and compound imaging using 1D parabola fitting in simulated data.

	Mean $\lvert b_{ax}\rvert$		Mean $\lvert b_{lat}\rvert$		Mean σ_{ax}		Mean σ_{lat}	
Method ($\pm\theta$)	sample	μm	sample	μm	sample	μm	sample	μm
PMP	0.0076	0.1464	0.0126	3.9575	0.0123	0.2367	0.0273	8.5925
BSP (±5)	0.0056	0.1073	0.0031	0.9907	0.0268	0.5161	0.0182	5.7217
BSP (±7.5)	0.0041	0.0789	0.0029	0.9026	0.0247	0.4751	0.0123	3.8634
BSP (±10)	0.0036	0.0697	0.0025	0.7938	0.0210	0.4048	0.0123	3.8681
BSP (±12.5)	0.0055	0.1063	0.0023	0.7318	0.0241	0.4640	0.0125	3.9289
BSP (±15)	0.0069	0.1322	0.0017	0.5408	0.0283	0.5454	0.0126	3.9727
BSP (±17.5)	0.0056	0.1080	0.0031	0.9792	0.0354	0.6810	0.0147	4.6354
BSP (±20)	0.0094	0.1813	0.0057	1.7796	0.0481	0.9250	0.0179	5.6406

phantom was inserted in a tank of degassed water and placed 2 mm away from the transducer, thus enabling the transducer to move without deforming the phantom producing rigid motions. The phantom was moved on a 6×6 2D grid in steps of 60 μm in both axes. This resulted in a square grid spanning approximately fifteen samples axially and one sample laterally.

The phantom was imaged using a linear transducer (L9-5/38) of a SonixRP ultrasound machine (Ultrasonix Medical Corporation, Richmond, BC). The phantom was imaged to a depth of 50 mm (2 mm water gap plus 48 mm phantom) using a 128-element transducer with a 5 MHz center frequency digitized at 40 MHz, with 300 μm lateral line spacing. For each displacement configuration RF frames corresponding to non-steered and 6 different steering angles including 3 pairs of angles (i.e. $0, \pm5, \pm10, \pm15$) were acquired. Including the reference position, a total of $7 \times (36 + 1) = 259$ RF frames were recorded for off-line processing. The acquired non-steered RF frames (i.e. 37 frames) were used to estimate the motion using 2D pattern matching methods (PMP, PMC) and the acquired steered RF frames (i.e. $6 \times 37 = 222$ frames) were used to estimate the motion using beam steering methods (BSP, BSC).

5.4.2 Experimental Results

The experimental results are shown in Fig. 5.9. It should be noted that in simulations (i.e. Figs 5.4 and 5.5), the distance between grid points in both directions was 1/10 of a sample, whereas the distance between grid points in experiments (i.e. Fig. 5.9) is 30 times larger axially (i.e. 3 samples *vs* 1/10 of a sample) and 2 times larger laterally (i.e. 1/5 of a sample *vs* 1/10 of a sample). For better visualization, the standard deviation ellipses are scaled by a factor of four in both directions.

The experimental results show very good agreement with the simulation results. Fig. 5.9 depicts that the performances of the 2D compound tracking techniques is a function of the steering angle employed for data acquisition. Smallest biases and standard deviations are achieved for steering angles of ±10 for 2D compound tracking techniques. Fig. 5.9 also shows that 2D tracking using beam steering has smaller biases compared to the 2D pattern matching. However, 2D tracking using beam steering exhibits larger standard deviations when transverse motion exists in the motion field, consistent with the simulation results.

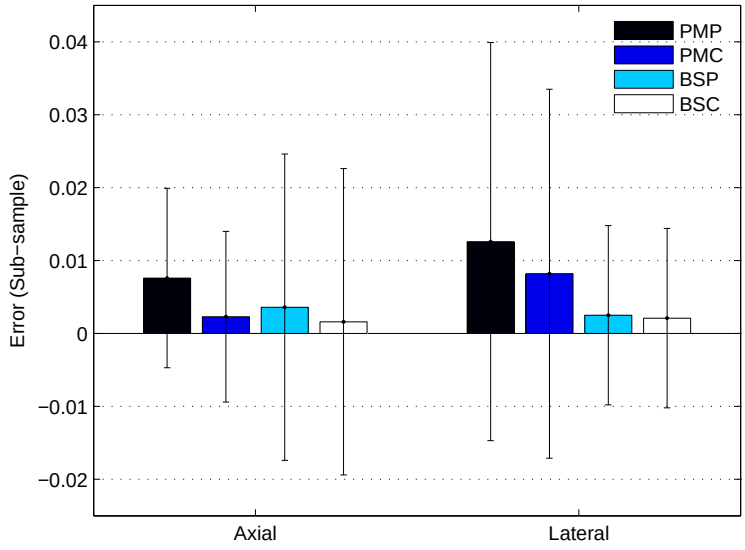

Figure 5.7: The overall performance of all methods averaged over the simulated motion grid. The bars correspond to the mean absolute biases and the lines corresponds to their mean standard deviations.

5.5 Discussions and Conclusion

In this work, in order to study the performance of the 2D compound tracking technique as a function of the steering angles, we only considered reconstruction of motion vectors from two angles which are acquired from the same steering angle but in opposite directions. However, as suggested by a number of authors, with a trade-off of longer data acquisition and processing time, motion vector can be reconstructed from multiple steering angles to improve the performance of the 2D tracking using angular compounding techniques. But as the results of this work show, different weighting needs to be employed to estimate result from different steering angles in the reconstruction process. This is consistent with the results reported in [29].

It should be noted that pattern matching techniques only require one set of the echo signals to estimate the motion vectors whereas in beam steering techniques, one set of the echo signals is required for each steering angle. Thus, the data acquisition time in beam steering techniques is proportional to the number of steering angles employed. This may introduce some limitation if high acquisition rate is of interest. A single run of the motion estimation is enough to generate the vector image in pattern matching techniques whereas in beam steering techniques, aside from reconstruction step, each set of steered echo requires to undergo the motion estimation process prior to the reconstruction of the final motion vector. As a result, their processing time is also proportional to the number of the steering angles employed in the data acquisition. Moreover, beam steering techniques are only able to reconstruct the motion vectors in the overlapping region. Thus, they introduce some limitations when large steering angles are employed or imaging deep structures is of interest, where it can be difficult to get the necessary acoustic window for beam overlap. This problem does not exist in motion vector

(a) Experimental Setup

(b) Sonogram

Figure 5.8: The experimental setup (a) showing the positioning of the transducer with respect to the phantom on the 3-axis motion stage inside the water tank. A sample sonogram (b) acquired from SonixRP ultrasound machine is also shown.

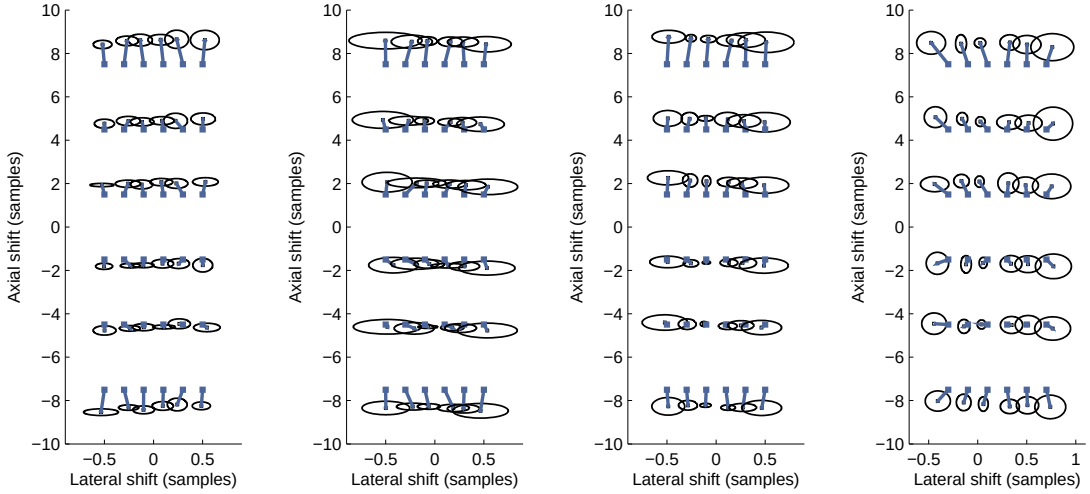

(a) PMC (b) BSC ±5 (c) BSC ±10 (d) BSC ±15

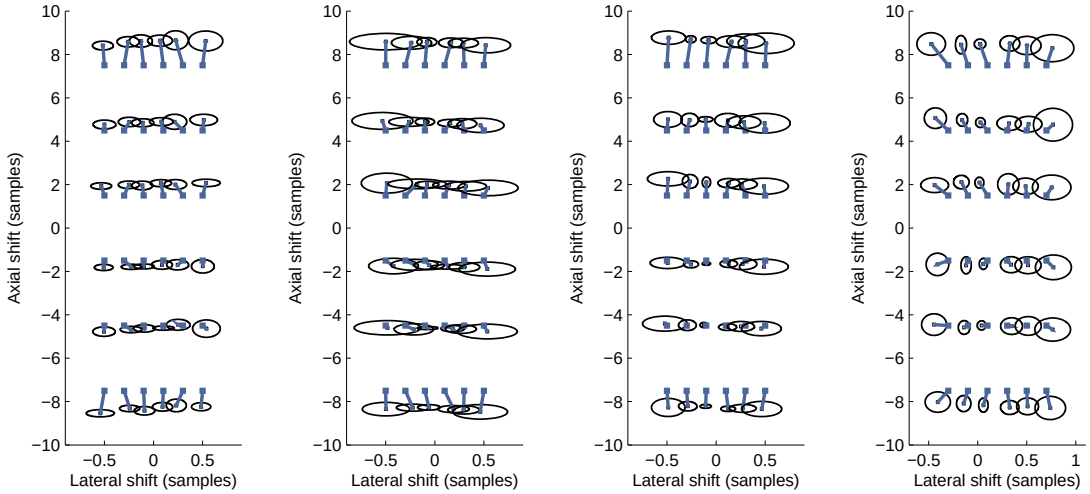

(e) PMP (f) BSP ±5 (g) BSP ±10 (h) BSP ±15

Figure 5.9: Experimental displacement estimates of 2D pattern matching techniques (1st column) and beam steering techniques employing different angles (2nd, 3rd, and 4th rows) on a 6×6 motion grid in units of samples. For better visualization of standard deviations, the radius of each ellipse in each direction corresponds to four times the standard deviation of motion estimation in that given direction. Data was acquired at a 40 MHz axial sampling rate and 300 μm line spacing. A total of 1000 realizations from unique speckle patterns inside a region of interest were used to generate each circle and ellipse (window size is $\approx 2 \times 2\,mm^2$, which is equivalent to 104 samples axially and 7 samples laterally).

estimation using pattern matching techniques.

In the simulation, the line spacing was intentionally set to 300 μm in order to be consistent with our experimental setup. However, this spacing is much larger than the typical line spacing in current ultrasound imaging systems. The biases and the standard deviations of all the methods are expected to improve with improved lateral resolution.

The performance of the 2D tracking using beam steering techniques is shown to be dependent on the steering angle being employed. However, the fact that the smallest biases and standard deviations are achieved for steering angles of ± 10 only holds for the transducer used in this work and should not be generalized to all transducers.

The result presented in this work should not be compared with the results reported in [23] where mechanical rotation of the transducer was employed to acquire the RF data from multiple views. When employing mechanical rotation or multiple transducers to acquire the data from multiple angles, the imaging system remains unchanged. However, as shown in this work, when employing beam steering techniques, image properties change as we change the steering angle (Fig. 5.3).

Amongst different techniques to acquire the data from multiple look angles, beam steering is studied in this work since it does not require any mechanical overhead which is clinically desired. The results presented in this work show that the performance of pattern matching techniques with 2D sub-sample estimation using 2D interpolations is close to that of 2D tracking employing beam steering techniques. However, with proper selection of steering angles, 2D tracking using beam steering techniques still outperform 2D pattern matching techniques especially in estimating lateral motions. This can be explained by the fact that in 2D tracking using beam steering techniques, motion vectors (both axial and lateral components) are reconstructed from multiple measurements along the direction of beam propagations where each has high accuracy and precision. However, in 2D tracking using pattern matching techniques, lateral motion is simply estimated from tracking in the direction transverse to the beam which results in less accurate and precise estimations.

In this work, we only studied and compared the performance of 2D pattern matching function equipped with 2D interpolation techniques with that of 2D compound tracking employing conventional 1D interpolation techniques. The results show that beam steering techniques exhibit large standard deviations in the presence of transverse motions especially in the axial direction. This can be explained by the fact that the performance of 2D tracking using beam steering techniques is still limited by the 1D interpolation techniques used for sub-sample motion estimation. Employing 2D interpolation methods is expected to improve the performance of 2D tracking using beam steering techniques both in terms of accuracy and precision. The adaptation of 2D interpolation methods in steered coordinates, in order to improve their accuracy and precision, will be the topic of our future work.

References

[1] C. Kasai, K. Namekawa, A. Koyano, and R. Omoto, "Real-time two-dimensional blood flow imaging using an autocorrelation technique." *IEEE Transactions on Sonics and Ultrasonics*, vol. 32, pp. 458–464, 1985.

[2] T. Loupas, R. Peterson, and R. Gill, "Experimental evaluation of velocity and power estimation forultrasound blood flow imaging, by means of a two-dimensional autocorrelation approach." *IEEE Transactions on Ultrasonics, Ferroelectrics and Frequency Control*, vol. 42, pp. 689–699, Jul 1995.

[3] H. Torp, K. Kristoffersen, and B. Angelsen, "Autocorrelation Techniques in Color Flow Imaging. Signal model and statistical properties of the Autocorrelation estimates." *IEEE Transactions on Ultrasonics, Ferroelectrics, and Frequency control*, vol. 41, pp. 604–612, 1994.

[4] A. Heimdal, A. Stoylen, H. Torp, and T. Skjaerpe, "Real-time strain rate imaging of the left ventricle by ultrasound." *Journal of American Soc Echocardiography*, vol. 11, pp. 1013–1019, Nov 1998.

[5] J. Ophir, I. Cespedes, H. Ponnekanti, Y. Yazdi, and X. Li, "Elastography: a quantitative method for imaging the elasticity of biological tissues," *Ultrasonic Imaging*, vol. 13, pp. 111–134, April 1991.

[6] L. Bohs, B. Friemel, and G. Trahey, "Experimental velocity profiles and volumetric flow via two-dimensional speckle tracking." *Ultrasound in Medicine and Biology*, vol. 21, pp. 885–98, 1995.

[7] M. Lubinski, S. Emelianov, and M. O'Donnell, "Speckle tracking methods for ultrasonic elasticity imaging using short-time correlation," *IEEE Transactions on Ultrasonics, Ferroelectrics and Frequency Control*, vol. 46, pp. 82–96, January 1999.

[8] K. Nightingale, M. Palmeri, R. Nightingale, and G. Trahey, "On the feasibility of remote palpation using acoustic radiation force," *Journal of the Acoustical Society of America*, vol. 110, pp. 625–34, July 2001.

[9] W. Walker, F. Fernandez, and L. Negron, "A method of imaging viscoelastic parameters with acoustic radiation force." *Physics in Medicine and Biology*, vol. 45, pp. 1437–1447, 2000.

[10] M. Fatemi and J. Greenleaf, "Probing the dynamics of tissue at low frequencies with the radiation force of ultrasound," *Physics in Medicine and Biology*, vol. 45, pp. 1449–64, June 2000.

[11] P. Wells, "Ultrasonic colour flow imaging," *Physics in Medicine and Biology*, vol. 39, pp. 2113–2145, 1994.

[12] R. Gill, "Measurement of blood flow by ultrasound: accuracy and sources of error." *Ultrasound in Medicine and Biology*, vol. 11, pp. 625–641, Aug 1985.

[13] E. Konofagou and J. Ophir, "Precision Estimation and Imaging of Normal and Shear Components of the 3D Strain Tensor in elastography," *Physics in Medicine and Biology*, vol. 45, pp. 1553–1563, 2000.

[14] M. Greenleaf J., Fatemi and M. Insana, "Selected methods for imaging elastic properties of biological tissues." *Annual Review of Biomedical Engineering*, vol. 5, p. 5778, 2003.

[15] H. Shi and T. Varghese, "Two-dimensional multi-level strain estimation for discontinuous tissue." *Physics in Medicine and Biology*, vol. 52, pp. 389–401, Nov 2007.

[16] L. Geiman, BJ.and Bohs, M. Anderson, S. Breit, and T. G.E., "A novel interpolation strategy for estimating subsample speckle motion." *Physics in Medicine and Biology*, vol. 45, pp. 1541–1552, 2000.

[17] L. Bohs and G. Trahey, "A novel method for angle independent ultrasonic imaging of blood flow and tissue motion," *IEEE Transactions on Biomedical Engineering*, vol. 38, pp. 280–286, March 1991.

[18] G. Trahey, J. Allison, and O. Von Ramm, "Angle independent ultrasonic detection of blood flow," *IEEE Transactions on Biomedical Engineering*, vol. 34, pp. 965–7, December 1987.

[19] I. Cespedes, Y. Huang, J. Ophir, and S. Spratt, "Methods for the estimation of subsample time-delays of digitized echo signals," *Ultrasonic Imaging*, vol. 17, pp. 142–171, 1995.

[20] P. de Jong, T. Arts, A. Hoeks, and R. Reneman, "Determination of Tissue Motion Velocity by Correlation Interpolation of Pulsed Ultrasonic Echo Signals," *Ultrasonics Imaging*, vol. 12, pp. 84–98, 1990.

[21] B. Geiman, L. Bohs, M. Anderson, S. Breit, and G. Trahey, "A comparison of algorithms for tracking sub-pixel speckle motion." in *Proceedings of the IEEE Ultrasonics Symposium.* Volume 2: IEEE, 5-8 Oct 1997, pp. 1239–1242.

[22] S. Foster, P. Embree, and W. O'Brien, "Flow velocity profile via time-domain correlation: error analysis and computer simulation," *IEEE Transactions on Ultrasonics, Ferroelectrics and Frequency Control*, vol. 37, pp. 164–175, May 1990.

[23] U. Techavipoo, Q. Chen, T. Varghese, and J. Zagzebski, "Estimation of displacement vectors and strain tensors in elastography using angular insonifications." *IEEE Transactions on Medical Imaging*, vol. 23, pp. 1479–1489, 2004.

[24] M. Rao, Q. Chen, H. Shi, T. Varghese, E. Madsen, J. Zagzebski, and T. Wilson, "Normal and shear strain estimation using beam steering on linear-array transducers." *Ultrasound in Medicine and Biology*, vol. 33, pp. 57–66, Jan 2007.

[25] H. Chen and T. Varghese, "Noise analysis and improvement of displacement vector estimation from angular displacements." *Medical physics*, vol. 35, pp. 2007–2017, 2008.

[26] L. Capineri, M. Scabia, and L. Masotti, "Vector Doppler: spatial sampling analysis and presentation techniques for real time systems." *Journal of Electronic Imaging.*, vol. 12, p. 489498, July 2003.

[27] O. Kripfgans, J. Rubin, A. Hall, and J. Fowlkes, "Vector Doppler imaging of a spinning disc ultrasound Doppler phantom." *Ultrasound in Medicine and Biology.*, vol. 32, pp. 1037–1046, 2006.

[28] L. Sandrin, M. Tanter, D. Cassereau, S. Catheline, and M. Fink, "ultrafast compound imaging for 2D motion vector estimation: Application to Transient elastography," *IEEE Transactions on Ultrasonics, Ferroelectrics and Frequency Control*, vol. 49, pp. 1363–1374, October 2002.

[29] M. Rao and T. Varghese, "Spatial angular compounding for elastography without the incompressibility assumption." *Ultrasonic imaging.*, vol. 27, pp. 256–270, 2005.

[30] J. A. Jensen, "A model for the propagation and scattering of ultrasound in tissue," *Journal of the Acoustical Society of America*, vol. 89, pp. 182–191, 1991.

[31] J. Jensen, Ed., *Ultrasound Imaging and its modeling.* Springer Verlag, 2002, ch. Chapter for the Springer Verlag book Imaging of Complex Media with Acoustic and Seismic Waves, Topics in Applied Physics.

[32] F. Viola, R. Coe, O. K., D. Guenther, and W. Walker, "MUlti-Dimensional Spline-Based Estimator (MUSE) for Motion Estimation: Algorithm Development and Initial Results." *Annals of Biomedical Engineering*, vol. 36, pp. 1942–1960, September 2008.

[33] R. Zahiri-Azar and S. Salcudean, "Time-Delay Estimation in Ultrasound Echo Signals Using Individual Sample Tracking." *IEEE Transactions on Ultrasonics, Ferroelectrics and Frequency Control*, vol. 55, pp. 2640–2650, 2008.

[34] S. DiMaio and S. Salcudean, "Needle insertion modelling and simulation," *IEEE Transactions on Robotics and Automation: Special Issue on Medical Robotics*, vol. 19, pp. 864–875, 2003.

Chapter 6

High Frame Rate Ultrasound for 2D Motion Estimation[5]

6.1 Introduction

High frame rate motion estimation has proved to be critical for a range of clinically used ultrasound imaging modes. These include blood flow estimation [1, 2], tissue velocity and strain rate imaging [3, 4], elasticity imaging [5–7], acoustic radiation force imaging (ARFI) [8–10], studying the propagation of mechanical waves in the tissue [11–13], and cardiovascular imaging [14, 15].

Conventional ultrasound systems are based on line by line acquisition of the echo signals in order to acquire the entire 2D image. As a result, the acquisition time of each frame in these systems is proportional to the number of scan lines and the acquisition time of each scan line in that frame. There exists a fundamental trade off between temporal resolution and image size. Several techniques have been attempted in the literature in order to increase the imaging frame rates. In one simple approach the number of scan lines can be reduced. This will increase the frame rates but will also result in reduction in the field of view (FOV) and/or spatial resolution depending on the spacing between scan lines. To study myocardial motion, a frame rate of 200 Hz was achieved in [16] by reducing the number of scan lines and keeping the spacing between scan lines the same thus significantly reducing the FOV. In [17] a frame rate of 450 Hz was achieved by reducing the number of scan lines and increasing the spacing between scan lines thus keeping the FOV full, but significantly reducing spatial resolution.

In another approach high temporal resolution is achieved by beam interleaving. This technique divides the region of interest (ROI) into small sectors and acquires each sector at a high temporal resolution (200 Hz to 10 kHz depending on the number of scan lines per sector and the imaging depth) for a short period of time before moving on to the next sector, etc until all the observations for the entire ROI are acquired. Assuming that the time between the acquisition of neighboring scan lines is small, the acquisition in each sector can be considered as a snapshot of the speckle movements. This technique will provide both high spatial resolution and temporal resolution. However, large delays are introduced between the data acquired from different sectors. This technique is commonly used in conventional color flow imaging, power Doppler imaging, and B flow imaging [18, 19]. The same technique is also used in [4] to evaluate regional myocardial deformation and in [12] to study the propagation of crawling waves in tissue using tissue Doppler imaging. Using the same acquisition scheme, compounding Doppler imaging has also been attempted in the literature to estimate the motion vectors using both beam steering and multi-synthetic aperture beamforming [20, 21]. In these techniques the

[5] A version of this chapter has been submitted for publication. Reza Zahiri-Azar, Ali Baghani, and Septimiu E. Salcudean, "High Frame Rate Ultrasound for 2D Motion Estimation".

data from the ROI is acquired from multiple look angles. Once the data from multiple angles are acquired, the motions estimated along multiple directions are compounded to construct the motion vectors inside the overlapping region.

With the help of parallel receive beamformers, techniques like multi-line-acquisitions (MLA) have also been used to increase the frame rate of conventional ultrasound machines where multiple echo signals (typically 2-8) are acquired from single transmit [22], thus, multiplying the effective frame rate at little cost to the resolution [14]. In [23], MLA was used to reduce transducer heating and acoustic exposure, and to facilitate data acquisition for real-time ARFI imaging. The idea of MLA was also extended to the acquisition of the entire image as opposed to multiple lines, thus, drastically increasing the effective frame rates (>5 kHz). This method is generally being referred to as ultrafast imaging where a single unfocused plane wave is used for transmit and parallel receive beamformers (typically 64-128) are used to generate the scan lines. In [11, 24], ultrafast imaging was used to capture the propagation of the transient shear wave in soft tissue and to estimate the tissue elasticity. In [25] ultrafast imaging was combined with angular compounding using multi-synthetic aperture beamforming to follow both the axial and the lateral components of the motion during the shear wave propagation at a frame rate of 6 kHz. Even though very effective, MLA and ultrafast imaging are not generally available on conventional ultrasound systems. Additional hardware overhead is required to implement each of these techniques on conventional ultrasound systems.

Techniques like coded excitations have also been introduced in the literature to increase the frame rate of the ultrasound acquisition [26–28]. However, these techniques increase the beam density and similar to MLA and ultrafast imaging require specialized hardware.

In another approach to achieve high frame rates, synchronization techniques have been suggested in the literature. The data acquisition in these techniques is similar to that of conventional color flow and power Doppler imaging to achieve high temporal resolution. However, to eliminate long delays between sectors, the start of data acquisition for each sector is synchronized with the exciter which varies from an external actuator (e.g. mechanical vibrator) to a signal generated in the body (e.g. electrocardiogram ECG). In [29], by synchronizing the data acquisition and an external exciter the shear-wave propagation in the scan plane was imaged at a frame rate of 6 kHz using a single element transducer. A similar approach was used in [30] to study both the transient and harmonic shear-wave scattering in both two and three dimensions using linear array transducers at a frame rate of 4 kHz. By synchronizing the image acquisition with the ECG signals, the propagation of several transient mechanical waves was imaged in different regions of the myocardium in mice at a frame rate of 8 kHz in [31] and in humans at a frame rate of 481 Hz in [15]. These techniques require additional hardware to synchronize the excitation and the data acquisition. The number of observations in these techniques is generally higher than in Doppler techniques (typically 20-100) since the temporal variation of the echo signal is of interest as opposed to the average time-shift/phase-shift in flow and Doppler measurement techniques. Also, at the end of imaging of each sector, the system needs to wait long enough to make sure the tissue returns back to its initial position prior to the next excitation. Otherwise, artifacts will appear in the final image when different sectors are stitched together. In the case of using an ECG the waiting time for each sector is determined by the heart rate. This waiting time will generally increase the total data acquisition time in these techniques.

Recently we have developed a high frame rate ultrasound imaging system that uses a custom

sequencer similar to the ones used in color flow imaging and power Doppler imaging followed by a delay compensation technique. Acquisition delays are compensated to reconstruct in-phase tissue motions at a virtual high frame rate using conventional ultrasound. In this work we combine this technique with that of angular compounding using beam steering to develop an ultrasound system that reconstructs 2D motion vectors from multiple 1D motion measurements estimated along different angles at a virtual high frame rate. The paper is structured as follows: Section 6.2 presents the data acquisition scheme. Section 6.3 presents the signal processing routines applied to acquire echo signals. Section 6.4 presents the experimental results. Finally, Sections 6.5 and 6.6 present discussions and conclusions along with avenues for future research.

6.2 Data Acquisition

The data acquisition in this technique is similar to compound Doppler imaging using beam steering techniques [21]. The data from the ROI are acquired from multiple steering angles, which forms the basis for motion estimation. For each scan line, a series of N pulses are acquired. This acquisition scheme is referred to as packet acquisition, and the number of pulses N as the packet size. Using this technique, the frame rate requirement is attained by beam interleaving techniques as described above, in which the frame rate for speckle pattern imaging is the pulse repetition frequency (PRF) used during acquisition. This technique can be described as follows. The ultrasonic pulse needs to propagate a distance equal to twice the image depth d_{img} before a new pulse can be transmitted. The maximum possible PRF is thus given by:

$$PRF_{max} = \frac{1}{T_l} = \frac{c}{2d_{img}}, \tag{6.1}$$

where T_l is the time required to acquire one scan line and c is the ultrasound speed. By decreasing the PRF by a factor K, there is time to acquire $K-1$ other scan lines. These K scan lines form a sector and the number K itself is called the sector size which can be expressed by:

$$K = \left\lfloor \frac{PRF_{max}}{PRF} \right\rfloor, \tag{6.2}$$

where the floor operator $\lfloor . \rfloor$ rounds to the next lower integer. The number of sectors S in the ROI is given by:

$$S = \left\lceil \frac{L}{K} \right\rceil, \tag{6.3}$$

where L is the number of scan lines (line density) determined by the image width and line spacing and the ceiling operator $\lceil . \rceil$ rounds to the nearest higher integer. It should be noted that for a fixed imaging depth, PRF_{max} can be decreased by adding additional waiting time at the end of each scan line acquisition (i.e. PRF_{max} is equal to $1/(T_l + T_w)$ instead of $1/T_l$, where T_w is the additional wait time). This technique can be used to make PRF a multiple of PRF_{max}. This way (6.2) will transform into $K = PRF_{max}/PRF$. Also, when using (6.3) L might not be a multiple of S (i.e. $SK > L$), as a result extra wait times need to be programmed in the sequencer to keep the PRF fixed for all the scan lines. This will virtually increase the number of scan lines to SK.

In order to add angular compounding to this technique, several strategies can be employed. In one straight forward approach, the process mentioned can be repeated for each steering angle

independently. This technique will result in large delays between the acquisitions of the same tissue location with different steering angles. In another approach, different steering angles can be acquired inside the same sector. This technique will minimize the delay between the acquisition of the same scan line when different steering angles are employed but will maximize the delay between the acquisition of the first and the last sector. These two techniques are shown in Fig. 6.1 when two steering angles are used. The numbers indicate the timing of each scan line acquisition. Note that the number of sectors is multiplied by the number of steering angles employed in data acquisition.

Apart from the pulsing strategy used to acquire the data, the total acquisition time is always equal to the number of lines SK, times the packet size N, times acquisition time of each line T_l. This can be formulated as follow

$$T_{total} = S \times K \times N \times T_l. \tag{6.4}$$

The observation time for each scan lines is also the number of observations N times the pulse repetition period (PRP) where PRP is equal to 1/PRF.

Following data acquisition, the input data available for processing are radio frequency (RF) echo signals arranged in packets independently. Each packet of data corresponds to time samples from one sample volume in the image, sampled at the PRF of the system. In Section 6.3 the signal processing performed on the input data will be described.

6.3 Signal Processing

A block diagram showing the basic signal processing blocks used in the 2D high frame rate system is given in Fig. 6.2. Using this block diagram as a reference, detailed description of each block will be presented in the following subsections.

6.3.1 Motion Estimation and Phasor Computation

Following the data acquisition, commonly used 1D delay estimation algorithms including time-shift and phase-shift estimators [32] can be applied to find the 1D motions along each steering angle, at each spatial location. This process is applied to each scan line independently and thus is not affected by the data acquisition scheme. We denote the estimated displacement by $u(n, l, d, \theta)$ where n is the packet index, l is the scan line index, d is the depth of the reference window used in motion estimation, and θ is the steering angle employed to acquire the data.

Once the motions at each spatial location are estimated for all the packets, the time series of displacements are transformed into the frequency domain. This way, the phasors can be extracted by selecting the frequency of interest from the list of permissible frequencies at every spatial location. We denote the estimated displacement phasor by $U(f_e, l, d, \theta)$, where f_e is the frequency of interest.

6.3.2 Phase Correction

Once the displacement phasors are estimated, to correct for all the delays introduced during the data acquisition, their phase needs to be compensated. This phase correction step can be formulated as follow:

$$U_c(f_e, l, d, \theta) = U(f_e, l, d, \theta) exp(-j2\pi f_e t_d), \tag{6.5}$$

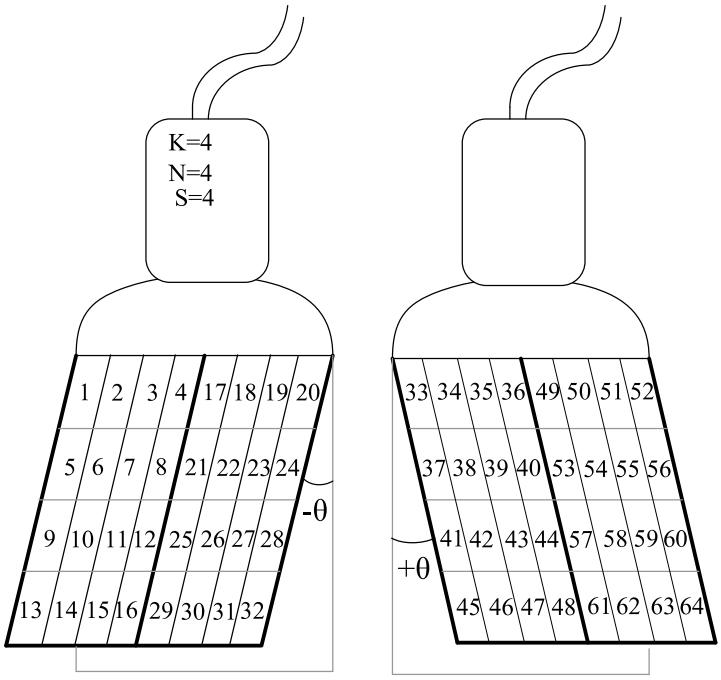

(a) Method I

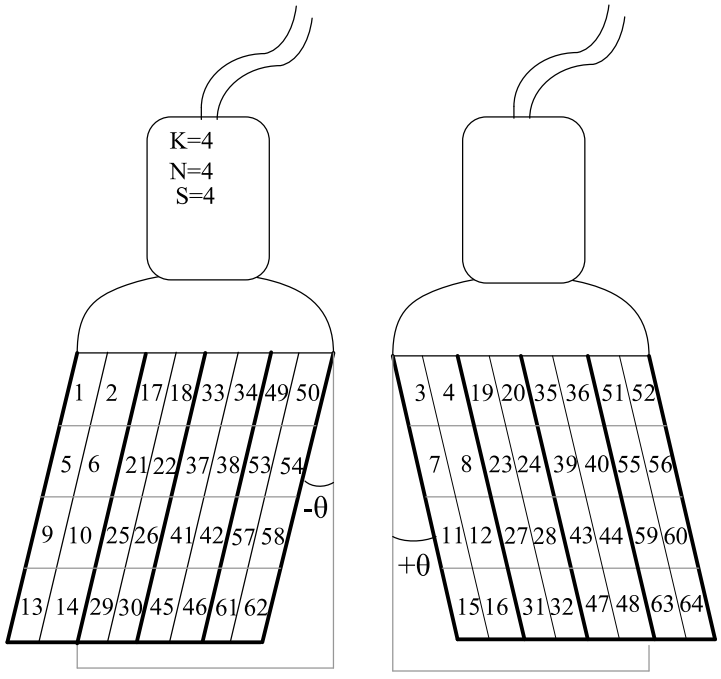

(b) Method II

Figure 6.1: Two different techniques to acquire high frame rate from two steering angles with eight scan lines ($L = 8$), sector size of $K = 4$ which results in four sectors $S = 2 \times 2 = 4$ and $PRF = PRF_{max}/4$, and packet size of $N = 4$. The numbers indicate the sequence of the 64 pulses.

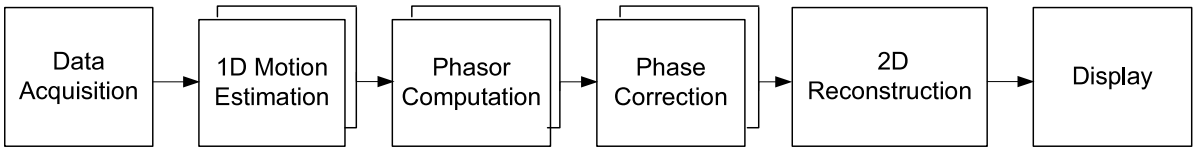

Figure 6.2: A diagram showing the basic signal processing blocks used in 2D high frame rate imaging.

where U_c is the corrected phasor and t_d is the acquisition delay with respect to the start of the sequencing corresponding to the same phasor, calculated based on the d, PRF_{max}, and the sequencing order used to acquire the data. The detailed description of this step is provided in [33] and is not repeated in here. It should be noted that adding the steering angle to data acquisition do not introduce difficulties for the phase correction process as long as the acquisition order is correctly considered in the phase correction routine.

6.3.3 2D Reconstruction

Once 1D phasors are corrected for all the delays, their coordinate needs to be transformed to Cartesian coordinates to correct for the steering angle employed in the data acquisition as follows:

$$U_c(f_e, l, d, \theta) \rightarrow \overline{U_c}(f_e, x, y, \theta), \tag{6.6}$$

where $\overline{U_c}$ is the corrected phasor in Cartesian coordinate and x, y are the axial and the lateral axes, respectively. For the purpose of this work, linear interpolation was employed for the spatial alignment.

Once 1D phasors are spatially aligned, the 2D phasors are reconstructed from the 1D phasors according to the following equations, at each spatial location [21]:

$$U_{ax}(f_e, x, y) = \frac{\overline{U_c}(f_e, x, y, \theta) + \overline{U_c}(f_e, x, y, -\theta)}{2\cos\theta}, \tag{6.7}$$

$$U_{la}(f_e, x, y) = \frac{\overline{U_c}(f_e, x, y, \theta) - \overline{U_c}(f_e, x, y, -\theta)}{2\sin\theta}, \tag{6.8}$$

where $U_{ax}(f_e, x, y)$ and $U_{la}(f_e, x, y)$ are the axial and the lateral phasors, respectively. This scheme is shown in Fig. 6.3.

6.4 Experimental Results

In order to study the performance of the proposed system, the following experiments were conducted. In one experiment the system was used to measure both axial and lateral component of the flow. This experiment was used to validate the data acquisition and 2D motion vector reconstruction steps of the system in Fig. 6.2 since phasor computation and phase correction steps are not required to measure the average flow velocity over a short period of time. In another experiment the system was used to measure both axial and lateral components of the motion resulted from propagation of mechanical waves in the tissue. This experiment was used to validate the entire system including phasor computation and phase correction steps.

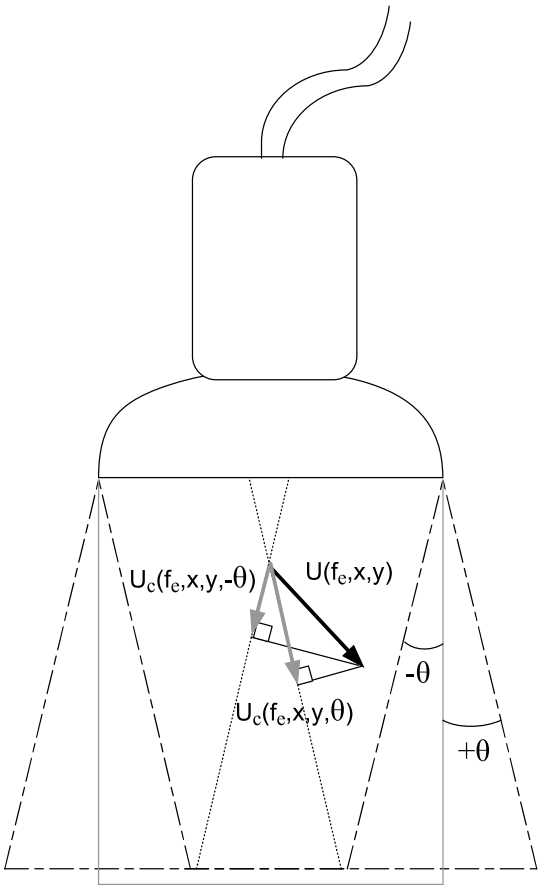

Figure 6.3: Schematics for the reconstruction of a 2D measurement using 1D measurements estimated from two steering angles.

6.4.1 2D Flow Measurements

The experimental setup is shown in Fig 6.4. The experiment was performed on a Doppler flow phantom (1425A LE Doppler Flow System, Gammex, Middleton, USA). The phantom was imaged using a SonixRP ultrasound machine (Ultrasonix Medical Corporation, Richmond, BC, Canada) with a L9-4/38 linear array transducer with 5 MHz center frequency and 300μm line spacing. The RF signal, digitized at 40 MHz, was collected to a depth of 50 mm.

Two steering angles were employed to acquire the data ($\pm$10 degrees). Referring to Fig. 6.1, in order to minimize the delay between the scan lines acquired from the same spatial location using different steering angles, the second sequencing strategy was employed.

Referring to (6.1), an imaging depth of 50 mm results in PRF_{max} of 15.4 kHz. Wait times were added to the end of each scan line acquisition to decrease the PRF_{max} to 10 kHz. This resulted in T_l of 0.1 ms. In the sequencer, the line density was set to be $L = 120$, the sector size was set to be six ($K = 6$), and the packet size was set to be eight ($N = 8$). This resulted in total of 40 sectors for both steering angles ($2 \times 120/6$), PRF of 1667 Hz (10,000/6) and PRP of 0.6 ms. The observation time for each scan line was $N \times PRP = 4.8$ ms. Referring to (6.4), the acquisition time was $40 \times 6 \times 8 \times 0.1$ ms $= 192$ ms which resulted in total frame rate of five

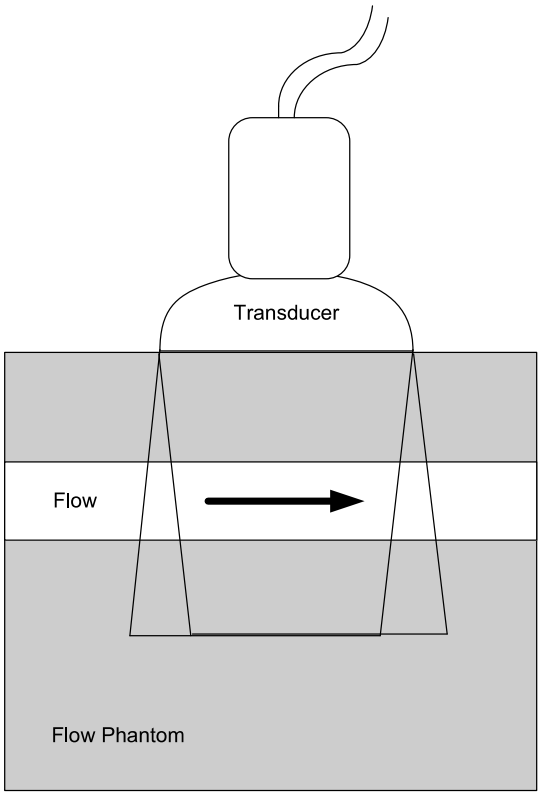

Figure 6.4: Schematics of the experimental setup used for testing the system using flow phantom.

frames per second (fps).

RF lines were recorded for off-line processing. It should be noted that real-time implementation is also possible and off-line processing is used only to avoid the overhead of the programming effort. This is not an inherent limitation of the system. The RF processing for each line was based on an autocorrelatoin technique, which converts the RF echo signals to complex I/Q data (basebanded inphase and quadrature components) and processes the complex I/Q data to measure the velocity. This method was first proposed by Kasai et al. [1] and is commonly used on commercial ultrasound machine to estimate the flow. Once 1D flow measurements were calculated, 2D flow vectors were calculated using the same processing scheme explained in Section 6.3.3.

The results calculated from one packet of data are shown in Fig. 6.5. No temporal filtering was used and a 2D spatial median filter with a kernel size of 3×3 was applied to remove the outliers. Fig. 6.5 shows that the system can reliably reconstruct the motion vector inside the region of overlapping beams acquired at high frame rates.

6.4.2 2D Wave Propagation Measurements

The experimental setup for this experiment is shown in Fig 6.6. The experiment was performed on a tissue-mimicking phantom. The phantom was constructed from 100% polyvinyl chloride (PVC) plasticizer (M-F Manufacturing Co., Inc. Fort Worth, TX, USA). Two percent cellulose

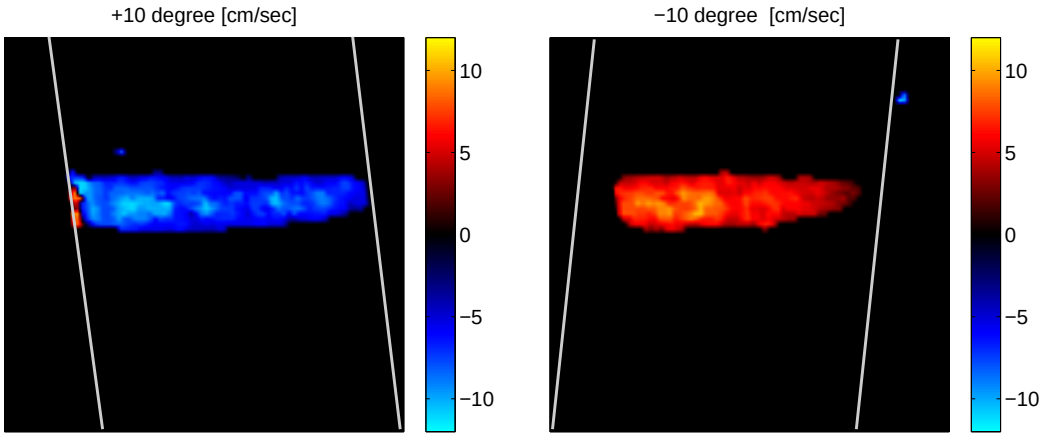

(a) 1D Motion Estimates

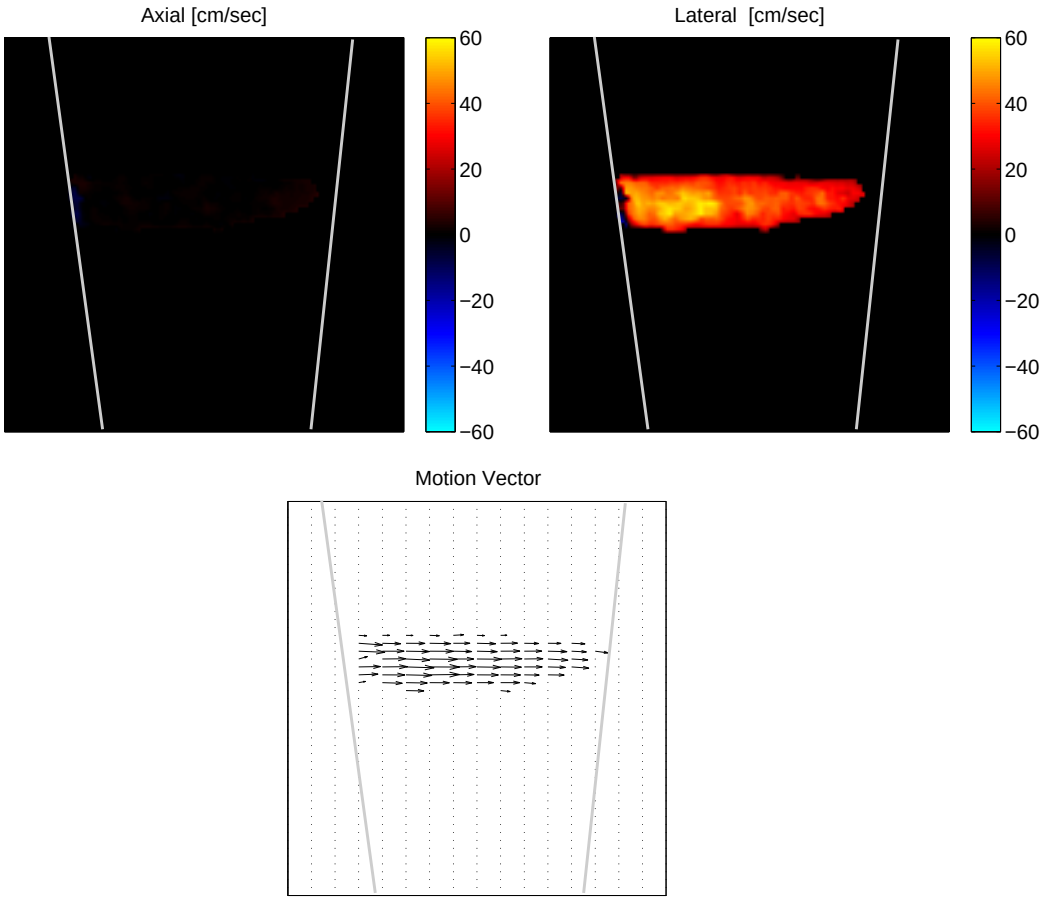

(b) 2D Reconstruction

Figure 6.5: Spatially aligned 1D motions estimated for different steering angles (a) and axial and lateral components of the motion reconstructed from the same set of data (b). The estimated motion vectors are also shown (b).

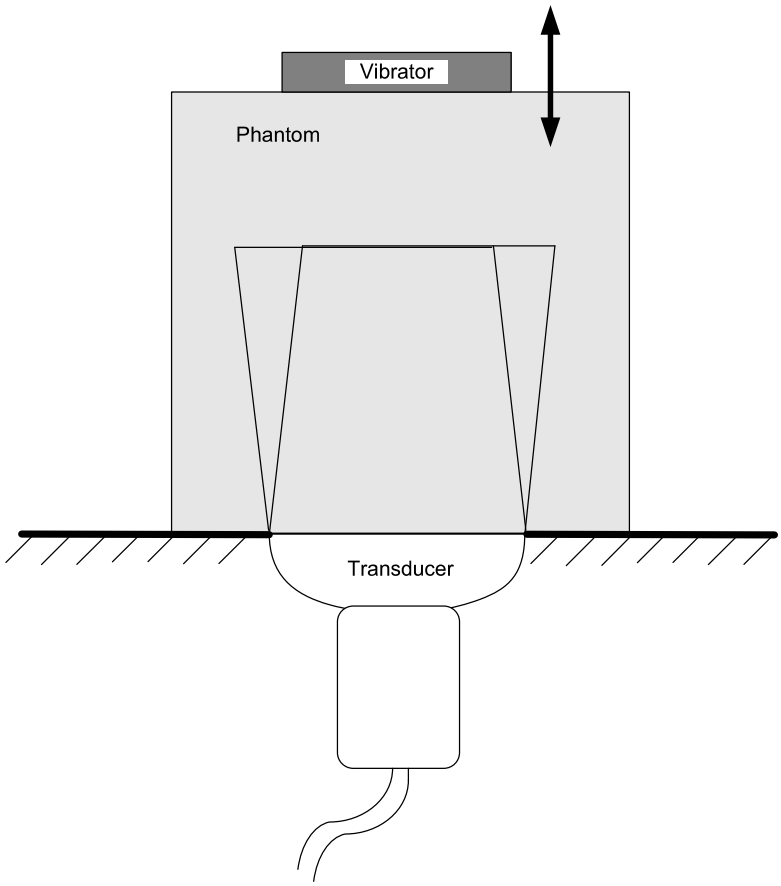

Figure 6.6: Schematics of the experimental setup used for testing the system using a mechanical vibrator.

(Sigma-Aldrich Inc., St. Louis, MO, USA) was added as scattering particles [32, 34]. The phantom was excited at 100 Hz continuously using an external shaker mounted on top of it. The phantom was imaged from the bottom using the same system mentioned above.

Similarly to the previous experiment the PRF_{max} was set to be 10 kHz. In the sequencer, the line density was set to be $L = 60$, the sector size was set to be six ($K = 12$), and the packet size was set to be eight ($N = 40$). This resulted in total of 10 sectors for both steering angles ($2 \times 60/12$), PRF of 833 Hz (10,000/12) and PRP of 1.2 ms. The observation time for each scan lines was (i.e. $N \times PRP = 48$ ms). The total acquisition time was $10 \times 12 \times 40 \times 0.1$ ms $= 480$ ms which resulted in a total frame rate of 2 fps.

The RF lines were recorded for off-line processing. The RF processing for each line was based on normalized cross correlation which is commonly used to estimate the tissue motion [5, 35]. Sub-sample accuracy was achieved using cosine fit [36]. For all the scan lines the motions were estimated with respect to the first observation of the same scan line. Once 1D motions were calculated, 2D motion vectors were calculated using the same processing scheme explained in Section 6.3.

The propagation of mechanical waves in the scan plane, imaged with the system are shown in Fig. 6.7. For better visualization, snapshots of wave images reconstructed at each step are

displayed. No temporal filtering was employed and a 2D spatial mean filter with a kernel size of 3×3 was applied to the images to improve the signal to noise ratio. Fig. 6.7 shows that the system reliably corrects for the phase shifts and reconstructs the 2D motion field at high frame rate.

6.5 Discussion

The notion for data acquisition in this work is taken from [19] and the notation for phasor calculation and phase compensation is taken from [33]. We used ± 10 as two steering angles to reconstruct 2D motion vectors from 1D estimates. However, as suggested by a number of authors, multiple steering angles can be used to improve the performance of the 2D tracking using angular compounding techniques [37, 38]. Unfortunately, in practice, there is a limit for the length of the sequence that can be programmed in ultrasound imaging systems. Thus, in addition to longer acquisition and processing time, employing several steering angles would introduce implementation issues since the total number of scan lines which should be acquired are multiplied by the number of steering angles being employed (Eq. (6.4)). As suggested in [33], to resolve this issue, the sequencer can be programmed multiple times to acquire the entire data. However, this approach will increase the acquisition time even further.

In this work, we only considered reconstruction of 2D phasors for a single frequency of interest f_e. In case we are interested in multiple frequencies, the process of phasor computation, phase correction, 2D reconstruction should be repeated for each frequency independently on the same set of data.

Techniques like multi-line-acquisition that were mentioned in the introduction can also be employed in this system in order to speed up the data acquisition process. However, care needs to be taken during the phase correction step since scan line acquisition will not be sequential anymore.

As shown in this work, to adjust the acquisition delays between the acquisition of the same tissue location when multiple steering angles are employed, different pulsing strategies can be used. However, it is important to note that when using phase correction techniques, the acquisition strategy does not play a role in the final estimation results. This is due to the fact that following the acquisition delay cancellation, all the data are virtually acquired at the same time.

Referring to Fig. 6.1, the maximum achievable PRF in the system is PRF_{max} and $PRF_{max}/2$ for the first and the second sequencing method, respectively. For example in the 2D flow measurement experiment by setting $K = 2$ (i.e. in each sector, acquire one line from each angle), the PRF can go up to 5 kHz. In the 2D wave propagation measurement by setting $K = 1$ (i.e. in each sector, acquire only one line), the PRF can go up to 10 kHz. However, as mentioned in the introduction, for a fixed number of observations, setting the PRF too high will significantly reduce the observation time. Thus, depending on the application, it is important to find the proper balance between these two parameters.

The proposed system can be implemented on conventional ultrasound machines without an extra hardware overhead to facilitate estimation of 2D motion at high frame rates. However, the proposed system has its own limitations as well. First, the tissue and the transducer should be stationary during the data acquisition to avoid motion artifacts. Second, even though there is no need for the excitation to be of a single frequency, the excitation needs to be periodic

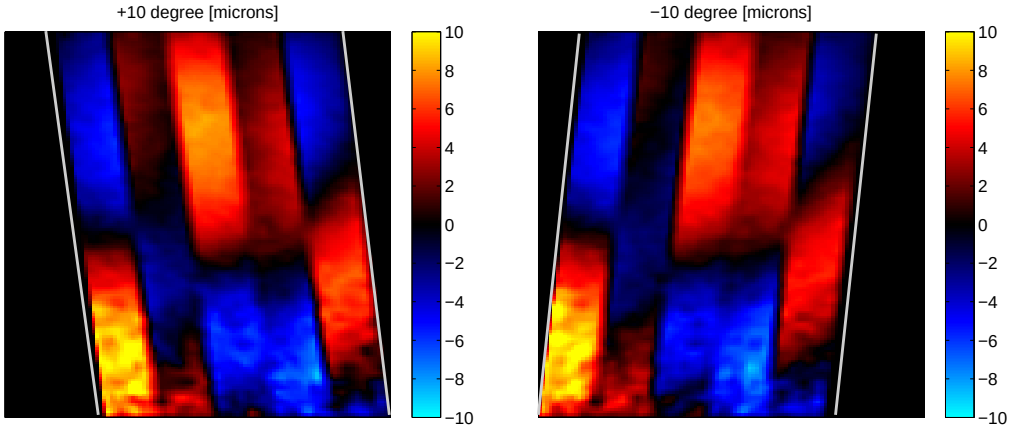

(a) After 1D Motion Estimation

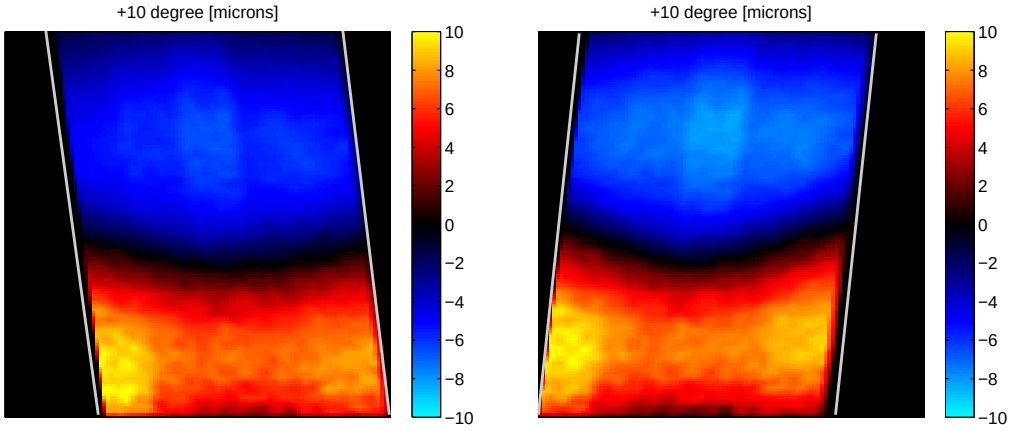

(b) After Phase Correction

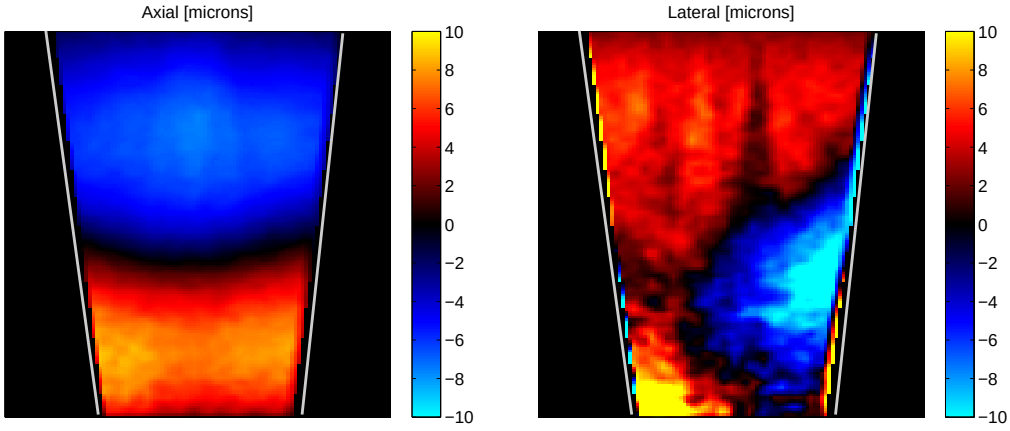

(c) After 2D Reconstruction

Figure 6.7: Snapshot of wave images after 1D motions estimation (a) and phase correction (b) for both steering angles are shown. The reconstructed images of the axial and lateral components of the wave are also shown (c).

and band-limited where the highest frequency content should be smaller than half of the PRF and the period of the lowest frequency needs to be short enough so that it can be observed during the imaging of each scan line. Third, without synchronization, the system can not be used to study the propagation of transient waves since all the scan lines should be acquired at the same time and long observation times are required to study the propagation of the waves. Techniques like ultrafast imaging are generally preferred for these applications. Fourth, beam steering techniques are only able to reconstruct the motion vectors in the overlapping region. Thus, they introduce some limitations when large steering angles are employed or imaging deep structures is of interest, where it can be difficult to get the necessary acoustic window for beam overlap. Techniques like split aperture [21] can be employed to alleviate this problem however the problem still remains.

6.6 Conclusion

A high frame rate ultrasound system is introduced in this article which can readily be implemented on conventional ultrasound systems in real-time without additional hardware overhead. The system uses a data acquisition scheme similar to that of compound Doppler imaging to achieve high frame rates. A previously introduced phase correction scheme is used in the system to compensate for acquisition delays. Finally, reconstruction techniques are employed to estimate the 2D motion vectors from individual 1D measurement estimated from multiple steering angles.

As shown in this work, the proposed system has potential applications in medical ultrasound. These applications include vascular imaging, studying the propagation of mechanical waves in the tissue, strain and strain rate imaging, and elasticity and viscosity imaging.

References

[1] C. Kasai, K. Namekawa, A. Koyano, and R. Omoto, "Real-time two-dimensional blood flow imaging using an autocorrelation technique." *IEEE Transactions on Sonics and Ultrasonics*, vol. 32, pp. 458–464, 1985.

[2] T. Loupas, R. Peterson, and R. Gill, "Experimental evaluation of velocity and power estimation forultrasound blood flow imaging, by means of a two-dimensional autocorrelation approach." *IEEE Transactions on Ultrasonics, Ferroelectrics and Frequency Control*, vol. 42, pp. 689–699, Jul 1995.

[3] H. Torp, K. Kristoffersen, and B. Angelsen, "Autocorrelation Techniques in Color Flow Imaging. Signal model and statistical properties of the Autocorrelation estimates." *IEEE Transactions on Ultrasonics, Ferroelectrics, and Frequency control*, vol. 41, pp. 604–612, 1994.

[4] A. Heimdal, A. Stoylen, H. Torp, and T. Skjaerpe, "Real-time strain rate imaging of the left ventricle by ultrasound." *Journal of American Soc Echocardiography*, vol. 11, pp. 1013–1019, Nov 1998.

[5] J. Ophir, I. Cespedes, H. Ponnekanti, Y. Yazdi, and X. Li, "Elastography: a quantitative method for imaging the elasticity of biological tissues," *Ultrasonic Imaging*, vol. 13, pp. 111–134, April 1991.

[6] L. Bohs, B. Friemel, and G. Trahey, "Experimental velocity profiles and volumetric flow via two-dimensional speckle tracking." *Ultrasound in Medicine and Biology*, vol. 21, pp. 885–98, 1995.

[7] M. Lubinski, S. Emelianov, and M. O'Donnell, "Speckle tracking methods for ultrasonic elasticity imaging using short-time correlation," *IEEE Transactions on Ultrasonics, Ferroelectrics and Frequency Control*, vol. 46, pp. 82–96, January 1999.

[8] K. Nightingale, M. Palmeri, R. Nightingale, and G. Trahey, "On the feasibility of remote palpation using acoustic radiation force," *Journal of the Acoustical Society of America*, vol. 110, pp. 625–34, July 2001.

[9] W. Walker, F. Fernandez, and L. Negron, "A method of imaging viscoelastic parameters with acoustic radiation force." *Physics in Medicine and Biology*, vol. 45, pp. 1437–1447, 2000.

[10] M. Fatemi and J. Greenleaf, "Probing the dynamics of tissue at low frequencies with the radiation force of ultrasound," *Physics in Medicine and Biology*, vol. 45, pp. 1449–64, June 2000.

[11] J. Bercoff, M. Tanter, M. Muller, and M. Fink, "Study of viscous and elastic properties of soft tissues using supersonic shear imaging," in *Proceedings of the IEEE Ultrasonic Symposium*, 2003.

[12] K. Hoyt, K. Parker, and J. Rubens, "Real-Time Shear Velocity Imaging Using Sonoelastographic Techniques," *Ultrasound in Medicine and Biology*, vol. 33, p. 10861097, 2007.

[13] E. Turgay, S. Salcudean, and R. Rohling, "Identifying Mechanical properties of Tissue by Ultrasound." *Ultrasound in Medicine and Biology*, vol. 32, pp. 221–235, 2006.

[14] K. Kaluzynski, C. Xunchang, S. Emelianov, A. Skovoroda, and M. O'Donnell, "Strain rate imaging using two-dimensional speckle tracking." *IEEE Transactions on Ultrasonics, Ferroelectrics and Frequency Control*, vol. 48, pp. 1111–1123, July 2001.

[15] S. Wang, W. Lee, J. Provost, L. Jianwen, and E. Konofagou, "A composite high-frame-rate system for clinical cardiovascular imaging." *IEEE Transactions on Ultrasonics, Ferroelectrics and Frequency Control*, vol. 55, pp. 2221–2233, Oct 2008.

[16] E. Konofagou, J. D'hooge, and J. Ophir, "Myocardial elastography - A feasibility study in vivo," *Ultrasound in Medicine and Biology*, vol. 28, pp. 475–482, October 2002.

[17] H. Kanai, Y. Koiwa, and J. Zhang, "Real-time measurements of local myocardium motion and arterial wall thickening." *IEEE Transactions on Ultrasonics, Ferroelectrics and Frequency Control*, vol. 46, pp. 1229–1241, 1999.

[18] J. Jensen and I. Lacasa, "Estimation of blood velocity vectors using transverse ultrasound beam focusing and cross-correlation," in *Proceedings of the IEEE Ultrasonics Symposium.* IEEE, Oct 1999, pp. 1493–1497 vol.2.

[19] L. Lvstakken, S. Bjaerum, D. Martens, and H. Torp, "Blood flow imaging–A new real-time, 2-D flow imaging technique." *IEEE Transactions on Ultrasonics, Ferroelectrics and Frequency Control*, vol. 53, pp. 289–99, Feb 2006.

[20] L. Capineri, M. Scabia, and L. Masotti, "Vector Doppler: spatial sampling analysis and presentation techniques for real time systems." *Journal of Electronic Imaging.*, vol. 12, p. 489498, July 2003.

[21] O. Kripfgans, J. Rubin, A. Hall, and J. Fowlkes, "Vector Doppler imaging of a spinning disc ultrasound Doppler phantom." *Ultrasound in Medicine and Biology.*, vol. 32, pp. 1037–1046, 2006.

[22] M. Fabian, K. Ballu, J. Hossack, T. Blalock, and W. Walker, "Development of a parallel acquisition system for ultrasound research." in *Proc. SPIE vol. 4325*, Feb 2001, pp. 54–62.

[23] J. Dahl, G. Pinton, M. Palmeri, V. Agrawal, K. Nightingale, and G. Trahey, "A Parallel Tracking Method for Acoustic Radiation Force Impulse Imaging." *IEEE Transactions on Ultrasonics, Ferroelectrics and Frequency Control*, vol. 54, pp. 301–312, 2007.

[24] S. Catheline, J.-L. Gennisson, G. Delon, and M. Fink, "Viscoelastic properties of soft solids using transient elastography," in *Second International Conference on the Ultrasonic*

Measurement and Imaging of Tissue Elasticity, Corpus Christi, U.S., October 2003, pp. 25–25.

[25] L. Sandrin, M. Tanter, D. Cassereau, S. Catheline, and M. Fink, "ultrafast compound imaging for 2D motion vector estimation: Application to Transient elastography," *IEEE Transactions on Ultrasonics, Ferroelectrics and Frequency Control*, vol. 49, pp. 1363–1374, October 2002.

[26] T. Misaridis and J. Jensen, "Use of modulated excitation signals in medical ultrasound. Part I: basic concepts and expected benefits." *IEEE Transactions on Ultrasonics, Ferroelectrics and Frequency Control*, vol. 52, pp. 177–191, Feb 2005.

[27] ——, "Use of modulated excitation signals in medical ultrasound. Part II: Design and performance for medical imaging applications." *IEEE Transactions on Ultrasonics, Ferroelectrics and Frequency Control*, vol. 52, pp. 192–207, 2005.

[28] ——, "Use of modulated excitation signals in medical ultrasound. Part III: High frame rate imaging." *IEEE Transactions on Ultrasonics, Ferroelectrics and Frequency Control*, vol. 52, pp. 208–219, 2005.

[29] V. Dutt, R. Kinnick, R. Muthupillai, T. Oliphant, R. Ehman, and J. Greenleaf, "Acoustic shear-wave imaging using echo ultrasound compared to magnetic resonance elastography," *Ultrasound in Medicine and Biology*, vol. 26, pp. 397–403, 2000.

[30] A. Henni, C. Schmitt, and G. Cloutier, "Three-dimensional transient and harmonic shear-wave scattering by a soft cylinder for dynamic vascular elastography." *Journal of the Acoustical Society of America*, vol. 124, pp. 2394–2405, Oct 2008.

[31] M. Pernot, K. Fujikura, S. Fung-Kee-Fung, and K. E., "ECG-gated, mechanical and electromechanical wave imaging of cardiovascular tissues in vivo." *Ultrasound in Medicine and Biology*, vol. 33, p. 10751085, 2007.

[32] R. Zahiri-Azar and S. Salcudean, "Time-Delay Estimation in Ultrasound Echo Signals Using Individual Sample Tracking." *IEEE Transactions on Ultrasonics, Ferroelectrics and Frequency Control*, vol. 55, pp. 2640–2650, 2008.

[33] A. Baghani, "A Wave Equation Approach to Ultrasound Elastography," Ph.D. dissertation, University of British Columbia, 2009.

[34] S. DiMaio and S. Salcudean, "Needle insertion modelling and simulation," *IEEE Transactions on Robotics and Automation: Special Issue on Medical Robotics*, vol. 19, pp. 864–875, 2003.

[35] R. Zahiri-Azar and S. Salcudean, "Motion Estimation in Ultrasound Images Using Time Domain Cross Correlation With Prior Estimates." *IEEE Transactions on Biomedical Engineering*, vol. 53, pp. 1990–2000, 2006.

[36] I. Cespedes, Y. Huang, J. Ophir, and S. Spratt, "Methods for the estimation of subsample time-delays of digitized echo signals," *Ultrasonic Imaging*, vol. 17, pp. 142–171, 1995.

[37] M. Rao and T. Varghese, "Spatial angular compounding for elastography without the incompressibility assumption." *Ultrasonic imaging.*, vol. 27, pp. 256–270, 2005.

[38] U. Techavipoo, Q. Chen, T. Varghese, and J. Zagzebski, "Estimation of displacement vectors and strain tensors in elastography using angular insonifications." *IEEE Transactions on Medical Imaging*, vol. 23, pp. 1479–1489, 2004.

Chapter 7

Conclusions and Future Research

In this Chapter the results of the collected works are related to one another and a unified goal of the thesis is discussed. The strengths and weaknesses of the research are then presented, along with future directions for research.

7.1 Multi-Dimensional Motion Estimation Techniques

In Chapters 2, 3 and 4 new algorithms are developed for the estimation of motion in the sequences of ultrasound echo signal in 1D (axial component only), 2D (both axial and lateral components), and 3D (axial, lateral, and elevational components). The performance of all the presented techniques is studied using both simulation and experimental data in terms of accuracy, precision, sensitivity, and resolution. A comparison is carried out with state of the art techniques. This way the first two objectives of the thesis are met.

In Chapter 2 a new class of delay estimators based on the tracking of the individual echo samples called sample tracking (ST) is presented. The use of the same interpolation approach to improve the performance of the ZCT delay estimator is also presented [1]. Simulation results show that these algorithms outperform conventional window based time-delay estimators in terms of bias and standard deviation when applied to high SNR echo signals. Simulation results also show that ST algorithms have higher resolution and sensitivity when used as strain estimators compared to commonly used strain estimation algorithms including recently introduced spline-based continuous time-delay estimators [2] as they provide the displacement of individual samples. However, their performance degrades rapidly as the SNR of the echo signals becomes low. Experimental results demonstrating the viability of ST are also presented.

In Chapter 3 we show that the standard approach of applying a separate 1D sub-sample estimation [3, 4] in multi-dimensional motion tracking is not valid when estimating motion in sequences of ultrasound echo signals. Several pattern-matching function interpolation schemes that are suited for 2D motion estimation were presented.

The techniques presented in Chapter 3 are extended to 3D in Chapter 4 where 3D sub-sample motion estimation schemes are presented. The performance of the proposed methods has been characterized through both simulations and experiments. The results show that the proposed methods significantly outperform other commonly used independent 1D algorithms in the literature in terms of bias and standard deviation.

Both techniques presented in Chapter 3 and Chapter4 assume small motions and deformations which is valid for fast imaging [5], where inter-frame displacements and deformations are small and the echo signals are highly correlated. This is also the case in acoustic radiation force imaging [5–8] where induced displacements and deformations are very small. However,

the assumption of small motions and deformations does not hold when large deformations exist and echo signals are decorrelated. This is generally the case in quasi-static elastography [9, 10] where large external compressions are applied to the tissue and cause the tissue to experience large deformations. This is also the case in myocardial elastography [11] where the tissue experiences large internal motions and deformations. The performance of all the pattern matching function interpolation techniques, including those presented in this work, is expected to degrade when the echo signals are decorrelated and can not be matched correctly. In order to adapt all these methods to the estimation of displacements resulting from large deformations, previously introduced compounding methods should be applied to the raw echo signals [12–14] prior to the motion estimation process. Once the effect of signal decorrelation is suppressed, the pattern matching algorithms followed by the proposed interpolation methods can be applied to estimate the motion. Alternatively, techniques such as iterative 1D cross correlation with recorrelation [11, 15], which are more robust in the presence of deccorelation, can be employed to estimate the motion.

In Chapter 3 and Chapter 4 we have only employed a standard polynomial fitting to generate the continuous representation of the pattern matching function in multi-dimension. However, several other polynomials may be used for this purpose, including multi-dimensional spline polynomials as in [3, 16]. The use of higher order splines are expected to improve the accuracy of the sub-sample estimation, but at higher computational cost.

The proposed methods have several potential applications throughout the field of signal processing. Specific applications in medical ultrasound include fine velocity vector imaging, strain tensor estimation, elastography, and acoustic radiation force impulse imaging.

7.2 Real-Time Motion Estimation

The proposed estimators in Chapter 2, Chapter 3, and Chapter 4 are shown to provide a good balance between accuracy, precision, and computational cost. All the proposed techniques add small computational overhead and are suitable for real-time applications. Based on the methods proposed in Chapter 3, a real-time 2D motion tracking software has been implemented that estimates the motions between the sequences of ultrasound echo signals in several dimensions at the native frame rate of the ultrasound machines used currently (up to 50 Hz). In this manner, the third objective of the thesis is met.

The system is currently being used in several clinical applications namely strain imaging of the prostate [17], monitoring kidney transplants, studying the tissue deformation following needle insertion [18], characterization of soft tissue from finite element models [19], 2D strain tensor estimation, tissue elasticity and viscosity imaging [20], and tissue motion vector imaging at the University of British Columbia (UBC) and in collaboration with Dr. Christopher Nguan at the Vancouver General Hospital (VGH) and Dr. Morris at the British Columbia Cancer agency (BCCA).

The system is also being used for real-time poro-elastography [21] for distinguishing between normal and lymphedematous tissues *in vivo* and shear strain imaging for breast tumor classification [22] in collaboration with Professor Jonathan Ophir and Dr. Arun Thitaikumar at medical school at Houston at the University of Texas and Dr. Brian Garra at Fletcher Allen Health Care at the University of Vermont.

A version of motion tracking software has also been implemented in a strain imaging soft-

ware and licensed for commercial use on ultrasound machines to the Ultrasonix Medical Corporation (Richmond, BC, Canada). So far, the software has been used in different sites on more than 1000 clinical cases varying from breast tumor imaging [23] to skin abnormalities [24].

Research are currently going on to implement the methods proposed in Chapter 4 and develop a real-time 3D motion tracking system. This would provide the opportunity to extend all the above mentioned application to three dimensions.

7.3 High Frame Rate Tracking

In Chapter 5 we show that the performance of our proposed 2D pattern matching techniques is close to that of 2D tracking employing beam steering techniques. However, 2D tracking using beam steering techniques still outperform 2D pattern matching techniques. This can be explained by the fact that in 2D tracking using beam steering techniques, motion vectors (both axial and lateral components) are reconstructed from multiple measurements along the direction of beam propagations where each has high accuracy and precision, whereas in 2D tracking using pattern matching techniques, lateral motion is simply estimated from tracking in the direction transverse to the beam which results in less accurate and precise estimations.

Despite better performance, the data acquisition time in beam steering techniques is longer and is proportional to the number of steering angles employed. This will introduce some limitation when high acquisition rate is of interest. In order to take advantage of beam steering techniques without sacrificing the frame rate, in Chapter 6 a high frame rate ultrasound system is introduced. The system uses beam interleaving techniques [25] in conjunctions with a delay cancellation method introduced by my colleague Ali Baghani to compensate for acquisition delays [26]. In this manner, the last objective of the thesis is met.

The system was implemented on conventional ultrasound machines without any additional hardware overhead and achieves both high spatial (line density of up to 128) and high temporal resolution ($>500\,\text{Hz}$) at an imaging depth of 5 cm and a 100% field of view. Applications of the system in studying the wave propagation in two dimensions, and flow vector imaging are presented with experimental results from phantoms. The proposed system has several other potential applications such as high frame rate strain and strain rate imaging, and quantitative elasticity and viscosity imaging using dynamic elastography and wave inversion techniques [25].

7.4 Summary of Contributions

The major contribution of this thesis is development of new algorithms for estimation of the tissue motion in sequences of ultrasound images in multi-dimensions with high accuracy and precision and small computational cost suitable for real-time applications. The specific contributions of this thesis can be outlined as follows:

- A new class of motion estimation techniques called sample tracking was introduced. Results from both simulations and experiments showed that the proposed techniques outperform all the the common and state-of-the art motion estimators in terms of accuracy, precision, resolution, and sensitivity. The extension of the proposed algorithms to multi-dimensional motion estimation is also presented.

- To maximize the accuracy and precision of motion estimation in multi-dimensions while adding a small computational overhead, sub-sample estimators were studied. Several sub-sample motion estimators were introduced, each offering different trade offs between performance and computational cost. Results from both simulations and experiments show that by adding a small computational cost, the proposed sub-sample estimation techniques significantly improve the performance of motion estimation in multi-dimensions.

- Based on the proposed sub-sample estimation methods, real-time 2D/3D motion tracking software has been implemented to estimate the motion vectors between sequences of ultrasound echo signals at commonly used ultrasound frame rates (up to 50Hz). The software was licensed for commercial use and currently being used in several clinical applications namely, normal/shear strain imaging [22], dynamic elastography [19], vibro-elastography [17], tumor detection and classifications [23, 24], and poro-elastography [21].

- The proposed 2D tracking method was compared with 2D tracking employing beam steering techniques. Results from both simulations and experiments showed that 2D tracking using beam steering techniques outperforms 2D motion estimation without compounding in terms of both accuracy and precision especially in estimating lateral motion.

- A custom pulse sequencer followed by a phase correction scheme was developed to estimate 2D motion vectors at a high frame rates ($> 500\,\text{Hz}$). Potential applications include studying the propagation of mechanical waves in tissue, visocoelasticity imaging of tissue, high frame rate strain/strain rate imaging, and vascular imaging.

7.5 Future Work

Simulation results show that ST algorithms have higher resolution and sensitivity when used as strain estimators compared to commonly used techniques. However, their performance degrades as the SNR of the echo signals becomes low. The use of smoothing splines is expected to improve the performance of these techniques in the presence of noise.

In this work, we only formulated and studied our proposed interpolation techniques in Cartesian coordinates to estimate the sub-sample motion. Further investigation is required to study the adaptability of the proposed interpolation methods to steered coordinates and coordinates which are typically introduced when data are acquire using curved linear transducers. This is expected to improve the performance of sub-sample estimation in these applications.

The requirement for motion tracking algorithms changes from one medical application to the next. For example in myocardial imaging large motions and deformations generally exist in the imaging plane thus the tracking algorithm needs to be robust in the presence of large decorrelation. However, in breast imaging the tissue is generally stationary and does not experience large deformations and sensitivity of the estimator is more important. Further studies and validations are required to optimize the tracking process for different clinical applications.

The studies and validations in this thesis were generally based on the simulated and experimental data acquired from tissue mimicking phantoms. The performance of the proposed techniques has also been evaluated in several clinical applications [22–24]. However, further

studies are required to quantify the performance of the proposed technique using ultrasound data acquired from real tissue *in vivo* and *in vitro*.

In this work we studied and compared the performance of different techniques in estimating translation and compression. However, due to different boundary conditions, the tissue may also experience slippage, rotation, and shearing. This is generally the case in tracking the kidney and the prostate. In the future, these behaviors also need to be studied to further optimize the motion tracking algorithms for these applications.

Through out this work, the tissue motions were estimated without assuming any underlaying model. However, including different models in the process is expected to improve the performance of tissue motion estimation. These will be the topics of our future work.

References

[1] S. Srinivasan and J. Ophir, "A zero-crossing strain estimator in elastography," *Ultrasound in Med and Bio*, vol. 29, pp. 227–238, 2003.

[2] F. Viola and W. Walker, "A Spline-Based Algorithm for Continuous Time-Delay Estimation Using Sampled Data." *IEEE Transactions on Ultrasonics, Ferroelectrics and Frequency Control*, vol. 52, pp. 80–93, January 2005.

[3] F. Viola, R. Coe, O. K., D. Guenther, and W. Walker, "MUlti-Dimensional Spline-Based Estimator (MUSE) for Motion Estimation: Algorithm Development and Initial Results." *Annals of Biomedical Engineering*, vol. 36, pp. 1942–1960, September 2008.

[4] R. Lopata, M. Nillesena, H. Hansena, I. Gerritsa, T. J., and C. de Korte, "Performance Evaluation of Methods for Two-Dimensional Displacement and Strain Estimation Using Ultrasound Radio Frequency Data." *Ultrasound in medicine and biology*, vol. 35, pp. 796–812, 2009.

[5] J. Bercoff, M. Tanter, and M. Fink, "Supersonic shear imaging: a new technique for soft tissue elasticity mapping," *IEEE Transactions on Ultrasonics, Ferroelectrics and Frequency Control*, vol. 51, pp. 396–4009, April 2004.

[6] K. Nightingale, M. Palmeri, R. Nightingale, and G. Trahey, "On the feasibility of remote palpation using acoustic radiation force," *Journal of the Acoustical Society of America*, vol. 110, pp. 625–34, July 2001.

[7] W. Walker, F. Fernandez, and L. Negron, "A method of imaging viscoelastic parameters with acoustic radiation force." *Physics in Medicine and Biology*, vol. 45, pp. 1437–1447, 2000.

[8] M. Fatemi and J. Greenleaf, "Probing the dynamics of tissue at low frequencies with the radiation force of ultrasound," *Physics in Medicine and Biology*, vol. 45, pp. 1449–64, June 2000.

[9] T. Varghese, J. Ophir, E. Konofagou, F. Kallel, and R. Righetti, "Tradeoffs In Elastographic Imaging, Ultrasonic Imaging," *Ultrasonic Imaging*, vol. 23, pp. 216–248, October 2001.

[10] E. Brusseau, J. Kybic, J. Deprez, and O. Basset, "2-D Locally Regularized Tissue Strain Estimation From Radio-Frequency Ultrasound Images: Theoretical Developments and Results on Experimental Data." *IEEE Transactions on Medical Imaging*, vol. 27, pp. 145 – 160, Feb 2008.

[11] W. Lee, C. M. Ingrassia, S. D. Fung-Kee-Fung, K. D. Costa, J. W. Holmes, and E. Konofagou, "Theoretical Quality Assessment of Myocardial Elastography with In Vivo Validation," *IEEE Transactions on Ultrasonics, Ferroelectrics and Frequency Control*, vol. 54, pp. 2233–2245, 2007.

[12] S. Alam, J. Ophir, and E. Konofagou, "An adaptive strain estimator for elastography," *IEEE Transactions on Ultrasonics, Ferroelectrics and Frequency Control*, vol. 45, pp. 461–72, March 1998.

[13] P. Chaturvedi, M. Insana, and T. Hall, "2D companding for noise reduction in strain imaging," *IEEE Transactions on Ultrasonics, Ferroelectrics and Frequency Control*, vol. 45, pp. 179–191, 1998.

[14] T. Varghese and J. Ophir, "Enhancement of echo-signal correlation in elastography using temporal stretching," *IEEE Transactions on Ultrasonics, Ferroelectrics and Frequency Control*, vol. 44, pp. 173–180, January 1997.

[15] E. Konofagou and J. Ophir, "A new elastographic method for estimation and imaging of lateral displacements, lateral strains, corrected axial strains and Poisson's ratios in tissues," *Ultrasound in Medicine and Biology*, vol. 24, pp. 1183–99, October 1998.

[16] R. Zahiri-Azar and S. Salcudean, "Time-Delay Estimation in Ultrasound Echo Signals Using Individual Sample Tracking." *IEEE Transactions on Ultrasonics, Ferroelectrics and Frequency Control*, vol. 55, pp. 2640–2650, 2008.

[17] S. Salcudean, D. French, S. Bachmann, X. Zahiri-Azar, R.and Wen, and J. Morris, "Viscoelasticity modelling of the prostate region using vibro-elastography." in *9th MICCAI Conference*. Denmark: MICCAI, Oct 2006, pp. 389–396.

[18] E. Dehghan, X. Wen, R. Zahiri-Azar, M. Marchal, and S. Salcudean, "Needle-tissue interaction modeling using ultrasound-based motion estimation: Phantom study." *Journal of Image Guided Surgery*, vol. 13, pp. 265 – 280, 2008.

[19] H. Eskandari, S. Salcudean, R. Rohling, and J. Ohayon, "Viscoelastic Characterization of Soft Tissue from Dynamic Finite Element Models." *Physics in Medicine and Biology*, vol. 53, pp. 6569–6590, Nov 2008.

[20] H. Eskandari, S. Salcudean, and R. Rohling, "Viscoelastic Parameter Estimation Based on Spectral Analysis." *IEEE Transactions on Ultrasonics, Ferroelectrics, and Frequency control*, vol. 55, pp. 1611–1625, July 2008.

[21] R. Righetti, J. Ophir, S. Srinivasan, and T. Krouskop, "The Feasibility of Using Elastography for Imaging the Poissons Ratio in Porous Media," *Ultrasound in Medicine and Biology*, vol. 30, pp. 215–228, 2004.

[22] A. Thitaikumar, L. Mobbs, C. Kraemer-Chant, B. Garra, and J. Ophir, "Breast Tumor Classification using axial shear strain elastography: a feasibility study," *Physics in Medicine and Biology*, vol. 53, pp. 4809–4823, 2008.

[23] E. Fleury, J. Rinaldi, S. Piato, J. Fleury, and D. Roveda Junior, "Appearance of breast masses on sonoelastography with special focus on the diagnosis of fibroadenomas." *European Radiology*, vol. 19, pp. 1337–46, Jan 2009.

[24] R. Gaspari, D. Blehar, M. Mendoza, M. Montoya, C. Moon, and D. Polan, "Use of Ultrasound Elastography for Skin and Subcutaneous Abscesses." *Journal of Ultrasound in Medicine*, vol. 28, pp. 855–860, 2009.

[25] L. Lvstakken, S. Bjaerum, D. Martens, and H. Torp, "Blood flow imaging–A new real-time, 2-D flow imaging technique." *IEEE Transactions on Ultrasonics, Ferroelectrics and Frequency Control*, vol. 53, pp. 289–99, Feb 2006.

[26] A. Baghani, "A Wave Equation Approach to Ultrasound Elastography," Ph.D. dissertation, University of British Columbia, 2009.

Appendix A

Local Polynomial Fitting

A fourth order polynomial $f(t) = at^4 + bt^3 + ct^2 + dt + e$ can be fitted to the reference echo signal around the ith sample using the following equation:

$$\begin{bmatrix} a \\ b \\ c \\ d \\ e \end{bmatrix} = \begin{bmatrix} 16 & -8 & 4 & -2 & 1 \\ 1 & -1 & 1 & -1 & 1 \\ 0 & 0 & 0 & 0 & 1 \\ 1 & 1 & 1 & 1 & 1 \\ 16 & 8 & 4 & 2 & 1 \end{bmatrix}^{-1} \begin{bmatrix} s_1[i-2] \\ s_1[i-1] \\ s_1[i] \\ s_1[i+1] \\ s_1[i+2] \end{bmatrix}, \tag{A.1}$$

Polynomials with different orders can also be fitted using the same approach.

Appendix B

Strain Signal to Noise Ratio

The signal-to-noise ratio in strain estimation characterizes the noise at which a value of strain is estimated and is defined by:

$$SNR = \frac{m_s}{\sigma_s}, \tag{B.1}$$

where m_s denote the statistical mean strain estimate and σ_s denotes the standard deviation of the strain noise estimated from the strain image.

Appendix C

2D Normalized Cross Correlation

Given a pair of sampled signals $s_1[i,j]$ and $s_2[i,j]$, where i is the sample index and j is the line index, their normalized correlation is defined by (C.2), where $u \in \{-K_a, ..., -1, 0, 1, ..., K_a\}$, $v \in \{-K_l, ..., -1, 0, 1, ..., K_l\}$, K_a, K_l are the search radii, and W_a, W_l represent the window length in both the axial and the lateral directions.

$$
\begin{aligned}
R[u,v] &= \frac{A}{B \cdot C}, \qquad \text{(C.1)} \\
A &= \sum_{j=-W_l/2}^{W_l/2} \sum_{i=-W_a/2}^{W_a/2} (s_1[i,j] \cdot s_2[i+u, j+v]), \\
B &= \sqrt{\sum_{j=-W_l/2}^{W_l/2} \sum_{i=-W_a/2}^{W_a/2} s_1[i,j]^2}, \\
C &= \sqrt{\sum_{j=-W_l/2}^{W_l/2} \sum_{i=-W_a/2}^{W_a/2} s_2[i+u, j+v]^2}
\end{aligned}
$$

Appendix D

1D Sub-Sample Estimation

Given the discrete 1D pattern matching function $R[u]$, the coarse location of the best match can be found in the discrete function (i.e. $d = \arg\max_u R[u]$) within the sampling accuracy. Sub-sample accuracy δ can then be achieved by fitting a local function or polynomial to discrete coefficient values around the best match.

Given the largest sample of the discrete pattern matching function $b = R[d]$, and its two neighbours $a = R[d-1]$ and $c = R[d+1]$, the estimated sub-sample shift $\hat{\delta}$ (correlation peak offset) and its corresponding correlation coefficient at the location $d + \hat{\delta}$ is given by:

$$\hat{\delta} = -\beta/\alpha, \tag{D.1}$$

$$\hat{R}(d+\hat{\delta}) = b/\cos(\beta) \tag{D.2}$$

For 1D cosine interpolation method ($f(x) = A\cos(\alpha x + \beta)$), where:

$$\alpha = \arccos(a + c/2b), \tag{D.3}$$

$$\beta = \arctan((a-c)/2b\sin(\alpha)) \tag{D.4}$$

and by:

$$\hat{\delta} = (a-c)/2(a-2b+c), \tag{D.5}$$

$$\begin{aligned}\hat{R}(d+\hat{\delta}) = {} & a(\hat{\delta})(\hat{\delta}-1)/2 \\ & -b(1+\hat{\delta})(\hat{\delta}-1) \\ & +c(1+\hat{\delta})(\hat{\delta})/2.\end{aligned} \tag{D.6}$$

for 1D parabolic interpolation method ($f(x) = ax^2 + bx + c$).

Appendix E

2D Sub-Sample Estimation

By fitting a local 2D function to discrete coefficient values around the best match (i.e. $[d_a, d_l] = \arg\max_{u,v} R[u,u]$), sub-sample accuracy in both directions (i.e. δ_a, δ_l) can be achieved by locating the exact value of the best match in the fitted 2D function.

E.0.1 2D Paraboloid Fitting

The following non-separable 2D polynomial $f(x,y) = a+bx+cy+dxy+ex^2+fy^2$ can be fitted to the eight points discrete pattern matching function around its maximum (i.e. (d_a, d_l)) using least squares fit according to (E.1). Each row in the 9×6 A matrix in (E.1) comes from setting x, y equal to their relative position with respect to the center (i.e. $x, y \in \{-1, 0, 1\}$) and each element in the 9×1 is the matching coefficient corresponding to the same location. The term $(A^T A)^{-1} A^T$ in (E.1) can be computed in advance and stored in memory for subsequent use. The location of the maximum of this fitted 2D paraboloid is found by setting $\nabla f(x,y) = 0$, leading to:

$$\begin{aligned} \delta_a &= \frac{2bf - dc}{d^2 - 4ef}, \\ \delta_l &= \frac{2ec - bd}{d^2 - 4ef}. \end{aligned} \tag{E.3}$$

E.0.2 2D Polynomial Fitting

Similarly to the above method, the following non-separable 2D polynomial $f(x,y) = a + bx + cy + dxy + ex^2 + fy^2 + gxy^2 + hx^2y + ix^2y^2$, resulted from multiplying $[1, x, x^2]$ and $[1, y, y^2]$ terms, can be fitted to the discrete pattern matching function using the eight points around its maximum (i.e. (d_a, d_l)) according to the (E.2). Each row in the 9×9 A matrix in (E.2) comes from setting x, y equal to their relative position with respect to the center (i.e. $x, y \in \{-1, 0, 1\}$) and each element in the 9×1 is the matching coefficient corresponding to the same location. Similarly to the above method, the inverse of the 9×9 matrix in (E.2) can be computed once and stored in memory for subsequent use. The location of the maximum of this fitted 2D polynomial can be found using a variety of iterative techniques. We use Newton's method:

$$\begin{bmatrix} x \\ y \end{bmatrix}^{k+1} = \begin{bmatrix} x \\ y \end{bmatrix}^{k} - \begin{bmatrix} \frac{\partial^2 f}{\partial x \partial x} & \frac{\partial^2 f}{\partial x \partial y} \\ \frac{\partial^2 f}{\partial y \partial x} & \frac{\partial^2 f}{\partial y \partial y} \end{bmatrix}^{-1} \begin{bmatrix} \frac{\partial f}{\partial x} \\ \frac{\partial f}{\partial y} \end{bmatrix} \Bigg|_{\substack{x=x^k \\ y=y^k}} \tag{E.4}$$

where $k = 0, 1, ..., n$ is the index of the iteration, n is the maximum number of iterations, and $\delta_a = x^n, \delta_l = y^n$. The stopping criterion for Newton's method for estimating the maximum of

$$\begin{bmatrix} a \\ b \\ c \\ d \\ e \\ f \end{bmatrix} = (A^T A)^{-1} A^T \begin{bmatrix} R[d_a-1, d_l-1] \\ R[d_a-1, d_l+0] \\ R[d_a-1, d_l+1] \\ R[d_a+0, d_l-1] \\ R[d_a+0, d_l+0] \\ R[d_a+0, d_l+1] \\ R[d_a+1, d_l-1] \\ R[d_a+1, d_l+0] \\ R[d_a+1, d_l+1] \end{bmatrix}, \quad A = \begin{bmatrix} 1 & -1 & -1 & 1 & 1 & 1 \\ 1 & 0 & -1 & 0 & 0 & 1 \\ 1 & 1 & -1 & -1 & 1 & 1 \\ 1 & -1 & 0 & 0 & 1 & 0 \\ 1 & 0 & 0 & 0 & 0 & 0 \\ 1 & 1 & 0 & 0 & 1 & 0 \\ 1 & -1 & 1 & -1 & 1 & 1 \\ 1 & 0 & 1 & 0 & 0 & 1 \\ 1 & 1 & 1 & 1 & 1 & 1 \end{bmatrix} \tag{E.1}$$

$$\begin{bmatrix} a \\ b \\ c \\ d \\ e \\ f \\ g \\ h \\ i \end{bmatrix} = \begin{bmatrix} 1 & -1 & -1 & 1 & 1 & 1 & -1 & -1 & 1 \\ 1 & -1 & 0 & 0 & 1 & 0 & 0 & 0 & 0 \\ 1 & -1 & 1 & -1 & 1 & 1 & -1 & 1 & 1 \\ 1 & 0 & -1 & 0 & 0 & 1 & 0 & 0 & 0 \\ 1 & 0 & 0 & 0 & 0 & 0 & 0 & 0 & 0 \\ 1 & 0 & 1 & 0 & 0 & 1 & 0 & 0 & 0 \\ 1 & 1 & -1 & -1 & 1 & 1 & 1 & -1 & 1 \\ 1 & 1 & 0 & 0 & 1 & 0 & 0 & 0 & 0 \\ 1 & 1 & 1 & 1 & 1 & 1 & 1 & 1 & 1 \end{bmatrix}^{-1} \begin{bmatrix} R[d_a-1, d_l-1] \\ R[d_a-1, d_l+0] \\ R[d_a-1, d_l+1] \\ R[d_a+0, d_l-1] \\ R[d_a+0, d_l+0] \\ R[d_a+0, d_l+1] \\ R[d_a+1, d_l-1] \\ R[d_a+1, d_l+0] \\ R[d_a+1, d_l+1] \end{bmatrix} \tag{E.2}$$

the 2D polynomial was set to be

$$\left\| \left[\frac{\partial f}{\partial x}, \frac{\partial f}{\partial y} \right]_{\substack{x=x^k \\ y=y^k}} \right\| < 10^{-5}, \tag{E.5}$$

where $\|.\|$ is the Euclidean norm. In all the simulations this criterion was met in less than five iterations (i.e. $\delta_a = x^5, \delta_l = y^5$ in (E.4)).

Appendix F

3D Normalized Cross Correlation

Given a pair of sampled signals $s_1[i,j,k]$ and $s_2[i,j,k]$, their normalized correlation is defined by (F.2), where u, v, w are integers $u \in \{-K_a, ..., K_a\}$, $v \in \{-K_l, ..., K_l\}$, and $w \in \{-K_e, ..., K_e\}$, K_a, K_l, and $K_e \in \mathbb{N}^+$ are the search radii, and W_a, W_l, and W_e represent the window lengths in axial, lateral, and elevational directions.

$$
\begin{aligned}
R[u,v,w] &= \frac{A}{B \cdot C}, \qquad \text{(F.1)} \\
A &= \sum_{k=-W_e/2}^{W_e/2} \sum_{j=-W_l/2}^{W_l/2} \sum_{i=-W_a/2}^{W_a/2} (s_1[i,j,k] \cdot s_2[i+u, j+v, k+w]), \\
B &= \sqrt{\sum_{k=-W_e/2}^{W_e/2} \sum_{j=-W_l/2}^{W_l/2} \sum_{i=-W_a/2}^{W_a/2} s_1[i,j,k]^2}, \\
C &= \sqrt{\sum_{k=-W_e/2}^{W_e/2} \sum_{j=-W_l/2}^{W_l/2} \sum_{i=-W_a/2}^{W_a/2} s_2[i+u, j+v, k+w]^2}
\end{aligned}
$$

Appendix G

3D Polynomial Fitting

The following 3D polynomial with 10 coefficients:

$$\begin{aligned} f_{10}(x,y,z) &= a_1 + a_2x + a_3y + a_4z + a_5xy \\ &\quad + a_6xz + a_7yz + a_8x^2 + a_9y^2 + a_{10}z^2, \end{aligned} \tag{G.1}$$

can be fitted to the 27 points discrete pattern matching function around its maximum (i.e. $[d_a, d_l, d_e]$) using a least-squares fit using (G.2) and (G.3). Each row in the 27×10 matrix in (G.3) is derived by setting x, y, and z equal to their relative positions with respect to the center (i.e. $x, y, z \in \{-1, 0, 1\}$) in the equation for 3D polynomial (i.e. $1, x, y, ..., z^2$) and the values in the 27×1 in (G.2) are the matching coefficients corresponding to these locations. The term $(A^TA)^{-1}A^T$ in (G.3) can be computed in advance and stored in memory for successive use. Other 3D polynomials can also be fitted to the data using the same approach.

$$\begin{bmatrix} a_1 \\ a_2 \\ a_3 \\ a_4 \\ a_5 \\ a_6 \\ a_7 \\ a_8 \\ a_9 \\ a_{10} \end{bmatrix} = (A^TA)^{-1}A^T \begin{bmatrix} R[d_a-1, d_l-1, d_e-1] \\ R[d_a-1, d_l+0, d_e-1] \\ R[d_a-1, d_l+1, d_e-1] \\ R[d_a+0, d_l-1, d_e-1] \\ R[d_a+0, d_l+0, d_e-1] \\ R[d_a+0, d_l+1, d_e-1] \\ R[d_a+1, d_l-1, d_e-1] \\ R[d_a+1, d_l+0, d_e-1] \\ R[d_a+1, d_l+1, d_e-1] \\ R[d_a-1, d_l-1, d_e] \\ R[d_a-1, d_l+0, d_e] \\ R[d_a-1, d_l+1, d_e] \\ R[d_a+0, d_l-1, d_e] \\ R[d_a+0, d_l+0, d_e] \\ R[d_a+0, d_l+1, d_e] \\ R[d_a+1, d_l-1, d_e] \\ R[d_a+1, d_l+0, d_e] \\ R[d_a+1, d_l+1, d_e] \\ R[d_a-1, d_l-1, d_e+1] \\ R[d_a-1, d_l+0, d_e+1] \\ R[d_a-1, d_l+1, d_e+1] \\ R[d_a+0, d_l-1, d_e+1] \\ R[d_a+0, d_l+0, d_e+1] \\ R[d_a+0, d_l+1, d_e+1] \\ R[d_a+1, d_l-1, d_e+1] \\ R[d_a+1, d_l+0, d_e+1] \\ R[d_a+1, d_l+1, d_e+1] \end{bmatrix} \tag{G.2}$$

$$A = \begin{bmatrix}
1 & -1 & -1 & -1 & 1 & 1 & 1 & 1 & 1 & 1 \\
1 & -1 & 0 & -1 & 0 & 1 & 0 & 1 & 0 & 1 \\
1 & -1 & 1 & -1 & -1 & 1 & -1 & 1 & 1 & 1 \\
1 & 0 & -1 & -1 & 0 & 0 & 1 & 0 & 1 & 1 \\
1 & 0 & 0 & -1 & 0 & 0 & 0 & 0 & 0 & 1 \\
1 & 0 & 1 & -1 & 0 & 0 & -1 & 0 & 1 & 1 \\
1 & 1 & -1 & -1 & -1 & -1 & 1 & 1 & 1 & 1 \\
1 & 1 & 0 & -1 & 0 & -1 & 0 & 1 & 0 & 1 \\
1 & 1 & 1 & -1 & 1 & -1 & -1 & 1 & 1 & 1 \\
1 & -1 & -1 & 0 & 1 & 0 & 0 & 1 & 1 & 0 \\
1 & -1 & 0 & 0 & 0 & 0 & 0 & 1 & 0 & 0 \\
1 & -1 & 1 & 0 & -1 & 0 & 0 & 1 & 1 & 0 \\
1 & 0 & -1 & 0 & 0 & 0 & 0 & 0 & 1 & 0 \\
1 & 0 & 0 & 0 & 0 & 0 & 0 & 0 & 0 & 0 \\
1 & 0 & 1 & 0 & 0 & 0 & 0 & 0 & 1 & 0 \\
1 & 1 & -1 & 0 & -1 & 0 & 0 & 1 & 1 & 0 \\
1 & 1 & 0 & 0 & 0 & 0 & 0 & 1 & 0 & 0 \\
1 & 1 & 1 & 0 & 1 & 0 & 0 & 1 & 1 & 0 \\
1 & -1 & -1 & 1 & 1 & -1 & -1 & 1 & 1 & 1 \\
1 & -1 & 0 & 1 & 0 & -1 & 0 & 1 & 0 & 1 \\
1 & -1 & 1 & 1 & -1 & -1 & 1 & 1 & 1 & 1 \\
1 & 0 & -1 & 1 & 0 & 0 & -1 & 0 & 1 & 1 \\
1 & 0 & 0 & 1 & 0 & 0 & 0 & 0 & 0 & 1 \\
1 & 0 & 1 & 1 & 0 & 0 & 1 & 0 & 1 & 1 \\
1 & 1 & -1 & 1 & -1 & 1 & -1 & 1 & 1 & 1 \\
1 & 1 & 0 & 1 & 0 & 1 & 0 & 1 & 0 & 1 \\
1 & 1 & 1 & 1 & 1 & 1 & 1 & 1 & 1 & 1
\end{bmatrix} \tag{G.3}$$